Copyright is owned by the Author of the thesis. Permission is given for a copy to be downloaded by an individual for the purpose of research and private study only. The thesis may not be reproduced elsewhere without the permission of the Author.



MASSEY UNIVERSITY
TE KUNENGA KI PŪREHUROA
UNIVERSITY OF NEW ZEALAND

Real-Time Measurement of Fill Volume in a Vessel Using Optical and Acoustical Means

---

A thesis presented by

Mohammad Amin Barzegar

in partial fulfilment of the requirements for the degree of Doctor of Philosophy in Engineering at Massey University, Manawatū, New Zealand.

Supervised by

Prof. Clive E. Davies

as the primary supervisor, with

Dr Miles C.E. Grafton,

Dr Luke Fullard and

Dr Gabe P. Redding

as co-supervisors.

Jan. 2024

Acknowledgements

I cannot express enough gratitude to my main supervisor, Professor Clive E. Davies, for his invaluable role that extended well beyond that of a supervisor. He has been not just a mentor but also a friend and a pillar of support. Therefore, I can only summarize my profound gratitude with these three simple yet heartfelt words: "Thank you, Clive."

I also deeply appreciate the invaluable guidance I received throughout this research from my co-supervisors, Dr Miles Grafton, Dr Gabe Redding, and Dr Luke Fullard.

My special thanks to Professor Julian Heyes, the former head of the school, whose generous support was vital to my research success. His assistance was especially critical during the pandemic crisis when I was stuck at home, enabling me to return to New Zealand and resume my PhD after nearly two years. The support I received from the GRS office in that regard should be acknowledged as well.

I extend my gratitude to the School of Food and Advanced Technology staff members, including but not limited to Brian Hewson, Karen Pickering, John Edwards, Nicholas Luke, Ann Marie Jackson, and Simon Lookmire. Without their help, this research could not have been accomplished.

I appreciate Professor John Bronlund and Professor Jim Jones, who examined my confirmation report. Their comments and insights into this research have been invaluable.

I am thankful to Massey University for funding this research through the Massey Doctoral Scholarship. I also acknowledge the additional support from the School of Agriculture and Food and Advanced Technology. Many appreciation to Ravensdown for facilitating experiments on a topdressing hopper at their fertilizer store in Whanganui.

I appreciate my friend Saleh Fazeli for his invaluable technical assistance with the 3D drawings and his insights into the project from day one.

My gratitude goes to Vivienne and Tony McGlynn, whose hospitality and support, especially during times of hardship, were priceless. I acknowledge that without their support, I could not have continued my PhD studies.

I appreciate John Askins for being a pillar of support during times of hardship. His support and encouragement have always been like a flash of hope in darkness. I miss the long nighttime walks, chats, movie nights and philosophical discussions.

My very special thanks are reserved for my mother, Fatemeh AsnaAshari, my father, Mahdi, and my two sisters, Somayeh and Faezeh, back home. They all have been a source of courage and strength. I would like to appreciate Ehsan Hazaveh, my best friend, for consistently being a source of strength and encouragement throughout my PhD studies.

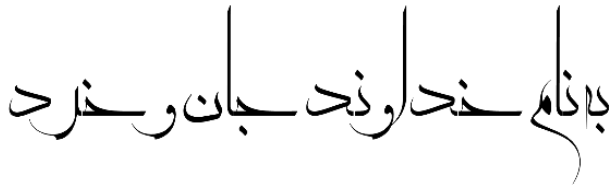
I must extend special acknowledgement to my mother, Fatemeh, who during the first year of my PhD, chose not to disclose the full extent of her health's fragility. This selfless act was made to ensure that I could remain in New Zealand and fully concentrate on my confirmation report.

I extend my thanks to everyone who was involved directly or indirectly in this project. Your contributions have been invaluable.

Last but not least, due to personal and family related circumstances, my PhD journey has been extraordinarily challenging and unique, with moments when dropping my studies seemed inevitable. What I learned the hard way was: "Every dusk has a dawn." I wish strength and success to all international students in their respective journeys.

Sincerely, this PhD thesis is dedicated to Narges Z.

M.Barzegar, 2023.



"*in the name of the architect*

of soul and wisdom" Ferdowsi

Abstract

This thesis investigates optical and acoustical methods for quickly determining the fill volume in cavities, vessels, or hoppers. The motivation for this study was the demand in the New Zealand aerial topdressing industry for a system that can accurately track the fill volume of vessels containing powders. A notable challenge in this industry is that topdressing aircraft lack systems for measuring the volume of discharge vessels during flight, leading to issues with flight safety and operational efficiency. This thesis specifically addresses the challenge of real-time fill volume determination in hoppers within New Zealand's aerial topdressing industry. Additionally, the outcomes of this thesis may offer insights and applicable methods for other industrial and scientific sectors that require real-time, contactless volume determination techniques.

Three contactless volume measurement approaches were investigated: ultrasonic range-finding, 3D scanning, and acoustical resonance. The first approach used an array of ultrasonic rangefinders installed in a 200-litre powder-containing vessel, resulting in material level readings from multiple points. This technique was tested under discharge and no-flow conditions. According to the results, this method provided readings of the vessel fill volume with a measurement rate of ~1 Hz and an uncertainty of ~3% of the vessel capacity.

The second approach used stereoscopic technique to provide real-time scans of the material surface in the vessel. A model was developed for calculating the volume of material in the vessel using the vessel internal scans. According to the test results on different bulk materials under discharge and no flow conditions for two vessels of sizes 50 and 200 litres, the real-time fill volume of the vessel was obtained with uncertainties less than 1% of the vessel's volume.

The third approach explored Helmholtz Resonance for determining the volume of powders and solids. This involved studying the impact of inserting a sample into Helmholtz Resonators on resonance parameters. Three models were developed for volume estimation: an extended Helmholtz Resonance model modifying the classical equation for resonators with long ports, a model for estimating solid volume in powders based on resonance frequency and quality factor, and a model for instantaneous volume measurement of a vessel's empty cavity using Helmholtz Resonance. The latter correlated the change in cavity sound pressure to its volume, showing it could accurately determine volume in real-time with less than 0.1% error relative to the vessel capacity.

Nomenclature

**All the symbols are defined locally in the text*

Symbol	Definition	Unit
$\%V_0$	Percent of Hopper/Vessel capacity	%
A	Application rate (Chapter 1)	kg.hectare^{-1}
$A(z_s)$	The cross-sectional area of the hopper at depth z_s	m^2
A_d	Displacement amplitude in driven oscillation	m
A_m	Missed area from the scanner	m^2
B	The baseline of image sensors	m
C	Cell side length	m
c	Speed of sound	m.s^{-1}
c_{T1}	Speed of sound in temperature *T1*	m.s^{-1}
c_{T2}	Speed of sound in temperature *T2*	m.s^{-1}
$C^2(f)$	Coherence index	-
D	Vessel diameter (Chapter 2)	m
d	The disparity of a pixel between image sensors	m
$D[3,2]$	Sauter mean diameter	m
F	Focal Length (Chapter 3)	m
f	Frequency	Hz
FF	Resonator Fill Factor 0~1. Indicates the fill level of a resonator	m^3.m^{-3}
FOV	Field of view	deg.
$FWHM$	Full Width at Half Maximum in Spectral Analysis	Hz
H	Vessel height (Chapter 2)	m
H	Point cloud height (Chapter 3)	m
$H(f)$	Complex Transfer Function in the frequency domain	-
h_i	Detected range from an ultrasonic sensor (Chapter 2)	m
I	Cell column number	-
i	Point number	-
J	Cell row number	-
K	The restorative constant of the air in the resonator cavity	N.m^{-1}
k_r	Resonance wavenumber	m^{-1}
k_0	Resonance wavenumber of the empty resonator	m^{-1}
L	swath width (Chapter 1)	m
L	Point cloud length (Chapter 3)	m
L	Cavity Length (Chapter 4)	m
l	Resonator port length	m
$l(i)$	An indicator function for the validity of point *i*	-
$L(I,J)$	An indicator function for the validity of the cells (*I, J*)	-
$l(z_s)$	An indicator function indicating the validity of a point	-
L'	Elonged path	m
m	The mass of air in the resonator port	kg
$\dot{m}$	mass flow rate	kg.s^{-1}
N	Count of available cells	-
n	Count of available neighbouring cells to a specific cell	-
$\bar{P}$	The ratio of sound pressure after inserting a sample inside the resonator to the resonator sound pressure when empty	-
Q	Resonance Quality Factor	-
r	Port radius	m
R	The complex acoustic reflection coefficient	-
R_M	Acoustic energy loss in the port due to viscous, thermal and radiation resistance	kg.s^{-1}

S_p	The cross-sectional area of the Port	m^2
S_v	The cross-sectional area of the cavity	m^2
$S_{rp(f)}$	Complex cross-power spectrum between the reference and port microphones	V^2
S_{XX}	Represents the power spectral density (PSD) of a signal	V^2
$S_{rr}(f)$	Auto power spectrum of the source microphone	V^2
T	Sinusoidal wave period (Section 4.3.13)	s
T	Air Temperature	°C
t	Time	s
TOF	Sound Time of Flight	s
V	Cavity volume	m^3
V_F	Hopper Fill Volume	m^3
v	Voltage	v
V_0	Vessel, hopper or cavity capacity	m^3
V_A	Actual solid, liquid or cavity volume	m^3
V_b	Bulk volume	m^3
V_c	Cavity volume	m^3
V_E	Hopper/Vessel free volume	m^3
v_g	Aircraft speed	$m.s^{-1}$
V_i	Volume element under the sensor S_i	m^3
V_s	Sample Volume	m^3
V_W	Volume obtained by weighing	m^3
$VFOV$	Vertical field of view	deg.
z	Distance from camera origin to an object	m
$Z_{I,J}$	Surface element average depth	m
$z_{x,y}$	Point coordination	m
Z_{full}	The minimum depth that the optical system provides a full view of the material surface	m
Z_{min}	The minimum range of the stereoscopic scanner	m
Z_s	Minimum distance from the scanner origin to the material surface	m
	---- Greek Letters ----	
α	Resonator geometrical constant	$m^{0.5}$
α	Angle of Repose	deg.
α_0	Tortuosity	-
β	The angle of sensor installation relative to the horizon	deg.
Γ	Damping Constant	s^{-1}
γ	The ratio of molar heat capacity	$J.K^{-1}\ mol^{-1}$
δ	Origin distance of the paired scanners	m
δV	cavity air volume change due to resonance	m^3
ε	The rate of change of the resonance Quality Factor with the volume of powders	m^{-2}
ζ	Damping Ratio	-
λ	wavelength	m
v	Apparent velocity of sound in the bed of particles	$m.s^{-1}$
ρ	Air density	$kg.m^{-3}$
ρ_A	Density	$kg.m^{-3}$
ρ_{bLP}	Loose bulk density	$g.ml^{-1}$
ρ_{bT}	Tapped bulk density	$g.ml^{-1}$
ρ_p	Particle solid density	$g.ml^{-1}$
σ	Deviation Index	-
$\sigma_{I,J}$	The standard deviation of depth in cell *(I, J)*	m
ϕ	Phase shift	rad.
ϕ	Porosity (void fraction) of powder sample bulk, not to be mistaken with ϕ: phase shift	$m.m^{-1}$
φ_0	Phase mismatch at resonance	°
ϕ_z	Vessel diameter at depth z_s (Chapter 3)	m

$\boldsymbol{\psi}$	The decay rate of displacement in the solution of the oscillation equation	
$\boldsymbol{\Omega}$	An experimentally obtained constant for a Resonator through line fit (Chapter 6)	m^2
$\boldsymbol{\omega}$	Angular Frequency	$rad.s^{-1}$
$\boldsymbol{\omega_n}$	Natural Frequency	$rad.s^{-1}$
$\boldsymbol{\omega_d}$	Frequency of underdamped undriven oscillation	$rad.s^{-1}$
$\boldsymbol{\omega_r}$	Frequency of underdamped driven oscillation	$rad.s^{-1}$
$\boldsymbol{\omega_0}$	The resonance frequency of the empty resonator	$rad.s^{-1}$
$\boldsymbol{\omega_{0T1}}$	The empty resonator resonance frequency at T1	$rad.s^{-1}$
$\boldsymbol{\omega_{0T2}}$	The empty resonator resonance frequency at T2	$rad.s^{-1}$
$\Delta\boldsymbol{l}$	Port length extension factor	m
$\Delta\boldsymbol{TOF}$	Increased Time of Flight due to the tortuose path in a bed of particles	s
$\Delta\boldsymbol{t}$	Zero-crossing time diffrence	s

Glossary

B250	Fine ballotini sample.
B710	Coarse ballotini sample.
CI.95	95% Confidence Interval (Error Analysis Equations).
Darcy	Permeability unit defined by Darcy's law with length dimension.
Chirp	A type of sound characterized by a steady, sweeping frequency increase or decrease over time.
Fill Factor	Indicates the fill level of a vessel/cavity as the ratio of bulk fill volume to the vessel/cavity volumetric capacity.
Litre	Cubic decimeter, a French metric system unit accepted for SI units with the symbol (*l*).
Mains Hum	A low-frequency noise emitted by electrical devices, often due to the alternating current power supply.
Parity Graph	A graph comparing two measurement methods, typically estimated versus actual values, is presented. The proximity of the observed data points to the Parity Line indicates the level of correlation and the accuracy of the measurement method.
PersPex	A trademark for a manufacturer of plastic material using Polymethyl Methacrylate.
PE1	Small polyethylene sample.
PE2	Large polyethylene sample.
PI.95	95% Predictive Interval (Error Analysis Equations).
PVC	Polyvinyl chloride, a synthetic polymer that can be used to create both hard and soft plastics.
Quality Factor	The relationship between stored energy and dissipated energy in one radian of oscillation.
RS232	Recommended Standard 232 for serial communication.
Span	Resonance frequency range covering a Fill Factor of zero to a Fill Factor of one.
White Noise	A type of random noise that is produced by combining sounds of all different frequencies. In white noise, every frequency across the spectrum has equal intensity or power.

Abbreviations

AL	*Agricultural Lime*
BB	*ball bearings*
CAA	*Civil Aviation Authority*
DAQ	*Data Acquisition Card*
DM	*Driven Method*
DGPS	*Differential Global Positioning System*
DFT	*Discrete Fourier Transform*
DPF	*Depth Penetration Factor*
EHR	*Extended Helmholtz Resonance*
FF	*Fill Factor*
FFT	*Fast Fourier Transform*
FTF	*Fourier Transform Function*
IC	*Integrated Circuit*
IR	*Infrared*
LMB	*large marbles*
LP	*Loose Poured*
LiDAR	*Light Detection and Ranging.*
LP	*Loose Poured*
PAL	*Pacific Aerospace Limited*
PSD	*Power Spectral Density*
MED	*Minimum Entropy Deconvolution*
MFF	*Maximum Fill Factor*
MLVM	*Multi-Level Volume Measurement*
MS	*mustard seeds*
QPS	*Quality Profile Shifting*
OFV	*Optical Fill Volume*
QWR	*Quality Wavelength Resonance*
RGB	*Red, Green, Blue*
RO	*Reverse Osmosis*
SDK	*Software Development Kit*
SMB	*Small Marbles*
SMD	*Sauter Mean Diameter*
SPQF	*Sound Pressure Quality Factor*
TF	*Transfer Function*
TOF	*Time of flight*
TSR	*Time in Service Recorder*
UM	*Undriven Method*

Basic Equations

Classical Helmholtz Resonance Equation	$f = \frac{c}{2\pi}\sqrt{\frac{S_p}{V_c l_p}}$	c: Speed of Sound S_p: Port Cross Sectional area l_p: Port Length V_c: Cavity Physical Volume
Classical Helmholtz Resonance Equation based on the resonance wavelength	$\boldsymbol{\lambda}^2 = \frac{1}{\alpha^2}V$	λ: Resonance Wavelength V: Empty Volum α: Resonator geometrical constant
Port Length Correction Factor	$\Delta l = 0.6r + \frac{8}{3\pi}r$	r: Port Radius
Resonator Fill Factor	$FF = \frac{V_b}{V_c}$	V_b: Sample Bulk Volume
Speed of Sound	$c = 331.73 + 0.587T$	T: temperature in °C
Damping Ratio	$\zeta = \frac{1}{2Q}$	Q: Quality Factor
Quality Factor	$Q = \frac{\omega_n}{FWHM}$	ω_n: Natural Frequency $FWHM$: Full-Width-at-Half-Maximum
Sound wavelength	$\lambda = \frac{c}{f}$	
Resonator geometrical constant	$\alpha = \frac{1}{2\pi}\sqrt{\frac{S_p}{(l_p + \Delta l)}}$	

Error Analysis Equations

Mean error of measurement ($\bar{E}$)	$\bar{E} = \frac{1}{n}\sum_{i=1}^{n}(V_i - \hat{V}_i)$	$\bar{E}$: Mean Error n: Number of measurements V_i: Actual value $\hat{V}_i$: Estimated value

Calculated the mean error between the estimated and actual values in parity graphs and where there are several volume estimations in a range of scales.

Standard deviation of Mean Error (SD)	$SD = \frac{1}{n-1}\sum_{i=1}^{n}(E_i - \bar{E})^2$	E_i: Error of the ith measurement

Describes how the individual measurement errors are scattered around the mean error; a descriptive method for presenting measurement precision.

Confidence interval of $\bar{E}$ ($CI.95$)	$CI.95 = \bar{E} \pm (t \times \frac{SD}{\sqrt{n}})$	t: critical t-value

Estimates the uncertainty in measurement mean error based on a 95% confidence interval.

Predictive interval ($PI.95$)	$PI.95 = \bar{E} \pm (t \times SD\sqrt{1 + \frac{1}{n}})$	

Estimates the error boundary of individual future measurements based on a 95% prediction interval.

Mean deviation of the estimated volume and actual volume based on percentage of vessel/cavity capacity $\%V_0$	$MD\% = \frac{100}{n}\sum\frac{\lvert V_i - \hat{V}_i\rvert}{V_0}$	V_0: *Vessel or cavity capacity*

Describes the absolute mean value of the deviation of actual values and estimated values based on vessel capacity when there are multiple observations or repeated experiments.

Deviation of the estimated volume and actual volume based on the percentage of vessel/cavity capacity $\%V_0$	$D\% = 100\frac{\lvert V_i - \hat{V}_i\rvert}{V_0}$	

Describes the absolute value of the deviation of actual value and estimated value based on vessel capacity.

Table of Contents

Abstract i
Nomenclature ii
Glossary v
Abbreviations vi
Basic Equations vii
Error Analysis Equations viii
Table of Contents ix
Table of Figures xvii
Table of Tables xxii
Chapter 1 Introduction and Literature Review 1
1.1. Introduction 2
1.1.1. Research Aim 5
1.2. Literature Review 7
1.2.1. The problem of fill volume determination in topdressing hoppers 7
1.2.2. Fill volume measurement by weighing 7
1.2.3. Use of Ultrasonic Sensors in fill volume measurement 8
1.2.4. Use of air pycnometers in fill volume determination 10
1.2.5. Helmholtz resonance 10
1.2.6. Non-ideal behaviour in a Helmholtz Resonator 17
1.2.7. Degree of fill measurement by stereo-digital image correlation 17
1.2.8. Methods for Fill Volume determination of silos 19
1.3. Research Questions 20
1.4. Summary 21
Chapter 2 Measurement of a Vessel Fill Level Using Ultrasonic Range Finders 22
2.1. Introduction 24
2.2. Materials 24
2.2.1. Ultrasonic Range Finders 24
2.2.2. Experimental apparatus 25
2.2.3. Software and hardware interface 26

2.2.4. Test sample 27
2.2.5. Scale Calibration 27
2.3. Methods 28
2.3.1. Fill Volume Determination 28
2.3.2. Experiment Procedure 31
2.4. Static Tests 31
2.5. Discharge Test 31
2.6. Results 31
2.6.1. Ultrasonic Sensor Calibration 32
2.6.2. Static Tests 33
2.6.1. Discharge Test 36
2.6.2. Estimation of flowrate from the volumetric data 37
2.7. Discussion 38
2.7.1. Sources of error in the sensors 38
2.7.2. The disparity in static tests 40
2.7.3. Discharge Test 40
2.7.4. Sensor Count 41
2.7.5. Sensor Position 41
2.8. Summary 43
Chapter 3 Measurement of vessel fill volume using optical imaging 45
3.1. Introduction 47
3.2. Materials 48
3.2.1. The Scanner 48
3.2.2. Storage vessels 48
3.2.3. Software 50
3.2.4. Test Material 51
3.3. Methods 52
3.3.1. The Model 52

3.3.2. Unified point cloud for two synchronized cameras 58
3.3.3. Computations 58
3.3.4. Experiment Procedure 59
3.4. Results 60
3.4.1. Experiments on the 50-litre vessel 60
3.4.2. Experiments with the 200-litre vessel 65
3.5. Discussion 67
3.5.1. Implementation of this concept in a topdressing aeroplane hopper 68
3.6. Summary 71
Chapter 4 Helmholtz Resonance 73
4.1. Introduction 75
4.1.1. Classical Helmholtz Resonance Therory 75
4.1.2. Resonance models for dimensions comparable to the resonance wavelength 76
4.1.3. Mass-Spring analogy 77
4.1.4. Undriven Damped Oscillation 79
4.1.5. Driven underdamped oscillation 82
4.1.6. Excitation 84
4.1.7. Resonator Frequency Hunting 85
4.1.8. Sound absorption in porous media 86
4.1.9. Sound absorption measurement using impedance tube 87
4.2. Materials 89
4.2.1. Small Scale Resonators (1, 2 and 3 litres) 89
4.2.2. Small Scale Resonator Ports 90
4.2.3. 50-litre Vessel 90
4.2.4. Topdressing hopper 91
4.2.5. Microphone 92
4.2.6. Sound Source Drivers 93
4.2.7. Temperature measurement 93

4.2.8. Data Acquisition Hardware 93
4.2.9. Software 94
4.2.10. Impedance Tube 94
4.2.11. Test Material 97
4.3. Methods 98
4.3.1. Resonance Hunting Method 1: Undriven 98
4.3.2. Resonance Hunting Method 2: Driven 98
4.3.3. Resonance Hunting Method 3: Transfer Function 100
4.3.4. Resonant frequency hunting in the 50-litre vessel 102
4.3.5. Resonance frequency detection in the topdressing hopper 102
4.3.6. Testing for non-linearities in the 3-litre lab-scale resonator 103
4.3.7. Volume determination using various ports and resonance hunting methods 104
4.3.8. Static volume measurement tests on powders 105
4.3.9. Dynamic resonance hunting using the lab-scale resonator 106
4.3.10. Quality factor assessment 107
4.3.11. Effect of powders on quality factor 108
4.3.12. Acoustic energy absorption tests 108
4.3.13. Compression uniformity test 109
4.3.14. Sound wave penetration speed 110
4.4. Results 112
4.4.1. Resonant frequency hunting in the 50-litre vessel 112
4.4.2. Resonant frequency detection in the topdressing hopper 116
4.4.3. Testing for non-linearities in the lab-scale resonator 117
4.4.4. Comparing ports and resonance hunting methods 119
4.4.5. Static volume measurement tests on particles 125
4.4.6. Dynamic resonance hunting using the 3-litre lab-scale resonator 136
4.4.7. Port length effect on the resonance quality 138
4.4.8. Effect of powders on quality factor 143

4.4.9. Acoustic Energy Absorption tests 148
4.4.10. Compression uniformity 151
4.4.11. Sound wave penetration speed 153
4.5. Discussion 157
4.5.1. Resonant frequency hunting in the 50-litre vessel 157
4.5.2. Resonant frequency detection in the Airplane hopper 158
4.5.3. Resonance non-linearity in the 3-litre resonator 158
4.5.4. Comparing ports and resonance hunting methods 159
4.5.5. Static volume measurement tests 160
4.5.6. Dynamic resonance hunting using the 3-litre lab-scale resonator 161
4.5.7. Port length effect on the resonance quality 161
4.5.8. Effect of powders on quality factor 163
4.5.9. Acoustic Energy Absorption Tests 163
4.5.10. Compression uniformity test 165
4.5.11. Sound wave penetration speed 166
4.6. Summary 168
Chapter 5 Extended Helmholtz Resonance model 170
5.1. Introduction 172
5.2. Model Development 173
5.3. Experimental Data 178
5.4. Results 180
5.4.1. Model Verification 180
5.4.2. Solids and powders volume measurement 182
5.5. Discussion 186
5.5.1. Model Verification 186
5.5.2. Solids and powders volume measurement 187
5.6. Summary 189
5.6.1. Summary of the Models developed in this chapter 190

Chapter 6 A semi-empirical model for solid volume measurement 192
6.1. Introduction 194
6.2. Experimental Data 195
6.3. Model Development 195
6.4. Model Verification 200
6.5. Discussion 203
6.6. Summary 204
6.6.1. Summary of the Model developed in this chapter 205
Chapter 7 A model for Instantaneous sample volume measurement 206
7.1. Introduction 207
7.2. Model Development 208
7.3. Materials 216
7.3.1. Resonator 216
7.3.2. Variable Chamber Resonator 217
7.3.3. Test Materials 218
7.4. Methods 220
7.4.1. Resonator calibration process 220
7.4.2. Experiments for model verification 222
7.4.3. Discharge Tests on powders 222
7.4.4. Experiments on the Variable Chamber Resonator 223
7.5. Results 223
7.5.1. Volume estimation of discharging water 223
7.5.2. Volume Estimation of solids 226
7.5.3. Variable Chamber Resonator 230
7.5.4. Dynamic volume measurement of powders 232
7.6. Discussion 236
7.6.1. Model Verification 236
7.6.2. Experimental approach for estimating the resonator Fill Factor 237

7.6.3. A technical note on using microphones with limited dynamic range 238
7.6.4. Determination of liquid flowrate 242
7.6.5. Other possible applications 243
7.7. Summary 245
7.7.1. Summary of the Model developed in this chapter 246
Chapter 8 Conclusion and Recommendations 247
8.1. Overview of the thesis 249
8.2. Fill Volume determination using UltraSonic range finders 251
8.3. Fill Volume determination using the stereoscopic technique 252
8.4. Helmholtz Resonance of a vessel filled with powders 253
8.4.1. Resonance Hunting Using Transfer Function Method 254
8.4.2. Resonance hunting in dynamic discharge tests 254
8.4.3. Compression Non-Uniformity 255
8.4.4. Resonance Quality Factor Measurement 255
8.4.5. Effect of powders on resonance Quality Factor 256
8.4.6. Speed of sound in the bed of particles 256
8.4.7. Extended Helmholtz Resonance Model 256
8.4.8. Estimation of volume of powders using the EHR Model 257
8.4.9. Categorization of powders in terms of acoustic response 258
8.4.10. Quality Wavelength Resonance (QWR) model 259
8.4.11. Instantaneous volume determination using the (SPQF) model 259
8.5. Questions Answered 261
8.5.1. Using Ultrasonic technology in a vessel fill volume measurement 261
8.5.2. Using stereoscopic optical technology in hopper fill volume measurement. 262
8.5.3. Fill-volume measurement of a vessel using Helmholtz Resonance 263
8.6. Future Study 265
Appendices 268
Appendix A: Flowcharts 269

Appendix B: Calculations 271

Appendix C: Technical information 275

Appendix D: Physical properties of the test materials 278

Appendix E: Drawings 283

Appendix F: Pictures 290

References 296

Table of Figures

Figure 1-1: Thesis Diagram 6
Figure 1-2: A Helmholtz Resonator 11
Figure 1-3: A schematic diagram of an automatic and continuous 12
Figure 1-4: Body volume measurement using a Helmholtz Resonator 13
Figure 1-5 Schematic of the apparatus for measuring liquid nitrogen's volume 15
Figure 1-6 Load speaker coil response (Nakano et al., 2006) 15
Figure 1-7 Depth from stereo image correlation. 19
Figure 2-1: Storage and Discharge vessel apparatus with the ultrasonic range-finder sensors 25
Figure 2-2 Scale calibration plot 27
Figure 2-3: Maximum distance between the vessel's cover plate and 29
Figure 2-4: Dividing the vessel's cross-sectional area into nine segments equal in area. 30
Figure 2-5: A preliminary test comparing sensor reading with tape measure reading 32
Figure 2-6: The position of ultrasonic sensors on the vessel's cover plate 33
Figure 2-7: Static sample volume determination in the 200-litre vessel. 34
Figure 2-8: Static sample volume determination in the 200-litre vessel. 35
Figure 2-9 Static sample volume determination in the 200-litre vessel. 35
Figure 2-10: Fill Volume measurement in dynamic discharge test of polyethylene 36
Figure 2-11: Fill Volume measurement in dynamic discharge test of polyethylene 37
Figure 2-12: Flowrate of the sample out of the vessel. 38
Figure 2-13: Possible scenarios in reflection of the ultrasound 39
Figure 2-14: Volume estimation disparity in the static tests. 40
Figure 2-15: Discharge test results when using various numbers of sensors 42
Figure 3-1: The 50-litre vessel. VFOV: Vertical Field of View 49
Figure 3-2: 200-litre vessel. Dimensions in millimetres. 50
Figure 3-3: 3D Printed Housing for the two sensors in 200-litre vessel experiment. 51
Figure 3-4: Field of View (FOV) of a depth camera in a hopper 52
Figure 3-5: An example of a point cloud captured from the material 53
Figure 3-6: An example of a point cloud captured from the surface 53
Figure 3-7: Breaking the depth camera projected field of view into matrix elements. 55
Figure 3-8: Side view of a surface element with dimension 56
Figure 3-9: The missed area from the surface grid from the hopper cross-section 57
Figure 3-10: Error distribution analysis for repeated measurement of the vessel empty volume 60
Figure 3-11: Comparison between the optically measured volume 61

Figure 3-12: Dynamic test on mustard seeds discharging from the 50-litre vessel 62
Figure 3-13: Dynamic test on mustard seeds dumping from the 50-litre vessel..... 62
Figure 3-14: Flowrate of sample mustard seeds out of 26 mm orifice 63
Figure 3-15: Visualisation of discharge profile; mustard seeds, 50 mm orifice. 64
Figure 3-16: (A): Comparison of the vessel fill volume..... 65
Figure 3-17: Dynamic discharge test of the polyethylene sample 66
Figure 3-18: Flowrate of polyethylene pellets out of the vessel 66
Figure 3-19: Keeping the optics clean using pressurized air surrounding the optics. 68
Figure 3-20: Implementation of the double-depth camera system in a topdressing aeroplane 69
Figure 4-1: An example to compare physical port (Solid port) and effective port (Dashed port)... 76
Figure 4-2: Mass-Spring analogy of a Helmholtz Resonator..... 77
Figure 4-3: Oscillation model of a Helmholtz Resonator (unforced)..... 79
Figure 4-4: Signal decay in an underdamped, undriven resonance 80
Figure 4-5: Natural logarithm of resonance amplitude peaks versus time. 81
Figure 4-6: Normalized amplitude versus driver frequency 82
Figure 4-7: Phase Shift $\boldsymbol{\phi}$ between driver and resonator for different quality factors..... 83
Figure 4-8: A two-microphone impedance tube 88
Figure 4-9: The modular Perpex Resonator..... 90
Figure 4-10: 50-litre resonator. Dimensions in mm..... 91
Figure 4-11: Topdressing hopper used as a Helmholtz Resonator. 92
Figure 4-12: Estimated resonant frequency range of the topdressing hopper..... 92
Figure 4-13: The Impedance Tube..... 95
Figure 4-14: Impedance tube electronics..... 96
Figure 4-15: Undriven Resonance Frequency Hunting..... 98
Figure 4-16: Driven resonance frequency Hunting method..... 99
Figure 4-17: Resonance frequency hunting using Fourier Transfer Function 101
Figure 4-18: Experimental setup for resonance frequency hunting 103
Figure 4-19: The dynamic resonance frequency hunting 107
Figure 4-20: Phase Mismatch between the top and bottom microphone 109
Figure 4-21: Sound velocity measurement apparatus..... 110
Figure 4-22: Resonance frequency and the sound pressure change of the 50-litre vessel..... 112
Figure 4-23: Linear fit of resonant frequency vs $1.v^{-2}$..... 113
Figure 4-24: Acoustically measured fill volume of the 50-litre vessel 114
Figure 4-25: Resonance frequency and sound pressure tracking..... 115

Figure 4-26: Resonant frequency change of the topdressing aeroplane hopper 116
Figure 4-27: Resonant frequency change of the topdressing aeroplane hopper 117
Figure 4-28: Water volume measurement in the 3-litre resonator 118
Figure 4-29: Distribution of volume estimation deviation 118
Figure 4-30: Resonance response of the 2-litre resonator with various port lengths. 119
Figure 4-31: Water volume estimation using Classical Helmholtz Resonance 122
Figure 4-32: Absolute Error of water sample volume estimation 123
Figure 4-33: Resonance Wavelength squared vs. cavity empty volume 124
Figure 4-34: Transfer Function magnitude change versus resonator fill factor 125
Figure 4-35: Resonance Frequency hunted for large marble Sample 126
Figure 4-36: Resonance Frequency hunted for ball bearings (BB) sample vs Fill Factor. 127
Figure 4-37: Ball bearings solid sample volume estimation using the 2-litre resonator 129
Figure 4-38: Resonance Frequency hunting for fine ballotini Sample vs Fill Factor. 130
Figure 4-39: Resonance amplitude decay versus resonator Fill Factor. 131
Figure 4-40: Effect of bed packing on resonance shift. 133
Figure 4-41: Comparison of resonance frequencies hunted 134
Figure 4-42: Normalised resonance amplitude comparison 135
Figure 4-43: Dynamic tests on resonance wavelength tracking 137
Figure 4-44: Signal Response from the 2-litre resonator 139
Figure 4-45: Port Root Microphone signal, 1000 mm Port, Driven Resonance. 140
Figure 4-46: Power Spectral Density of Driven Resonance Signal 141
Figure 4-47: Quality factor for driven resonance vs Speaker Level 141
Figure 4-48: Phase shift between the driver and the resonator port microphone signals 142
Figure 4-49: Quality factor comparison between Water and agricultural lime samples 143
Figure 4-50: Resonance Quality vs Fill Factor for the six samples mentioned in the graphs 144
Figure 4-51: Resonance quality measured using Undriven and Driven methods Fill Factor. 145
Figure 4-52: Driven Resonance Quality Factor when the resonator is full 146
Figure 4-53: Phase Shift between driver and resonator signal vs resonance frequency 147
Figure 4-54: Normal Incident Sound Absorption for fine sand (FS) Sample. 148
Figure 4-55: Normal Incident Sound Absorption for fine ballotini (B250) Sample 149
Figure 4-56: Normal Incident Sound Absorption for coarse ballotini (B710) Sample.. 149
Figure 4-57: Normal Incident Sound Absorption for black mustard seeds (BMS) Sample 150
Figure 4-58: Normal Incident Sound Absorption for ball bearings (BB) Sample 151
Figure 4-59: Pressure signal phase mismatch 152

Figure 4-60: Pressure phase mismatch between. 153
Figure 4-61: Verification of the speed of sound measurmeent apparatus 154
Figure 4-62: Time of flight measurement 155
Figure 4-63: Non-uniformity in air compression 166
Figure 5-1: Numerical approximation 175
Figure 5-2: Comparision of the estimated wavenumber 176
Figure 5-3: Comparison of estimated fill factor versus actual fill factor. 180
Figure 5-4: Average deviation of the estimated volume from the actual volume 181
Figure 5-5: Resonance Wavelength squared vs cavity empty volume 182
Figure 5-6: Estimated solid volume V_S vs actual solid volume V_{A} 183
Figure 5-7: Volume fraction of the samples vs. Fill Factor of the resonator. 185
Figure 6-1: Estimated sample volumes V_S vs the actual values V_A with trendlines. 196
Figure 6-2: The linear trend (Dashed Line) of resonance quality factor 198
Figure 6-3: The linear relationship between the Deviation Index and 199
Figure 6-4: Estimated sample solid volume from the QWR model 201
Figure 6-5: Sample No.7 (Left) and Sample No.5 (Right) 203
Figure 7-1: A Helmholtz Resonator analogous to a mass-spring-damper system 208
Figure 7-2: Two resonator states before and after putting a sample with volume $\mathrm{V_s}$ into it. 211
Figure 7-3: Numerical comparison of the Full model vs. its approximated form 214
Figure 7-4: Resonator Apparatus for static and discharge experiments. 217
Figure 7-5: Variable Chamber Resonator apparatus. All dimensions are in mm. 218
Figure 7-6: Quality Factor and Resonance Frequency from power spectral analysis. 221
Figure 7-7: Normalized sound pressure ratio versus estimated resonance frequency 224
Figure 7-8: Water volume prediction using the model 225
Figure 7-9: Error analysis of the estimated volume 225
Figure 7-10: The change in $log\ (\overline{\mathbf{P}})$ with increasing cavity Fill Factor using solid marbles 226
Figure 7-11: Estimated volume of marbles in the 3-litre resonator. 227
Figure 7-12: Absolute error in volume estimation of marbles 227
Figure 7-13: Volume estimation of marbles in the 1-litre resonator.. 228
Figure 7-14: Estimation of cavity volume in the variable chamber resonator 230
Figure 7-15: Estimation of cavity volume in the variable chamber resonator 231
Figure 7-16: Estimating cavity volume in the variable chamber resonator 232
Figure 7-17: Amplitude variation based on the fill level of the resonator 233
Figure 7-18: The estimated discharged mass 234

Figure 7-19: Repeatability of sample mass estimation..... 235
Figure 7-20: Solid volume of marbles estimated using an array microphone..... 241
Figure 7-21: Measured Sound Pressure Level vs. occupied solid volume 242
Figure 7-22: *Flowrate estimation of water*..... 240

Table of Tables

Table 3-1:Physical properties of the test material 51
Table 3-2: Average volumetric flowrate comparison 64
Table 4-1: Physical Properties of the variety of the test materials. 97
Table 4-2: Resonance frequency range for the 2-litre resonator at 343 °c 99
Table 4-3: Frequency response of the 2-litre resonator. 120
Table 4-4: Maximum Fill Factor at which resonance frequency was possible to hunt (MFF). 132
Table 4-5: Sample Volume as a function of resonance wavelength 136
Table 4-6: The effect of air leak in the resonator on resonance hunting parameters 147
Table 4-7: Sound propagation analysis 154
Table 5-1: Comparison of three algebraic equations of Helmholtz Resonance and their scope .. 177
Table 5-2: Depth Penetration Factor for selected tapped and loosely packed materials. 184
Table 5-3: A comparison between particle diameter and measured volume deviation 186
Table 6-1: Deviation Index of the samples tested 197
Table 6-2: Rate of change of quality factor with resonance wavelength squared 198
Table 6-3: Mixed samples and estimated solid volumes. 202
Table 7-1: Agricultural products. 219
Table 7-2: Results of solid volume estimation for various samples 229

Chapter 1 Introduction and Literature Review

1.1. Introduction

Volume determination of solids has long posed a technical challenge. The historical narrative on this subject likely traces back to Archimedes' "Eureka!" moment and extends into the era of artificial intelligence, where various optical reconstruction methods are employed for volume measurement. The extensive and interdisciplinary approach to volume determination underscores its significance across various domains.

For liquids, In the case of a known mass, volume can be calculated from density. The volume of the liquids is measurable from its level in a storage vessel, e.g. a tank. fill level can be determined using a contacted apparatus like a floater or by using contactless methods, including capacitive sensors (Malik et al., 2020) or ultrasonic range finder sensors (Oduah & Ogunye, 2023; Olisa et al., 2021).

On the other hand, the volume determination of bulk solids and powders is not straightforward; how the bulk of a powder is distributed, stored or handled alters its volume. Moreover, unlike in liquids, point level measurement in a powder is not the best solution as the powders usually don't have a flat free surface. Thus, a single-point level measurement. Rapid measurement of the volume of a bulk solid in a storage or discharge vessel in real-time is often desirable and sometimes mandatory but is a process that continues to be challenging across the process industries (Louge et al., 2021).

An industrial problem related to fill volume measurement in the topdressing industry planted the seed for this research. Specifically, there is a demand for a method to measure the amount of material in the hopper of a topdressing aeroplane. This challenge expanded this study into non-invasive methods of measuring fill volume in a vessel, especially one that holds bulk solids. In the following section, we will discuss the problem in the aviation industry in more detail.

Operators of fixed-wing topdressing aeroplanes and their clients are concerned about material flow issues, especially regarding safety and accuracy when delivering fertiliser at the desired application rate. This concern relates to material discharge monitoring and handling in topdressing aeroplanes. Material discharge monitoring includes measuring the degree of fill and real-time flow rate, while material handling refers to the control and conveying of material flow out of a topdressing aeroplane.

Topdressing aeroplanes are widely used in New Zealand, where they apply over 40% of the fertiliser used on the country's farms, amounting to over two million tonnes per year (Maber, 2008). For most of the active topdressing fleet in New Zealand, the aeroplane’s wedge-shaped hopper is located behind the pilot with a discharge gate at the bottom. A window is installed in the hopper wall, allowing the pilot to inspect the material load inside visually. However, in some models, including various types

of Pacific Aerospace Limited (PAL) Cresco, the preferred aircraft type in New Zealand, the window inside the hopper is not easily visible unless the pilot removes their shoulder harness to check the degree of fill. The window is intended for visual estimation of the load and to check if the discharging fertiliser is clogged, which triggers a safety alert described later. The pilot manually controls the flow rate by adjusting the opening of the discharge gate (Yule et al., 2008).

When a topdressing aircraft with the speed v_g (m.s^{-1}) and swath width *L* (m) flies over a field, the application rate *A* in kilograms per hectare is:

$$A = \frac{10000\dot{m}}{LV_g} \qquad 1\text{-}1$$

where $\dot{m}$ is the mass flow rate (kg.s^{-1}).

The flow rate of fertiliser out of the hopper directly affects the application rate, as stated in Equation 1-1. However, little research has been done to evaluate the evenness of flow from topdressing aircraft (Yule et al., 2008). Several flight parameters, such as acceleration and angle of attack, and material properties, such as bulk density, mean diameter, surface adhesion, cohesion, and moisture content, can affect the flow rate (Grafton, 2010). Flight parameters can vary for each topdressing flight, and the physical properties of fertilisers are subject to change based on storage and transportation conditions. As a result, after the discharge gate of a topdressing aeroplane's hopper is opened, there are no means to measure and control the flow rate accurately. This limitation may result in the rate being higher or lower than the desired application rate, compromising the quality of fertiliser spreading and reducing efficiency, leading to extra costs.

According to Grafton (2010), the only practical means of overcoming this difficulty is to automate the delivery system based on information received from the Differential Global Positioning System (DGPS) and, if possible, a means of measuring the rate of material discharged from the hopper. Murray & Yule (2007) have shown that actively controlling the application rate can save up to 26% of application costs per hectare.

Lewis et al. (2008) studied agricultural aircraft safety for the New Zealand Civil Aviation Authority (CAA). The study found that there were accidents and incidents related to aircraft experiencing hopper overloading issues. Overloading issues occur when material from the previous application is not fully discharged from the hopper, and the next load is added, assuming the hopper is empty. For example, if 250 kg of fertiliser remains in the hopper and a standard load of 2000 kg is added, the aircraft takes off with a 12.5% overload. This overload can accelerate airframe fatigue and compromise the safe take-off and flight weight. The Lewis report reveals over thirteen topdressing accidents in New Zealand

and approximately four deaths per 100,000 flying hours. Over 75% of operational topdressing aeroplanes in New Zealand have many incidents attributed to overloading (Lewis et al., 2008).

In December 2008, a Pacific Aerospace Cresco 08-600 crashed in Tarata, New Zealand. A report by the Civil Aviation Authority (2011) on the accident advised a review of Civil Aviation Regulations Part 137, which sets the regulations for agricultural aircraft operations. Section 259 of the document urges an agricultural aircraft operator to ensure that the aircraft is equipped with "a means of indicating to the pilot the upper level of the hopper contents" (Civil Aviation Authority, 2017). Appendix D, part 137 of the document indicates that the hopper upper-level contents can be indicated by "observation" or "indication". Visual observation through the window installed behind the pilot satisfies this regulation. However, the difficulty of having a visual on the hopper window and the possibility of human error justifies moving from visual observation of the fill level to indication of the fill level by other means.

An inverse relationship exists between an aircraft's payload and its manoeuvrability, meaning the heavier the aeroplane's load, the less manoeuvrable it becomes. When the hopper is overloaded due to the failure to discharge a prior load, it further reduces the pilot's control of the aircraft. This aircraft's controllability hazard comes from the overloaded aeroplane not responding as expected during manoeuvres, making it difficult for the pilot to control and increasing the risk of an accident.

It may crash if the aeroplane cannot respond promptly to the pilot's control, especially on hill terrains. There are several cases of hopper load-related incidents due to the absence of a dependable monitoring system for the hopper's fill level (Grafton et al., 2009). With the increased horsepower in modern topdressing aeroplane engines, the top compartment of the hoppers has become rounder by following the aircraft fuselage contours. As a result, the hopper's capacity has increased, and it occupies a larger volume within the available space (Grafton et al., 2009). As a result, hopper wall angles have become less steep, which can adversely impact hopper drainage capabilities and increase the possibility of clogging with certain materials. A system that can notify the pilot about clogging is necessary, which could be accomplished by monitoring the fill volume. The pilot's awareness of such conditions is critical in determining flight and landing strategies. The primary issues related to accurately monitoring the hopper fill level can be summarized in three points:

- Reduced manoeuvrability leading to the possibility of a crash due to a hung discharge: A hopper fill monitoring system could inform the pilot about the payload volume and expected manoeuvrability.
- Unsafe take-off due to an excessive load: An active monitoring system for the hopper fill volume can alert the pilot about the safe load for take-off and warn the pilot in case of clogging.

- Lack of feedback to control the flow rate: Reliable monitoring of the material flow rate from the hopper is essential for developing a system to control the flow rate, potentially improving the efficiency of topdressing.

1.1.1. Research Aim

This research aims to explore new contactless volume determination methods, focusing on optical and acoustical methods. Three approaches are investigated: multi-point ultrasonic level measurement, volume measurement from three-dimensional scans of the material surface, and volume measurement using the Helmholtz Resonance acoustic principle.

These are parallel approaches with the same goal in mind. Most of the research is dedicated to the physical phenomenon of Helmholtz Resonance due to its high potential in volume measurement while having limited coverage in the literature. Additionally, exploring volume measurement using Helmholtz Resonance creates opportunities for expanding knowledge applicable to other fields, including volume determination of solids and liquids.

This thesis comprises eight chapters, where chapters two and three focus on the fill volume measurement of a vessel using the ultrasonic technique and optical surface scanning, respectively. Chapter four introduces Helmholtz resonance theory and the techniques for this method for volume measurement of liquid and solids in various scales. Chapters five, six, and seven are dedicated to developing three mathematical models based on the results from chapter four to expand Helmholtz Resonance's applicability in volume measurement further. Finally, the last chapter is dedicated to the conclusion and recommendations. Figure 1-1 guides how this thesis is developed in the following chapters.

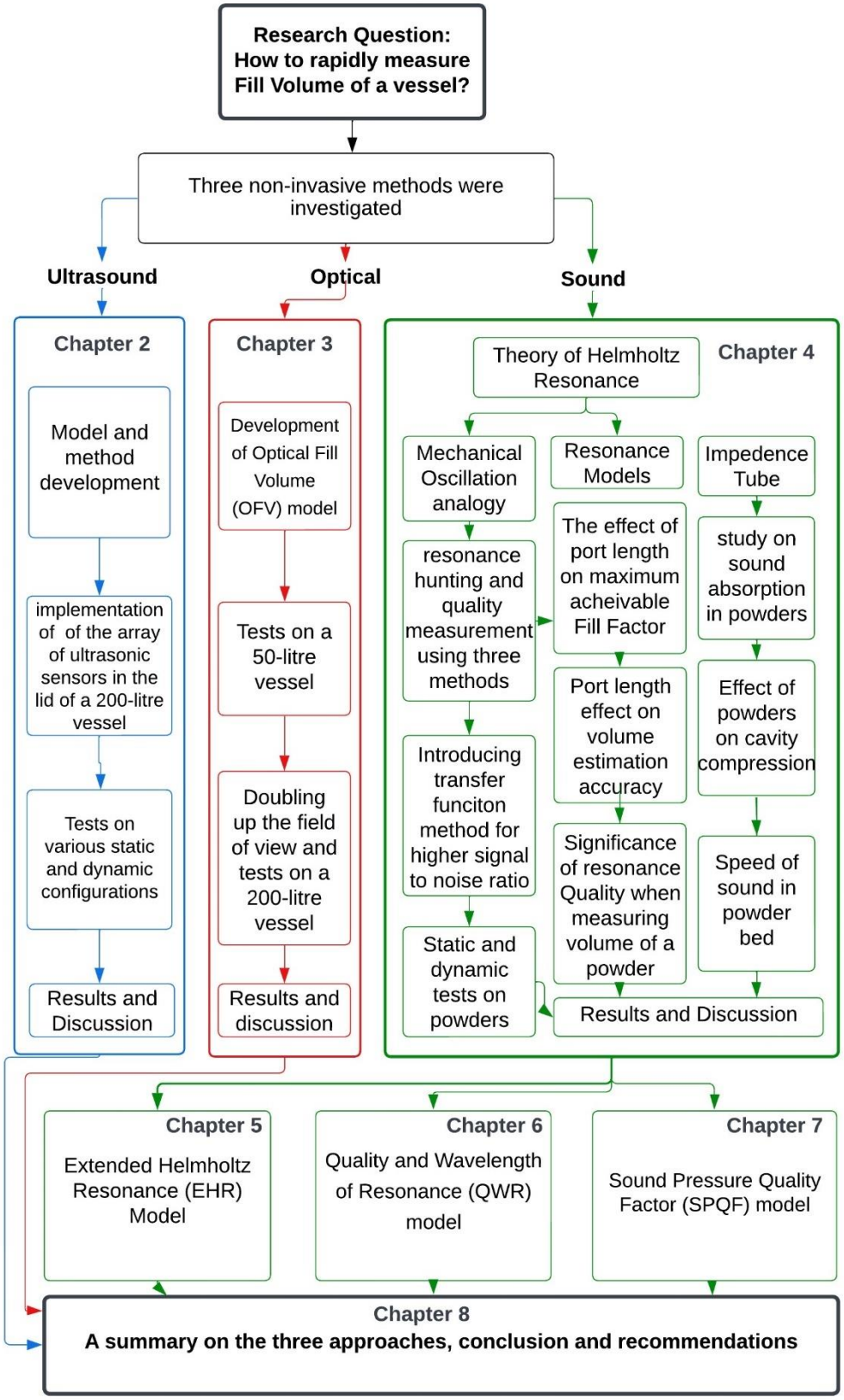


***Figure 1-1**: Thesis Diagram.*

1.2. Literature Review

1.2.1. The problem of fill volume determination in topdressing hoppers

Accurately measuring powder fill volume in a hopper is complex for many reasons. In a topdressing hopper, mass measurement is complicated and unreliable, as is discussed. Single point level measurement also does not provide a reliable fill level reading because the powder's free surface during discharge is irregular and asymmetric, making it challenging to measure the fill volume accurately.

The load carried by a topdressing aeroplane is a critical safety factor in the maintenance record of the aircraft. Part 91.509 of the Civil Aviation Authority (CAA) mandates using a Time in Service Recorder (TSR) to record loads and ensure that maintenance intervals are respected. However, TSR records payload information indirectly by tracking the number of flights within a specific period and comparing it to the loaded material on the ground, providing an average load per flight (CAA Consolidation, 2018). Although this regulation could improve flight safety by tracking maintenance intervals and preventing gross overloading, it can not identify or prevent instances of overloading on a particular flight.

1.2.2. Fill volume measurement by weighing in a topdressing hopper

Chapter 9 of the Civil Aviation Authority (2008) represents the results of a questionnaire survey of topdressing pilots. The answer by one of the pilots to a question about the necessity of installing a device to monitor the hopper's weight is as follows:

"Weight indicators should be considered - even cockeys can weight their cattle digitally!"

The Pacific Aerospace Corporation 750XL-AG topdressing aeroplane was designed with the capability to measure the hopper mass in real-time during flight. The hopper was suspended on a load-cell device integrated with a vertical g-force accelerometer, and the data from these sensors were analysed to obtain load and flow rate information. This system could provide the pilot with real-time load readouts, regardless of variations in gravity due to manoeuvring and contour flight. However, the system was reportedly unreliable and subject to failure. As a result, the development of this type of aeroplane has ceased, and all those that entered service in New Zealand have been decommissioned (Grafton, 2010)

Lewis et al. (2008) discuss a technical issue using load cells for hopper weight measurement. The problem is that to provide sensitive and accurate load measurement with a load cell, the hopper should be installed on adequately flexible joints, as the strain in the joints is measured and used to calculate the weight of the hopper. However, the hopper mounting structure should withstand

manoeuvre and gust loads of at least 3 g and crash loads of up to 12 g, which limits the feasibility of using flexible joints. In other words, the hopper is part of the aircraft's mechanical structure, and modifying the hopper joints affects the aircraft structure, which is not a reliable approach. Even in newer designs such as the 750XL-AG, implementing flexible joints in the hopper fixture has proven difficult. For existing designs where the hopper mounting accommodates existing engineering criteria, fitting a reliable hopper load measurement device becomes even more challenging.

The other approach for weighing the aeroplane before take-off to prevent overloading is the measurement of undercarriage deflection or pressure of the 'air springs' that support the aircraft weight in an oleo-pneumatic piston undercarriage. According to the Lewis report, deflection measurement devices have suffered from the aggressive (wet, dirty) environment to which the undercarriages are subjected. The undercarriage pneumatic mechanism air pressure measurement sounds simple but has issues. Due to friction in the undercarriage suspension mechanism, environmental conditions and the fact that the aeroplanes are not always level when loaded, it is difficult to correlate the suspension pressure to the hopper fill level accurately (Lewis et al., 2008).

Despite encouraging advances in the field, attempts to determine the load of a hopper through weighing, either in-flight or before takeoff, have faced technical impediments, as described above. Weighing has been tried but has proven not to be a valid approach, which necessitates the investigation of other approaches to address the problem of hopper fill level monitoring.

1.2.3. Use of ultrasonic sensors in fill volume measurement

Distance measurement using ultrasonic sensors is a widely used technique. These sensors generate high-frequency sound waves, usually within the range of 20 kHz to 100 kHz, which bounce back from an object and return to the sensor, enabling the calculation of the time of flight (TOF) of the ultrasound waves. Consequently, the sensor can readily measure the distance to the object. Ultrasonic sensors offer several benefits for level measurement, such as their non-contact nature, which makes them suitable for use in severe or hazardous environments, and their ability to detect transparent or soft objects, which are difficult to detect with other sensors. They have wide applications in fields such as automation, robotics, and automotive safety for tasks including obstacle detection.

In terms of distance measurement, ultrasonic sensors are also frequently used for liquid volume measurement in a tank. In this case, the sensor emits ultrasound pulses towards the liquid's surface and measures the pulse's travel distance from its flight time. This method is accurate and is widely used for this application. However, the use of ultrasonic systems in hoppers and silos is constrained by various technical and environmental conditions, such as compromised accuracy in dusty conditions, sensitivity to air pressure and temperature fluctuations, vessel geometry that can reflect or deflect

ultrasound, and the formation of material clumps or coatings on the vessel surfaces that can also compromise accuracy. These conditions can alter how sound waves reflect off a surface, potentially creating false echoes that may interfere with the actual level signal (Lewis Sr, 2004).

Ultrasonic rangefinders, single or in an array, can be adopted for bulk volume measurement through level detection. Ultrasonic sensors are low-cost solutions commercially available in rugged and industrial packaging. Unlike radars, they have a low minimum detection range, usually less than 200 mm and unlike LiDARS and other optical methods, they are less affected by dust and are reliable in harsh environments like the use in waste bins (Kristanto et al., 2016; Ramson et al., 2022).

Morimoto et al. (1991) investigated hopper fill level measurement using an array of ultrasonic receivers. They installed an ultrasonic transmitter encircled by eight sensing elements in the cover plate of a hopper. This setup enabled the construction of three-dimensional representations of the hopper's material surface from the sensing elements' phase difference. All their results were for a concave surface and were reported to be within ±8 mm of the levels of the reference surface; they also noted that the material surface played a role in the practicality of this approach. Sonbul et al., (2012) used a line array of ultrasonic sensors to construct three-dimensional images of objects in a bulk material volume remote sensing study. Every sensor acted as a pixel in a low-resolution image and demonstrated an accuracy better than 95% in the volume measurement of a rectangular box.

In another study, Pozzebon et al. (2023), based on the method proposed by Bocci et al., (2020), suggested using a grid of ultrasonic sensors to estimate the volume of a bulk of granular materials. Pozzebon et al. (2023) have shown that the bulk volume can be calculated through a geometrical model from the local levels obtained using individual ultrasonic sensors. They used several configurations of the position of the sensors and reported that sensor position had a significant effect on measurement accuracy. The study conducted by Pozzebon et al. (2023) aims at measuring the volume of powders in an open space large-scale area.

However, a notable gap in the literature is the application of an array of ultrasonic sensors for continuous monitoring of the fill level in powder discharge vessels. In such vessels, the feasibility of this method is challenged by factors like the reflection of ultrasonic sensor pulses off the vessel walls and potential interference between sensors. Additionally, the dynamic flow of the material within the vessel may also influence the accuracy of this method.

If an array of off-the-shelf ultrasonic sensors is used in a hopper, they could offer a cost-effective and readily deployable method for determining fill volume.

1.2.4. Use of air pycnometers in fill volume determination

Based on the principle of the Boyle-Mariotte Ideal Gas law, there is a relationship between the temperature, pressure, and volume of a gas in a system. Thus, a system's temperature and pressure change can be related to its volume change. Air/Gas pycnometers work based on this law and are widely used for free air space determination of solid objects to very high accuracy for various scales (Agnew et al., 2003; Tamari, 2004; Thudium, 1976). Despite the accuracy, air pycnometers are slow (Nishizu et al., 2001). Furthermore, applying the pycnometer principle to determine the fill volume of a hopper is impractical, as a hopper, in contrast to an air pycnometer, is not airtight.

1.2.5. Helmholtz resonance

The resonance of a cavity is a phenomenon we often experience in our everyday daily lives. Many musical instruments and engine mufflers are examples of Helmholtz Resonators (Munjal, 1987). A Helmholtz Resonator consists of a cavity and one or more openings that can be extended to form Port(s) (Figure 1-2). When a Helmholtz resonator undergoes an acoustical or mechanical excitation, the air mass in the port (M) moves up and down. The air inside the cavity provides a spring restoration force (K). Analogous to a Mass-Spring system, the mass of the air in the port resonates in an angular frequency (ω_n) of:

$$\omega_n = \sqrt{\frac{K}{m}} \qquad 1\text{-}2$$

A musical instrument, e.g., a guitar, is a Helmholtz Resonator. The guitar's body is the resonator's cavity; its hole is the resonator's port. Playing the strings on the guitar oscillates the guitar's face, which excites the air inside the guitar's body. The air compression pushes the air mass within the guitar's port out. The mass of air moves out for a short distance, and then the elasticity of air in the cavity retraces the mass of air back into the body to the equilibrium position. The mass of air in the port pushes the air further into the body until the elasticity in the body overcomes the port air momentum and forces it back out again. This cycle forms resonance.

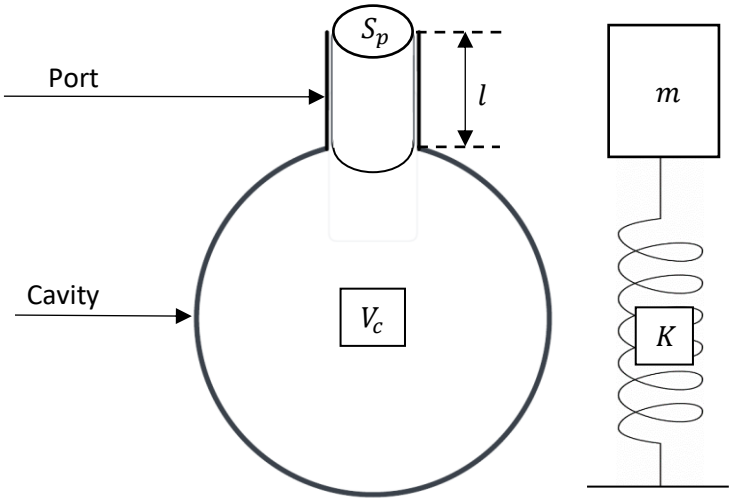


Figure 1-2: *A Helmholtz Resonator.*

The resonance frequency of this system can be calculated by solving the momentum equation, which is thoroughly discussed in the related textbooks (for example, Rienstra & Hirschberg, 2004).

Calculating the air mass in the port (m) and spring constant of air in the cavity (K), Equation 1-2 develops into Equation 1-3, the basic formula for calculating Helmholtz resonant frequency. It is mainly a result of the works of Helmholtz (Helmholtz, 1877), Rayleigh (Lord Rayleigh, 1916), Sondhauss and Wertheim (Cited by Alster, 1972):

$$f = \frac{c}{2\pi}\sqrt{\frac{S_p}{V_c l}} \qquad 1\text{-}3$$

where c is the speed of sound (m.s^{-1}), S_p is the cross-sectional area of the port (m^2), V_c is the volume of the chamber (m^3), and l is the length of the port (m).

Equations 1-3, despite their simplicity, do not provide accurate frequency locations for all geometries, especially when the resonator's dimensions become comparable with resonance wavelength (Lord Rayleigh, 1916). Further studies detected non-linearities of this equation, introduced correction factors, and introduced alternative models for expanded geometrical constraints.

Nishizu et al. (2001) Investigated the application of Helmholtz resonance for agricultural product volume determination. They made a resonator with three ports excited by a loudspeaker in one of the ports. The other two ports were used as inlet and outlet of samples (Figure 1-3). Each sample occupied volume V_s inside the resonator cavity, with the volume V_c. The frequency response of the system to

the applied excitation sound by the loudspeaker was picked up by a microphone attached to the wall of the top port. The resonant frequency was then detected using discrete Fourier transform and minimum entropy method. The detected frequency was used to back-calculate the sample volume through the following equation:

$$freq = \frac{c}{2\pi}\sqrt{\frac{(3)S_p}{(V_c - V_s)(l+\Delta l)}} \qquad 1\text{-}4$$

The cross-sectional area of the port in the numerator of the square root in Equation 1-4 is multiplied by three because the three ports used in the experiment are identical in dimensions. In practice, the effective length of the port exceeds its physical length. The exceeding is due to a mass of air on both sides of the port resonating with the air inside the port, with an extension of air outside the port. The extended length of air is called the port extension term Δl. It is calculated using the following equation (Blackstock, 2000):

$$\Delta l = 0.6r + \frac{8}{3\pi}r \qquad 1\text{-}5$$

where *r* is the port's internal radius. Equation 1-5 is valid for the ports that do not have a flange surrounding their opening.

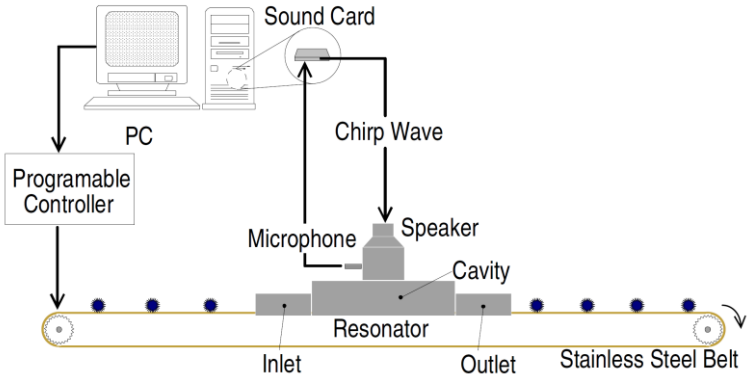


***Figure 1-3**: A schematic diagram of an automatic and continuous measurement system for food volume. Extracted from Nishizu et al. (2001).*

The experimental apparatus in Figures 1-3, devised by Nishizu et al. (2001), measures the resonance frequency and determines the volume of the objects as quickly as possible. The maximum speed for the conveyor to measure the volume accurately was 45 mm.s^{-1}. The quickest achievable volume measurement was ~ 0.5 s. They reported that the coefficients of determination between the

actual and predicted volumes were ~0.99. However, they did not report the absolute accuracy of their method.

One of the key findings of Nishizu et al. (2001) was the inverse relationship between the accuracy of volume measurement and the speed of the moving object. They have found that, in practice, the measurement quality is restricted to the duration of the measurement. The acoustical response of a resonator at its natural frequency is a function of the duration of the applied chirp, the duration of the recorded response and the sample's velocity.

Another example of the practical use of Helmholtz Resonators is given in a patent by Johnson (1995), which describes a method for the non-invasive determination of body volume. Johnson employed the principle of Helmholtz Resonator to simultaneously measure the resonant frequency of a chamber that a person fits into and a separate resonator located within the container (Figure 1-4).

The apparatus shown in Figure 1-4, extracted from a patent by Johnson (1995), which was presented in Johnson's (1995) patent, consists of several components: a blower at Number 7, with a fixed rotation rate to excite the main resonator (Number 1); a secondary resonator at Number 9, which is excited by another blower; and a microphone at Number 12, which picks up the resonant frequency of both resonators.

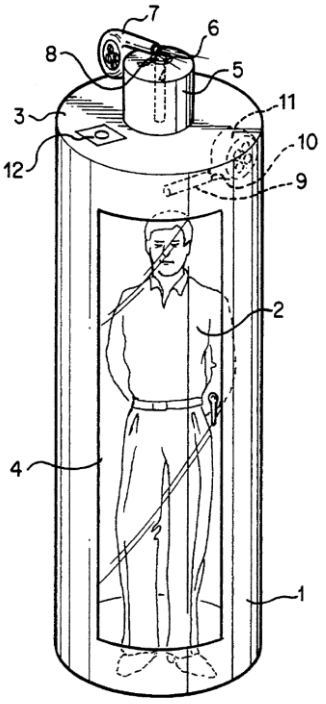


Figure 1-4: *Body volume measurement using a Helmholtz Resonator.*

Assuming that V_b is body volume, and by rearranging and expanding Equation 1-3, the ratio of body volume and empty volume of the resonator is:

$$\frac{V_b}{V_c} = 1 - \frac{S_p c^2}{V_c 4\pi^2 (l+\Delta l) f^2} = 1 - \alpha^2 \frac{c^2}{f^2} \qquad \textit{1-6}$$

where α is the resonator's geometrical constant. Considering the secondary resonator as an organ pipe with known dimensions, the resonant frequency f_t is:

$$f_t = K_t' c \qquad \textit{1-7}$$

Substituting Equation 1-7 into Equation 1-6 generates the following equation with K'' as a new constant that can be experimentally obtained:

$$\frac{V_b}{V_c} = 1 - K'' \left(\frac{f_t}{f}\right)^2 \qquad \textit{1-8}$$

Equation 1-8 correlates body volume to resonance frequency by cancelling the incorporation of the environmental effects, such as temperature and humidity, on volume measurement. Nevertheless, in this literature search, no results were found regarding the accuracy of this proposed method. Interference between the two resonators and added error in hunting the frequency of the second resonator could decrease accuracy.

A contrast between this invention and similar literature is the use of a blower for excitation. The proposed frequency resonance measurement by Johnson (1995) is the zero-crossing detection method after applying a bandpass filter. It may not be a successful approach for resonance hunting in a noisy environment.

Nakano et al. (2006) applied the Helmholtz resonance principle to measure the volume of liquid nitrogen to confirm the applicability of Helmholtz Resonators under microgravity conditions. They used an experimental cell, a closed Helmholtz Resonator, with about 50 ml of liquid nitrogen (Figure 1-5).

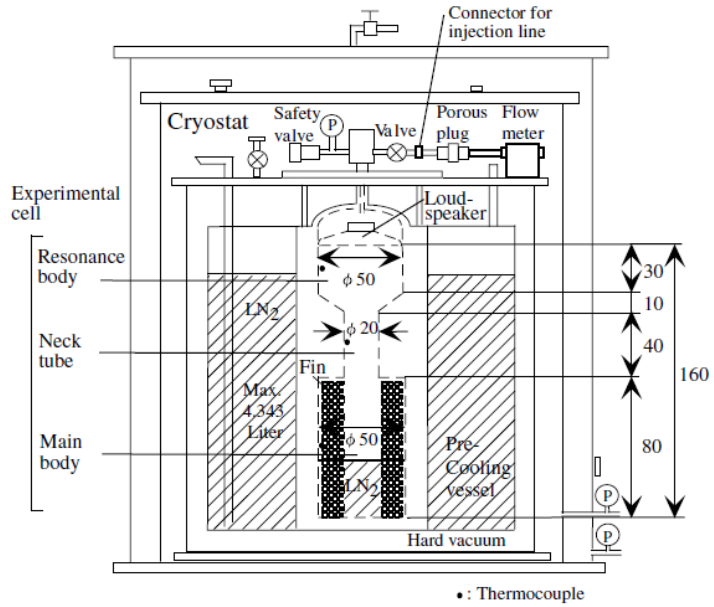


Figure 1-5: *Schematic of the apparatus for measuring liquid nitrogen's volume (Nakano et al., 2006).*

For picking up resonance frequency, Instead of using a microphone, they recorded the impedance of the loudspeaker coil after generating a chirp inside the resonator. The feedback of the resonator was applying a voltage around the speaker's coil proportional to the resonant frequency (Figure 1-6).

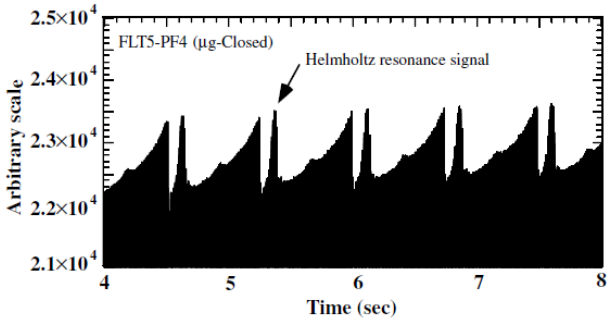


Figure 1-6: *Load speaker coil response (Nakano et al., 2006).*

Nakano et al. (2006) reported that the acceleration of the whole system does not significantly alter resonant frequency. They tested their experiment for simulating different gravity accelerations in an aeroplane. It is reassuring that flight acceleration is not likely to be a source of non-linearity for the resonance frequency of a resonator. They also could successfully filter out the noise of the input signal by Minimum Entropy Deconvolution (MED). In this method, which is a digital signal processing filtration technique, the resonance spike is isolated from the rest of the signal in the system. The resonance signal is assumed to have the least statistical entropy or randomness. In MED, the raw signal is deconvoluted to remove the effect of the noisy data based on its impulse response (Wiggins, 1978). They reported the liquid volume measurement error to be less than 20% of the canister volume.

Despite the novelty, the accuracy seems to be low. They suggested that the reason for the measurement error in the final volume measurement was the liquid sample distribution in the resonator cavity during the test.

Webster & Davies (2010) showed that Helmholtz resonance theory can be utilized for solid and liquid volume measurement in a static setup for accuracy within ±0.1% of the resonator volume when appropriate statistical correction factors are considered. A comprehensive evaluation of a Helmholtz Resonator as a device for volume measurement was undertaken by Webster (2010). His investigations extended to analyses of different chamber sizes, materials, sample placement and resonance detection methods. The main novelty of the research was the development of a new technique for rapidly measuring a solid volume object, termed Quality Profile Shifting (QPS). In this method, the resonator is excited by a monotone, and the presence of a sample disturbed the resonator's response to the monotone in terms of resonance quality and amplitude. Throughout numerous experiments, sample volume was correlated to the resonance quality of the resonator. This technique was fast, with a volume determination of ~3 s, but was limited to samples smaller than 10% of the chamber volume.

Parts of Webster's study involved volume measurement of powders and particles using Helmholtz Resonance. In this study, experiments on powders demonstrated complex behaviour occurring within the resonator. This complexity was reported to be because of extensive acoustic energy attenuation by the sample powders. According to the results of this study, the accuracy of solid volume measurement for sub-millimetre particles dropped tenfold. The non-ideal behaviours of a Helmholtz Resonator for measuring the bulk volume of powders, according to Webster (2010), are as follows:

- The sound absorption properties are a function of particle size and geometry, not particle type. When a sound wave hits the granular bed material, the particles absorb part of its energy. Also occurring is acoustic attenuation due to viscous interstitial effects due to boundary layer dimensions comparable to interparticle space size. As the sound penetrates the bed, the viscous forces dominate the inertial ones.
- The maximum occupied space percentage of the resonator cavity (Fill Factor) is greatly affected by the particle mean diameter of the material being tested. The resonant frequency is not practically measurable for fill factors above 30% due to high sound absorption by the powder bed. At higher fill levels, the reemitted sound level becomes more prominent than the resonant frequency amplitude, rendering the resonance frequency undetectable.
- The sound pressure level becomes independent of the Helmholtz Resonator's frequency at a certain depth of material inside a Helmholtz resonator. That is where the viscous forces related to particle size completely attenuate the sound wave. This depth is called cut-off depth

in the literature. However, the penetration intensity profile of the sound to the inner layers of a particle bed can be altered by sound frequency.

- The frequency response of the particle bed is picked up to be much different from the frequency of the incoming wave. The adjacent particles in the bed can form miniature Helmholtz Resonators, generating broadband noise. The result is a broad resonance peak, which significantly restricts volume measurement. However, this broadening in resonance peak is not well examined for different materials and resonators.

1.2.6. Non-ideal behaviour in a Helmholtz resonator

The fundamental Helmholtz equation, Equation (1-3), is simple and applicable for volume determination in laboratory conditions. However, in practice, there are non-linearities associated with the resonator geometry:

- Irregular and asymmetric geometry of the resonator: Alster (1972) conducted mathematical analyses of variations in chamber shape and how they affect resonant frequency. His studies show that resonant frequency is highly dependent on chamber shape, and if the chamber is sufficiently regular to be described by a mathematical function, a chamber irregularity compensation term of l_c can be defined and added to the port extension factor.
- Sample location: Liscovius and Sondhauss (Cited by Alster, 1972) suggested that the resonant frequency of a bottle partially filled with water is independent of its inclination. Modern replications reject this and give variations of up to 30% (Alster, 1972). Webster (2010) showed that sample position can alter resonant frequency due to the change in air velocity and pressure profile within the chamber.
- Irregularity in port shape: Various factors like port placement, geometry, and physical length in a Helmholtz Resonator can affect the resonant frequency (Ingard, 1953; Selamet & Lee, 2003).

1.2.7. Degree of fill measurement by stereo-digital image correlation

One approach to contactless volume determination is optical surface reconstruction (Kim et al., 2019; Kurkuri et al., 2020), which involves volume calculation from image processing of a single optical camera. Kim et al. (2019) suggested that using a single camera which takes side images from the material surface, the fill volume of an excavator bucket can be calculated from the shape of the heap. For this specific application, they report an error of 6.3% in laboratory conditions. The limitations of this method are the lack of generality, the sensitivity of the optics to dust, and limited accuracy.

The fill volume of the bulk material can be assessed using optical 3D scanning (Altuntas, 2014; Rackl et al., 2017) or LiDAR, which reconstructs material surfaces from 3D scans. The use of lidars, due to the limited minimum detection range, is limited to applications with enough space between the scanner and the material surface. For example, Schmid et al. (2022) used LiDAR to measure the volume of dunes. Amorim et al. (2019) used LiDARS to measure the load of trucks from the line scans obtained above as the trucks pass through a gate. The point clouds obtained from the line scans provided a reference for truckload volume determination with an error of ~2%. LiDARS are expensive, and their use for volume determination is restricted to large spaces.

Stereo-digital image correlation (stereo-DIC) or stereoscopic vision is an optical technique proposed initially for surface deformation measurements (Luo et al., 1993). Stereoscopic vision is an area of study within computer vision; it aims to derive three-dimensional depth maps from a pair of two-dimensional images. These two views are typically obtained using two separate camera sensors with a different scene perspective.

This technique, continually improved by several other researchers (Sutton et al., 2007; Xue et al., 2017), has greatly matured and has been adopted as a reliable and practical method for non-contact, full-field three-dimensional deformation measurements. Manufacturers of stereoscopic depth vision cameras sometimes claim the technology to be identical to and adopted from human binocular vision, which uses a pair of eyes to understand depth (Stereolabs, 2019).

Stereo-digital image correlation works by detecting the displacement of image pixels in the photos taken by two cameras a known reference distance apart. Based on this disparity, the actual distance to each pixel can be calculated (Figure 1-7). This technique calculates the distance to each image pixel based on the disparities between matching key points in the left and right images, as shown in Equation 1-9 (Keselman et al., 2017).

$$z = \frac{F.B}{d} \qquad 1\text{-}9$$

where Z is the distance to the pixel, B is the baseline of image sensors, F is the focal length, and d is the disparity of the projected image between two image sensors. There are multiple algorithms for finding disparities in pixels in an image using block-matching image processing techniques (Brown et al., 2003; Koschan et al., 1996).

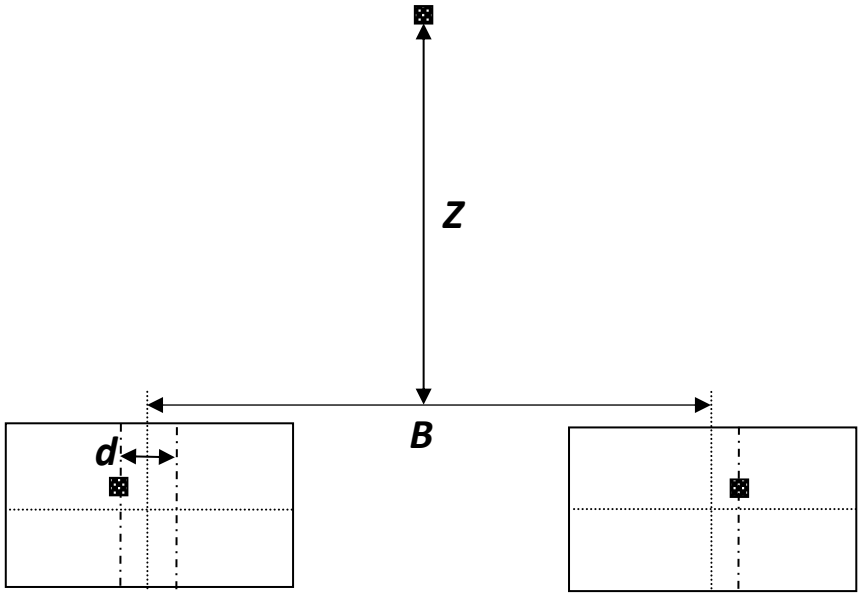


Figure 1-7: *Depth from stereo image correlation.*

Minimal research has been done on measuring the volumetric properties of powders in a hopper by optical means. To the best of the knowledge of the author of this thesis, there are no reported studies on the use of the stereo-DIC technique in dynamic volume measurement in hoppers or measuring flowrate of material out of a hopper except two studies by Barzegar et al. (2019b) and (2019a) which are the works by the author of this PhD thesis and the supervision team.

Barzegar et al. (2019a, 2019b) used the stereoscopic technique to measure the fill volume of a laboratory scale hopper. They tested different materials under no-flow and free-flowing conditions at various flow rates and measured fill volume and flow rate at almost 4 measurements per second. They have demonstrated that in all tests, the results indicate good agreement between the optically measured fill volumes and the predicted volumes based on material mass and bulk density.

1.2.8. Methods for fill volume determination of silos

In recent literature, there are novel methods for estimating the bulk volume in silos that are worth mentioning, though they fall outside the scope of this thesis.

There are available commercial devices for silo volume determination which utilize ultrasonic 3D mapping systems, such as BINMASTER (2023), applicable for estimating the fill content of silos.

A recent method is the Radar range finding, which applies to silos and large vessels. Vogt & Gerding (2017) provide a comprehensive reference for the application of radar in tank level measurement. Yigit (2018) successfully used radar technology to measure the volume of barley in a silo. While this method has proven feasible, its limitations include a narrow field of view and a restricted minimum

detection range. These constraints make it mainly specialized for large scales, such as silos and dunes, which are not the focus of this thesis.

1.3. Research Questions

To address the problem of fill volume measurement in a vessel, and following the literature review on the developed studies in the field, the questions that this study tries to answer are presented in bullet type as follows:

Using Ultrasonic technology in a vessel fill volume measurement

One of the approaches to address the research problem of rapid fill volume measurement in a vessel is the Implementation of an array of ultrasonic sensors in a vessel lid. It can provide enough distance data from multiple points in the material's surface to measure fill volume. However, the corresponding chapter addresses and discusses multiple research questions. These questions are as follows:

- If material is under discharge from a vessel, can ultrasonic sensors track level change and translate it into fill volume and flow rate?
- Can we operate multiple ultrasonic sensors in the tight space of a vessel simultaneously?
- What are the noise sources and operability limitations?
- What is the relationship between the number of sensors per surface area and accuracy?

Using stereoscopic optical technology in hopper fill volume measurement

The other approach for real-time fill volume measurement in a vessel is using optical means, more specifically, stereoscopic vision for real-time meshing of the material's surface to extract volumetric data based on the knowledge of the hopper geometry. The following are some of the main questions

- How to translate a surface 3D deformation map into volume?
- How accurate is this method?
- What scales of vessels can this method cover?
- Is it possible to extract real-time flow rate data of material by this technique?
- What are the limitations of this method?
- What are the limitations in the maximum fill level for volume measurement?
- How to increase the field of view of the optical system?
- How can the optical system's survivability and reliability in a harsh environment be improved?

Fill-volume measurement of a vessel using Helmholtz Resonance

The other approach this study investigates to address the problem of fill volume measurement in a vessel is Helmholtz Resonance. This method is shown to have many capabilities in measuring the volume of solids and liquids; however, there are limited reports on the application of Helmholtz Resonance on the volume measurement of bulk solids. The physical complexity of this method raises several research questions as follows:

- Is it possible to estimate the volume of bulk solids using Helmholtz Resonance?
- When estimating the volume of bulk solids using Helmholtz Resonance, does the estimated volume refer to the bulk or solid volume?
- How can the maximum measurable fill level in a Helmholtz Resonator be improved when a resonator is loaded with powders?
- How to hunt the resonance frequency of a resonator containing bulk solids?
- How can powders and particles affect the quality of volume measurement?
- What Helmholtz Resonance model can be used for estimating fill volume?
- Is it possible to instantaneously measure fill volume to measure flow rate change in real-time?

1.4. Summary

Real-time measurement of the fill volume of a vessel in a topdressing aeroplane poses a challenging problem. This issue raises concerns about safety hazards that have claimed pilots' lives, loss of profit, and compromised evenness in the distribution of fertilizers in the fields. Hopper weighing has already been tried and is not considered a solution. This thesis investigates three other approaches for measuring fill volume in a vessel: material surface scanning using stereoscopic techniques, multipoint level measurement using ultrasonic sensors, and Helmholtz Resonance for fill volume measurement. The stereoscopic optical technique and ultrasonic level measurement are viable applied science methods. The third method, volume measurement using Helmholtz Resonance, relates to the mechanics of acoustics. Knowledge in this field is mainly limited to the volume measurement of solid objects and liquids. This thesis aims to investigate further different aspects of applying the Helmholtz Resonance concept to accurately measure the volume of various solids, including powders in hoppers and vessels, to develop the field of rapid volume measurement.

Chapter 2 Measurement of a Vessel Fill Level Using Ultrasonic Range Finders

The outcomes presented in this chapter have been published by Barzegar et al. (2024) in 'Powder Technology', an Elsevier journal, under the title:
'Ultrasonic Measurement of Fill Volume of Bulk Solids in Discharge Vessels'.

2.1. Introduction

In the context of a bed of bulk solids in a vessel, it is typical for the surface not to be flat; thus, a single-point level measurement of the material does not accurately estimate the volume inside the vessel. The main question that prompted this part of the thesis was how to obtain level measurements from multiple points on the surface of a bulk solid in a vessel, as this has the potential to increase measurement accuracy compared to single-point level measurement.

As discussed in Chapter 1, level measurement using ultrasonic sensors is a reliable solution for many applications. However, there is limited reporting on implementing this method for real-time bulk solids volume measurement of powders in vessels. The concept involves using an array of ultrasonic sensors to obtain multiple-level readings from various points on the bulk solid surface.

One of the reasons for choosing to investigate this method was its ease of application. Ultrasonic sensors are available in various industrial packaging options, making them suitable candidates for implementation in harsh industrial environments.

2.2. Materials

2.2.1. Ultrasonic Range Finders

The ultrasonic range finder sensors used in the experiments were MB7138 and MB7139 (MaxBotix, USA), with the operating principle of pulse time of flight measurement. These sensors detect distances ranging from 200 mm to 3500 mm, with a claimed accuracy of ±10 mm, operating at 42 kHz with a range reading rate of 6.7 per second. The distance readings were obtained through pulse width modulation. The sensor MB7138 reports the distance based on the most robust reflection, and MB7139 reports the distance to the closest object. These sensors are classified as narrow beam sensors with an angle of view of 11 degrees. This characteristic minimizes the potential for corner and side reflections in closed environments, providing more reliable distance measurements in the context of installation in a tight space. The ultrasonic sensors are IP67 water intrusion standard and can be fitted using a 3/4 inch PVC pipe fitting. They come in compact PVC housing. The technical information and distance calibration charts of the MB7138 sensor are covered in Appendix C.

2.2.2. Experimental apparatus

Figure 2-1 shows the experimental setup featuring the sensor arrangement on the plywood cover plate of a 55-U.S. gallon standard oil drum with a capacity of approximately 0.2 m^3. In this thesis, this drum is also called the 200-litre vessel. This drum served as the storage and discharge vessel for the granular sample during the experiments. Nine ultrasonic range finder sensors were mounted on the vessel cover plate for the material level measurements from multiple points. This number of sensors provides approximately full coverage of the vessel bottom.

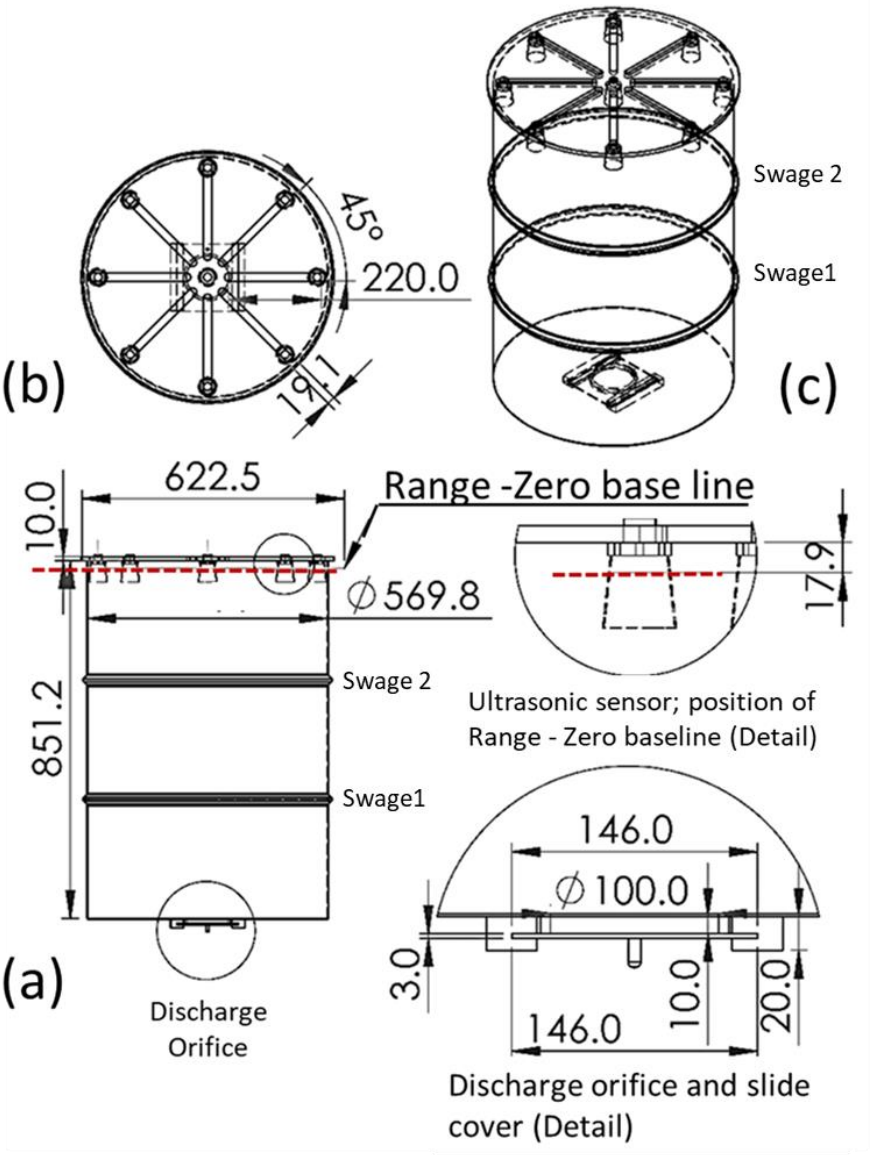


Figure 2-1: *Storage and Discharge vessel apparatus with the ultrasonic rangefinder sensors: (a) Principal dimensions and disposition of sensors; (b) plan view of sensors in vessel lid showing radial adjustment channels; (c) assembly.* **- - -** *Range-Zero baseline*. Dimensions in mm.

One sensor (MB7139) was centrally positioned on the vessel cover plate, while the remaining eight sensors (MB7138) were arranged in a circular pattern with an angular spacing of 45 degrees. Eight channels, each 19.1 mm wide, were laser cut into the vessel cover plate to provide flexibility and precision in adjusting the distance of a sensor from the centre of the cover plate. The eight side sensors were the type that reported the most robust reflection (MB7138) and rejected weak reflections from the walls of the vessel. The baseline for a sensor reading marked as "Range-Zero baseline" in Figure 2-1 is the reference point for a sensor's distance reporting; the baselines of all nine sensors lie in the same plane relative to the drum top plate.

For real-time mass measurement of the content of the vessel, a rectangular frame was utilized, with one side resting on a pair of point contacts and the other on a load cell (PT Ltd, New Zealand) with a capacity of 1 tonne. The Picture of this frame is available in Appendix F. The load cell was connected to a driver/signal conditioner (EMC 2060, New Zealand) for sensor readout. The driver was connected to an Arduino MEGA 2560 microcontroller board (Arduino, ITALY) via variable current output (4-20 mA). The Arduino microcontroller received the load cell driver current output after conversion to voltage using a 270-ohm resistor and relayed the data to a computer through serial communication. The mass measurement accuracy was estimated at ±0.2 kg.

A sliding wooden plate was installed beneath a circular opening as a flow control orifice at the bottom of the drum to control the material flow (see Figure 2-1). The wooden slider could be set to two positions. These were fully closed for static tests and fully open for discharge tests.

The ultrasonic sensors used in this study work at a fixed frequency. If they run simultaneously, they may misleadingly receive the reflection from another sensor pulse. They were driven sequentially to prevent sensor interaction, as the manufacturer advised. The ultrasonic sensor data were sequentially collected with a total measurement duration of 1.1 s for all nine sensors. The sensor pulse-width output was fed to the Arduino microcontroller for distance calculations.

2.2.3. Software and hardware interface

The ultrasonic range finder sensors were interfaced through the Arduino MEGA 2560 microcontroller coded with Arduino IDE Integrated Development Environment (IDE) version 2.0.3. LabVIEW (National Instruments, 2018) was used to interface with the Arduino microcontroller, log the sensor data and calculate the fill volume of the vessel, which was carried out in real-time.

2.2.4. Test sample

Due to availability and convenience, the experiments were conducted on semi-cylindrical polyethene pellets prepared by screening with two BS 410 sieves. The test sample was the fraction that passed through a 4000 µm aperture sieve and was retained by a 2800 µm aperture sieve. The loose poured bulk density of the polyethylene pellets was 600 kg.m^{-3}, determined using the apparatus and method in New Zealand Standard NZS 3111 (Standards Association of New Zealand, 1980) with three replicates.

2.2.5. Scale Calibration

The vessel was placed on a three-point connection. Two were support point contacts, and the other sat on a loadcell. It was assumed that weight distribution in the vessel while discharging material from its central vertical axis is homogeneous. For loadcell calibration, a mass of 55 kg of the polyethylene pellets was loaded into the vessel. The surface of the material was levelled using a ruler. The flow control orifice was slightly opened to let almost 10 kg of material discharge, and the orifice was closed again to stop the material from discharging. The collected material was weighed using a platform scale. The mass of material inside the vessel was calculated. The sensor reading was recorded, and the whole process was repeated. The sensor readout against the actual mass of the material inside the vessel at each reading was plotted. The plot was used to calibrate the load cell. Figure 2-2 shows the loadcell calibration plot. The mass measurement accuracy was estimated at ±0.2 kg.

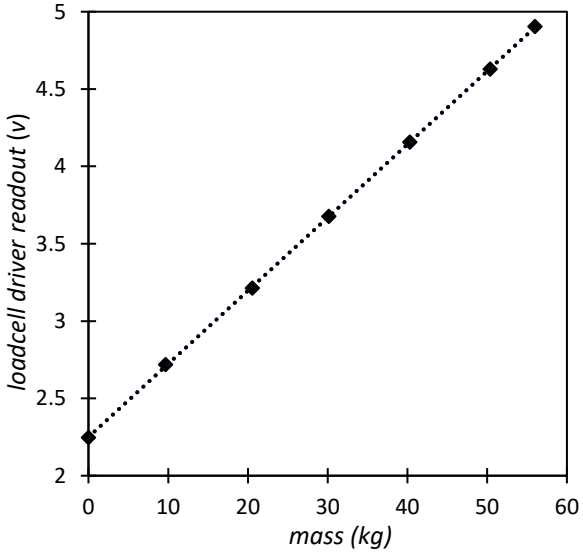


Figure 2-2: *Scale calibration plot.*

2.3. Methods

2.3.1. Fill Volume Determination

Experiments were carried out for fill fractions up to approximately ~ 0.8 on three different surface geometries, *viz* flat, convex and concave. The fill fraction was varied by making incremental additions of polyethylene pellets to the drum; the required surface shape was then fashioned manually, as depicted schematically in Figure 2-3. The convex surface is shown as a conical heap with base angle α, and the concave surface as a conical dish with base angle β; α and β were not measured but were similar to the angle of repose of the polyethylene pellets, nominally 30°.

For each incremental addition and surface geometry, the volume of material in the drum was obtained both from sensor measurements and from the cumulative mass in the drum divided by bulk density; these are reported as estimated volume, V_E , and bulk volume, V_W , respectively.

Under no-flow conditions, the sensors' output was stable; thus, repeating and averaging the output value from the sensors was unnecessary. In discharge experiments, the mass in the drum, at any instant, was measured directly by the load cell; instantaneous volume was found by dividing this by bulk density.

The measurement sought by sensor i is the distance, h_i, from the Range-Zero baseline to the surface of the bulk solids, as shown for a flat surface in Figure 2-3 (a). The ultrasonic sensors, all located in the same plane on the vessel cover plate, each return a measurement of the distance from the sensor to the surface of the powder within its field of view. Some of these measurements were tagged as "off-the-track" because they were significantly higher than physically reasonable distances. This aberrant behaviour is attributed to wall and corner reflections inside the vessel. The maximum discrepancy between the measured and actual distance to the surface should be limited to $0.5D * \tan\alpha$ or $0.5D * tan\,\beta$ for conical or convex surfaces, respectively. For α = β = 30°, a measurement, h_i was defined as "off the track" if the inequality in Equation 2-1 was fulfilled. "Off-the-track" measurements were discarded and replaced with the average reading from the adjacent sensors. This criterion identified "off-the-track" readings for convex, concave, and flat surfaces.

$$h_i > 0.5D * tan\,30 + \bar{h} \qquad 2\text{-}1$$

In Equation 2-1, D is the vessel diameter and $\bar{h}$ is the average of the readings from all sensors. Each finalized measurement is termed h_i^* , and this is used in volume calculations. The associated depth of the powder bed, z_i , for each sensor reading is $(H - h_i^*)$, where H is the actual distance from

the bottom of the drum to the "Range-Zero baseline". With reference to Figure 2-1, H = (851.2- 17.9), which is 833.3 mm.

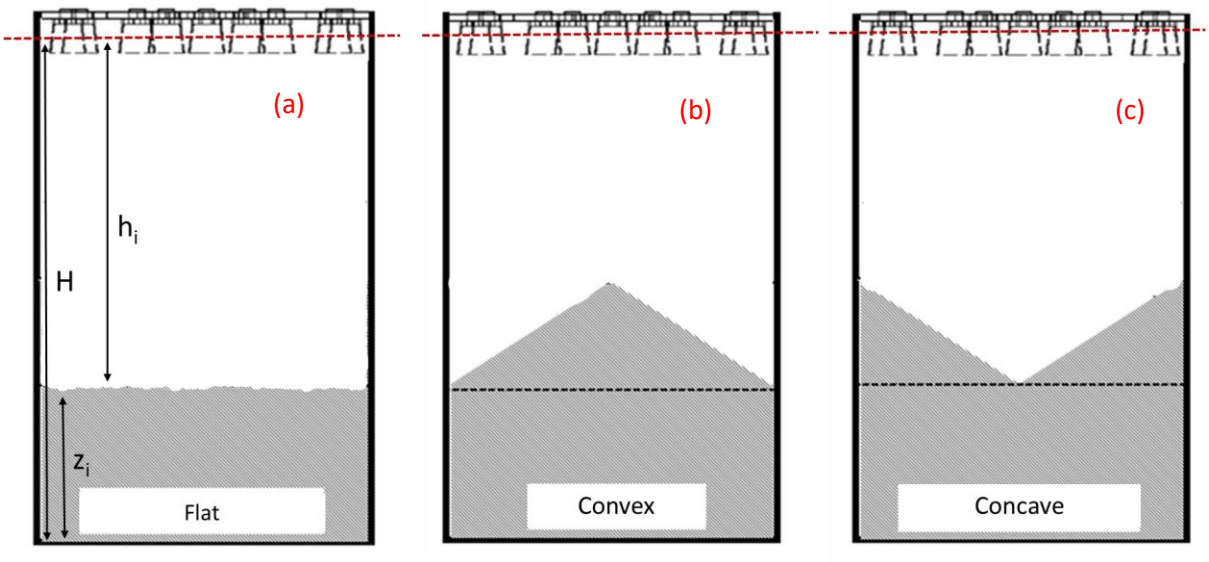


Figure 2-3: *Schematic diagram of the three surface configurations used. (a) flat; (b) convex; (c) concave.* ▬▬▬ *Range-Zero baseline.*

Figure 2-4 shows the cross-sectional view of the vessel virtually divided into nine subsections for approximation of the fill volume by adding up the volume of the nine subsections. The central subsection is a circle with a diameter equivalent to the vessel diameter divided by 3 ($\approx 190\ \mathrm{mm}$). The area between this circle and the vessel's wall was divided into eight subsections. With this division, all nine subsections have an area equal to $\pi D^2/36$. The associated ultrasonic sensor ($S_{0\text{-}8}$) obtained the approximate level of each subsection.

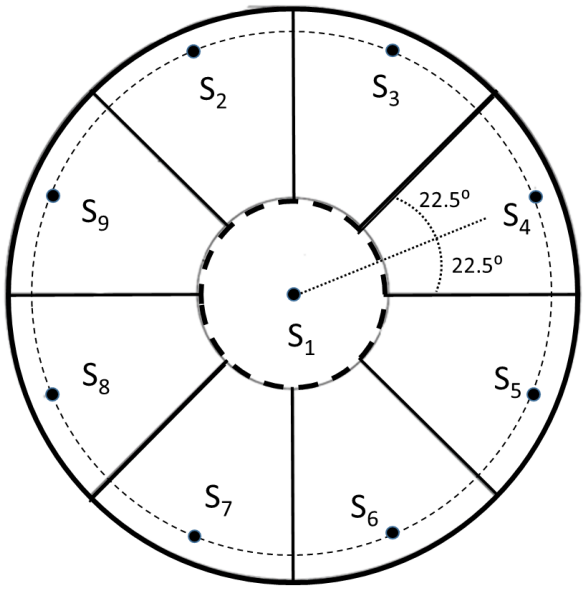


Figure 2-4: *Schematic of the virtual cross-section of the vessel showing nine subsections of equal area and location of sensors, ●.*

The fill volume under each subsection (V_i) is given by the height of the subsection multiplied by its area:

$$V_i = (H - h_i) * \frac{\pi D^2}{36} \qquad 2\text{-}2$$

where H is the vessel height. The estimated vessel's fill volume (V_E), was obtained by adding the volume of all nine subsections as shown in Equation 2-3. Equation 2-3 is referred to as the Multi-Level Volume Measurement (MLVM) model.

$$V_E = \sum_{i=1}^{9} \frac{(H-h_i)\pi D^2}{36} \qquad 2\text{-}3$$

2.3.2. Experiment Procedure

2.4. Static Tests

Static tests were conducted to estimate the fill volume of the vessel under no-flow conditions. The polyethylene pellets were added to the vessel in increments of 5 kg. The material surface was manually fashioned to be flat, convex or concave as required, using a metal ruler or flat wooden rectangular paddle. After the material surface was carefully configured to the desired shape, the vessel cover plate, with the attached sensors, was returned to its marked position on the vessel. The material fill volume was estimated from the sensor readings and cumulative mass and bulk density, as described above, and saved for analysis.

2.5. Discharge Test

Before each test, the drum was filled with the test material, polyethylene pellets, by pouring into the drum from a height of 0.5 m above the open top and the surface carefully flattened with a wooden paddle. The vessel cover plate with the sensors attached was fixed to the top of the vessel. The electronics were checked. Each test was initiated by manually opening the discharge gate at the bottom of the vessel. The vessel fill volume was estimated at intervals of 1.1 s and 0.9 Hz and logged.

2.6. Results

Before beginning the volume determination experiments, the feasibility of using ultrasonic sensors for range detection in powder beds was evaluated. Ultrasonic rangefinders were tested on various powder beds to assess the reflectivity of these beds and determine whether the powder acoustic absorption would hinder the ultrasonic sensor operation. The beds tested included polyethylene pellets, introduced in Section 2.4, a bed of mustard seeds with a Sauter Mean Diameter (SMD) of 1.98 mm, a solid density of 1100 $kg.m^{-3}$, and a loose poured bulk density of 720 $kg.m^{-3}$; stainless steel ball bearings with an SMD of 3.17 mm, a solid density of 7860 kg/m^3, and a loose poured bulk density of 4800 $kg.m^{-3}$; and a bed of ground lime fertilizer with an SMD of 0.06 mm, a solid density of 2700 $kg.m^{-3}$, and a loose poured bulk density of 1410 $kg.m^{-3}$.

Powders were loaded into the bottom of the vessel to form a flat bed with a 100 to 150 mm depth. An ultrasonic sensor (MB7139) was mounted on a tube and positioned toward the centre of the bed inside the vessel, 30 mm above the bed surface. Readings from the sensor were recorded. The sensor

was then elevated in increments of 50±5 mm, and the distance was recorded at each elevation. In all tests and for all powder beds, the ultrasonic sensor successfully recorded the range with a precision of ±10 mm. This finding suggests that for the range of powders tested, the reflectivity of the ultrasonic waves was sufficient for the rangefinder to accurately calculate the wave's time of flight and perform range finding.

2.6.1. Ultrasonic Sensor Calibration

The sensors' accuracy in reporting the sample surface distance was tested. For this test, Two ultrasonic range finders, one in the middle of the vessel cover plate and the other adjacent to the vessel wall, were used to measure the distance between the vessel cover plate and the powders. The material height was adjusted by adding the polyethylene sample layer by layer to the vessel (Each load was 5 to 10 kg of the sample). The distance between the sensor and a point on the material surface right beneath the sensor was gauged using a tape measure. The distances obtained using the tape measure were compared to the sensor readings. Figure 2-5 shows this comparison.

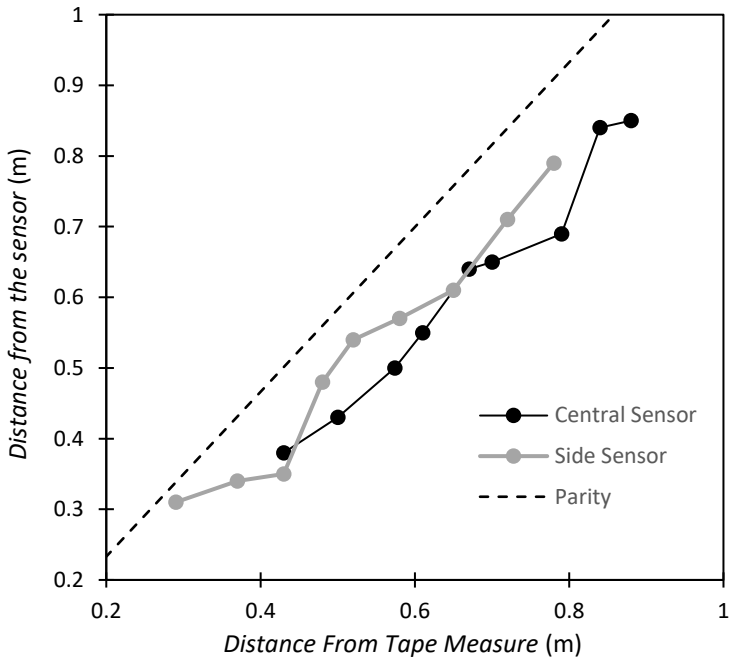


Figure 2-5: *A preliminary test comparing sensor reading with tape measure reading.*

On average, the sensor readings were 6.4% and 1.6% lower than the central and side sensors' tape measure readings, respectively. The corresponding sensor reported a distance reading for each data point based on the most robust reflection from the material's surface. This robust reflection did not necessarily reflect from the point directly beneath the sensor.

2.6.2. Static Tests

For the static tests, the positions of the eight side ultrasonic sensors were modified to determine where most sensors consistently provided readings within the expected range. With the vessel filled halfway and configured with a convex material surface, the sensors were gradually moved from the centre to the sides, with increments of 10 mm in radius. The only position where all the sensors consistently provided readings within range was when the sensors were pressed against the vessel walls. Figure 2-6 illustrates that the standard drum exhibits two extrusion steps on its walls. These extrusions seemed to reflect the ultrasonic pulses and led to malfunctions in the ultrasonic sensors. By positioning the sensors along the grooves closer to the vessel's side wall, all the side sensors provided readings within their field of view in over 90% of the static tests. Additionally, the reflections from the walls were minimized. As shown in Figure 2-6, for both the static and dynamic tests, all the sensors were secured against the vessel's side wall within a radius of 263 mm.

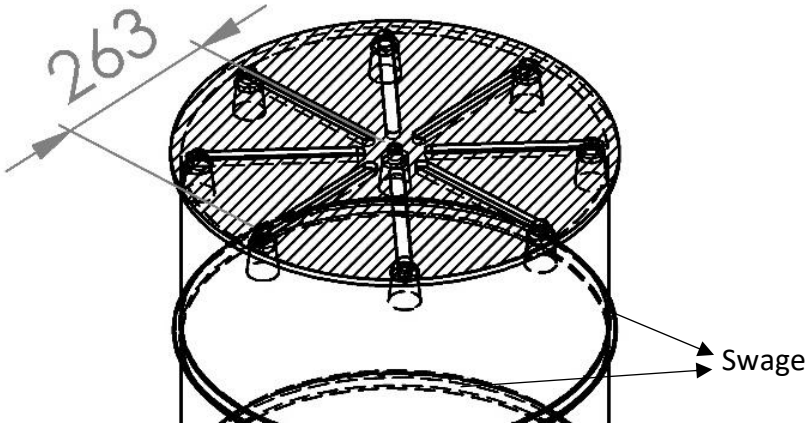


Figure 2-6: *The position of ultrasonic sensors on the vessel's cover plate with minimum faulty readings. The side sensors were installed in a radius of 263 mm. touching the vessel's wall.*

Figures 2-7, 2-8, and 2-9 show the results of the static tests for the polyethylene pellets sample with convex, flat, and concave surfaces, respectively. The ordinate of these figures represents the estimated fill fraction of the vessel, calculated by dividing the estimated fill volume using the ultrasonic sensors V_E by the volume of the vessel V_0. The abscissa of the figures is the fill fraction of the vessel, obtained by dividing the fill volume from material mass V_W by V_0 .

Figure 2-7 shows that the ultrasonic sensor volume estimation method has underestimated the sample volume throughout the measurement range. The estimated volume was 5 litres lower than the volumes obtained by material mass, equivalent to 2.5% of the vessel capacity of 200-litres. The

maximum disparity between the actual and estimated volumes was almost 12 litres at a fill fraction of 0.68%. The results show that the central sensor has recorded off-the-track readings 11 out of 13 times, and its value was substituted with other sensors' average readings.

For a flat material surface, as shown in Figure 2-8, the estimated volumes had better agreement with the volume from weighing than when the material surface was convexed. The disparity was ~2.6 m^3, equivalent to 1.13% of the vessel capacity. The disparity was higher for fill fractions up to 0.5. There was a better agreement for the limited data for fill fractions greater than 0.5, and the average disparity was 0.3 m^3, equivalent to 0.15% of the vessel volume.

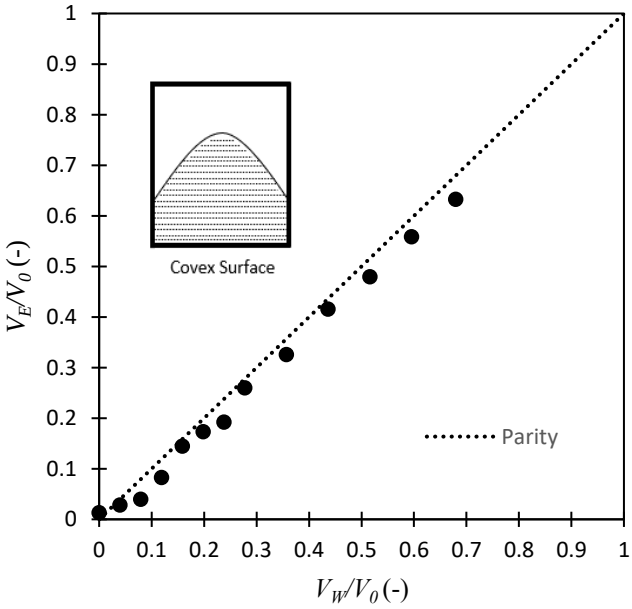


Figure 2-7: *Static sample volume determination in the 200-litre vessel. The material surface was modified to become convex.*

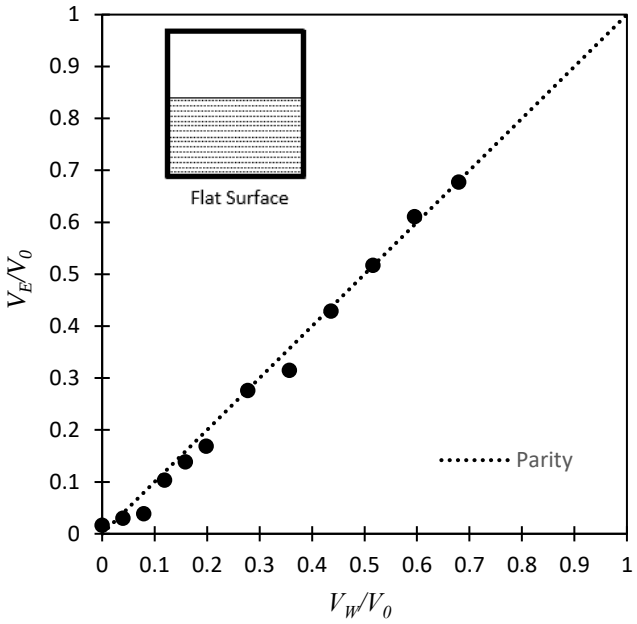


Figure 2-8: *Static sample volume determination in the 200-litre vessel. The material surface was modified to become flat.*

As the results for the static tests on the material with a concave surface in Figure 2-9 suggest, the fill volume was slightly overestimated using the ultrasonic method. This observation is in contrast to the results of the convex surface tests. The average disparity was 2 litres, with a maximum value of 7 litres, equivalent to 2.5% of the vessel volume.

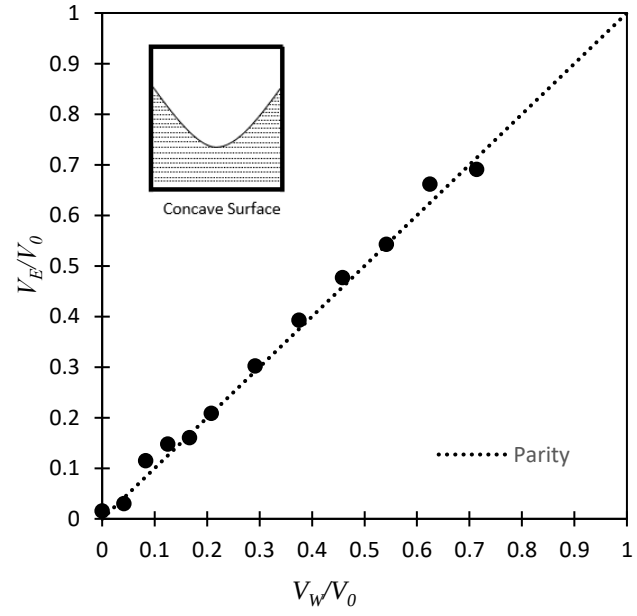


Figure 2-9*: Static sample volume determination in the 200-litre vessel. The material surface was modified to become concave.*

2.6.1. Discharge Test

Figure 2-10 shows the results for the discharge of polyethylene pellets from a 50 mm orifice. The plot has similar features to the discharge results for the 100 mm orifice, Figure 9, with the largest disparities in the induction period following flow initiation at fill factor circa 0.71 and again for the fill fractions less than ~0.3 in the final stages of the discharge.

Off-the-track readings were observed in discharge from both orifices. The frequency of off-the-track readings was ~6% of all readings from the sensors in the discharge test from the 100 mm orifice. This Figure was ~10% for the discharge from the 50 mm orifice.

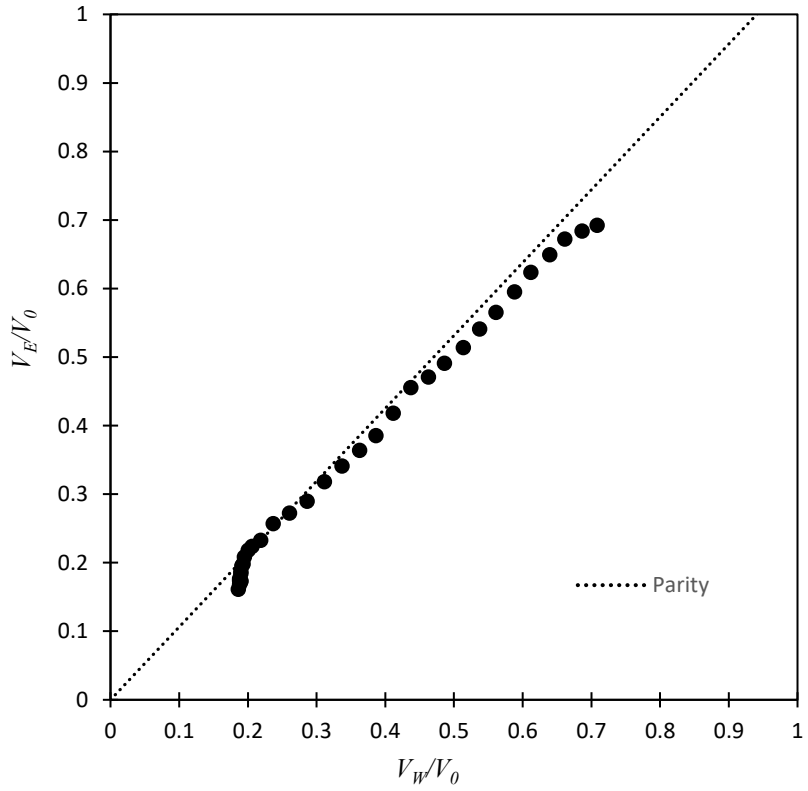


Figure 2-10: *Fill Volume measurement in dynamic discharge test of polyethylene pallets through a 100 mm orifice.*

Figure 2-11 shows the results of the discharge of the sample from the 50 mm orifice. The mean disparity was -0.3±0.5 (*CI.95*) litres and the standard deviation was 2.9 litres, with a maximum disparity of 8.3 litres, equivalent to 4% of the vessel capacity.

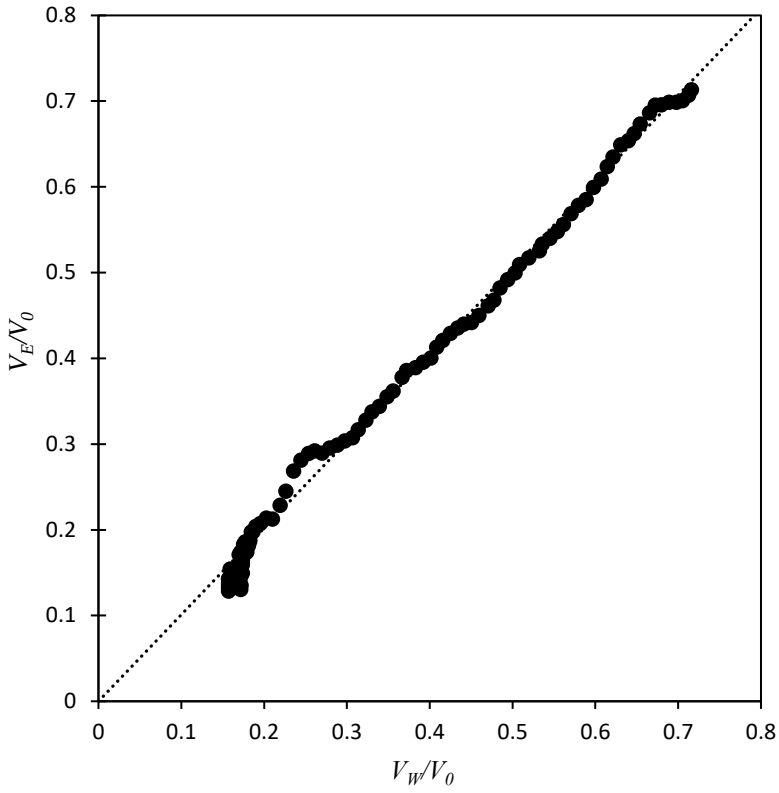


Figure 2-11*: Fill Volume measurement in dynamic discharge test of polyethylene pallets through a 50 mm orifice.*

2.6.2. Estimation of flowrate from the volumetric data

The estimated rate of change in vessel volume was assumed to be equal to the material's volumetric flow rate out of the vessel. Consecutive measurements of vessel volume (Every 1.1 s) provided enough data points to estimate the material flow rate out of the vessel. Figure 2-12 compares the estimated volumetric flow rate of the material through weighing and the ultrasonic method. These Figures were generated by dividing volume changes by the time between three measurements (~3.3 s). Flow rates from both methods tracked each other despite some fluctuations.

From 5 s to 25 s, a stable rate of mass change in the vessel was recorded. In this range, the flow rates from the ultrasonic method and weighing were 4.71 x 10^{-3} $m^3.s^{-1}$ and 4.84 x 10^{-3} $m^3.s^{-1,}$ respectively.

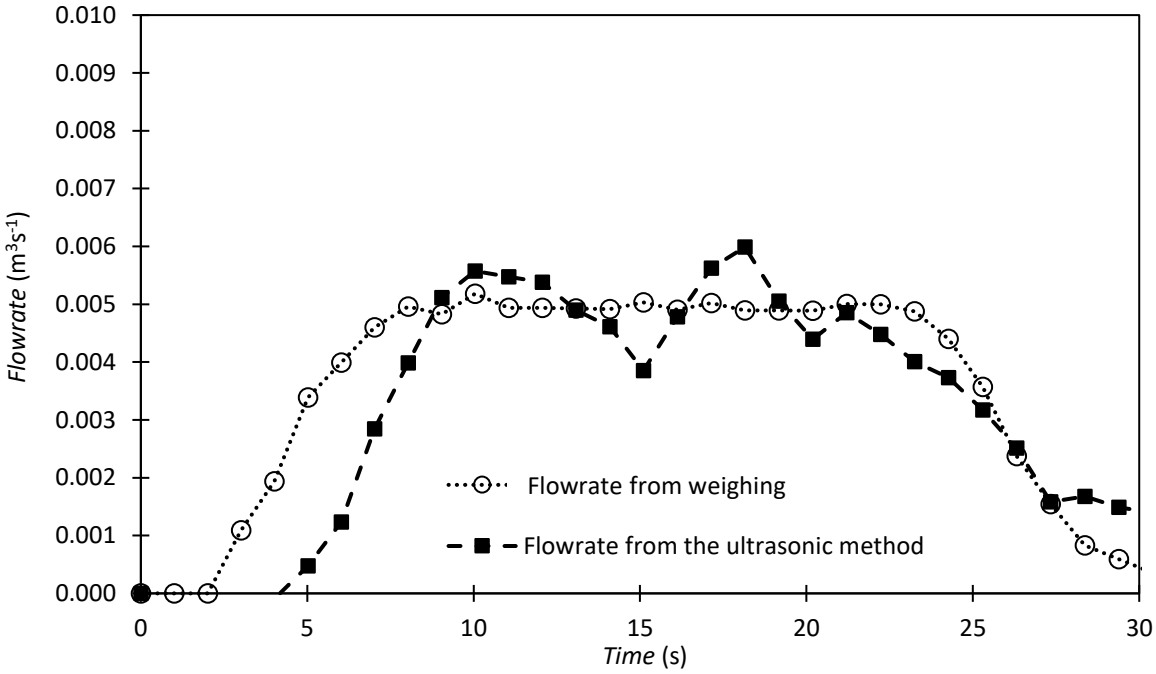


Figure 2-12: *Flowrate of the sample out of the vessel.*

2.7. Discussion

2.7.1. Sources of error in the sensors

Ultrasonic rangefinders have an intrinsic accuracy based on their ability to measure the time of flight of the transmitted pulses. Environmental conditions, including ambient air temperature, contribute to distance measurement uncertainty. The intrinsic accuracy of the ultrasonic rangefinders used in this study is 10 mm, equivalent to a maximum disparity of 1.28 % of the vessel volume.

Ultrasonic sensors require a surface almost perpendicular to the pulse travel direction to reflect the emitted pulses to the sensor (Figure 2-13, *A*). The pulse may bounce off when reflecting from an inclined surface (Figure 2-13, *B* and *C*). When the material freely gets discharged from a vessel, it forms an inclined surface based on its dynamic angle of repose. In this case, The transmitted ultrasonic pulse may hit the vessel's wall and bounce off towards the sensor (*B*) or miss the sensor (*C*).

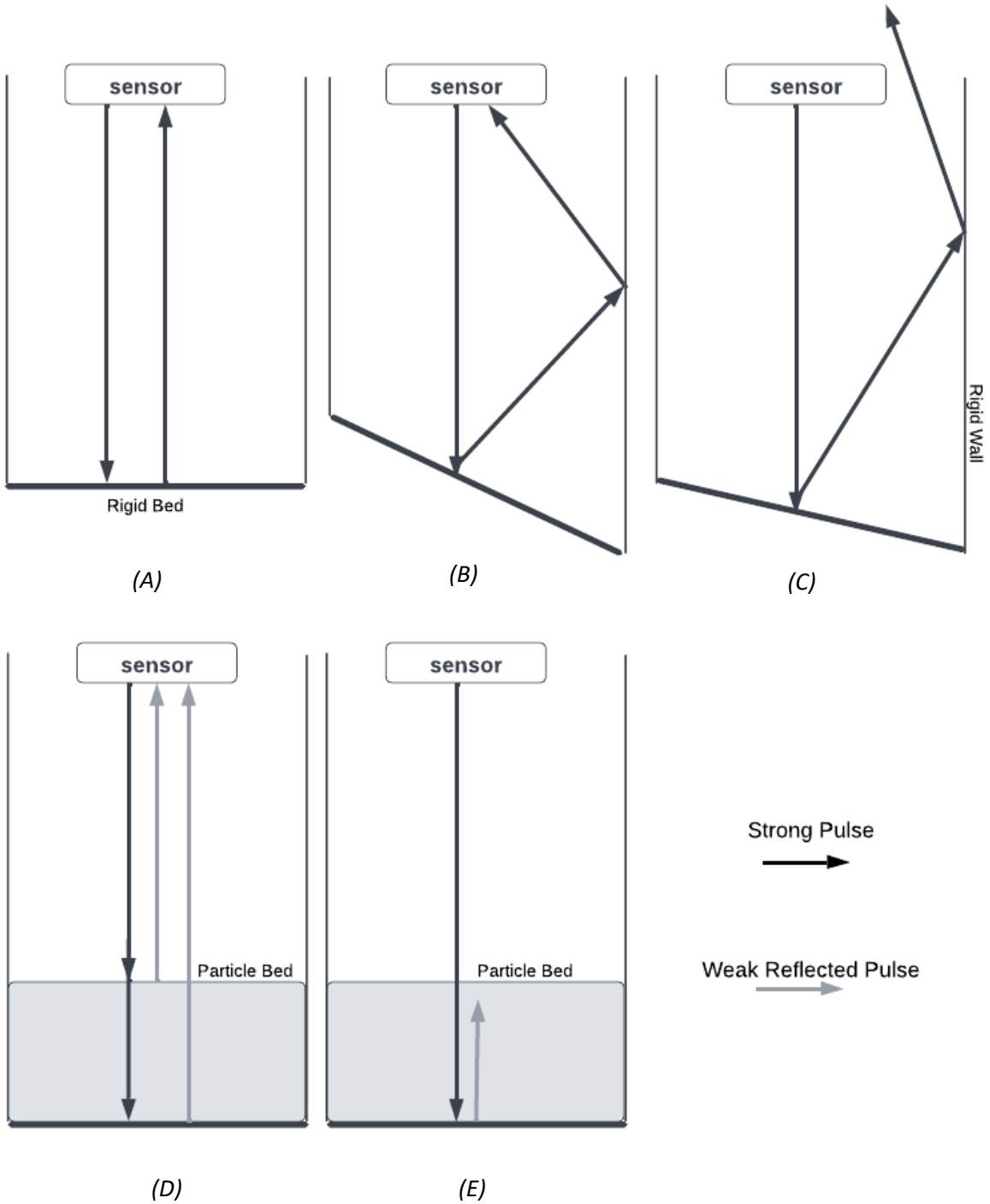


Figure 2-13: *Possible scenarios in reflection of the ultrasound wave from the surfaces in a vessel.*

When ultrasonic waves hit a porous material (Figure 2-13, *D* and *E*), a portion of the wave can reflect from the solid phase back to the sensor. Another portion of the wave can penetrate the bed and reflect from the vessel's rigid bottom to the sensor (*D*). This dual reflection can negatively affect the sensor's distance reading ability. The other possible source of the faulty reading is the absorption of the incident ultrasonic wave in the bed of particles (Figure 2-13, *E*). The acoustic energy can be

dissipated in the material's pores through various thermal and viscous mechanisms (Kuczmarski & Johnston, 2011), limiting the amount of reflected energy to the ultrasonic receiver.

2.7.2. The disparity in static tests

Figure 2-14 shows the disparity ($D\%$) between the sample volumes estimated using the ultrasonic-based method and the volumes obtained by weighing, which was calculated using the following equation:

$$D\% = 100 * \frac{V_E - V_W}{V_0} \qquad 2\text{-}4$$

For all material volumes and surface configurations, $D\%$ was under 5 (*SD*=2.7% of vessel capacity) for all three surface configurations. The mean disparity based on a 95% confidence interval was -0.6±0.9% of vessel capacity.

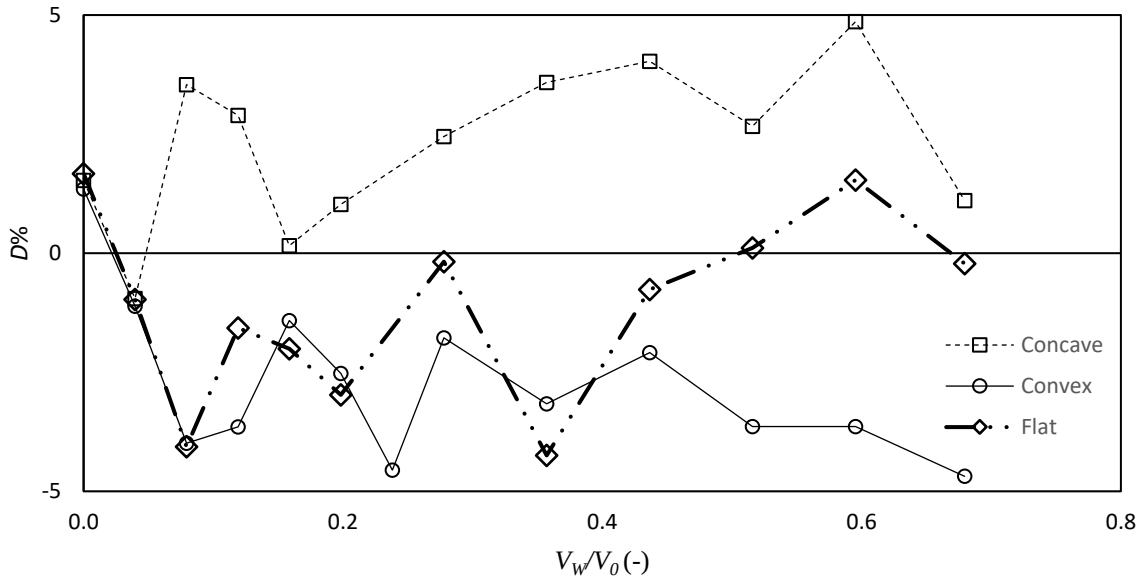


Figure 2-14: *Volume estimation disparity in the static tests.*

2.7.3. Discharge Test

The discharge test results suggest that implementing an array of ultrasonic sensors in a discharge vessel has the potential for real-time sample volume estimation. Consecutive measurements made it possible to estimate the material flowrate.

One measurement cycle may be significantly prolonged when the sensors with equal pulse frequency run sequentially. In this study, it took 1.1 s for one measurement cycle. If a higher measurement rate is needed, it is suggested to use ultrasonic sensors at different working frequencies

to run them in parallel. In the dynamic tests, the maximum disparity in volume estimation was 5.3% vessel capacity. In the Fill Factor range of 0.2-0.7, a higher agreement between the estimated volumes by weighing and ultrasonic sensors was observed with a standard deviation less than ±1.5% of the vessel capacity in the repeated tests.

Based on a 95% predictive interval, the uncertainty in volume estimation for the repeated discharge tests from the 200-litre vessel is ±3%V_0 ($PI(.95)$= -0.3±5.9 litre = -0.15±2.9%V_0).

2.7.4. Sensor Count

Experiments were initially conducted using an array of nine ultrasonic sensors. Lowering the number of sensors impacts measurement accuracy, and this has been investigated by varying the selection of active sensors in the vessel using the same data set obtained using the nine-sensor array. Figure 2-15 shows the active ultrasonic sensors' arrangement located as star markers indicate. In case (A), a single sensor is located at the centre of the vessel cover plate. In case (B), a single sensor is positioned at the side of the cover plate. For case (C), two sensors are employed: one measures the level from a virtual central circle with a diameter equal to one-fifth of the vessel diameter, while the other measures the material level from the sides. In case (D), five sensors are utilized: one covers the central circle, and the other four covers the cross-section.

The discharge test results for these sensor arrangements, presented in Figure 2-15, are compared to those obtained using all nine ultrasonic sensors (case E). The parity graph in Figure 12 indicates that using a single sensor (in cases A and B) results in disparities as high as 10.7% of the vessel capacity. Case (C) results were more consistent with Case (E), the nine-sensor data. Case (D), which employed five ultrasonic sensors, closely tracked the data from case (E). Comparing cases (D) and (E) suggests that reducing the number of sensors from nine to five achieves similar precision; in both cases, the standard deviation is ~2% of the vessel capacity. Using five sensors instead of nine for the application discussed in this paper yields comparable results, but a single sensor or a combination of a sensor at the wall and a central sensor increases measurement uncertainty. These results suggest that when absolute precision is not required, a small number of ultrasonic rangefinder sensors located in the cover plate of a powder discharge vessel or suitably positioned in the upper part of the vessel can provide reliable information on fill levels under either no-flow or free-flowing conditions.

2.7.5. Sensor Position

The positioning of the sensors significantly influences the feasibility of this volume measurement method. The type of sensor chosen is also critically important. From our observations, sensors that report the distance to the most robust reflection are better suited for monitoring the vessel sides, while those that report the distance to the closest object are more appropriate for the vessel centre.

Occasionally, sensor readings significantly higher than expected, off-the-track readings, were observed. These were likely due to wall effects and ultrasonic pulses bouncing from internal surfaces. Such anomalous values can be identified using geometric criteria and replaced with an average value.

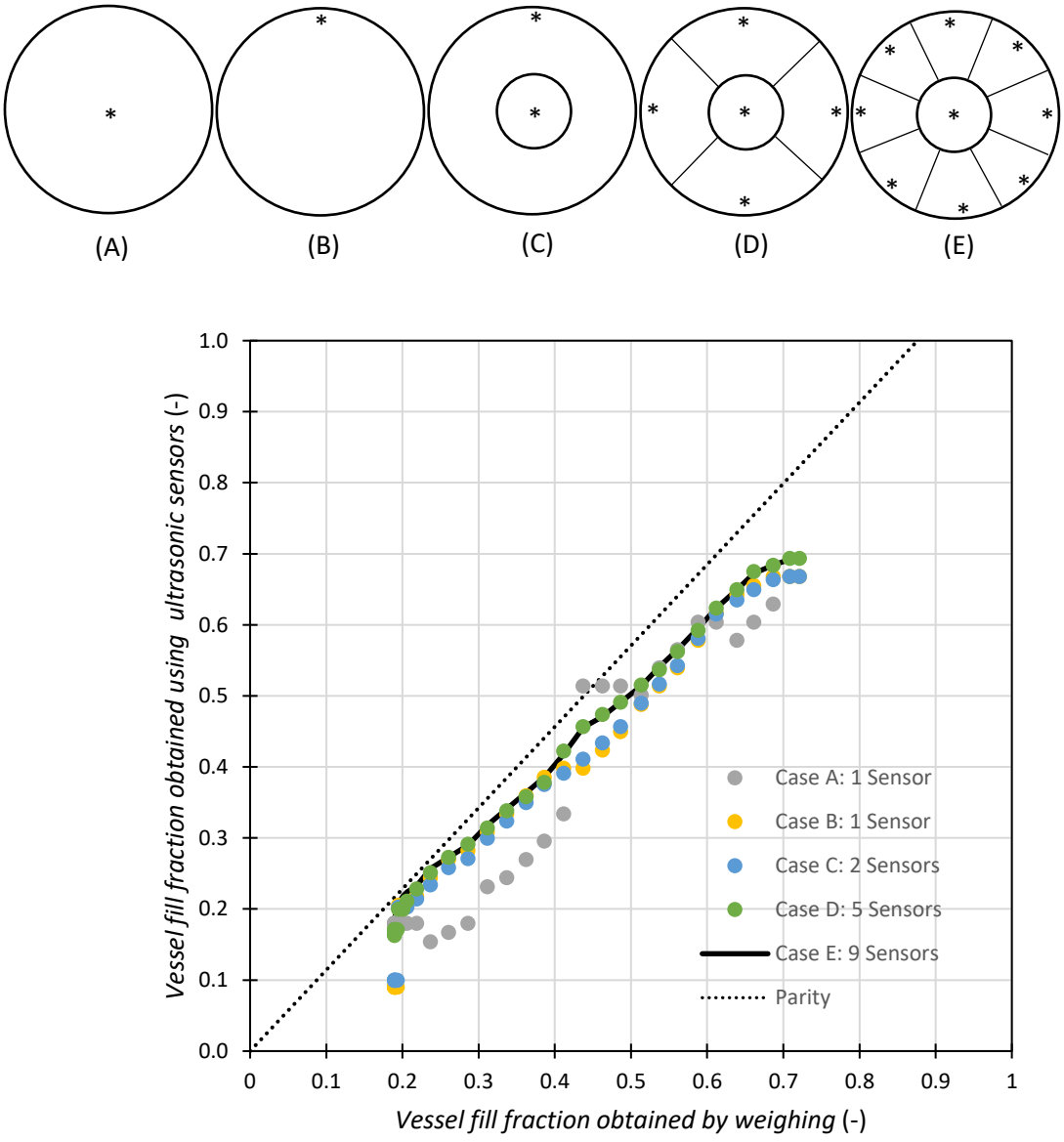


Figure 2-15: *Discharge test results when using various numbers of sensors.*

2.8. Summary

This chapter explores a non-invasive technique for measuring a powder discharge vessel fill volume using an array of off-the-shelf ultrasonic range finders and demonstrates a method for calculating fill volume using the MLVM model outlined in this chapter.

A standard 55 US-gallon drum was used as a powder storage and discharge vessel. An array of nine ultrasonic sensors was integrated with the cover plate of the vessel, with each sensor responsible for detecting the material level in one of nine virtual subsections of the vessel cross-section. The sensors were arranged, with one positioned at the centre and eight others adjacent to the vessel wall. The central sensor estimated range based on the closest object, and the side sensors estimated range based on the most robust reflection. With this arrangement and choice of sensors, the fill volume of the vessel discharging powders from an opening at the bottom was measured at intervals of 1.1 s, 0.9 Hz. The results suggest that implementing ultrasonic range finders in a powder discharge or storage vessel can provide real-time estimation of the vessel fill volume. The maximum disparity between the actual and estimated volumes in all static and discharge tests was within 5% of the vessel capacity. The standard deviation for measurement precision between the actual and estimated volumes, as determined through powder discharge tests using the ultrasonic method, was within 2% of the vessel capacity.

Chapter 3 Measurement of vessel fill volume using optical imaging

The outcomes presented in this chapter have been published by Barzegar, Redding, et al., (2024) in 'Powder Technology', an Elsevier journal, under the title:

'Fill volume in a storage vessel determined by optical scanning'

3.1. Introduction

The surface of the bed of the material freely discharging from a hopper is not flat and naturally becomes concave. In aircraft manoeuvres, and likely in other applications with high levels of dynamic movement, a single-point level measurement cannot provide the desired accuracy in fill volume measurement. Chapter 2 addressed this problem with multi-point level measurements using ultrasonic range finders. This chapter discusses the same strategy using stereoscopic optical imaging. Chapter 1, section 1.2.7, briefly introduces the technology and its applications.

Depth cameras generate surface maps, which are called point clouds. A point cloud refers to an array of points with spatial coordination. The point cloud obtained from a surface scan provides three-dimensional coordination of the various points on the scanned surface. Breaking down the scanned surface into a matrix of cells with known geometrical locations provides a surface map with depth-associated elements. Depth refers to the distance from the surface element to a reference plane, usually the plane on which the depth camera sensors are located. This is analogous to having many level gauges hanging from the lid of a hopper, each utilized for measuring the level of a particular area of the material bed. The point clouds obtained are interpreted as vessel fill volume, which requires an algorithm to transform the point cloud obtained from the material surface into bulk volume. The bulk volume can be correlated to material mass. The repeated measurement of material mass estimates the real-time flow rate of material out of a hopper and provides awareness of material clogging, which was discussed as a hazard in Chapter 1.

Bulk volume estimation using a depth camera has its challenges. Depth cameras are optical devices with sensors that must be kept clean. The cleanness of the optics is a concern, primarily when implemented in a dusty industrial environment. Depending on the make, they have a limited field of view; therefore, utilizing them in a tight space can be problematic in obtaining a full or reasonably wide view of the surface. This chapter addresses these challenges and introduces an algorithm for estimating a powder discharge vessel's real-time fill volume using three-dimensional (3D) surface scans of the material inside.

3.2. Materials

3.2.1. The Scanner

Intel RealSense D435 depth cameras (Intel Corporation, 2018, United States) performed surface scans of the material in the experimental vessels. The D435 sensor package includes a pair of RGB (Red-Green-Blue) cameras, an IR random pattern projector, and a processor to handle the block-matching algorithm for generating point clouds. This sensor is widely used in human gesture analysis (Das & Kumar, 2016) and other applications such as face recognition (Anggraini et al., 2016).

The sensor was interfaced with the computer using the manufacturer-supplied Software Development Kit (SDK) version 2 (Intel RealSense SDK v2.0, 2021). The SDK allows internal parameter adjustment. Using the SDK, the resolution of the sensors was set to 640X480 pixels, the point cloud capture rate was set to 30 frames per second, and the infrared pattern emitter was set at 100% power. In these settings, the sensors covered a horizontal and vertical Field of View (FOV) of 90±3 and 55±3 degrees, respectively. The minimum detectable range (z_{min}) was 130±20 mm. According to the manufacturer, the sensor provides a depth measurement accuracy of 2% of the distance at 80 % of its Field of View. The distance calibration tests against a flat wall 1 meter away from the sensor face parallel to the wall resulted in accuracy values in agreement with the manufacturer's claim.

3.2.2. Storage vessels

The fill volume measurement experiments were conducted on two storage vessels: a 50-litre vessel monitored using a single depth sensor and a 200-litre vessel monitored with a pair of sensors.

50-litre vessel

Figure 3-1 shows the 50-litre discharge vessel components. The vessel was made out of a PVC pipe with a diameter of 300 mm and a length of 720 mm, with a 150 mm hole at the bottom and a housing for interchangeable flow control orifices. The orifices with diameters 26, 50, 71, and 90 mm controlled the flow rate. The orifices were cut from a 1.2 mm thick stainless steel sheet and attached to the bottom housing of the container with eight bolts. The orifice housing was 130 mm wide. Before initiation of discharge, orifices were blanked off using duct tape. For discharge initiation, the duct tape was quickly removed.

The storage vessel was placed on a table with a hole at the bottom, and the discharged material was collected in a bucket. The distance between the bucket and the 50-litre vessel was roughly 0.5 m.

The bucket was placed on a platform scale (IND221, Mettler Toledo, USA) with a resolution of 0.005 kg. The scale was connected to the computer via an RS232 serial data link.

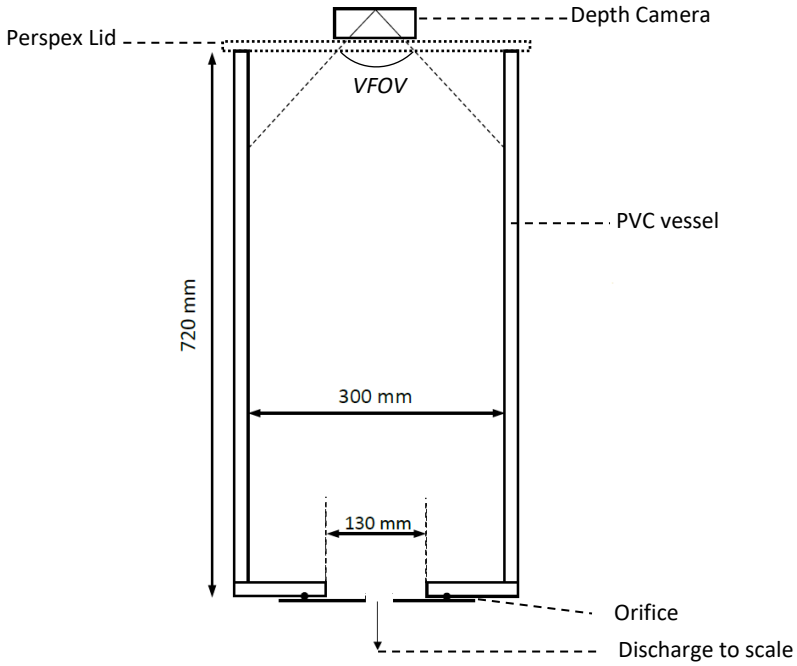


Figure 3-1: *The 50-litre vessel. VFOV: Vertical Field of View.*

The vessel was covered using a circular cover plate cut from an acrylic sheet 12 mm thick. The sensor was glued on the centre of the outer side of the lid, facing downwards.

200-litre vessel

Figure 3-2 shows a standard 55-US gallon drum, referred to as the 200-litre vessel in this thesis. This drum was used to test the method of fill volume measurement using the optical method. The dimensions of the drum are provided in Figure 3-2. The oil drum was placed in the centre of a rectangular frame, the same platform scale introduced in Chapter 2. One side of the frame sat on a pair of point contact joints. The other side of the frame sat on a 1,000 kg load cell (PT Ltd, New Zealand). The sketch of the assembled structure of the 200-litre vessel apparatus is provided in Appendix E. The load cell was connected to a driver (EMC 2060, New Zealand) for sensor readout. The load cell driver was connected to a microcontroller (Arduino Mega 2560, Arduino, Italy). The microcontroller was interfaced with a computer using an RS232 serial data link. The load cell was calibrated by filling the vessel with a bulk solid (polyethylene sample introduced in Section 3.2.4) with known weight in five steps and calibrated to an accuracy of ±0.2 kg.

A sliding wooden plate was installed beneath the 50 mm circular flow control orifice at the bottom of the drum. The discharge was initiated by pulling out this plate.

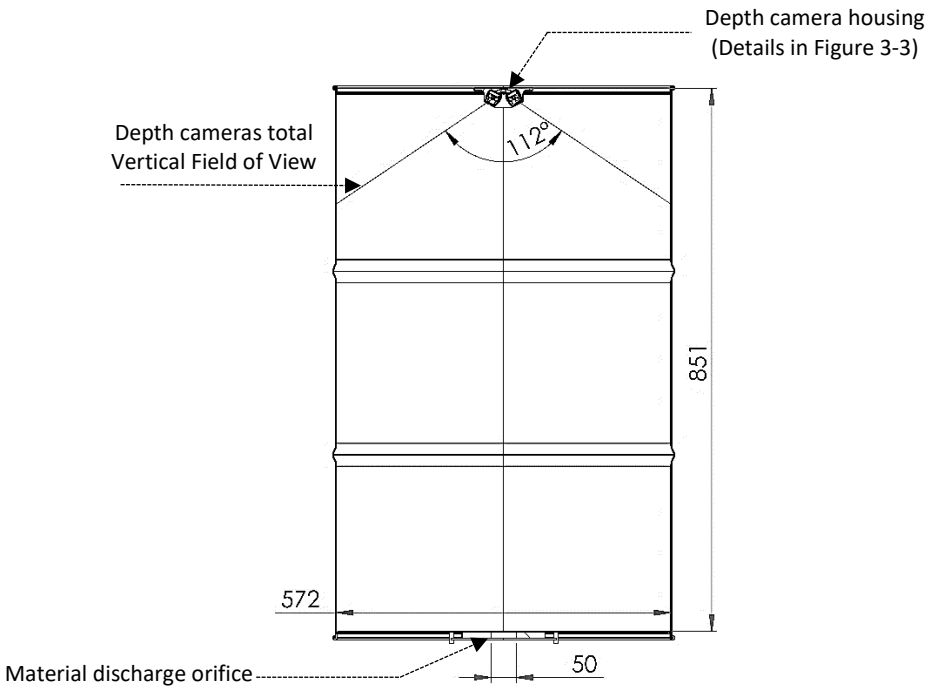


Figure 3-2: *200-litre vessel. Dimensions in millimetres.*

The vertical viewing angle of the optical system was doubled by installing two depth cameras in a 3D-printed housing. Figure 3-3 shows the camera housing with details available in Appendix E. This expansion of the field of view from 57° to roughly 112° enabled the experiments to be conducted on the broader cross-sectional area of a 200-litre vessel. The dust buildup issue on the optics was addressed using purge air. A high-pressure air tube was connected to the camera housing. This solution created an air passage around the sensors, allowing high-pressure air to enter from the side of the housing and exit through a 0.5 mm gap on the sides of the sensor face, forming an air blade cover that helped to keep the optics dust-free (Graphical drawing provided in Appendix E).

3.2.3. Software

A computer program was coded in C++ using Microsoft Visual Studio Compiler (2016) to communicate with the camera and scales for volume and weight measurement. The program handled real-time measurement and data logging. The mass and volume flow rates were calculated and displayed in real-time. Graphical depictions of surface meshes were generated using the open-source software MeshLab (Cignoni, P. et al., 2008).

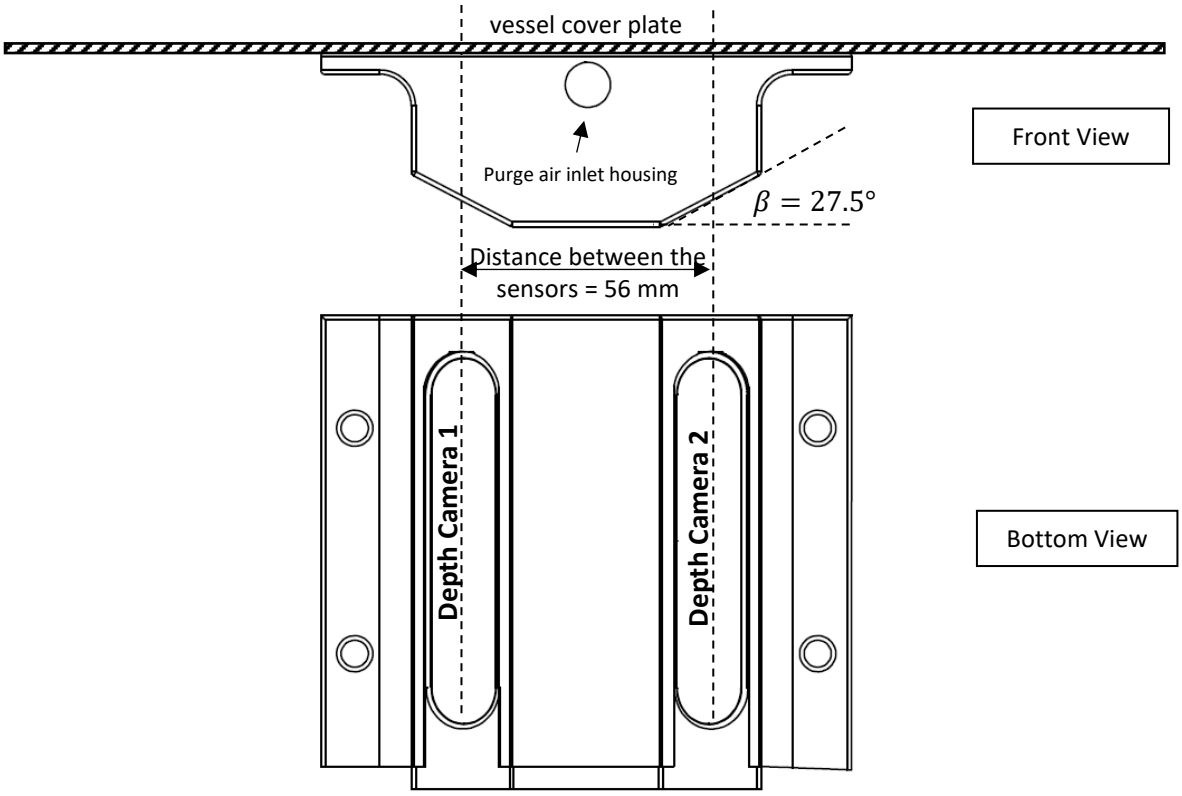


Figure 3-3: *3D Printed Housing for the two sensors in 200-litre vessel experiment. This housing sat in the centre of the 200-litre vessel's lid.*

3.2.4. Test Material

Two test materials were used in the discharge experiments on the 50-litre vessel: Mustard seeds, an approximately spherical and free-flowing test material, and agricultural lime, a cohesive test material with fine particles. The 200-litre vessel tests were conducted on polyethylene plastic pellets with a semi-cylindrical shape, the same sample used in the experiments in Chapter 2 and introduced in Section 2.2.4. The physical properties of these samples are presented in Table 3-1.

Table 3-1*:Physical properties of the test material.*

Sample	Loose density ($kg.m^{-3}$)	Tapped density ($kg.m^{-3}$)	Particle diameter (mm)
mustard seeds	720	730	1.98
Agricultural Lime	141	148	0.31
Polyethylene	600	620	3.35

The loose bulk density was determined using the apparatus and method in New Zealand Standard NZS-3111 (Standards Association of New Zealand, 1980) with three replicates. Tapped density was measured by tapping 100 ml of samples using a Stampfvolumeter STAV 2003 tapping machine (STAV,

Germany). A Mastersizer 3000 (Malvern, UK) was used for particle size distribution analysis of mustard seeds and agricultural lime (Sauter mean diameter).

3.3. Methods

3.3.1. The Model

Figure 3-4 shows a 3D surface scanner installed above an arbitrary vessel. The vessel is filled with a powder that discharges from the bottom. The scanner generates point clouds from the surface of the powder in the vessel.

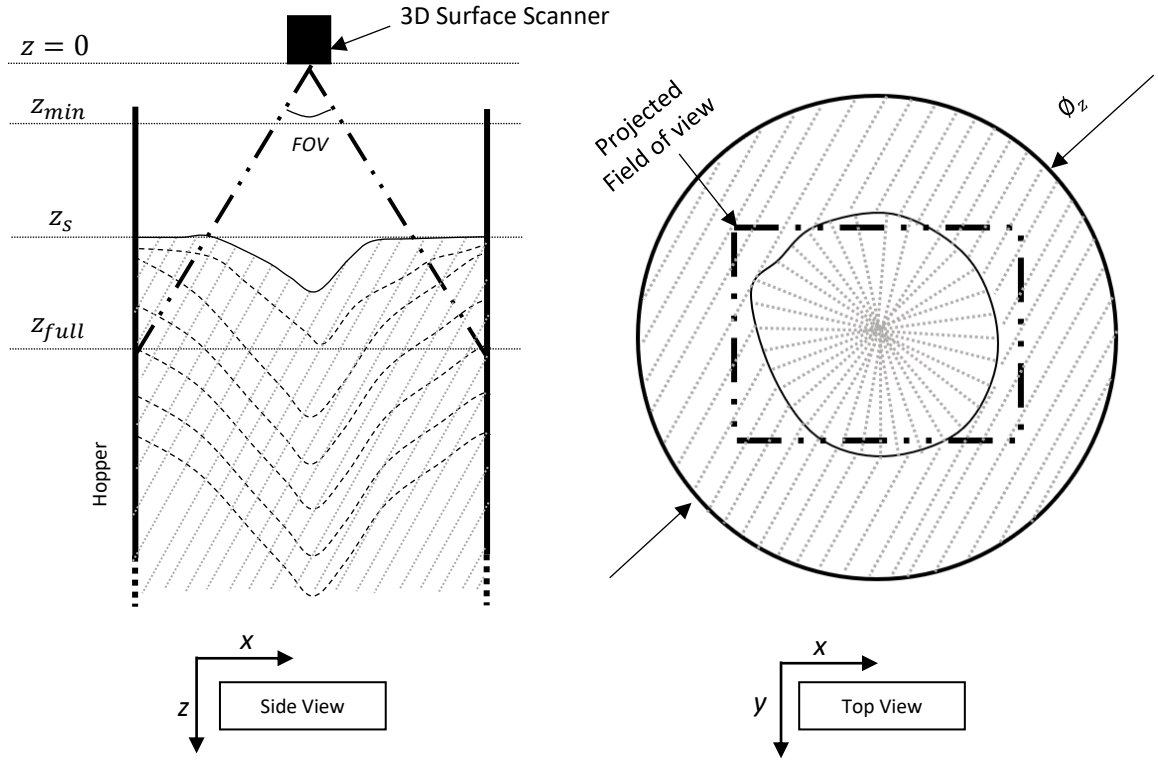


Figure 3-4: *Field of View (FOV) of a depth camera in a hopper.*

The minimum material depth that the scanner is capable of scanning is shown by z_{min}. This parameter is the minimum working range of the scanner and should be considered a geometrical constraint. The scanner in Figure 3-4 has a field of view that partially covers the material surface at the depth z_s. Once the material falls below the depth z_{full}, the scanner provides full-view coverage of the vessel side walls. The depth, z_{full}, can be calculated as follows:

$$\boldsymbol{z_{full} = \frac{0.5\phi_z}{tan\frac{FOV}{2}}} \qquad \textit{3-1}$$

where FOV is the minimum field of view of the scanner, which might be either the vertical or horizontal field of view. $\emptyset_z$ is the diameter of the circular hopper at the depth *z.*

In Figure 3-4, the depth camera, in its field of view, captures a point cloud similar to what is shown in Figure 3-5. Every depth point in the point cloud array has an index of i. The i^{th} depth point in the point cloud array is associated with a Cartesian coordination denoted as x_i, y_i and z_i.

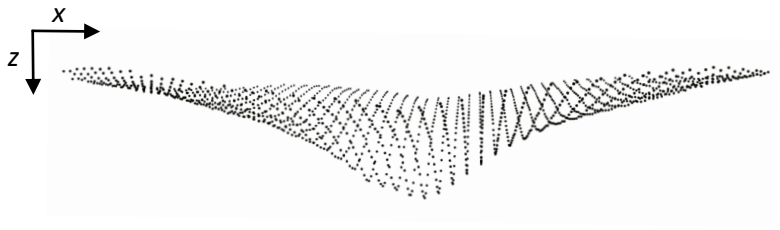


Figure 3-5: *An example of a point cloud captured from the material surface where the hopper walls are not in the Field of View.*

When the surface of the material in the hopper discharges to the levels below z_{full} (Figure 3-4), the associated point cloud contains points scanned from the walls of the hopper. Figure 3-6 show a point cloud typical for the Hopper walls scans. As is shown in Figure 3-6, the points on the wall do not follow a perfect vertical line and are scattered around the wall due to the wall being parallel with the scanner optics, which results in distorted patterns. The points on the hopper wall must be identified and removed from the point cloud to prepare it for further analysis.

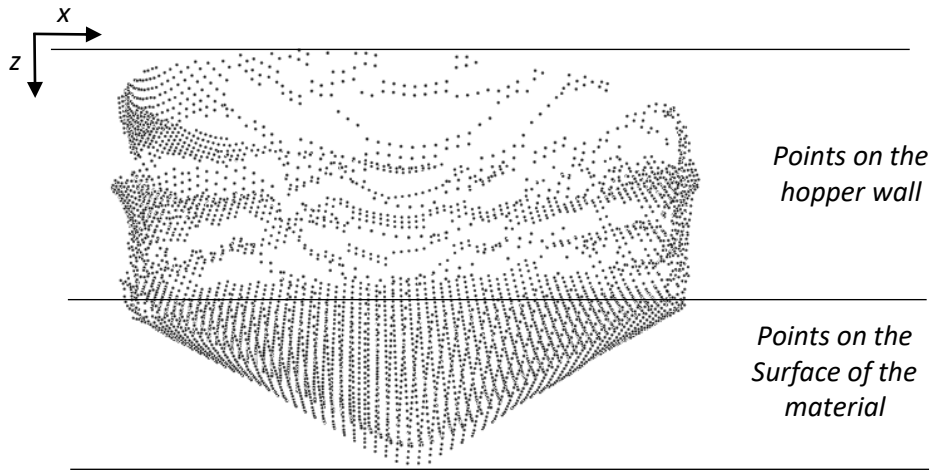


Figure 3-6: *An example of a point cloud captured from the surface of the material and the hopper wall.*

For a circular hopper, an indicator function $l(i)$ can be defined. This function takes a value of 1 for a point on the material surface and 0 for the points out of the material surface, on the vessel wall or random noise located outside the vessel walls, and should be discarded. The indicator function can be calculated as follows:

$$l(i) = \begin{cases} 1, & \sqrt{\left(x_i - \frac{L}{2}\right)^2 + \left(y_i - \frac{H}{2}\right)^2} < 0.95\frac{\emptyset_z}{2} \\ 0, & \sqrt{\left(x_i - \frac{L}{2}\right)^2 + \left(y_i - \frac{H}{2}\right)^2} \geq 0.95\frac{\emptyset_z}{2} \end{cases} \quad \textit{3-2}$$

where L is the point cloud length in the x axis, H is the point cloud length in the y axis. Vessel diameter ($\emptyset_z$) for the circular vessels used in this study was constant for all depths. As seen in Equation 3-2, a tolerance of 0.05 of the vessel radius was used to identify the points falling on the wall.

A similar approach can locate the points on the hopper walls for a hopper without a simple geometrical cross-section. When empty, a 3D point cloud of the hopper can be used as a reference geometry. Using the reference scans of the hopper wall generated by the same scanner at the exact location, every point $z_{x,y}$ that falls on the hopper wall point cloud can be identified and discarded.

The next step in trimming the point cloud is finding noise points. Noise refers to the points not connected to the network of the point cloud. The appearance of these points can be due to the formation of dust, computational faults of the sensor or the distortion of the images. These points can be identified by their geometrical location in relation to the rest of the points. Each point in a point cloud that lacks a connection to the network of points is considered a noise point and is assigned $l(i) = 0$. To identify these points, an experimentally determined distance 'X' was selected. Any point at a distance greater than 'X' from its nearest neighbour is considered noise.

The point cloud from the material's surface can be broken into elements of a grid of square cells with side length C. Each element is denoted as $Z_{I,J}$ where I and J are two integers ranging from 0 to $\left[\frac{L}{C}-1\right]$ and $\left[\frac{H}{C}-1\right]$, respectively (Figure 3-7).

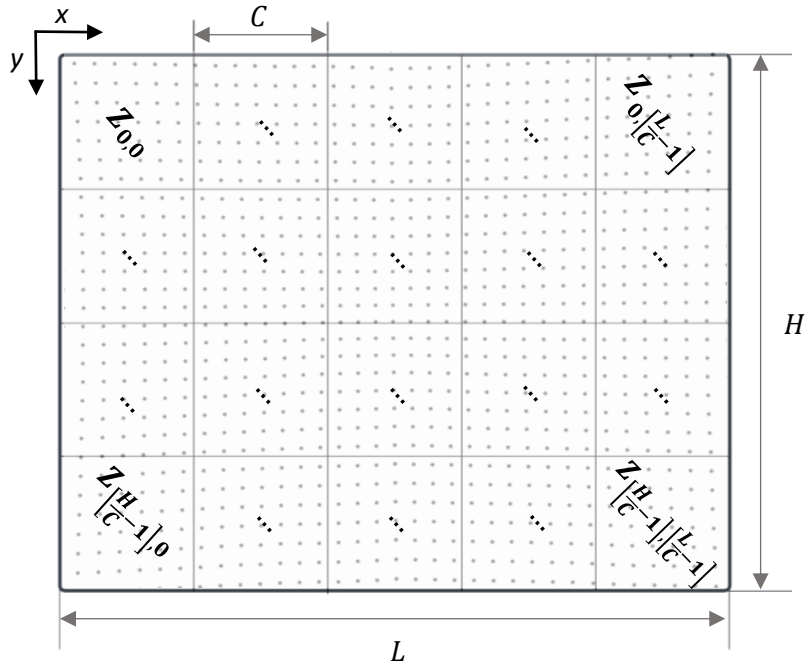


***Figure 3-7**: Breaking the depth camera projected field of view into matrix elements.*

Each surface grid cell houses depth points in the area that falls within the spatial location of the element. The number of points in each cell depends on the cell size, the resolution of the scanner and the distance between the scanner and the material surface. The next step is identifying the cells with an unreliable average depth value. These cells can occur around the hopper walls where some points related to the wall fall into them. Some cells can have unreliable depth values because of undetected noise points falling in those cells.

The average depth of the points in each cell is calculated and assigned as the cell value: $Z_{I,J}$. The depth points in each cell have a standard deviation of $\sigma_{I,J}$. The maximum possible deviation D of the depth points in a cell is limited to the angle of repose α of the material (Equation 3-3), as shown in Figure 3-8. This criterion can be used to find the cells with incorrect depth data.

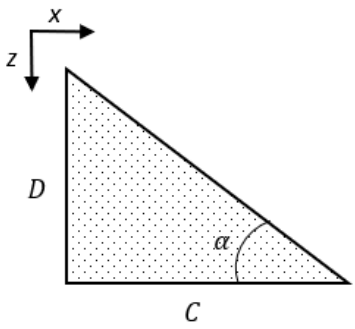


Figure 3-8: *Side view of a surface element with dimension C holding depth points with the maximum deviation of depth equivalent to D.*

$$D = Ctan(\alpha) \qquad \textit{3-3}$$

The statistical Range Rule (Triola et al., 2006) assumes the following:

$$\sigma_{I,J} \approx \frac{1}{4}D \qquad \textit{3-4}$$

The value for each surface cell can be calculated using 3-5, and the indicator function $L(I,J)$ can be defined to tag the cells with incorrect data based on 3-4 and 3-3 (Equation 3-6).

$$Z_{I,J} = \frac{\sum_i z_i}{\sum_i l(i)} \qquad if: \begin{cases} l(i) = 1 \\ JC < x_i \leq JC + 1 \\ IC < y_i \leq IC + 1 \end{cases} \qquad \textit{3-5}$$

$$L(I,J) = \begin{cases} 1, & \sigma_{I,J} \leq \frac{1}{4}Ctan(\alpha) \\ 0, & \sigma_{I,J} > \frac{1}{4}Ctan(\alpha) \end{cases} \qquad \textit{3-6}$$

Some cells in the generated surface grid may contain no depth points and form void cells. For the void cell Z_{I_h,J_h}, a value can be assigned by averaging the values of the adjacent cells using the following:

$$Z_{I_h,J_h} = \frac{1}{n} \sum_{\substack{I=I_h-1 \\ I \neq \left[\frac{H}{C}-1\right] \\ I \neq 0}}^{I_h+1} \sum_{\substack{J=J_h-1 \\ J \neq \left[\frac{L}{C}-1\right] \\ J \neq 0}}^{J_h+1} Z_{I,J} \qquad 3\text{-}7$$

where *n* is the number of valid cells adjacent to Z_{I_h,J_h}.

In the previous steps, the cells that contained depth points from the hopper wall were identified and removed. The missed area (A_m) around the hopper wall that falls out of the surface grid must be calculated. This area is shown in grey in Figure 3-9. The cross-sectional area of the Hopper at depth z_s is $A(z_s)$. The average depth of the material on the sides of the hopper wall, the area that is not covered by the surface matrix or is covered but the values are noisy ($L(I,J) = 0$), is shown by z_s in Figures 3-4 and 3-9.

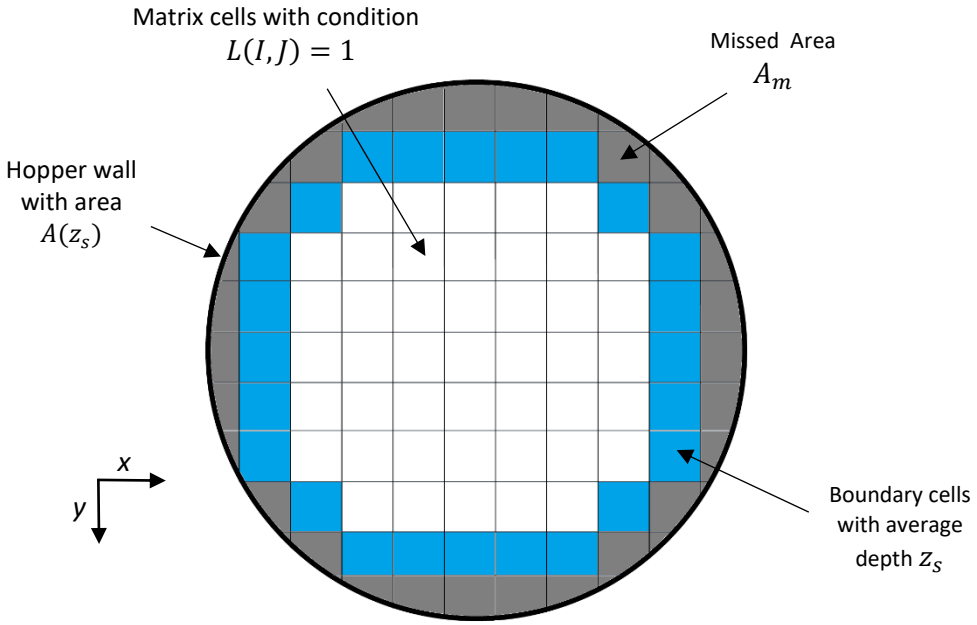


***Figure 3-9**: The missed area from the surface grid from the hopper cross-section at depth z_s.*

The value of z_s can be calculated by averaging the value of the boundary cells in the surface grid, which are coloured blue in Figure 3-9. The missed area can be calculated as follows:

$$A_m = A(z_s) - NC^2 \qquad 3\text{-}8$$

where *N* is the count of $Z_{I,J}$ conditional to $L(I,J) = 1$.

The free volume above the scanned surface up to the sensor reference plane (*z=0*) bounded by hopper walls can be calculated as follows:

$$V_E = \sum_I \sum_J Z_{I,J} \times C^2 \times L(I,J) + A_m \times z_s \qquad 3\text{-}9$$

Combining Equations 3-8 and 3-9, the fill volume V_F of the hopper from a surface scan can be calculated using Equation 3-10 as follows:

$$V_F = V_0 - \sum_I \sum_J Z_{I,J} \times C^2 \times L(I,J) - \ z_s \times (A(z_s) - NC^2) \qquad 3\text{-}10$$

where V_0 is the empty volume of the hopper with the upper boundary of the depth camera reference plane ($z = 0$). V_0 can be calculated using Equation 3-9 from the scans of the empty hopper. Equation 3-10 is referred to as the Optical Fill Volume (OFV) model.

3.3.2. Unified point cloud for two synchronized cameras

When using two cameras in tandem to expand the field of view, as is shown in Figure 3-3, the point cloud generated needs to be merged first. A spatial transformation of the point cloud obtained from the sensors can form a unified point cloud. The transformation was performed using a reduced form of the Affine Transformation for each point $\begin{bmatrix} x \\ y \\ z \end{bmatrix}$ as follows:

$$\begin{bmatrix} X \\ Y \\ Z \end{bmatrix} = \begin{bmatrix} 1 & 0 & 0 \\ 0 & cos(\beta) & sin(\beta) \\ 0 & -sin(\beta) & cos(-\beta) \end{bmatrix} \times \begin{bmatrix} x \\ y \\ z \end{bmatrix} - \begin{bmatrix} 0 \\ \delta \\ 0 \end{bmatrix} \qquad 3\text{-}11$$

where $\begin{bmatrix} X \\ Y \\ Z \end{bmatrix}$ is the coordination of the rotated point. The sensor pitch angle is denoted as β. The slot pitch angle for the designed camera housing was +27.5° for depth-camera-one and -27.5° for depth-camera-two. δ is half of the distance between the coordination system origins of the sensors. This is the distance that the new coordinate system is shifted. This value was +28 mm and -28 mm for the depth-camera-one and depth-camera-two, respectively.

3.3.3. Computations

Real-time fill volume measurement was achieved by parallel processing using the multi-threading concept.

For the 200-litre vessel where a pair of depth cameras in tandem were used, scans had to happen simultaneously. Two parallel threads opened independent communication channels with each depth camera. Multithreading ensured a maximum delay of 27 ms between the depth cameras to send their point cloud. The point clouds obtained from both cameras were merged after transformation using Equation 3-11 into a unified point cloud from the vessel.

Each point cloud, or unified point cloud when using two depth cameras, was stored in a buffer with the time of capture and weight of the material from scales. For the volume measurement analysis, 10 to 15 parallel processing threads were opened and loaded with the buffered data. Each thread

calculated the fill volume from the point cloud in the buffer and stored the results in log files. The logged data were the record of the processed surface grids, the vessel's fill volume, the timestamp of the scans, the weight of the material and the rate of fill volume change. Then, another thread was opened and filled with the buffered data, and the buffer was refreshed with a new capture.

3.3.4. Experiment Procedure

The tests were conducted under both static and dynamic conditions. Static tests are those conducted under no-flow conditions, and dynamic tests are those where the material freely lows out of the vessel.

For the static tests in the 50-litre vessel, the discharge orifice was blanked off, and the vessel was placed on platform scales. A mass of approximately 16,000 g of mustard seeds was added to the hopper in increments of around 300-400 g. The material was poured down the vessel's longitudinal axis from about half a meter height. After each load, the fill volume of the vessel was measured using the optical method.

For the dynamic tests in the 50-litre vessel, a flow control orifice plate of choice was bolted in place and covered with duct tape. The test material at known weight was filled to a height of approximately 300-400 mm. The camera, scales, and data collection systems were checked and activated before starting the flow by quickly removing the duct tape. The sample was discharged to the collection bucket, which sat on scales. One test run was performed for each control orifice. The same procedure was followed for both mustard seeds and agricultural lime samples.

In the static tests for the 200-litre vessel, the polyethylene sample with masses ranging from 5 to 10 kg was poured into the hopper, and the total mass was recorded with an accuracy of ±50 g. The bed of powder was kept untouched to keep its surface shape undisturbed. The volume of the material was measured by the double-sensor optical method and averaged over twenty measurements.

For the dynamic tests in the 200-litre vessel, 82 kg of polyethylene were added, and the surface was flattened. The 50 mm orifice cover was removed to start the experiment. Both masses from the load cell and volume from the double-sensor optical method were recorded for analysis.

3.4. Results

3.4.1. Experiments on the 50-litre vessel

Precision analysis

The accuracy and precision of the proposed method for measuring the empty volume (V_0) of the vessel was conducted before the static and dynamic tests. The depth camera protruded roughly 20 mm inside the vessel on the vessel's centerline using a monopod for this experiment. The distance between the depth camera zero origins and the bottom of the vessel was 680±5 mm. The bottom of the vessel was covered with white paper sheets. The lab lights were turned off, and the top of the vessel was covered to prevent light from entering. It was done to test if the depth camera's internal infrared pattern projector provides sufficient visibility for imaging. The actual volume of the vessel with the upper boundary intersecting with the depth camera's origin plane ($z = 0$ plane) was 48,060 ml ±0.7%. The software was programmed to measure empty volume with 1000 iterations. The recorded data underwent statistical analysis for the precision check. The results follow a normal distribution with a mean value of 48,227 ml and a standard deviation of 22 ml. Figure 3-10 shows the results of the precision analysis. According to the data analysis shown in the Figure, the measured empty volume was repeatable with an error of ±40 ml with a confidence interval of 95%, resulting in a precision higher than ±0.1%. In Figure 3-10, the ordinate indicates the percentage of the recorded data that falls in the corresponding deviation range.

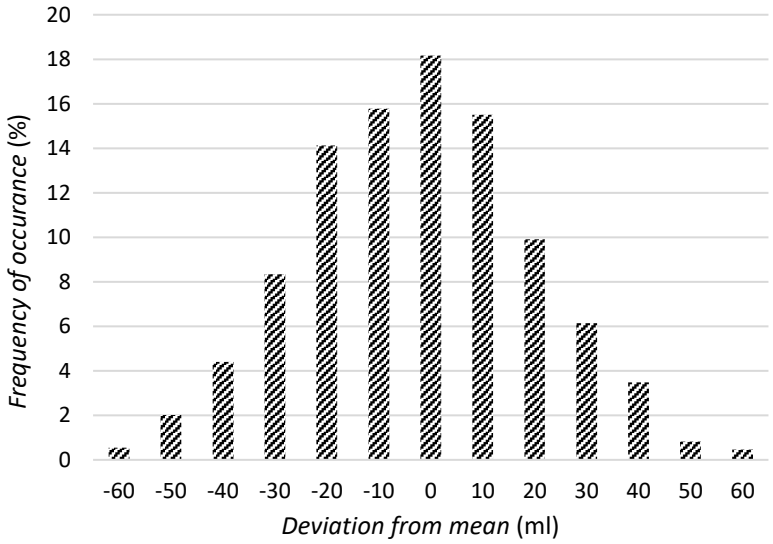


Figure 3-10: *Error distribution analysis for repeated measurement of the vessel empty volume.*

Static tests

Figure 3-11 shows the results of the static volume measurement on the mustard seeds. The volumes obtained using the optical method are compared with those obtained by weighing. The latter was performed by dividing the material mass by loose and tapped densities.

When a data point is on the parity line, both methods for obtaining fill volume yielded identical results. The comparison of the two volumes shows that the volume calculated using the sample mass and the loose poured density tracks the volume measured optically. The volumes calculated from the tapped density were slightly lower than the parity line, as expected, indicating the lower limit of the fill volume in the vessel.

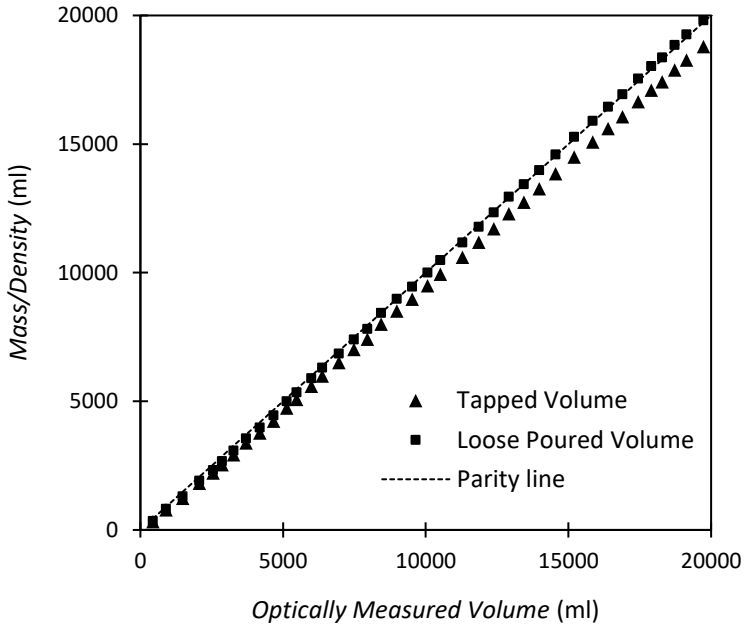


***Figure 3-11**: Comparison between the optically measured volume and predicted tapped and loose poured volumes based on the measured mass of mustard seeds added to the 50-litre vessel.*

Dynamic Tests

Results of the dynamic tests on the mustard seeds sample discharged from the 50 mm, typical of all flowrates tested, are presented in Figures 3-12. This Figure shows that the discharged mass and volume closely track each other.

The purpose of the discharge tests using the 130 mm opening was to evaluate the speed of the optical volume measurement method. The results for sample mustard seeds are presented in Figure 3-13. The results for the agricultural lime sample, not presented here, showed a similar trend.

The discharge through the 130 mm opening was similar to dumping the material out of the vessel. The impact of the material on the scale reading can be seen in Figure 3-13. There is a bump in the scale reading at 0.5 s from the discharge initiation. The total discharge occurred in three seconds, and in this period, the computer software measured fill volume in 15 timestamps, a measurement rate of approximately 5 Hz.

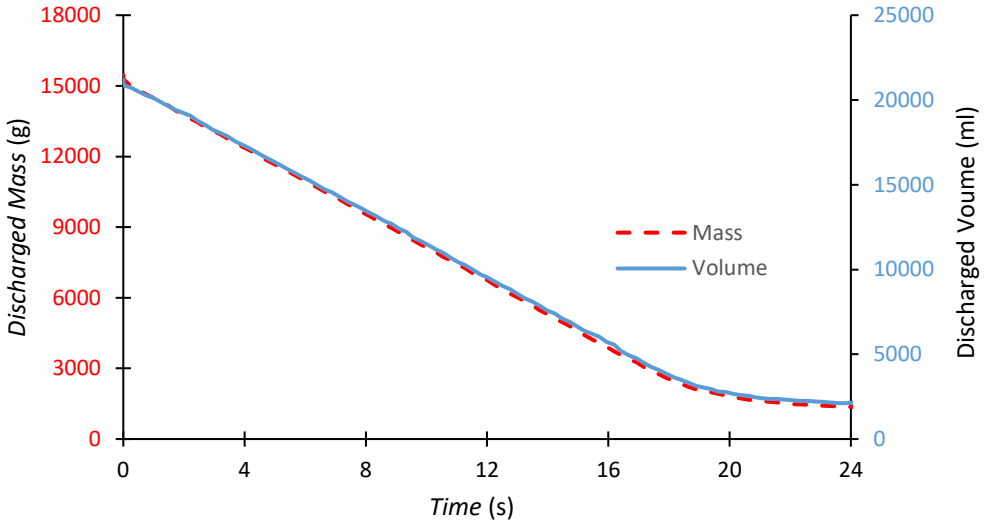


***Figure 3-12**: Dynamic test on mustard seeds discharging from the 50-litre vessel through the 50 mm orifice.*

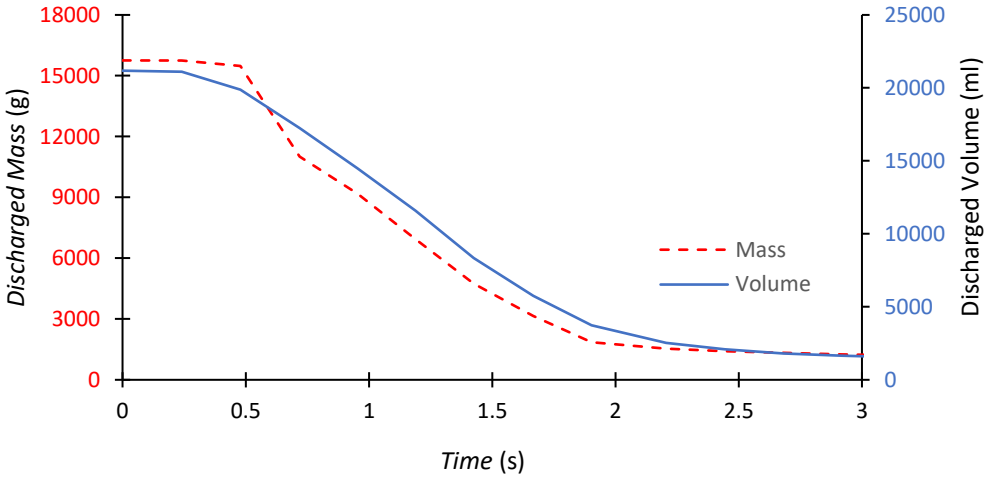


***Figure 3-13:** Dynamic test on mustard seeds dumping from the 50-litre vessel through the 130 mm opening.*

The consecutive volume measurements provided sufficient data points to estimate the real-time measurement of the sample flow rate out of the vessel. Figure 3-14 shows flow rate measurement of the mustard seeds sample out of the 26 mm orifice, typical for all the flow rates tested and both tested

samples. Figure 3-14 shows that the volumetric flow rate displays periodicity with a period of roughly six seconds.

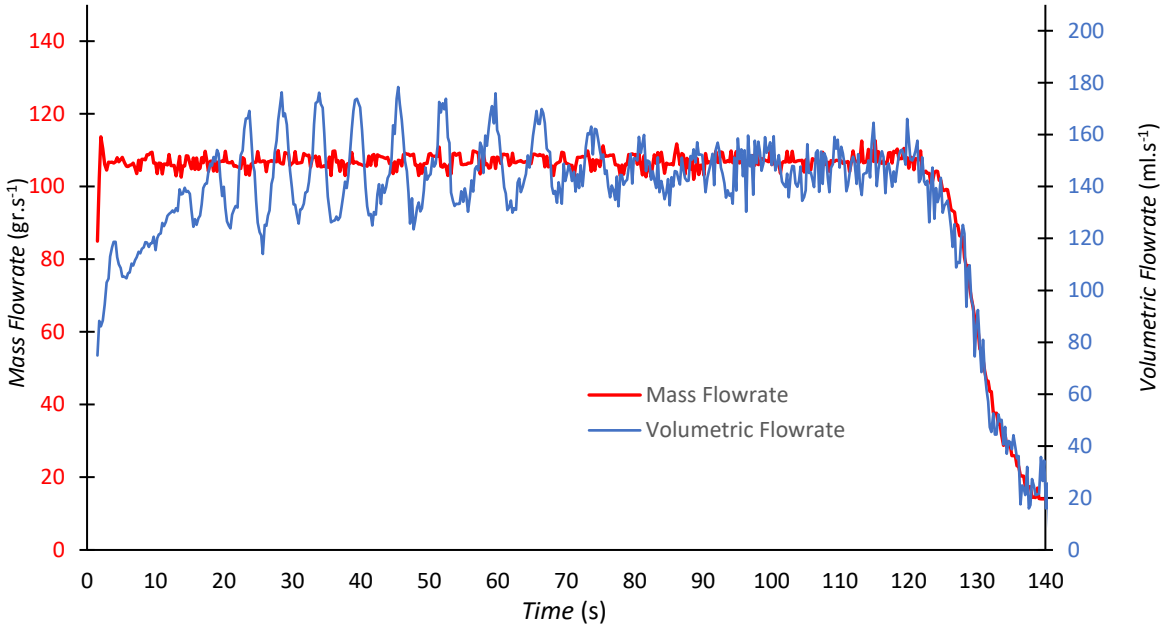


***Figure 3-14**: Flowrate of sample mustard seeds out of 26 mm orifice.*

The development of the surface profile for timestamps 0, 3, 6, 11, 14, 16, and 22 seconds is shown in Figure 3-15; the points on each surface mesh represent a corresponding surface cell $Z_{I,J}$. Each point represents a 6x6 mm cell. For clarity, only seven profiles are shown, starting with the relatively flat surface at t=0 s and finishing with a dished profile when discharge is complete. It is seen that the surface of the seeds during discharge forms a funnel shape; after a few seconds, the slope has an angle of ~20^{o} to the horizontal, which increases to ~30^{o} after the flow stops at the bottom of the container, and the seeds drain to their angle of repose. The summary of the estimated average flowrates for all test conditions is provided in Table 3-2. Flowrate increased with orifice diameter. Mustard seeds had a lower flowrate when discharging from 26 mm and 71 mm compared to agricultural lime. For orifices 50 and 90 mm, the trend reversed. The deviation between the flow rate of the two samples was maximised when using the 50 mm orifice. Mustard seed is discharged with a flow rate up to 30% higher than agricultural lime for this orifice.

The average mass-based volumetric flow rate was obtained by dividing the average mass change rate by the sample's loose bulk density. As is shown in Table 3-2, the values obtained using the optical method are very close to those obtained by weighing with a maximum deviation of 6% for the 90 mm orifice group. This value for the 26 and 71 mm groups was less than 1%. Considering the uncertainties on the bulk density variations in different regions of the sample bed as it discharges and the effect of

the impact of the samples on mass reading as they impact the platform scales, the agreement between the flow rates using both methods was very high.

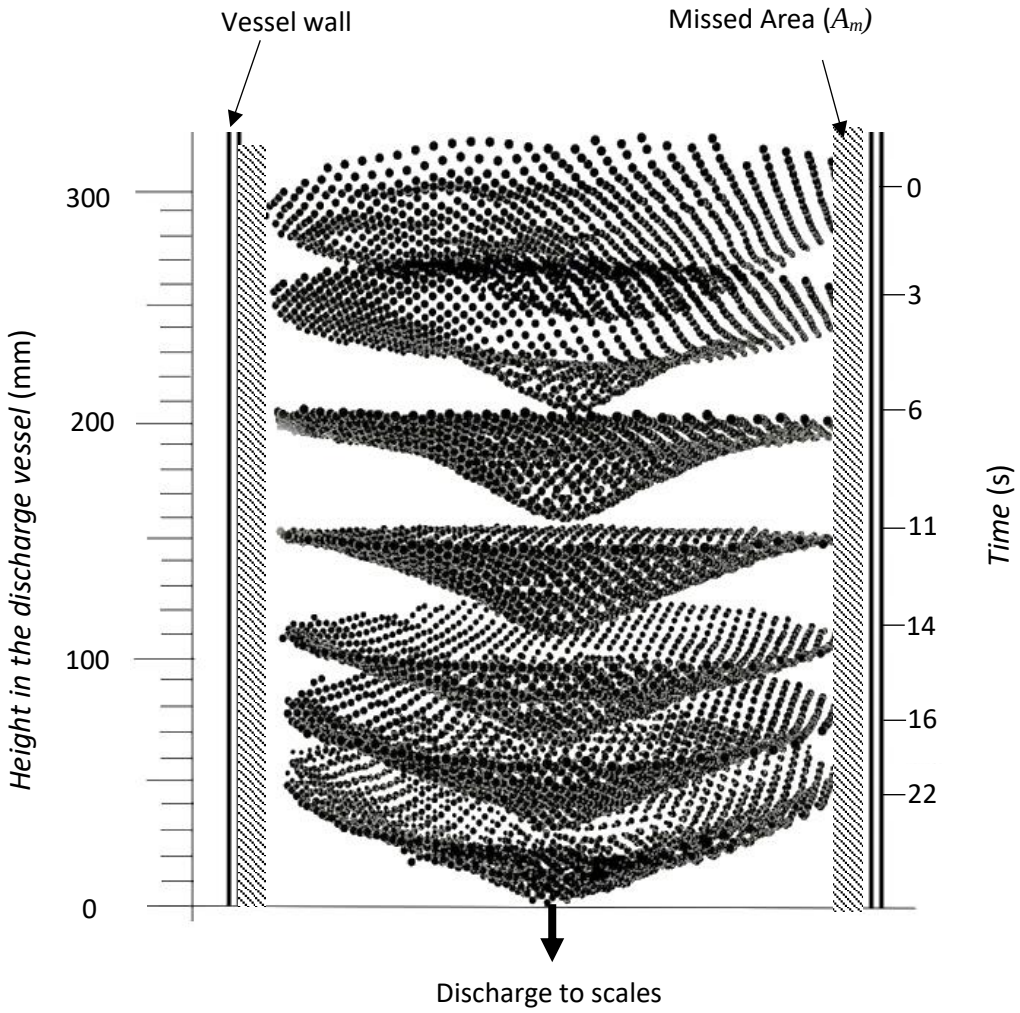


***Figure 3-15**: Visualisation of discharge profile; mustard seeds, 50 mm orifice. The record time for each surface is displayed on the right.*

***Table 3-2**: Average volumetric flowrate comparison.*

Sample	Method of obtaining volumetric flowrate	Control Orifice Opening (mm)			
		26	**50**	**71**	**90**
mustard seeds	From the discharged **mass** ($ml.s^{-1}$)	144	963	2401	4821
	From the **optical** method ($ml.s^{-1}$)	143	945	2402	4571
agricultural lime	From the dibscharged **mass** ($ml.s^{-1}$)	163	668	2501	4087
	From the **optical** method ($ml.s^{-1}$)	163	668	2497	4000

3.4.2. Experiments with the 200-litre vessel

Static Tests

The results of the static volume estimation of the polyethylene sample in the 200-litre vessel are shown in Figure 3-16 **(A)**. The loose-poured density of the polyethylene sample was used to calculate the ordinate of the Figure. The mean error from parity was 0.19%V_0.

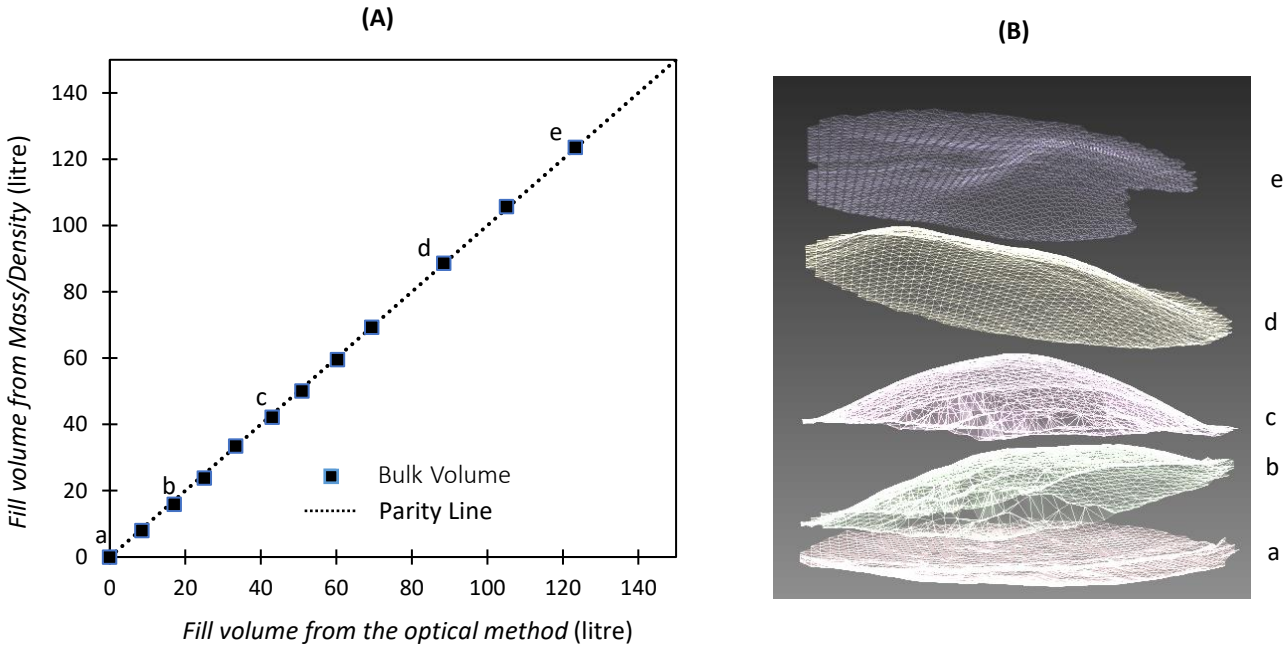


Figure 3-16: *(A): Comparison of the vessel fill volume obtained using the optical method and by weighing (B): graphical representation of the meshes with 10x10 mm cells obtained from the material surface at different depths.*

As seen in Figure 3-16 **(B)**, for every load of the sample into the vessel, there is an associated mesh beginning with mesh (a), which is the bottom of the empty vessel, mesh (b) where there was almost 20 litre of material inside the vessel, continuing to mesh (c) which shows the surface at almost 40 litres of the material in a convex form and mesh (d) where the material was dumped to the side of the vessel. There are missing elements in the surface mesh corresponding to the data point (e), marked with white circles. The missing elements resulted from the limited depth camera field of view when the material was close to the vessel lid. The OFV model compensated for the missing cells and reported the fill volume of material in that stage to an accuracy of 0.12V_0, equivalent to 0.24 litre.

Discharge Tests

Figure 3-17 shows the results of the estimated volume of the sample under discharge from the 50 mm orifice of the 200-litre vessel. The volume values determined from mass were subject to a maximum deviation of 1%V_0. After 20 seconds from the initiation of discharge, the optics had full coverage of the material surface in the vessel. From this moment until the discharge finishes, the

maximum deviation between the measured volume and the volume obtained from weighing was less than 0.65%, with an average deviation of 0.2%V_0. The deviation between the optically measured volume and the volume calculated from mass falls within the uncertainty range. In the total discharge time of almost 165 s, fill volume was measured 600 times, a rate of 3.6 per second on average.

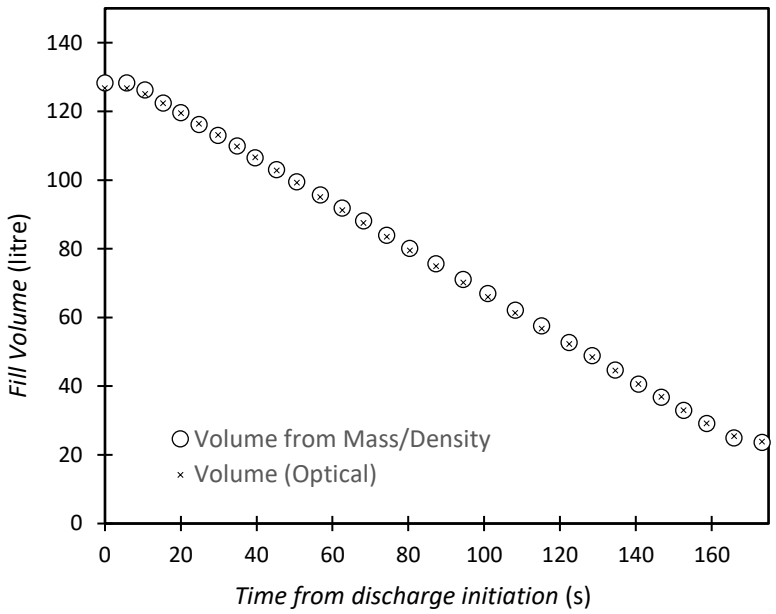


Figure 3-17: *Dynamic discharge test of the polyethylene sample using the 200-litre vessel through the 50 mm orifice.*

Figure 3-18 compares the flow rate of the sample as measured by the optical method and by weighing.

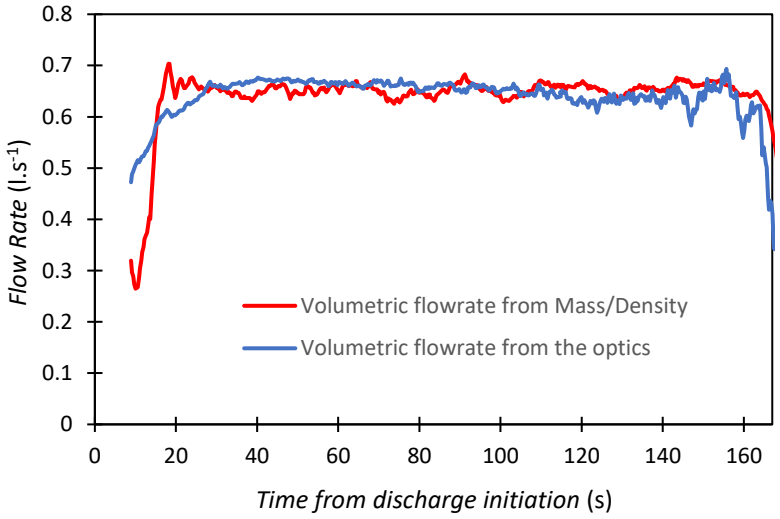


Figure 3-18*: Flowrate of polyethylene pellets out of the vessel using the 200-litre vessel through the 50 mm orifice.*

A moving average of 10 measurements was used to generate the data in the figure, so each data point represents the average flow rate over 2.5 to 4 seconds.

3.5. Discussion

The incremental additions of the samples and associated volume scans in static tests provided proof of the fill volume estimation from the surface point cloud concept. Inspection of Figure 3-11 indicates that fill volume, calculated by dividing sample mass in the vessel by loose poured density, is close to the volume measured optically.

The discharge experiments on the 50-litre vessel were carried out with shallow beds, approximately 300 mm deep, and with reference to Figure 3-16, it is seen that the surface of the mustard seeds sample during discharge forms a funnel shape; after a few seconds, the slope has an angle of ~20^{o} to the horizontal which increases to ~30^{o} after the flow stops at the bottom of the container and the seeds drain to their angle of repose.

Consecutive measurements of a vessel fill volume make it possible to estimate material flowrate out of the vessel in real time. It was demonstrated for both 50-litre and 200-litre vessels that the flowrate obtained by the optical method is comparable to the volumes obtained by weighing. In the experiments on the 50-litre vessel, the average flowrates obtained by the two methods had deviations of less than 2% when using 26, 50 or 71 mm orifice. In the 200-litre vessel experiments, the average flowrates obtained by the optical method and by weighing were 0.649 and 0.648 $l.s^{-1,}$ respectively, a deviation less than 0.2%.

The limited field of view of the depth camera was doubled up by pairing two sensors together. The results from the 200-litre vessel experiments were obtained from the paired scanners. The material surface in these experiments was divided into more than 2000 10x10 mm cells, each corresponding to the average depth of material in a known spatial location, equivalent to having more than 2,000 level metres in a 200-litre vessel.

One of the challenges was real-time data analysis, which was addressed using multi-threading architecture. This approach resulted in a volume calculation duration of 0.2~0.3 s. Because the sensor used in this study has a maximum scan rate of 30 Hz, the volume measurement duration can theoretically be decreased to 0.033 s, subject to the hardware processing capability and the decision on the cell size of the surface meshes. The chosen cell size in this study was 6x6 mm and 10x10 mm for the 50 and 200-litre vessels, respectively. Increasing the cell size reduces the processing required to propagate the surface mesh.

The OFV model compensated for the missing area from the optical scanner field of view.

The dual camera housing used in the 200-litre vessel was connected to high-pressure air. The air pushed through the housing and released from the 0.5 mm gap surrounding the optics. It formed an air blade, pushing the dust away and cleaning the optical surfaces. The other purpose of the purge air was to stabilize the temperature of the optics. Figure 3-19 shows the purge air in operation with an air feed of 100 litres per minute, blowing away a stream of sand falling in the optics, shown by the weight arrow. Dashed red lines show the high-pressure air blade formed around the optical glasses, pushing the fine sand stream away.



Figure 3-19: *Keeping the optics clean using pressurized air surrounding the optics.*

3.5.1. Implementation of this concept in a topdressing aeroplane hopper

Figure 3-20 shows a topdressing hopper, typically found on various Cresco models. These aeroplanes have a hatch above the hopper hinged to the fuselage. The hatches open towards the front of the aeroplane. The fertilizers are loaded into the hopper after mechanically opening this hatch. The inside of the hatch provides an ideal position for installing depth cameras in terms of the maximum field of view. This spot is also less likely to be impacted by the material when they are being loaded into the hopper. If installed inside the hatch, the wedge-shaped field of view of the double-depth camera apparatus is shown in Figure 3-20. The optical system provides a complete view when the material levels surpass almost two-thirds of the hopper height. Above that point, the sensor has partial

coverage of the material surface. However, the OFV model estimates the volume of the material in the missing area.

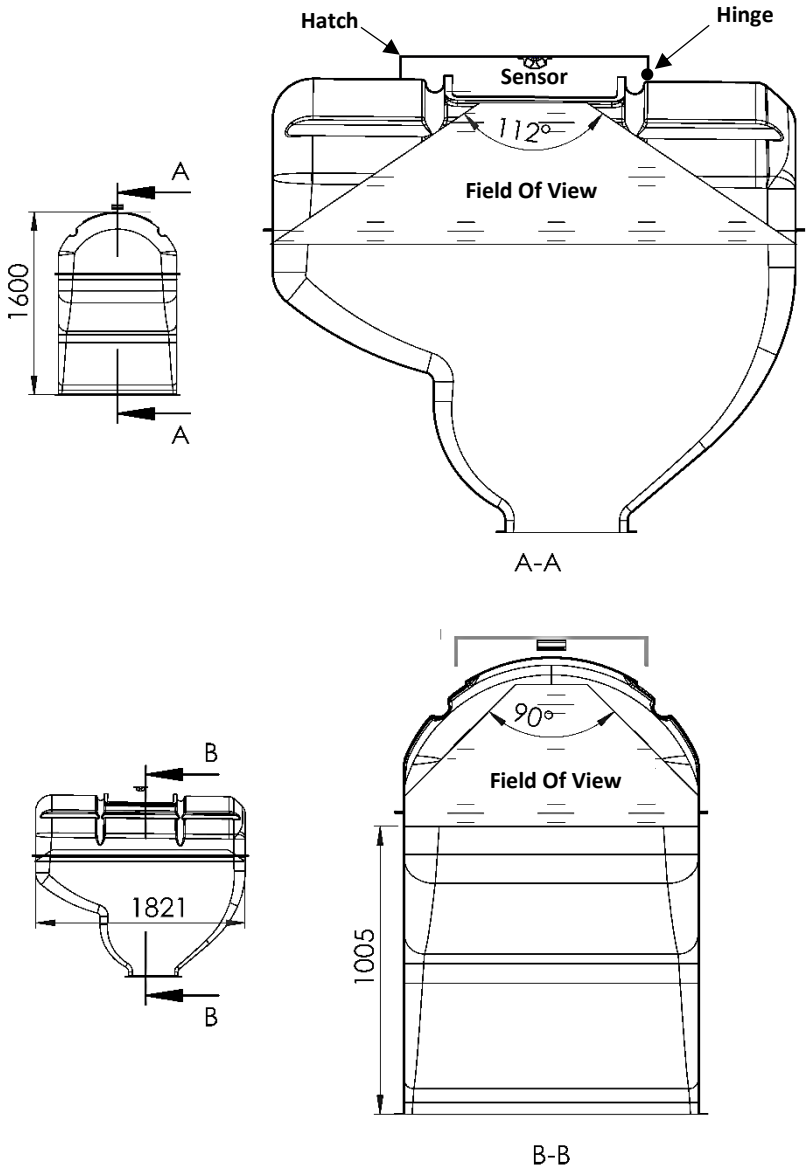


***Figure 3-20**: Implementation of the double-depth camera system in a topdressing aeroplane.*

The optical sensor package could be installed inside the hatch, almost at the centre, and the hatch has to be closed to a fixed position every time with minimum displacement. When the hopper is empty and the discharge gate is closed, the optical system can scan the geometry and determine the empty volume using the same method for fill volume determination. The cross-sectional area of the hopper at different depths is also required for an accurate fill volume estimation. No further

calibration data are required for the OFV model to estimate hopper fill volume and material flow rate in real-time.

Another matter to consider is the durability of the optical system and keeping the optics clean. One solution to keep the sensor package safe from fertilizer dumping impact is putting it in a rugged box with a retractable or sliding hardcover. The cover can be automatically closed when the hatch is opened before material discharge. The optics with an anti-static coating can also be installed behind hard glass, such as sapphire. The use of purging air in front of the optics, as implemented into the dual camera optical housing, can help to keep the optics dust-free. It is also noteworthy that fertilizers are dense material. Some observations not covered in the text confirmed that agricultural lime dust does not tend to stick to the depth camera's shield glass.

The depth camera used in this project (Intel RealSense D435) was chosen and purchased in 2019. The more recent models are waterproof and dustproof and generally are better for industrial applications. Recently, other manufacturers such as ZED (StereoLabs, San Francisco) have marketed depth cameras for industrial applications with a broader field of view compared with what has been used in this study, which can potentially be better options for the application in a topdressing aeroplane.

3.6. Summary

The concept of estimating the fill volume of a hopper/vessel by using 3D scans obtained from the material surface was investigated in this chapter. The 3D views of the surface were obtained using the optical stereoscopic technique. A model was developed to calculate the fill volume of a vessel using the point cloud captured from inside the vessel using the stereoscopic scanner. The concept was tested on two vessels with volumes of 50 and 200 litres. A single scanning device was used for the 50-litre vessel, while a pair of scanning devices were used in tandem for the 200-litre vessel to double the vertical field of view. The pair was installed in a 3D-printed housing, which received high-pressure air to create an air blade in front of the optics to keep them dust-free while stabilizing the sensors' temperature.

The experiments on each vessel were conducted under two conditions: static tests, where the test material was not flowing, and dynamic tests, where the test material freely flowed out of the vessel. The results provided proof of concept for measuring the fill level of a vessel using the stereoscopic technique and the proposed model. The estimated volume in all conditions and vessels agreed with the values obtained by measuring the material mass. According to the results, the volume of the samples inside both vessels was estimated with an accuracy of less than $1\%V_0$. The optical method provided measurement updates with a refresh rate of up to 5 measurements per second. Real-time analysis of the fill volume provided sufficient data for instantaneously estimating the material discharge flow rate from the vessel. The estimated volumetric flow rate obtained by the optical method agrees with the volumetric flow rate obtained by real-time weighing.

Chapter 4 Helmholtz Resonance

"The author's first encounter with Helmholtz Resonance dates back to when he was five years old. He would spend hours listening to the sound emanating from a spiral whelk shell. Initially, he believed that the shell somehow captured and preserved the sound of the Caspian Sea, a place he had not yet visited at that age. He imagined that holding the shell to his ear allowed him to hear these distant sounds. This whimsical notion led him to generalize the concept, applying the theory to the sound of rainfall, concluding that it was the sound of heaven where angels were cheering and dancing. Further studies, however, revealed that the sound from the whelk shell was its Helmholtz resonance. Similarly, the sound of rainfall, and likely any other phenomena in the universe, sadly turned out to be explainable by relatively absurd physical principles."

'Philosophy will clip an angel's wings.' (Keats, 1888)

4.1. Introduction

4.1.1. Classical Helmholtz Resonance Theory

Helmholtz resonance is commonly observed in musical instruments such as flutes and organs. It is also vital in designing car mufflers and other noise-reduction systems and, more recently, for the volume determination of objects. A Helmholtz resonator consists of a cavity and one or more openings referred to as port(s), as shown in Chapter 1, Figure 1-2.

Classical Helmholtz Resonance describes the resonance frequency of a Helmholtz Resonator as a function of resonator geometry and speed of sound. When the resonator is excited by an external sound source, the air inside oscillates at a resonance frequency determined by the resonator geometry and the speed of sound. The governing equation of classical Helmholtz Resonance is attributed to Helmholtz (1877)and can be derived from lumped parameters and represented as analogous to the natural frequency of a simple harmonic mass-spring system $\sqrt{(K/m)}$ (Blackstock, 2000), as follows:

$$\omega_n = c\sqrt{\frac{S_p}{V_c l}} \qquad 4\text{-}1$$

where ω_{n} is the angular resonance frequency, c is the speed of sound in the fluid, S_p is the port cross-sectional area, V_c is the resonator cavity volume, and l is the port length. In this thesis, the resonator saturated fluid in the air with the assumption that it has the behaviour of an ideal gas (see Figure 1-2).

Alster (1972) investigated the effects of motions of mass within different parts of a resonator and presented an extended analytical theory about the effect of the resonator shape on the resonant frequency. The physical length of the port is less than the amount that should be considered as the port length. Some air outside the port oscillates along with the air inside the port and acts as an added mass to the air inside the port. The port length is extended by a factor determined by the port radius and the quantity of port flange material at each port end (Chanaud, 1994; Ingard, 1953; J. W. S. Rayleigh, 1945).

According to Ingard (1953), the port end correction factor, which accounts for the air moving beyond the actual port ends, cannot be calculated as simply as those derived from the standard methods, such as for a piston on a flat surface. These corrections are closely linked to the geometrical complications that occur at the end of the port, and solving them can be challenging because it requires prior knowledge of the pressure distribution in the port.

Figure 4-1 shows the significance of the end correction factor. The resonator in this figure has a port that is 51 mm long with an internal diameter of 44 mm attached to the top of a resonator on a flange. Blackstock (2000) suggested a value $\mathrm{of}\ 0.6a$ for the internal flanged end correction and $8a/3\pi$

for this port's outer unflanged end correction factor, where *a* is the port's internal radius. The effective port length for the resonator in Figure 4-1 is thus more than 55% higher than its physical length.

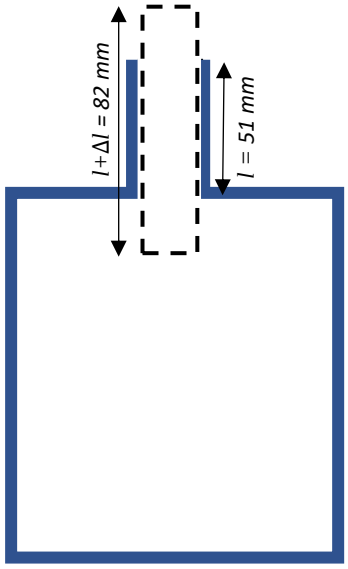


***Figure 4-1**: An example to compare physical port (Solid port) and effective port (Dashed port).*

In developing the classical Helmholtz Resonance equation, Helmholtz assumed that all resonator dimensions are small compared to the resonance wavelength. When the port or cavity length of a Helmholtz Resonator reaches 5-10% of the resonance wavelength, the resonance frequencies predicted by the classical Helmholtz Resonance model start to deviate from the actual resonance frequencies (Panton & Miller, 1975; Selamet et al., 1994).

4.1.2. Resonance models for dimensions comparable to the resonance wavelength

In the classical Helmholtz Resonance theory, the air passage through the port is considered incompressible, and the air within the cavity is assumed to be compressible with uniform compression (Lord Rayleigh, 1916). Tang & Sirignano (1973) proposed Generalized Helmholtz Resonance. They combined the continuity and momentum equations in various regions of a Helmholtz Resonator and derived an expression for the resonance location based on a Helmholtz Resonator with cylindrical and concentric dimensions as follows:

$$tan(k_r l) \times tan(k_r L) = \frac{S_p}{S_v} \qquad 4\text{-}2$$

where L is the cavity length, S_v is the cavity cross-sectional area and k_r is the resonance wavenumber. This model covers the regions where the cavity and port dimensions become comparable to resonance wavelength.

Panton & Miller (1975) proposed a model for Helmholtz Resonance by calculating the lumped mass in the port and distributed mass in the cavity as Equation 4-3. This non-linear equation provides accurate results for port lengths much shorter (<10%) than the resonance wavelength:

$$\frac{lS_v}{LS_p} k_r L = cot(k_r l) \qquad 4\text{-}3$$

Panton & Miller also introduced the improved Helmholtz Resonance Model based on cavity volume rather than cavity dimensions using the numerical approximation of Equation 4-3 as follows:

$$f = \frac{c}{2\pi} \sqrt{\frac{S_p}{lV_c + \frac{1}{3}L^2 S_p}} \qquad 4\text{-}4$$

Selamet et al. (1994) studied the transmission loss of a Helmholtz resonator attached to a tube. They investigated the effect of changing a resonator cavity length to diameter (L/D) ratio while considering a fixed cavity volume. They developed their model using the one-dimensional wave propagation equation in various regions of the resonator and ran a computational time-domain technique to model Helmholtz resonator transmission loss in an impedance tube. Their results were consistent with Tang and Sirignano's model in Equation 4-2.

4.1.3. Mass-Spring analogy

A Helmholtz Resonator can be pictured as a mass-spring oscillation system, as shown in Figures 1-2 and 4-2. Such a system resonates analogous to a mechanical oscillator. The air mass inside the port can be calculated as:

$$m = \rho S_p l \qquad 4\text{-}5$$

Where ρ is the mass density of air (Region 1 in Figure 4-2), the resonance of the Helmholtz Resonator causes this mass of air to oscillate, similar to the kinetic energy of the vibration of an incompressible fluid. The resonator's potential energy comes from the fluid's compression inside the cavity (Region 2).

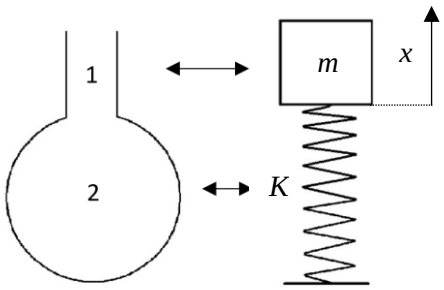


Figure 4-2: *Mass-Spring analogy of a Helmholtz Resonator.*

In this analogy, the force acting on the elasticity of the cavity air is defined by:

$$F = -Kx = S_p \delta P \qquad 4\text{-}6$$

where x, is the displacement of the air column, k is the spring constant, and δP is the pressure difference across the port. Taking the differential pressure of the adiabatic law, $PV^{\gamma} = constant$, yields $\frac{\delta P}{P} = -\gamma\left(\frac{\delta V}{V}\right)$. Considering that $\delta V = S_p x$, the spring constant of the air in the cavity can be obtained as follows:

$$K = \frac{\gamma P S_p^2}{V} \qquad 4\text{-}7$$

where γ is the heat capacity ratio. The natural frequency (ω_n) is as follows:

$$\omega_n^2 = \frac{c^2 S_p}{lV} \qquad 4\text{-}8$$

Which can be written as the classical Helmholtz Resonance equation (Equation 1-3) in linear frequency format as $f = \frac{c}{2\pi}\sqrt{\frac{S_p}{lV}}$.

As thoroughly described in the literature (For example, see Inman, 2001), the mechanical oscillator of a mass-spring-dashpot can be described by Equation 4-9. This equation is essentially the sum of acting forces in the system.

$$m\frac{d^2x}{dt^2} + R_M\frac{dx}{dt} + Kx = F_0 e^{i\omega t} \qquad 4\text{-}9$$

The first term $m\frac{d^2x}{dt^2}$ is the force of the mass of air in the port based on Newton's second law. The second term $R_M\frac{dx}{dt}$ represents acoustic energy loss in the system (damping) through mechanical and radiation resistance. The system's radiation resistance represents energy dissipation into the environment. The third term Kx is the restorative spring force induced by the cavity air. The right side of the equation describes a periodical driving force into the system with angular frequency ω.

The response of an oscillatory system contains information regarding the resonance frequency of the system and the energy damping of the system. The damping part of the equation is of great interest in this research due to the impact of bulk solids' effect on acoustic damping. Therefore, in this section, the governing theory behind the oscillation response of the resonator is discussed for later use in data analysis.

4.1.4. Undriven Damped Oscillation

Figure 4-3 represents the vibration model of a Helmholtz Resonator. The undriven response, free vibration, comes from the system immediately after removing an excitation force. The system displacement in the x direction can be described as follows:

$$\ddot{x} + \Gamma\dot{x} + \omega_n^2 x = 0 \qquad 4\text{-}10$$

where $\Gamma = R_M/m$ is the damping constant.

The solution for Equation 4-10 for such a system, as thoroughly discussed in vibration engineering textbooks (for example, see Inman, 2001; Rao, 2017), is in the form of Equation 4-11.

$$x(t) = C_0 e^{\psi t} \qquad 4\text{-}11$$

were ψ, the decay rate of displacement is a function of Γ and ω_n. Substituting Equitation 4-11 and its first and second derivations into Equation 4-10, ψ can be described as follows:

$$\psi = \frac{-\Gamma \pm \sqrt{\Gamma^2 - 4\omega_n^2}}{2} \qquad 4\text{-}12$$

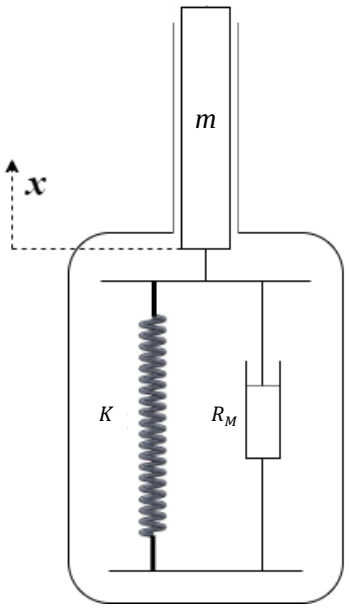


Figure 4-3: *Oscillation model of a Helmholtz Resonator (undriven).*

When measurement of the cavity volume of a Helmholtz resonator is of interest, the system must be heavily underdamped to provide a high-quality resonance (Webster, 2010). The undriven resonance frequency of this system (ω_d) is described as follows:

$$\omega_d = \omega_n\sqrt{1 - \zeta^2} \qquad 4\text{-}13$$

where ζ is the damping ratio, a dimensionless parameter equal to $\Gamma/2\omega_n$. This parameter characterises the decay rate of the resonance and is defined as the ratio of damping to critical damping of the system (Rao, 2017). As in Equation 4-13, the resonance frequency of the system in the undriven, underdamped setup is slightly lower than the natural resonance frequency of the system

The solution of 4-10 for the displacement of the air in the port in underdamped oscillation is (Inman, 2001):

$$x(t) = Ae^{-\zeta\omega_n t}cos(\omega_d t + \phi) \qquad 4\text{-}14$$

where the constants A and ϕ are determined by the initial conditions.

The resonance of the air mass in the port follows a logarithmic decay. Measuring this decay rate $\zeta\omega_n$ gives the damping ratio corresponding to all the system losses.

Figure 4-4 shows the normalised displacement $x(t)/A$ of the air mass in a Helmholtz resonator port versus time. Displacement in x corresponds to the pressure fluctuations inside the cavity. Therefore, the pressure change of the chamber (spring force) follows the displacement of the air mass in the port. As shown in Figure 4-5, a line can be obtained by locating the pressure maxima, taking logarithms, and plotting against time. The slope of this line is the decay rate $\zeta\omega_n$ in Equation 4-14. Dividing the line-slope value S by ω_n, which can be worked out from the number of fluctuations in time, gives the value of the damping ratio ζ.

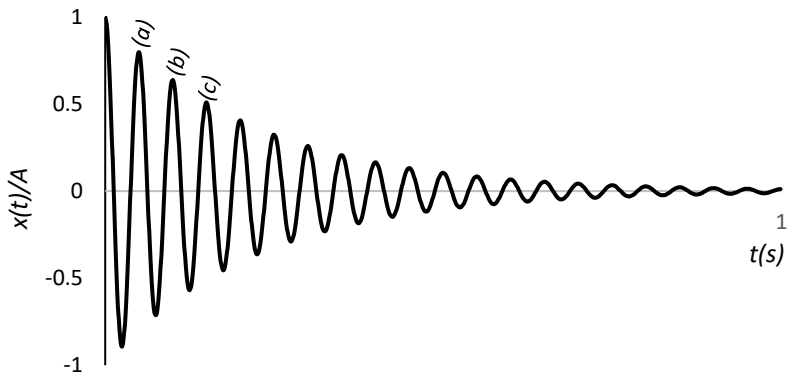


***Figure 4-4**: Signal decay in an underdamped, undriven resonance of a Helmholtz resonator. This resonator is resonating at 20 Hz with a damping ratio **ζ** of 0.035.*

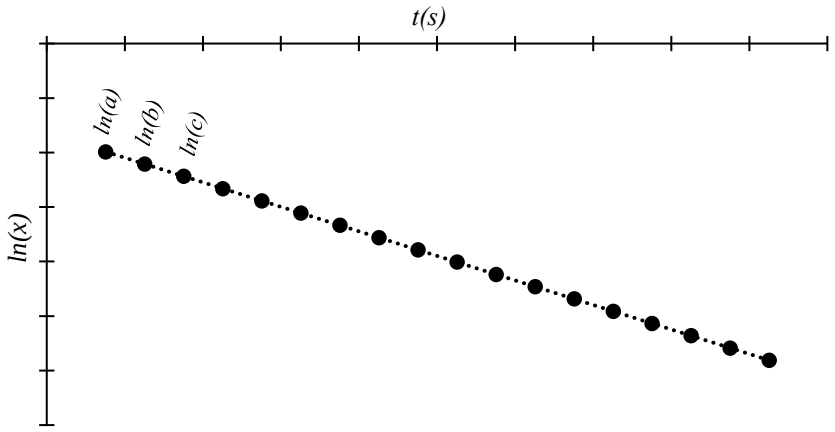


***Figure 4-5**: Natural logarithm of resonance amplitude peaks versus time.*

The number of fluctuations per second in Figures 4-4 represents the damped resonance frequency, which is slightly lower than the system's natural frequency, as calculated in Equation 4-13. For a very underdamped resonance ($\zeta \ll 0.05$), $\omega_d \cong \omega_n$

The line slope in Figure 4-5 is the amplitude decay rate in Equation 4-14:

$$ln(x) = -\zeta\omega_n t \qquad 4\text{-}15$$

In Equation 4-15, $-\zeta\omega_n$ can be substituted with S, the decay line slope in Figure 4-5. The quality factor Q of a resonator has an inverse relation with the damping ratio of the system (Inman, 2001):

$$Q = \frac{1}{2\zeta} = \frac{\omega_n}{\Gamma} \qquad 4\text{-}16$$

By combining equations 4-15 and 4-13, the quality factor can be written as:

$$Q = \frac{1}{2}\sqrt{\frac{\omega_d^2+S^2}{S^2}} \qquad 4\text{-}17$$

4.1.5. Driven underdamped oscillation

For the Helmholtz Resonator in Figure 4-2, one can assume a periodic driving force of the form $F_d cos\omega t$ applied to the mass of air in the port. The angular frequency ω is independent of ω_d (damped resonance frequency) and ω_n (natural frequency of the system). For this system, the displacement can be expressed by:

$$\ddot{x} + \Gamma\dot{x} + \omega_n^2 x = F_d cos\omega t \qquad 4\text{-}18$$

The steady-state solution of Equation 4-19 is discussed in vibration engineering textbooks (For example, see Rao, 2017) is in the form of:

$$x(t) = A_d cos(\omega t + \phi) \qquad 4\text{-}19$$

where A_d is the displacement amplitude of the air in the port, and ϕ is the phase.

A_d can be expressed as a function of ω as described in Equation 4-20, where F is F_d/m. This function is plotted in Figure 4-6 for different damping ratios.

$$A_d(\omega) = \frac{F}{\sqrt{\left(\omega_n^2 - \omega^2\right)^2 + \Gamma^2\omega^2}} \qquad 4\text{-}20$$

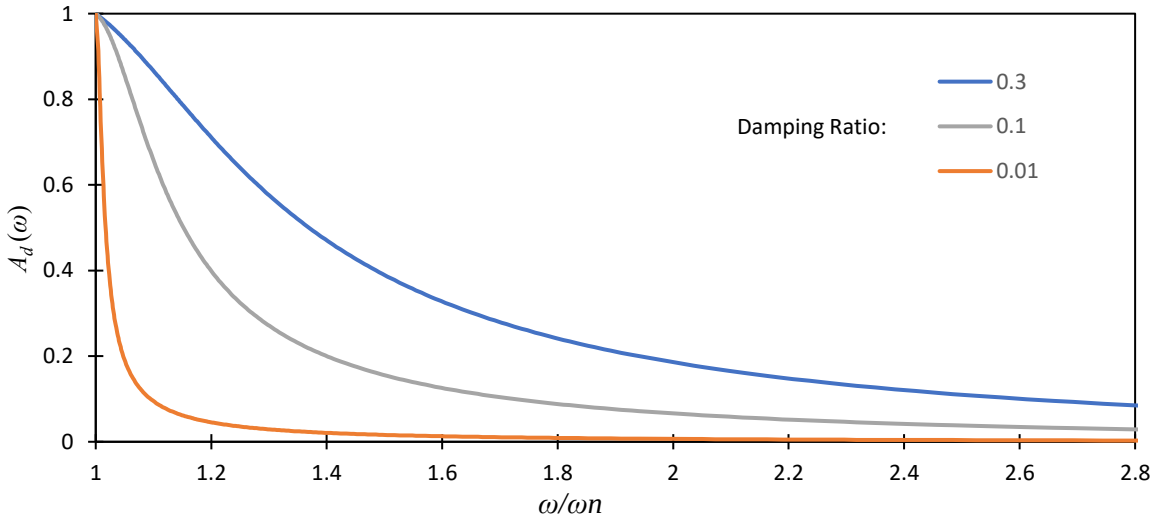


Figure 4-6: *Normalized amplitude versus driver frequency (as a multiplier of natural frequency) for different damping ratios.*

Amplitude peak occurs when the derivation of Equation 4-20 equals zero. It can be seen that the maximum amplitude is not achieved when the driving frequency equals the system's natural frequency; it occurs when there is a slight offset between the driving and natural frequencies of the system. The damped resonance frequency ω_r of this is (Rao, 2017) as follows:

$$\omega_r = \omega_n\sqrt{1 - 2\zeta^2} \qquad 4\text{-}21$$

Plotting A_d^2 as a function of ω gives a Lorentzian curve (Vandegrift, 1993a). The width of this curve is related to the resonator quality factor using the following equation (Inman, 2001):

$$Q \approx \frac{\omega_n\sqrt{1-2\zeta^2}}{FWHM} \qquad 4\text{-}22$$

where $FWHM$ (Full Width at Half Maximum) is the distance between the two frequencies that A_d^2 falls to half of its maximum value.

The term ϕ in equation 4-19 is the phase shift between the driving and natural frequency and is expressed as:

$$tan\phi = \frac{-\Gamma\omega}{\omega_n^2-\omega^2} = \frac{\omega\omega_n Q^{-1}}{\omega_n^2-\omega^2} = \frac{-2\xi\omega_n\omega}{\omega_n^2-\omega^2} \qquad 4\text{-}23$$

Around the resonance frequency (where ω approaches ω_n), the phase difference between the driver and the resonator approaches $\pi/2$. It contradicts Webster's assumption for a Helmholtz Resonator: "*The closer the driving frequency is to the resonance frequency, the larger the phase shift*" (Webster, 2010, p.99).

Figure 4-7 is ϕ versus ω/ω_n. This plot provides a supplementary method for locating resonance quality along with resonance frequency where $\frac{\omega}{\omega_n} = 1$.

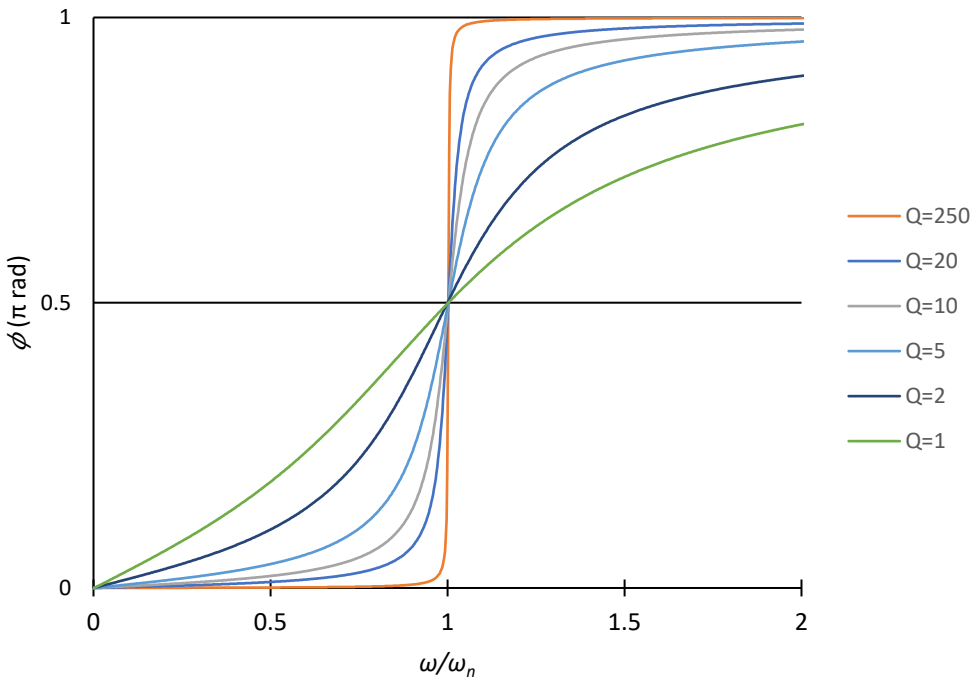


***Figure 4-7**: Phase Shift ϕ between driver and resonator for different quality factors.*

Vandegrift (1993) measured violin quality factor using the driven underdamped oscillation phase shift described in Equation 4-24 and undriven underdamped oscillation amplitude decline (Equation 4-15). He concluded that these two methods yield approximately equal values of the quality factor of the violin as a Helmholtz Resonator.

4.1.6. Excitation

When measuring volume using acoustical excitation in a Helmholtz Resonator, it's crucial to achieve a high-quality resonance with an easily detectable, isolated frequency at the highest possible resolution (Webster, 2010). To meet these requirements, the method for exciting the resonator becomes of significant importance. One common excitation method is grazing, similar to blowing into the neck of a bottle. In grazing excitation, the air speed around the resonator port is a driving force, significantly influencing the resonator response frequency. This is primarily due to the effect of boundary layer turbulence on the resonator response (Gloerfelt, 2009; Meissner, 2002). However, since grazing introduces air speed as a second governing factor for the resonance frequency, it adds further complexity as it is not the method under investigation in this study. Johnson (1955) patented a body volume measurement method utilizing grazing. However, he did not report on the accuracy of his volume measurement method.

Excitation by acoustical means is commonly reported in the literature. The excitation sound can be a broadband noise (Chanaud, 1997; Piana et al., 2022), a non-driving Chirp (Nishizu et al., 2001) or a driving chirp (Webster & Davies, 2010).

Two commonly used types of broadband noise in the excitation of a Helmholtz Resonator are random frequencies with equal power (White Noise) or random frequencies with decreases in intensity at a rate of 3 dB per octave with increasing frequency (Pink Noise). The benefit of excitation by broadband noise is the broad spectrum of frequencies it covers. Webster (2010) has utilised this method to excite a Helmholtz Resonator quickly to detect the approximate resonance frequency.

A chirp is a signal that increases or decreases in frequency over time. A chirp is either linear or logarithmic. In a linear chirp, the frequency increases or decreases constantly over time. A logarithmic chirp changes frequency at a rate that increases or decreases exponentially. A linear chirp provides constant power for all frequencies, while a logarithmic chirp power increases or decreases linearly with frequency. The limited range of frequencies in a chirp makes them denser in terms of energy per frequency bin in comparison with broadband noise, resulting in a higher signal-to-noise ratio in the excitation of a Helmholtz Resonator (Nishizu et al., 2001).

A non-driving chirp is a burst of sound that excites a Helmholtz Resonator briefly at its port. In contrast, a driving chirp continuously excites the resonator, acting as a periodic force while sweeping through various frequencies. These excitation methods are sometimes combined for optimized measurements. Webster & Davies (2010) used a sequential technique that starts with excitation by broadband noise, followed by a broad chirp and then a narrow chirp, to make a three-litre resonator resonate at its maximum quality.

After exciting a Helmholtz resonator for volume measurement, the response is sampled and processed to locate the resonance frequency.

4.1.7. Resonator Frequency Hunting

In this thesis, resonance frequency hunting refers to the process of experimentally determining resonance frequency. The commonly reported method (Nishizu et al., 2001; Webster, 2010; Webster & Davies, 2010; Xu et al., 2014) in the literature for resonance hunting involves sampling the chamber pressure fluctuation signals using a microphone and performing spectral analysis. The digitized signal from the microphone is subjected to digital signal processing for power analysis in the frequency domain. A Fast Fourier Transform (FFT) or Discrete Fourier Transform (DFT) converts the microphone signal from the time domain to the frequency domain. The frequency maxima in the microphone signal's power spectral density (PSD) correspond to the Helmholtz Resonator resonance modes.

The frequency resolution of a signal in the time domain is a function of sampling duration (Sabatini, 1995). The longer the measurement duration, the more accurate the volume measurement becomes. Webster & Davies (2010) reported an error margin of ±0.1% of the resonator's volume capacity when spending 40 seconds on resonance hunting. Reducing this measurement time to 20 seconds led to a fourfold increase in error.

Another approach to resonance frequency hunting is described in the literature (Inoue et al., 2021; Nakano et al., 2006), which involves tracking the electronic impedance of the acoustic driver. In this method, the loudspeaker that excites the resonator also gauges the resonance frequency. The loudspeaker emits a chirp, and at the resonance frequency, the coil impedance of the loudspeaker reaches a maximum. The electrical impedance of the coil is measured simultaneously, and the frequency at which this impedance peaks is identified as the resonance frequency.

Webster (2010) proposed a method for the instantaneous volume measurement of objects in a Helmholtz Resonator based on monitoring phase shifts. The resonance hunting via phase shift concept involves measuring the signal phase difference between the driver, i.e., the loudspeaker and the

resonator. Webster assumed the phase shift between the driver and the resonator would be maximized when the system reached its natural frequency. By setting the driver to operate at the natural frequency of an empty Helmholtz Resonator, any change in the chamber volume could proportionally affect the phase relationship between the resonator and the loudspeaker. However, Webster reported that this approach was impractical due to extreme uncertainty in phase-shift measurements. He also noted that sound attenuation within the resonator changes as its cavity volume varies. This change in sound attenuation corresponded with alterations in the spectral analysis of the signal. Consequently, Webster proposed an experimental model based on the shape of the resonator response signal—specifically, vertical and horizontal shifts of the resonance peak in spectral analysis—for quicker sample volume measurements (3 seconds instead of 40 seconds). However, this faster method came at the cost of limiting the maximum measurable sample volume to 15% of the resonator cavity volume.

4.1.8. Sound absorption in porous media

When acoustic energy impacts a surface perpendicular to the direction of sound propagation, part of it reflects, while the remainder penetrates the medium. Some energy transmits through the medium from this penetrated portion, and some get absorbed. Acoustic energy dissipation within the medium can occur through various mechanisms, mainly viscous and frictional losses (Kuczmarski & Johnston, 2011). A significant part of the pressure wave penetrates the medium in highly porous surfaces, such as powders. Within the material, the penetrated wave reflects off solid surfaces, and these numerous reflections make porous media effective acoustic absorbers (Allard & Atalla, 2009; Kuczmarski & Johnston, 2011).

Powders are known for their high sound absorption. According to Webster (2010), using such materials makes volume measurement via Helmholtz Resonance impractical. He reported that hunting the resonance frequency in a three-litre resonator with a 170 mm port for some powders, including sand and sub-millimetre ballotini, becomes impossible for fill ratios above 30% due to excessive sound absorption.

The sound absorption index in a porous medium, represented by α, ranges from 0 to 1 and varies with the frequency of the incident sound. The material thickness should be less than a tenth of the incident wavelength to avoid significant sound absorption by the quarter-wavelength mechanism (Cox & d'Antonio, 2016, p.131). At a quarter of the wavelength, the material absorbs most of the incident sound (Allard & Atalla, 2009).

Factors affecting sound absorption in powders primarily include porosity and permeability (Kalauni & Pawar, 2019). Porosity is the ratio of void volume to the total volume of the medium, and permeability is essentially the inverse of flow resistivity or the material's resistance to fluid flow through it. Other parameters, such as viscous and thermal characteristic lengths and tortuosity, are usually empirically derived. Viscous characteristic length describes the effect of viscosity in the mid-to-high frequency range, while thermal characteristic length accounts for the high-frequency behaviour of fibrous material (Allard & Atalla, 2009). Tortuosity is another significant parameter affecting both sound absorption and the acoustical properties of porous media.

Tortuosity is a governing factor in the sound absorption of a porous material (Cox & d'Antonio, 2016; Kalauni & Pawar, 2019) and is defined as the elongation of fluid passageways within the pores relative to the physical thickness of the sample. Various models have been developed to predict sound absorption in porous materials based on these and other parameters, as discussed in multiple studies (Allard & Atalla, 2009; Cox & d'Antonio, 2016; Kalauni & Pawar, 2019).

Due to the challenges in measuring the specified parameters for all powder samples in this study, the objective is to measure sound absorption in the powders directly. The amount of sound absorption for different frequency ranges is the most relevant parameter to investigate in this study. This parameter is beneficial for optimising the design of a resonator to resonate in a frequency range so that the sample inside the resonator has minimal acoustic absorption. For this purpose, the Impedance Tube method can provide a means for directly measuring the acoustic properties of material, such as sound absorption.

4.1.9. Sound absorption measurement using impedance tube

A porous material's most significant acoustic property is its coefficient of sound absorption α (not to be confused with the resonator's geometrical constant, also commonly denoted as α). This property can be measured using a device known as an impedance tube. Acoustic impedance refers to a medium's resistance to the propagation of a sound wave. In an impedance tube, a material is exposed to sound, and the ratio of the reflected acoustic intensity to the incident acoustic intensity is measured.

A standard impedance tube can be made using one microphone that travels along the tube, generating a single monotone sound towards a sample (ASTM Standard C384-04, 2004) or uses two (ASTM E1050-19, 2019) or four microphones (ASTM E2611-19, 2019) while the sample is exposed to a broadband signal. The advantage of using an impedance tube with multiple microphones is that

sound absorption of the sample can be measured in a wide range of frequencies in a single measurement, and this method is widely accepted as the standard method (Kuczmarski & Johnston, 2011).

Figure 4-8 depicts a two-microphone impedance tube which uses the transfer function method introduced by Chung & and Blaser (1980). In this method, The Complex Reflection coefficient R is calculated by:

$$R = \frac{P_r}{P_i} \qquad 4\text{-}24$$

where P_r is the reflected noise complex pressure, and P_i is the incident noise complex pressure. The normal incidence sound absorption coefficient is calculated by:

$$\alpha = 1 - |R|^2 \qquad 4\text{-}25$$

Okudaira et al. (1993) used this technique to evaluate the dynamic physical properties of a powder bed with a mean particle diameter under 400 µm. They reported a strong correlation between sound absorption peak frequencies and the tortuosity of the material.

An Impedance Tube was designed and constructed. The acoustic absorption coefficients of the samples under study were directly measured, and the data obtained were used to study the sound absorption level of different samples and optimize the Helmholtz resonator design to achieve maximum fill levels when loaded with powders for volume determination.

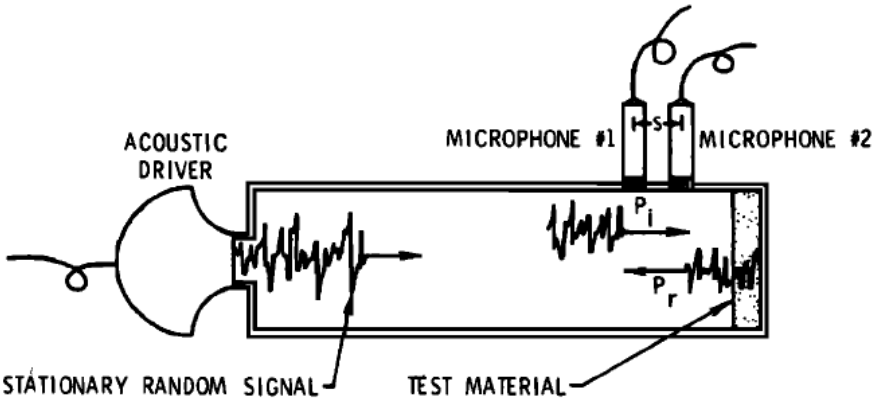


Figure 4-8: *A two-microphone impedance tube to measure the sound absorption coefficient in a medium (Chung & Blaser, 1980).*

4.2. Materials

4.2.1. Small Scale Resonators (1, 2 and 3 litres)

For the laboratory experiments involving Helmholtz Resonance, a modular Helmholtz Resonator constructed from Perspex was utilized. The base of this modular system was initially designed by Webster (2010); however, modifications were made for this study concerning the microphone's location and the port compartments. A graphical representation of this resonator is provided in Appendix E, and a schematic of the apparatus is shown in Figure 4-9.

The primary structure of the resonator comprises a bottom plate, a cavity, and a top plate, all made of Perspex. These three components are interconnected using four 6-millimeter threaded rods and are sealed airtight with O-rings.

The bottom plate has a 50 mm hole and serves as a housing for discharge control orifices, the bottom microphone plate, or a blank-off termination plate. When using the termination plate, a disk is employed to fill the empty cavity in the bottom plate.

The cylindrical walls of the resonator are interchangeable pieces fabricated from a Perspex tube. Three interchangeable cylindrical cavities are available, each with an internal diameter of 140 mm and a wall thickness of 5 mm. The cavities have 60, 123, and 195 mm heights, corresponding to nominal volumes of 1, 2, and 3 litres, respectively. According to the manufacturer, a 5 mm Perspex sheet has an average sound reduction index of 30 dB, effectively making it a sound insulator.

The top plate was used to seal the cavity. Four 6 mm screws for the port flange seating were in the middle of this part. The port flanges and the top plate were sealed using 3 mm o-rings.

For the signal phase-shift tests between the top and bottom sections of the resonator cavity, a microphone was positioned at the centre of the bottom plate, which was mounted on a 12 mm thick flange plate. The 12 mm deep, 50 mm wide hole on the bottom of the plate provided a clean, empty cavity to distance the microphone from the samples above it. For this purpose, three melt-blown layers collected from surgical masks were stretched on the bottom plate and fixed in the contact area of the cavity and bottom plate. Tightening the bolts around the resonator provided enough stretch on the melt-blown layers to form a sturdy basement for the powders above the 50 mm hole.

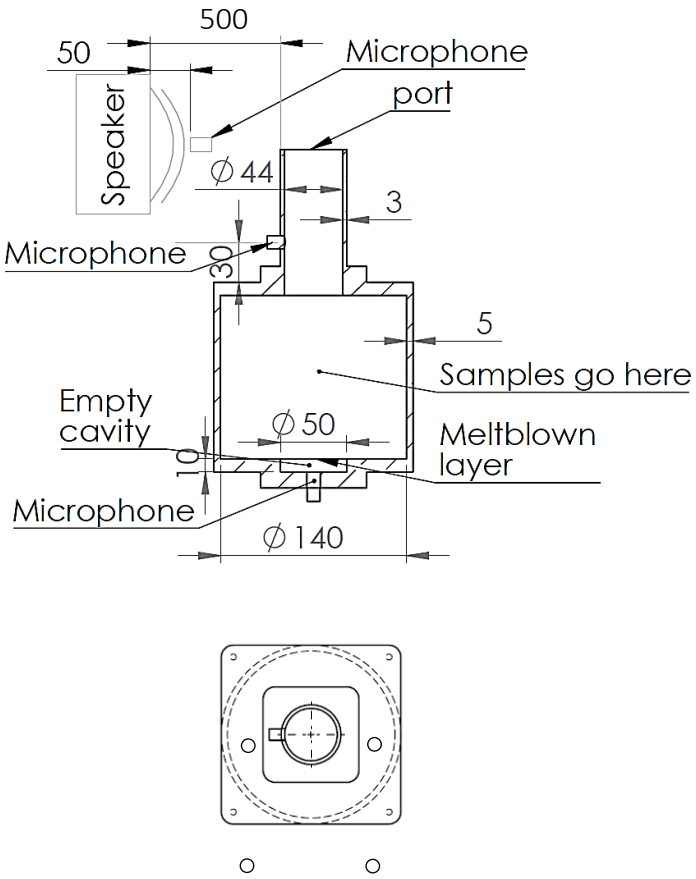


Figure 4-9: *The modular Perspex Resonator: sliced front view (Top figure) and top view (Bottom figure). The dimensions are in mm.*

4.2.2. Small Scale Resonator Ports

The resonance frequency range of the Helmholtz Resonator was altered by using ports of different lengths. The ports were cut from aluminium tubes with an internal diameter of 44 mm and a wall thickness of 3 mm. The ports were fixed at the top of the resonator cavity using Perspex flanges and four bolts. The port lengths were 51, 250, 500 and 1000 millimetres. Holes were drilled 30 mm above the root on each port to install the microphones. The microphone housing was 1.5 mm deep into the port side. The port ends were machined to have 90-degree edges.

4.2.3. 50-litre Vessel

A 50-litre vessel was designed to investigate dynamic volume measurement based on Helmholtz Resonance. The experiments conducted on this vessel were among the initial experiments on Helmholtz Resonance. The results obtained from these tests were crucial for developing the amplitude tracking method and developing a mathematical model for instantaneous volume measurement (Chapter 7) using the Helmholtz resonator. This vessel, shown in Figure 4-10, is the 50-litre vessel introduced in Chapter 3 for the optical method (Section 3.2.2) with modifications on the top

compartment. A transparent cover plate covered the 50-litre vessel top with a port and a microphone housing.

A 26 mm orifice was laser cut from a steel sheet with a thickness of 1.2 mm. The orifice was flanged into the vessel's bottom plate with eight bolts. Duct tape was used to close the orifice and was quickly removed to initiate the discharge of the samples in dynamic tests. The vessel was placed on a support structure, and the discharged material was collected in a bucket 500 mm beneath the discharge orifice. The bucket sat on a platform scale (Metler Toledo IND221) with a resolution of 0.005 kg. The scale was interfaced with a computer with an RS232 serial data link.

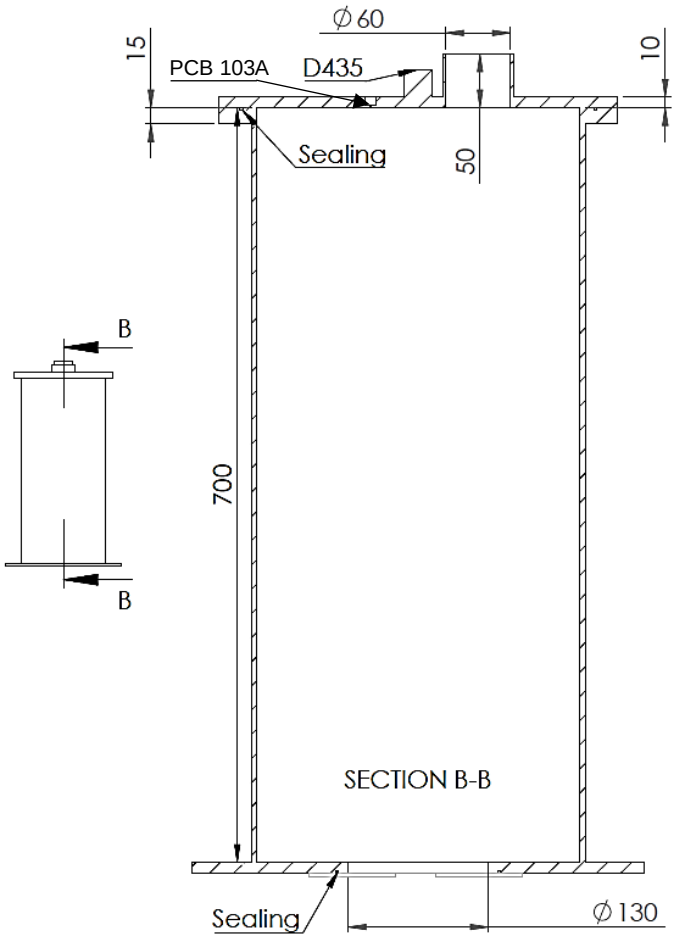


Figure 4-10: *50-litre resonator. Dimensions in mm.*

4.2.4. Topdressing hopper

A Cresco topdressing hopper with a nominal volume of 2,000 litres hung by a pair of calibrated load cells (Mettler Toledo ind556) was used to test for resonant frequency variation with different fill degrees. Figure 4-11 shows a drawing of the hopper. This hopper was considered a Helmholtz Resonator with two ports, one on top, the opening, and another at the bottom, the discharge gate.

Figure 4-12 shows this hopper's estimated resonance frequency for the range of fill volume capacity.

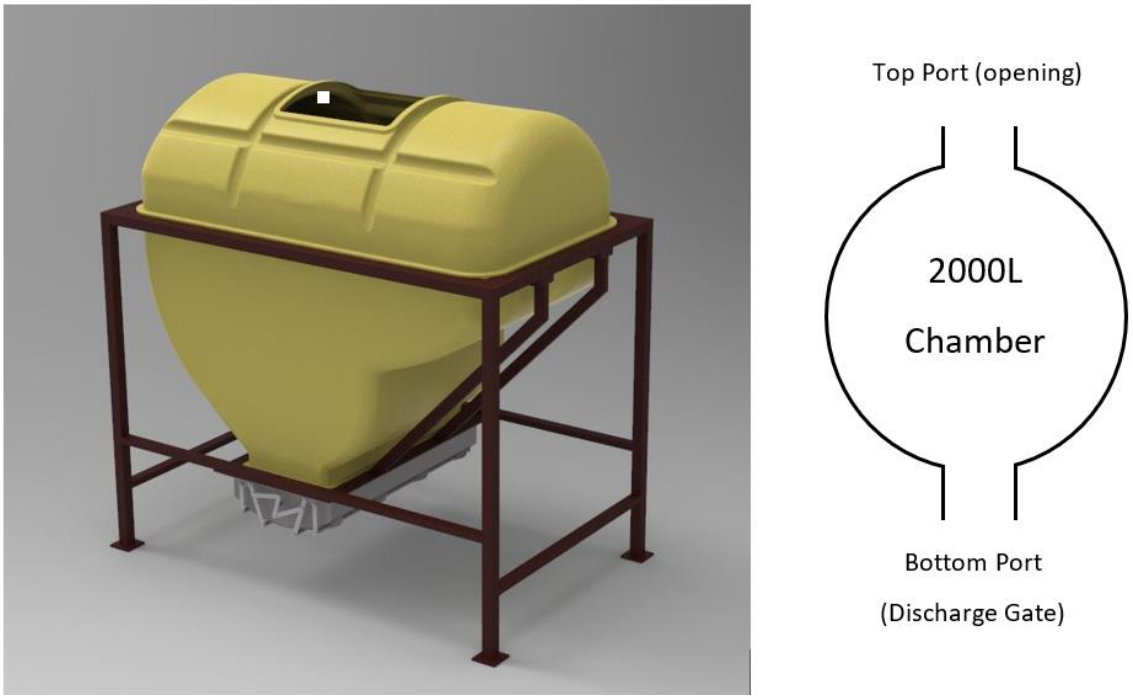


Figure 4-11: *Topdressing hopper used as a Helmholtz Resonator. The white dot shows the position of the microphone.*

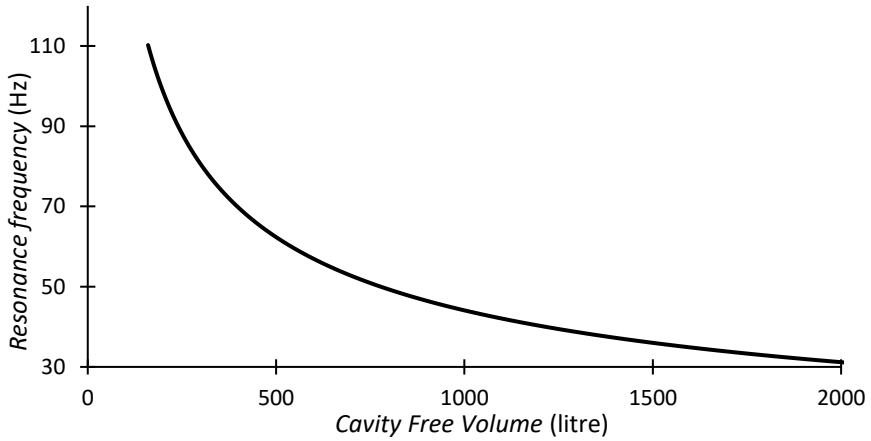


Figure 4-12: *Estimated resonant frequency range of the topdressing hopper.*

4.2.5. Microphone

The dynamic sound pressure sensor used for the acoustic tests in this study was a pressure-field microphone, model PCB103A, from PCB Piezotronics, USA. This microphone features a 10 mm capsule

with a minimum frequency response of 5 Hz and a resonance frequency of 17 kHz. Its sensitivity is 217.5 mV/kPa. More technical details are provided in Appendix C.

Microphones were positioned at different locations. In the small-scale resonator tests, they were placed at the root of the port, at the bottom of the resonator, and in front of the loudspeaker (as shown in Figure 4-10). In the 50-litre vessel, a microphone was installed on the cover plate (Figure 4-10). For the aeroplane hopper, the microphone was suspended inside the hopper, 20 mm below the opening at the centre of the side curve (indicated by the white square in Figure 4-11).

The microphone signals were amplified using a dedicated PCB amplifier, model 482C05, also from PCB Piezotronics, USA.

4.2.6. Sound Source Drivers

For low-frequency measurements (<150 Hz), a 12" Pioneer subwoofer (Pioneer, Japan) with part number TS-A300S4 was used to excite the resonators. The subwoofer was installed in a sealed wooden enclosure with sound-absorbing glass wool covering on internal walls, keeping the loudspeaker resonant frequency below 20 Hz and minimising distortion. The subwoofer output power was equalized using a digital equalizer to improve the linearity of the power response in the range of 30~200 Hz. The loudspeaker signal was amplified using a mono-channel amplifier (Pioneer GMD8601).

A 100 mm pioneer speaker (pioneer TS-G1020F) with a linear frequency response (±2 dB) between 100 and 3000 Hz was used for higher frequencies. The manufacturer's claim on the linearity in the speaker’s response was investigated using a PCB A103 microphone and confirmed.

4.2.7. Temperature measurement

A Texas Instrument Integrated Circuit (IC) temperature sensor with part number LM35 (Texas Instruments, USA) was used to measure ambient temperature as the main factor in calculating sound speed in air. This sensor is pre-calibrated, and the manufacturer claims a ±0.5°C accuracy. The LM35 IC was calibrated using a mercury thermometer (Brannan-England 5~50°C with an accuracy of ±0.1°C).

4.2.8. Data Acquisition Hardware

All the signal generation and sampling operations were conducted using NI USB-6211 (National Instruments, USA) Data Acquisition Card (DAQ card). The signal generation and sampling rates were 44.1 kHz.

4.2.9. Software

In this chapter, all computer programs for data logging, digital signal processing, control, and simulation were coded using LabVIEW software (National Instruments, 2018, USA), a graphical data flow programming language. This software was chosen because of its versatility in digital signal processing and generation. The technical drawings were generated using SolidWorks (Dassault Systèmes, France, 2018).

4.2.10. Impedance Tube

A two-microphone impedance tube was designed according to ASTM 1050 standard (ASTM E33 Committee, 2019). The calculations of this standard are based on the theory developed by Chung & Blaser (1980). The details of this design and validation are published by Barzegar & Davies (2024).

Figure 4-13 is an illustration of the design. The detailed calculations implemented into the design of the impedance tube are covered in Appendix B. Appendix F provides a picture of the impedance tube. The top compartments, labelled (A) and (B), house a 4" speaker driver (F1034 R, Pioneer, Japan). These components were machined from a cylindrical block of recycled high-density polyethylene. Compartment A was filled with sound-absorptive glass wool (Earthwool Glasswool R3.6, Knauf Insulation Ltd, New Zealand) to prevent resonance in the speaker driver. Compartment B featured a funnel shape to smoothly reduce the acoustic transfer channel diameter from 102 to 70 mm, preventing strong channel reflections. It was also filled with glass wool according to ASTM 1050 to prevent tube resonance. The speaker driver installation ring was mechanically isolated from compartments (A) and (B) using five layers of melt-blown material (extracted from blue surgical masks) on each side to dampen mechanical vibrations. A layer of grease was applied between the speaker enclosure and the impedance tube to seal the connection acoustically.

The impedance tube (Compartment C) was machined from a mild steel pipe with an outer diameter of 90 mm and a wall thickness of 5.69 mm. Two pieces of steel were welded to one side of the tube using a bolt to accommodate a bench fixture housing (Figure 4-13, Section C). On the other side, three 10 mm housings were made (Part D) for microphone fitting. O-ring beds were machined inside microphone housings to seal the microphones from the outside of the tube. The machined tube was coated using hard chromium to avoid corrosion.

The impedance tube was designed with three microphone holes to work in two modes: High Frequency (110 to 2800 Hz) and low frequency (55 to 2200 Hz). The low-frequency mode is for when the microphones are 60 mm apart, and the high-frequency mode is for when the microphones are placed 30 mm apart. The operating frequency range of the impedance tube for the given dimensions was calculated using the criteria expressed in ASTM 1050. Compartment (E) is a piston made from an

aluminium block to adjust sample thickness from 0 to 70 mm. Compartment (F) is a stainless-steel sample holder that accommodates the piston and the sample. An O-ring sealed the gap between the sample holder and the tube. Figure 4-13 (3D View) shows that three adjustable clamps spaced 120° apart radially secure the sample holder to the tube.

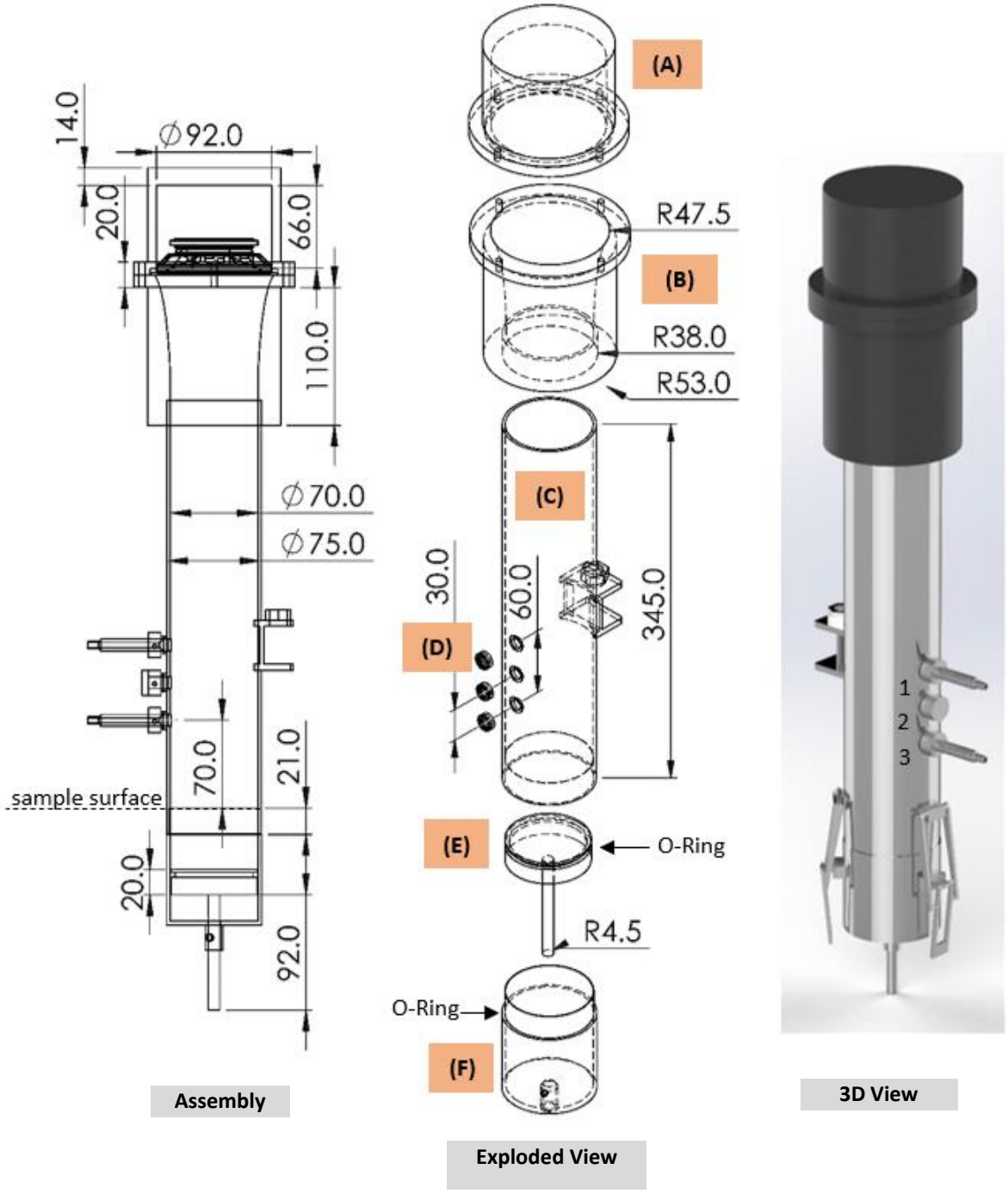


Figure 4-13: The Impedance Tube. Dimensions are in mm.

Electronics

The schematic of the electronics of the impedance tube is illustrated in Figures 4-14. The speaker driver was a 4-inch Pioneer (TS-F1034R, pioneer, Japan) speaker advertised for car stereo system. The amplifier (Amp) used to drive the speaker was a 100-watt mono-channel amplifier (XH-M542, China). A computer sound card (no part number, branded Kebidu, China) with dual-channel line-in input was used as the data acquisition hardware. This sound card uses a CM6206 (Cmedia, Taiwan) audio chipset. Initially, two separate sound cards with mono input channels were tested, and it was observed that such a setup resulted in an inconsistency in signal phase ratio between the audio channels.

An unbranded external sound card was used as data acquisition hardware. This sound card uses a CM6206 (Cmedia, Taiwan) audio chipset. This sound card has an output to feed the speaker amplifier and a stereo line-in input to read signals from the microphones with a sampling rate of 44.1 kHz and a resolution of 16 bits. The soundcard line-in channels were tested for consistency in phase and amplitude response. The initial tests revealed no significant difference between the channels regarding the repeatability of the signal phase. For ten repeats, the signal phase variation between the two channels for a monotone signal remained under 0.01% throughout the cycle.

The microphone setup consisted of dedicated pressure microphones, typically used and advertised for impedance tubes. The model of the microphones was 377A10 (PCB Piezotronics, USA). The microphones were powered using dedicated preamps (426B03, PCB Piezotronics, USA) and amplified using a dedicated signal conditioner, model 482C05 (PCB Piezotronics, USA). These microphones provide a highly linear (±2dB) output in a 4 to 70 kHz frequency range.

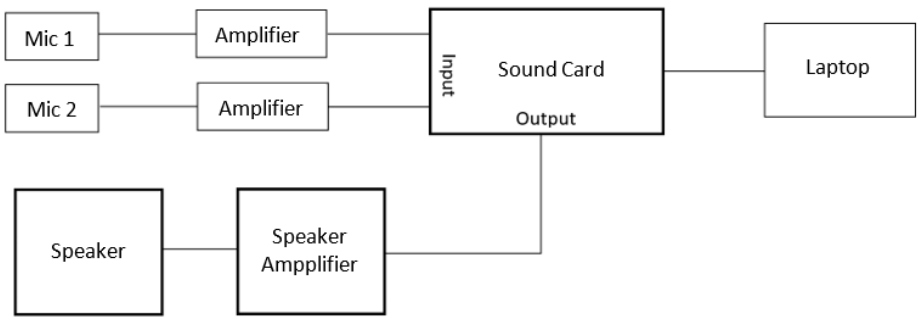


Figure 4-14: *Impedance tube electronics.*

4.2.11. Test Material

Table 4-1 provides the physical properties of the test materials. The materials not included in the table are introduced in the corresponding sections. Supplementary information on the sample permeability and size range is presented in Appendix D.

The particle diameters for materials BB, LMB, and SMB were measured by taking an average of 30 readings using a vernier gauge. The diameter of the rest of the sample materials was determined using a Mastersizer 3000 (Malvern, UK). The loose poured particle density was determined according to the ASTM D1895B standard, and the tapped bulk density was measured using a tapping machine (Stampfvolumeter STAV 2003, Germany) with 100 taps. The voidage figures were calculated by averaging the voidage values from both tapped and loosely poured samples. The solid density for agricultural lime samples (Al and AL2) were obtained from the supplier's datasheet (AgLime, ravensdown, New Zealand). The properties of ballotini samples B250, B710, and fine sand samples were measured using a specific gravity bottle. Permeability was measured using a fluidized bed apparatus made in-house at Massey University.

Table 4-1: *Physical Properties of the variety of the test materials.*

	Sample name											
Property	**Large Marbles (LMB)**	**Small Marbles (SMB)**	**Ball bearings**	**Mustard seeds**	**Black Mustard seeds**	**Coarse Ballotini**	**Fine Ballotini**	**Fine Sand**	**Agricultural Lime**	**Agricultural Lime**	**Symbol**	**Unit**
Abbreviation	**LMB**	**MB**	**BB**	**MS**	**BMS**	**B710**	**B250**	**FS**	**AL**	**AL2**		
Particle Diameter	24.76	15.97	3.175	1.98	1.56	0.67	0.24	0.11	0.06	**0.31**	***D[3,2]***	**mm**
Bulk density (Tapped)	*	*	*	730	*	1500	1500	1500	1490	*1420*	ρ_{bT}	**kg.m^{-3}**
Bulk density (Loose poured)	1410**	1420	4800	720	670	1450	1440	1360	1410	*1290*	ρ_{bLP}	**kg.m^{-3}**
Average Voidage	43**	43	38	29	41	37	37	33	48	50	**ϕ**	***%***
Solid Density	2450	2510	7860	1100	1140	2410	2390	2380	2700	*2700*	ρ_{p}	**kg.m^{-3}**
Permeability	>10000	>10000	3260	1500	*	256	55	11	15	*	***k***	**darcy**

*Not measured **Estimated

The uncertainty in the diameter of marble samples was calculated using the readings from 30 marbles of each sample type. The uncertainty for sample diameter for large marbles and small marbles

was 0.16 and 0.09 mm, respectively. The average volume of large and small marbles was 7.94±0.15 ml and 2.13±0.03 ml, respectively.

4.3. Methods

4.3.1. Resonance Hunting Method 1: Undriven

The undriven resonance hunting method refers to measuring the resonator oscillation frequency to an impulse excitation. As introduced in Section 4.1.4, it is called an undriven response. A linear chirp signal (refer to section 4.1.6: Excitation) for 200 ms was played on the loudspeaker. After a delay of 5 ms, the pressure signal from the port microphone was recorded for 0.5 s (22,050 samples with a sampling rate of 44,100 Hz). For digital signal processing of the recorded data, the microphone signal was taken to the frequency domain by Discrete Fourier Transform (DFT) and the power spectral density graphs were plotted. The interpolated peak frequency in the graph was recorded as the resonance frequency. This process is graphically shown in Figure 4-15.

The undriven resonance frequency hunting was repeated three times with various excitation signals for sample volume estimation: first, a white broadband noise played for 0.5 seconds and the approximate resonance frequency was detected; second, the resonator was excited by a linear chirp signal 10 Hz wide around the estimated resonance frequency and last, a 1 Hz wide chirp, ±0.5 Hz of the resonance frequency detected from the previous stage, was used. The resonance frequency hunted on the third round was reported as the resonance frequency.

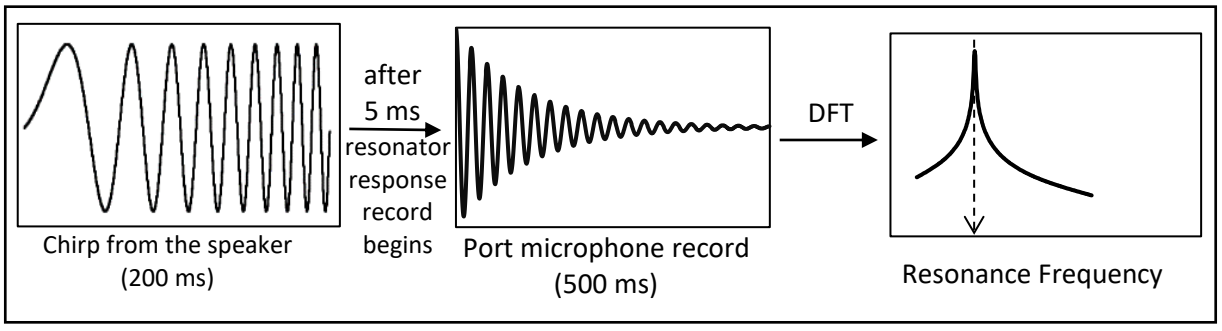


***Figure 4-15**: Undriven Resonance Frequency Hunting.*

4.3.2. Resonance Hunting Method 2: Driven

The resonator was excited by a linear chirp for 5 seconds for the driven resonance hunting. The chirp frequency range started from a frequency 10% lower than the minimum resonance frequency of the resonator (empty resonator) and continued to 10% higher than the maximum possible

resonance frequency, which occurs when the resonator free volume approaches zero. The highest possible resonance frequency reflects the quarter wavelength resonance frequency of the port. The driven response of the resonator was sampled simultaneously using the port microphone. The signal from the microphone was taken to the frequency domain through the discrete fourier transform, and the spectral density graph was plotted. The highest peak was recorded as the resonance frequency along with resonance magnitude and quality factor. Figure 4-16 shows the steps followed in this method. Table 4-2 lists the resonance frequency range of the 2-litre resonator.

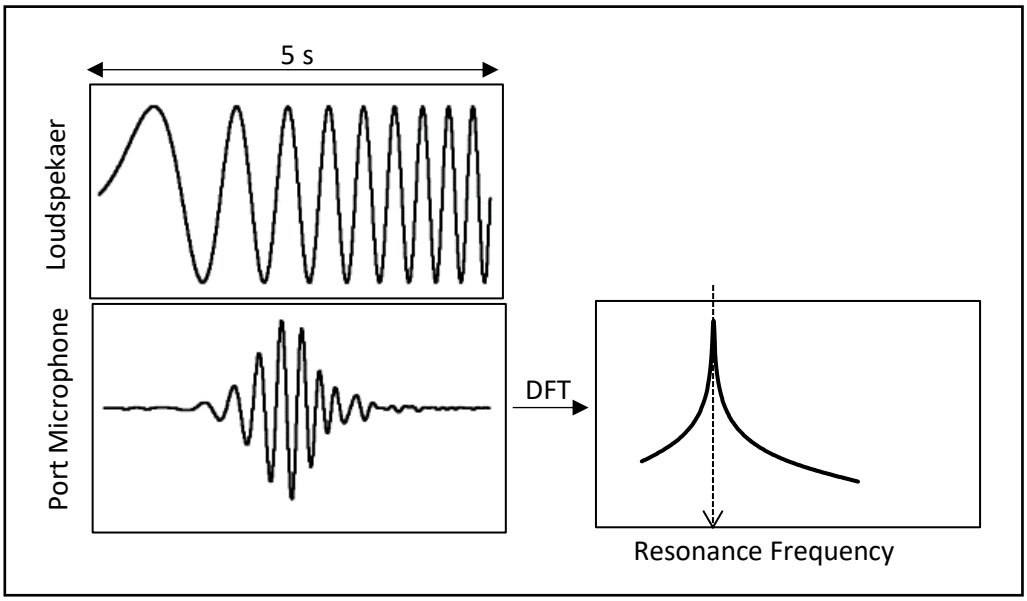


Figure 4-16: *Driven resonance frequency Hunting method.*

Table 4-2: *Resonance frequency range for the 2-litre resonator at 343 °c.*

Port Length (mm)	51	250	500	1000
Empty Resonator RF* (Hz ±1)	171	89	63	42
Full Resonator RF (Hz ±1)	1640	343	168	84

*RF: Resonance Frequency

4.3.3. Resonance Hunting Method 3: Transfer Function

This study introduces an alternative method for driven resonance frequency hunting. In this method, a secondary microphone was introduced to eliminate noise and compensate for the non-linearities in microphones and loudspeakers.

This method was conducted by locating the peak magnitude of a Fourier Transfer Function (FTF) between two signals obtained from two separate microphones. The microphone installed in front of the loudspeaker provided the reference audio signal collected from the audio driver, shown in Figure 4-9, and the other collected the audio signal from the port. Both signals were collected simultaneously as the audio driver played a chirp. The complex transfer function $H(f)$ provides a relation between these two signals in terms of signal phase and relative magnitude per frequency bin using the following equation (for example, see Roberts & Mullis, 1987):

$$H(f) = \frac{S_{rp(f)}}{S_{rr}(f)} = |H(f)|e^{j\varphi(f)} \qquad 4\text{-}26$$

where $S_{rp(f)}$ is the complex cross-power spectrum between the reference and port microphones, $S_{rr}(f)$ represents the auto power spectrum of the source microphone, $|H(f)|$ Is the magnitude, and $\varphi(f)$ is the phase shift between the two signals (Section 4.1.5, Equation 4-23).

The transfer function calculates the relative power of the microphones, so the transfer function's magnitude for each frequency bin is independent of the speaker power or non-linearity in the response of the microphones as long as they are of the same type.

For resonance hunting, a broad linear chirp signal was generated. The chirp frequency range was 100-2000 Hz, 70-250 Hz, 50-180 Hz and 30-90 Hz for the 51, 250, 500 and 1000 mm ports, respectively. Simultaneously, the signals from the microphones were recorded.

The process of resonance frequency hunting using the transfer function method was repeated five times and averaged. The coherence function $C^2(f)$ was calculated as follows:

$$C^2(f) = \frac{[Magnitude\ (S_{rp})]^2}{S_{rr}(f).S_{pp}(f)} \qquad 4\text{-}27$$

Noise in the port microphone signal that was not coherent with the source signal can be identified using the coherence function and was considered an outlier. An experimentally determined value of 0.95 was used as a reliable coherence for the measured resonance frequency. Frequencies with a coherence of less than 0.95 were considered to be influenced by external noise.

Figure 4-17 demonstrates the simulated capabilities of the transfer function resonance hunting method compared with the Discrete Fourier Transform method, introduced in Section 4.3.2. As shown

in Figure 4-17, the transfer function method requires feed from two microphones and generates three outputs in the frequency domain. The top-right graph (Graph *a*) is the Magnitude graph of the transfer function between the port and reference microphones. The ordinate is the magnitude of the transfer function, dimensionless, and the abscissa is frequency. The simulated resonance peak at 33 Hz and the introduced noise at 60 Hz are detectable. In this graph, the Mains hum, a noise induced by the AC power supply to both microphones, is cancelled. Graph (*b*) is the phase shift (Radians) vs frequency. In the resonance, the phase shift is 90 degrees. Graph (*e*) is signal coherence. The ordinate of this graph is a dimensionless index in the range of 0~1. The noise *n(t)* introduced in the port microphone is not coherent with the resonator driver signal *r(t);* therefore, it is detected in graph (*c*) and thus can be labelled as a False resonance.

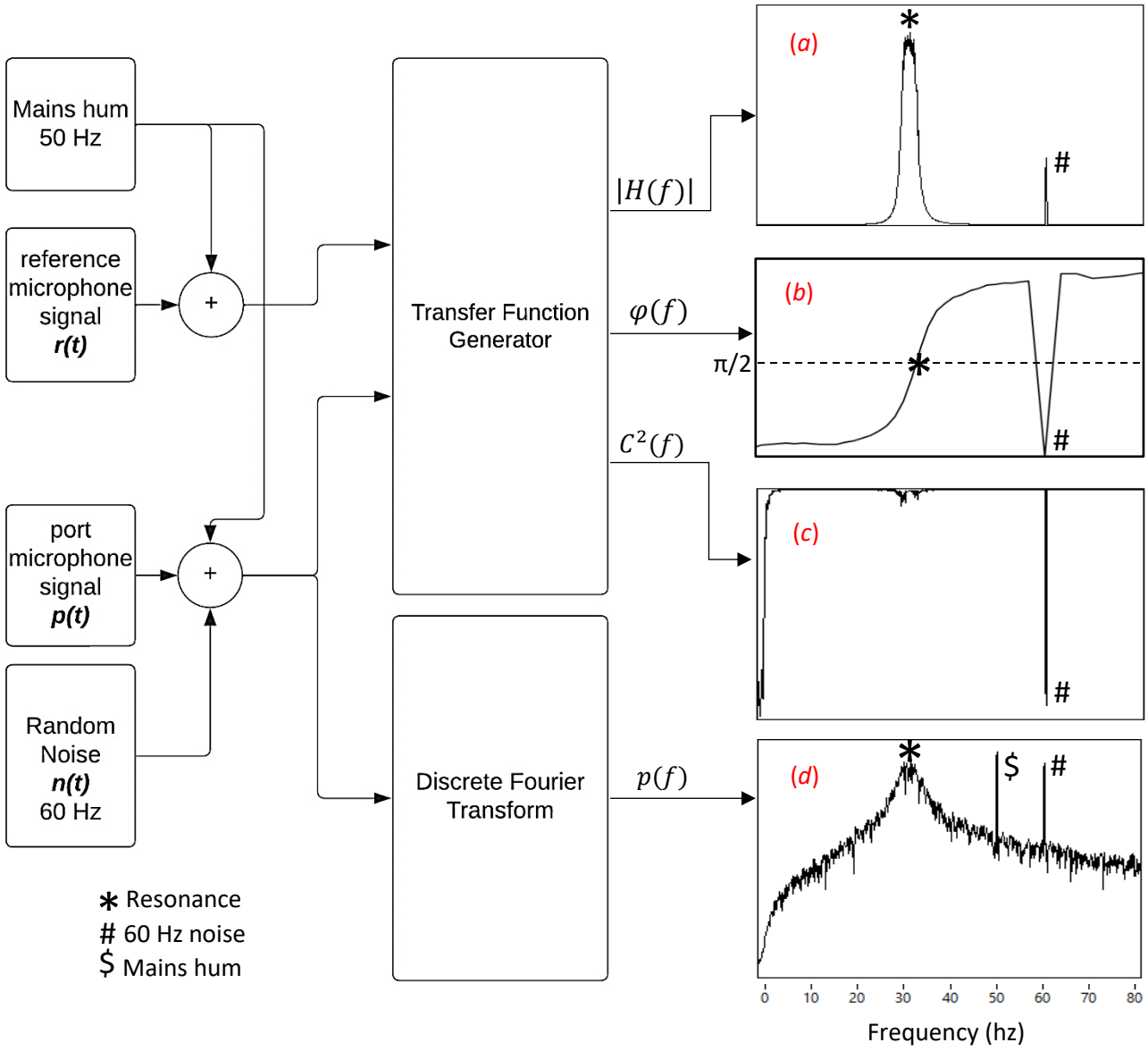


Figure 4-17: *Resonance frequency hunting using Fourier Transfer Function method (Two microphones) compared with ordinary driven resonance hunting using Dicrete Fourier Transfor Method (single microphone).*

Graph (*d*) is the port microphone signal transferred to the frequency domain using a discrete Fourier transform, as discussed in Section 4.3.2: Resonance Hunting Method 2. The Mains hum signal and the 60 Hz noises peaked and could be falsely recorded as the resonance frequency.

4.3.4. Resonant frequency hunting in the 50-litre vessel

The resonant frequency was detected using the undriven resonance hunting method (Section 4.3.1). Mustard seeds and agricultural lime were chosen as the test materials due to their vastly different physical properties. Mustard seed is a monosized spherical free-flowing particle, and agricultural lime is a cohesive fine powder with a broad particle size distribution. Mustard seed has similar flow characteristics to urea powders that are widely used in topdressing operations in New Zealand. The physical properties of these materials are provided in Table 4-1.

About 20 litres of mustard seeds (MS) and agricultural lime (AL) were loaded into the 50-litre vessel for each test. The flange on the top was bolted to the resonator top with 16 bolts and sealed with an O-ring to ensure no leaks in the system. Duct tape was used to close the 16 mm orifice flanged to the bottom, and the duct tape was quickly removed to initiate the discharge. The calibrated optical method, introduced in Chapter 3, was used to track the actual volume change in the vessel. The scanner was attached to the outer side of the transparent top flange. Volume changes were constantly logged into the computer throughout the discharge process at ~4 Hz. The other recorded parameters include resonance frequencies, sound pressure level, and resonance power.

4.3.5. Resonance frequency detection in the topdressing hopper

This Experiment was among the initial tests for fill volume measurement using Helmholtz Resonance. This experiment was conducted in the Ravensdown fertiliser store at Aramaho, Wanganui. The test materials were fertilizers, urea and agricultural lime. The hopper was filled to roughly three-quarters of its volume with the test material. A forklift lifted the hopper's frame so the discharge gate had a ground clearance of 1 m. The discharge was initiated by opening the discharge gate and fixing the gate control rod to a horizontal bar in the frame. This setting allowed the gate to be opened for 20 to 30 mm, allowing the material to discharge at a relatively low flow rate. The resonance hunting was performed using the Undriven Method (Section 4.3.1). In the initial tests, it was noticed that a 0.2 s excitation was not adequate to make the hopper resonate; therefore, the duration of the excitation was increased to 0.5 s.

Trial test runs showed that the resonant frequency in the discharge process was hard to track, especially for urea with a particle diameter of roughly 2.5 mm and a bulk density of 0.75 $kg.l^{-1}$. A

two-stage resonance hunting approach was utilised to track resonance frequency during material discharge. For the first hunting stage, a broad chirp sound 0.3 s long with a frequency span from 20 to 60 Hz was generated, and the system response was filtered using a 20 Hz bandpass filter. The filtered signal was analysed to detect all the peak frequencies. In the second hunting stage, the peaks were isolated by generating a chirp, 0.1 s long and 1 Hz wide, centred at each. The response was filtered using a bandpass filter 1 Hz wide. Then, the peaks detected in stage two were compared for amplitude, and the peak with the highest power was logged as the resonant frequency. The cycle is repeated during the discharge. Resonant frequency, resonance power and sound pressure were logged. The scale measured the material mass for each hunted frequency. Figure 4-18 shows the experimental setup.

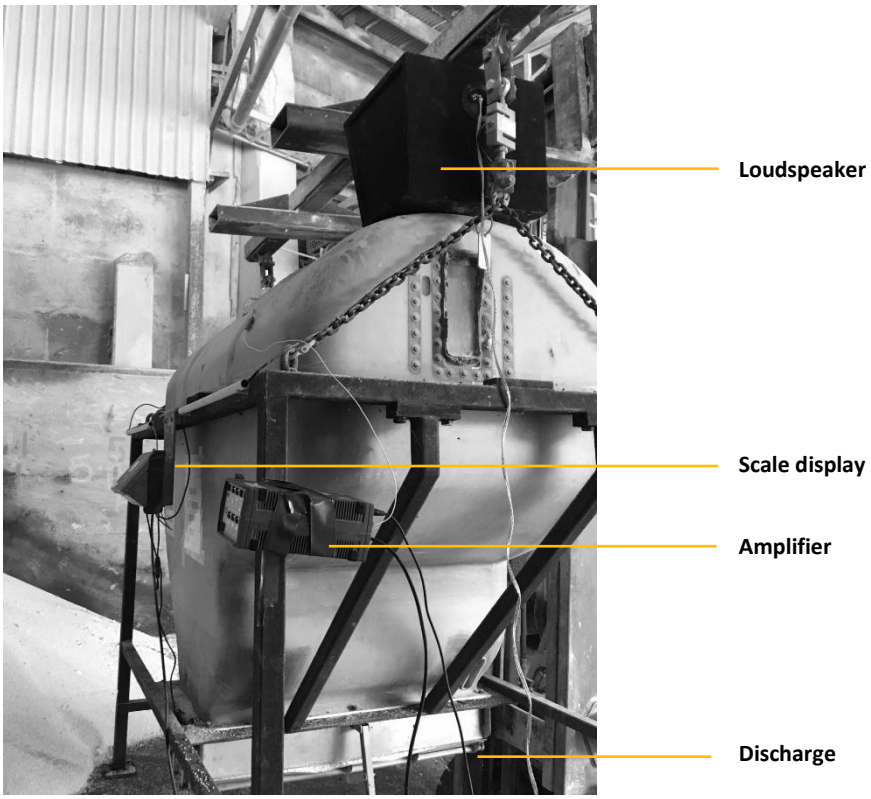


Figure 4-18: *Experimental setup for resonance frequency hunting in a topdressing aeroplane hopper.*

4.3.6. Testing for non-linearities in the 3-litre lab-scale resonator

This experiment investigated and demonstrated non-linearities in the Helmholtz resonance model in estimating cavity volume. For this purpose, water with increments of ~100 ml was poured into the 3,000 ml resonator with the 51 mm port attached. The resonance frequency was detected using the undriven resonance frequency hunting method. The water volume estimated using the classical Helmholtz Resonance equation was compared with the actual water volume from weighing. Deviation

of these two volumes was plotted to indicate the non-linearity and the accuracy of the resonance frequency hunting method for different cavity volumes.

4.3.7. Volume determination using various ports and resonance hunting methods

These experiments were conducted to investigate the effect of port length on the volume measurement estimation using the classical Helmholtz Resonance model. The experiments were conducted using the 2-litre resonator with four ports of 51, 250, 500 and 1000 mm lengths. For each port connected to the resonator, water was added in 300 ml increments until the cavity was filled. After each increase, Resonance Frequency was hunted using Undriven, Driven and Transfer Function resonance Frequency hunting methods (Sections 4.3.1 to 4.3.3). Resonance frequencies *f* was replaced with resonance wavelength λ so the temperature variation effect on the speed of sound c is accounted for, using the following:

$$\lambda = \frac{c}{f} \qquad \textit{4-28}$$

The resonance wavelength for each fill level for different port lengths was compared and plotted. The accuracy and linearity of the three resonance frequency hunting methods were compared.

The classical Helmholtz Resonance Equation was algebraically manipulated to override the need to accurately measure the Port extension factor constant Δl. The classical Helmholtz Resonance Equation can be rearranged in the form:

$$f = \frac{c\alpha}{\sqrt{V_c}} \qquad \textit{4-29}$$

where $\alpha = \frac{1}{2\pi}\sqrt{\frac{S_p}{(l_p+\Delta l)}}$ is the resonator port geometrical constant. Taking f_0 as the resonance frequency of the resonator when the resonator is empty and taking the f_s as the resonance frequency of the resonator when the cavity volume has changed by volume V_s, Equations 4-30 and 4-31 can be written:

$$f_0 = \frac{c_0\alpha}{\sqrt{V_c}} \qquad \textit{4-30}$$

$$f_s = \frac{c_s\alpha}{\sqrt{(V_c - V_s)}} \qquad \textit{4-31}$$

where c_0 and c_s are the speed of sounds measured in the corresponding tests. Assuming an insignificant change in the ambient temperature, the speed of sound remains constant $(c_s = c_0)$. Dividing 4-31 by 4-30 and doing algebraic manipulations, V_s can be written as:

$$V_s = V_c\left(1 - \left(f_{0/}f_s\right)^2\right) \qquad 4\text{-}32$$

4.3.8. Static volume measurement tests on powders

These experiments were conducted on particles with mean diameters ranging from 0.06 mm for agricultural lime (AL) to 25 mm for large marbles (LMB). The packing of the powders was both loose poured and tapped states. For a loose poured state, a Perspex perforated plate with circular holes 4 mm, square pitch with holes 1 mm apart and a handle attached to its centre (Drawing in Appendix E) was placed at the bottom of the empty resonator. A weighed amount of a powder sample (mustard seeds MS, fine ballotini B250, coarse ballotini B710, fine sand FS, ball bearings BB or agricultural lime AL1) was poured onto the perforated plate, and the perforated plate was gently lifted to increase the sample porosity and form a loose poured state. The top resonator flange was placed and tightened with the four bolts to an almost equal torque in a cross order to minimize the possibility of the presentation of air leaks in the resonator. Then, one of the three ports, 51 mm, 250 mm or 1000 mm port, was fixed to the top plate flange of the resonator using the four bolts tightened to compress a greased O-ring to avoid air-leaks. The resonator resonance frequency was measured using the Undriven, Driven and Transfer Function methods (Section 4.3.1, 4.3.2 and 4.3.3).

After finishing the resonance hunting for a sample load, the port was gently replaced with another port with extreme care not to shake the material inside the resonator, and then, the process of resonance frequency hunting using the three mentioned methods was repeated. For each port, the total height of the resonator (Resonator height + port length) was different. Therefore, the speaker distance and placement were carefully readjusted to the exact concentric distance to the resonator.

After completion of resonance frequency hunting using all ports for a load of material in the cavity, the port was removed, and the resonator was mounted on a tapping machine modified for this experiment with a wooden chassis that firmly held the resonator. The machine was fitted with a 5 kg chassis plate that dropped 10 mm at 90 drops per minute. Each tapping process continued for 90 seconds, equivalent to 120 drops. After tapping the powder samples, the process of resonance frequency hunting using the three methods on all three ports was repeated. In the end, the samples were removed, and a new load were poured into the resonator. The total number of test runs in this section was 570 tests.

4.3.9. Dynamic resonance hunting using the lab-scale resonator

The 1000 mm port was fitted on the 3-litre resonator for these tests. The test samples were black mustard seeds and an agricultural lime sample, which was sieved to remove dust with a diameter of less than 450 um diameter. The mean diameter *D[3,2]* of the agricultural lime sample used in these tests was 0.78 mm. Orifices of 5.6 and 10 mm in diameter were fitted for the black mustard seeds and the agricultural lime test materials, respectively. The orifices were covered using a tape measure. For each sample, the resonator was filled to the top over the perforated plate introduced in Section 4.3.8; the perforated plate was gently pulled up to create an open pour structure in the sample. The surface of the powder was flattened using a metal ruler. The resonator top compartment and port were replaced. To initiate the test, the tape covering the discharge orifice was quickly removed to let the sample discharge into a bucket on a platform scale (Mettler Toledo IND221) with a resolution of 0.005 kg. The scale was interfaced with a computer with an RS232 serial data link. The resonance frequency during the discharge process was measured using the Driven resonance frequency hunting method (Section 4.3.2). The resonance hunting process was repeated at 1 Hz. The mass, time, and resonance location of the discharged material were recorded in log files for statistical analysis. The schematic of the dynamic discharge setup is presented in Figures 4-19.

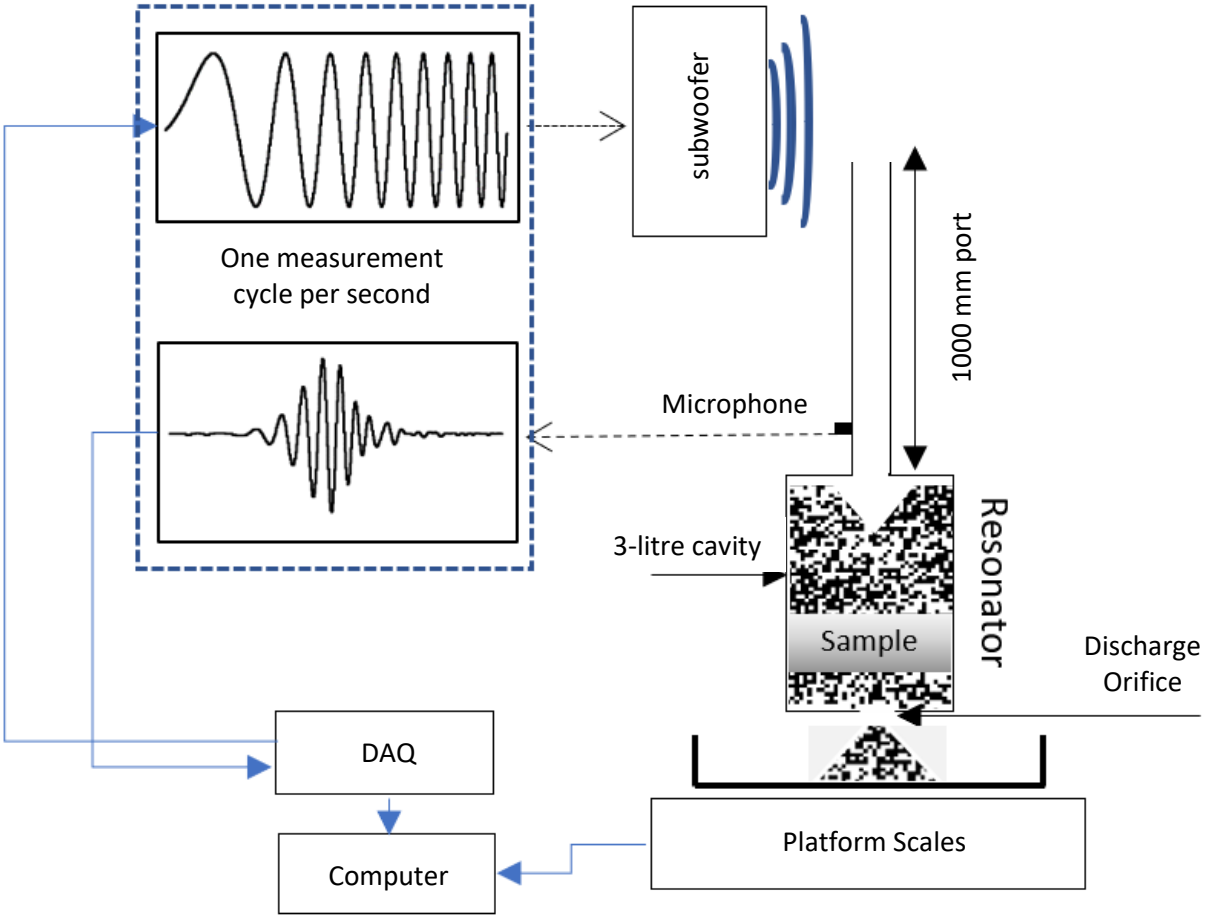


Figure 4-19: *The dynamic resonance frequency hunting experimental setup in a discharging vessel.*

4.3.10. Quality factor assessment

The resonance quality factor of the 2-litre resonator for three different port lengths of 51, 250 and 1000 mm was measured using three different methods. The 2-litre resonator volume was chosen because it is consistently used in static resonance hunting measurements for various samples.

The first resonance quality factor assessment method was analysing the resonator response's decay rate, as discussed in Section 4.1.4.

The second method was resonance quality measurement from the power spectral density shape of the driven response of the resonator when using the Driven method (See Section 4.3.2). The quality factor was calculated by dividing the resonance frequency by full width at half maximum (Section 4.1.5, Equation 4-22).

The third method was calculating the quality factor of the resonance by tracking the phase shift pattern between the source and the port microphone when the resonator is excited in the driven mode, as is depicted in Figure 4-7 in Section 4.1.5.

4.3.11. Effect of powders on quality factor

The effect of the presence of powder samples in the resonator cavity on the reduction of the resonance Quality Factor Q on different samples was investigated. The experiments were conducted on the 2-litre resonator with a 1000 mm port. The samples were agricultural lime (AL), fine ballotini (B250), fine sand (FS), coarse ballotini (B710), black mustard seeds (BMS) and ball bearings (BB) with the detailed physical properties provided in Section 4.2.11, Table 4-1. The other test samples in this experiment were small polyethylene pellets (PE1) with a mean diameter of 3.16 mm and large polyethylene pellets (PE2) with a mean diameter of 4 mm. Polyethylene samples PE1 and PE2 had loose poured bulk densities of 630 and 590 $kg.m^{-3}$ respectively. All samples but PE2 were poured over the perforated plate introduced in section 4.3.8, and the plate was gently pulled up to form a loose pour structure. PE2 with a diameter of more than 4 mm, which was not suitable for the use of the perforated plate, was poured from 100 mm above the resonator from a funnel with a 20 mm opening, and then the surface was flattened by shaking the resonator gently and using a ruler with circular motion. The samples were added to the resonator in increments of about 300 ml increments of bulk volume for each step. The final load filled the resonator to the top.

The resonance quality factor for each sample load was measured using the three resonance hunting methods: Undriven from the signal decay rate (Section 4.1.4), Driven using FWHM spectral analysis (Section 4.1.5, Equation 4-22) and the phase shift between the driver and the resonator using the Transfer Function method (Section 4.3.3).

4.3.12. Acoustic energy absorption tests

The sound absorption coefficient of a range of powder samples was measured using the impedance tube depicted in Section 4.2.10. The test samples were agricultural lime (AL2), ballotini (B710 & B250), ball bearings (BB), black mustard seeds (BMS), fine sand (FS), mustard seeds (MS), small polyethelene (PE1) and large polyethylene (PE2).

The experiments were conducted on two sample bed thicknesses of ~42 mm and ~70 mm. The sample under study was poured into the sample holder using a funnel with a discharge diameter of 10 mm from 30 mm above the sample holder to overflow. The material surface was flattened using a metal ruler. The sample holder was gently placed into the impedance tube, and the three locking clamps around the impedance tube were gently locked to fix the sample holder. The Impedance Tube set on Low-Frequency mode (<2250 Hz) measured the sound absorption coefficient.

4.3.13. Compression uniformity test

This experiment examined the uniformity of air pressure distribution inside the resonator cavity when filled with powders and subjected to resonance.

The classical Helmholtz Resonance model assumes an almost uniform compression within the cavity of a Helmholtz Resonator at resonance when the cavity dimensions are much smaller than the resonance wavelength. This assumption was tested by measuring the signal phase of microphones that sampled pressure fluctuations from the top and bottom sections of the cavity of the 2-litre resonator, which had a 1000 mm port attached. This setup was also used for static volume determination tests on powder samples.

The test materials agricultural lime (AL1), fine sand (FS), Small polyethylene (PE1), large polyethylene (PE2), black mustard seeds (BMS), ballotini (B250 & B710) and mustard seeds (MS) were added to the resonator in increments of 250 ml increments for each test with the last load filling the resonator to the top. The perforated plate was used to form loose sample packing in each load. The resonance frequency was hunted using the Transfer Function Method (Section 4.3.3). The resonator was driven at the measured resonance frequency, and the phase mismatch between the pressure waves at the bottom and the top of the resonator was recorded. The phase match was the pressure phase delay between the cavity top and bottom (Figure 4-20).

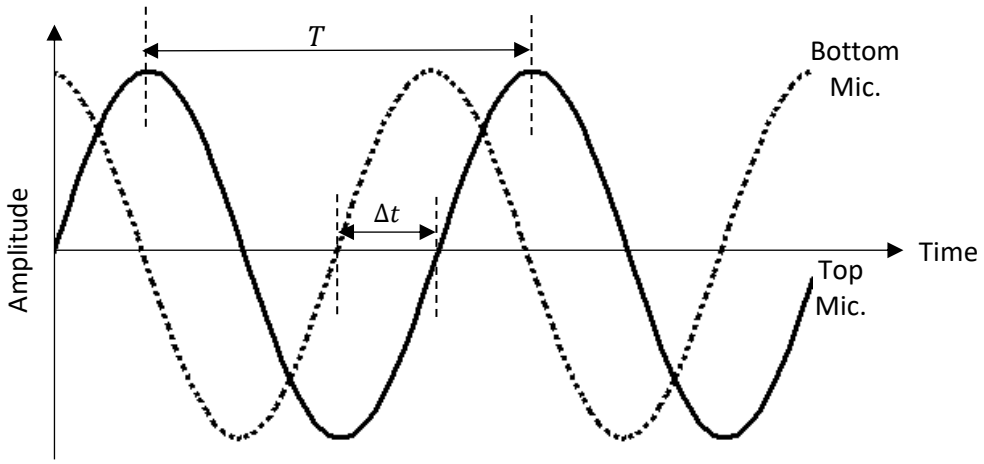


Figure 4-20: *Phase Mismatch between the top and bottom microphone as an indicator of compression non-uniformity.*

The pressure phase mismatch was calculated by measuring the zero-crossing time difference Δt of the signals and using Equation 4-33 (Figure 4-20):

$$\varphi_0 = 360\frac{\Delta t}{T} \qquad 4\text{-}33$$

where φ_0 is phase mismatch at resonance in degrees, and T is the period.

4.3.14. Sound wave penetration speed

When sound propagates in the filling fluid of a powder, it follows a tortuous path. Porous air-saturated media slows sound propagation due to the material's tortuous path elongation (Allard & Atalla, 2009; Okudaira et al., 1993; Sadouki, 2018).

An experiment was designed to measure the effect of sound propagation path elongation in powder samples on slowing down a propagating sound wave. The results in this section complement the Compression Uniformity Tests (Section 4.3.13) and are implemented to interpret the data collected from the compression uniformity tests.

Figure 4-21 shows the experimental apparatus for these tests. The 3-litre resonator was modified at the top and bottom. At the top, the port was removed, and the speaker box from the impedance tube (Section 4-2-10) was directly placed over the 50 mm opening of the resonator. The speaker generated a 150 Hz monotone burst for a duration of 0.1 s. At the bottom, three layers of melt-blown (Extracted from the surgical mask) were used to seal the microphone at the bottom of the resonator from samples through a 12 mm air gap.

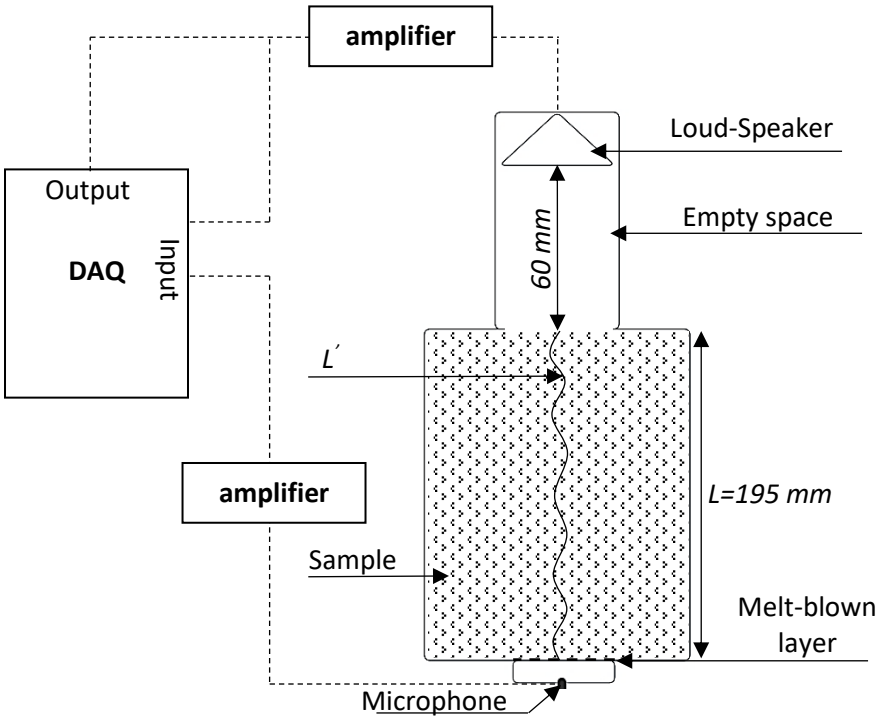


Figure 4-21: *Sound velocity measurement apparatus.*

The loudspeaker output was fed back into the DAQ card input. The signal from this channel was recorded simultaneously with the signal from the microphone. The time of flight for the acoustic sound from the speaker to the microphone at the bottom was measured when the cavity was empty by comparing the time markers for the rising edges of the two signals and recording it as Δt_1. This procedure was repeated when the cavity was filled with samples, recording the time as Δt_2. The increase in time of flight (ΔTOF) due to the presence of the samples was calculated as follows:

$$\Delta TOF = (\Delta t_2 + \Delta t_0) - (\Delta t_1 + \Delta t_0) \quad \textit{4-34}$$

where Δt_0 is the sum of the delay time from signal generation to the loud-speaker acoustical response, the time of flight in the speaker box void, the time of flight in the 12 mm void in the microphone chamber at the bottom of the resonator and the delay from the phase mismatch between the microphone and the loud-speaker channels.

The total time of flight TOF and the tortuous sound wave travel path (L') was calculated using Equations 4-35 and 4-36:

$$TOF = \frac{L}{c} + \Delta TOF \quad \textit{4-35}$$

$$L' = c \times TOF \quad \textit{4-36}$$

The estimated tortuosity (α_0) and the sound wave penetration speed (v) was calculated using Equation 4-37 and Equation 4-38:

$$\alpha_0 = \frac{L'}{L} \quad \textit{4-37}$$

$$v = \frac{L}{TOF} \quad \textit{4-38}$$

4.4. Results

4.4.1. Resonant frequency hunting in the 50-litre vessel

Figure 4-22 demonstrates the resonance frequency and sound pressure change in the discharge of agricultural lime through the 26 mm orifice. Resonance was detectable throughout most of the discharge process. At the beginning of the discharge, 44% of the vessel volume was filled with material. At the end of the discharge, 12% of the resonator was still filled with agricultural lime and could not be discharged due to getting piled up around the discharge orifice on its angle of repose.

As shown in Figure 4-22, the sound pressure at resonance and the trend of frequency change during discharge can be divided into three regions that best describe the results. For region (a), before the material level reached the bottom of the vessel, the agricultural lime bed kept acoustic energy from leaking from the vessel discharge at the bottom, and they blocked the bottom orifice until the empty volume of the system was roughly 38 litres. In region (b), the system responded to the excitation as a Helmholtz Resonator with a variable volume chamber.

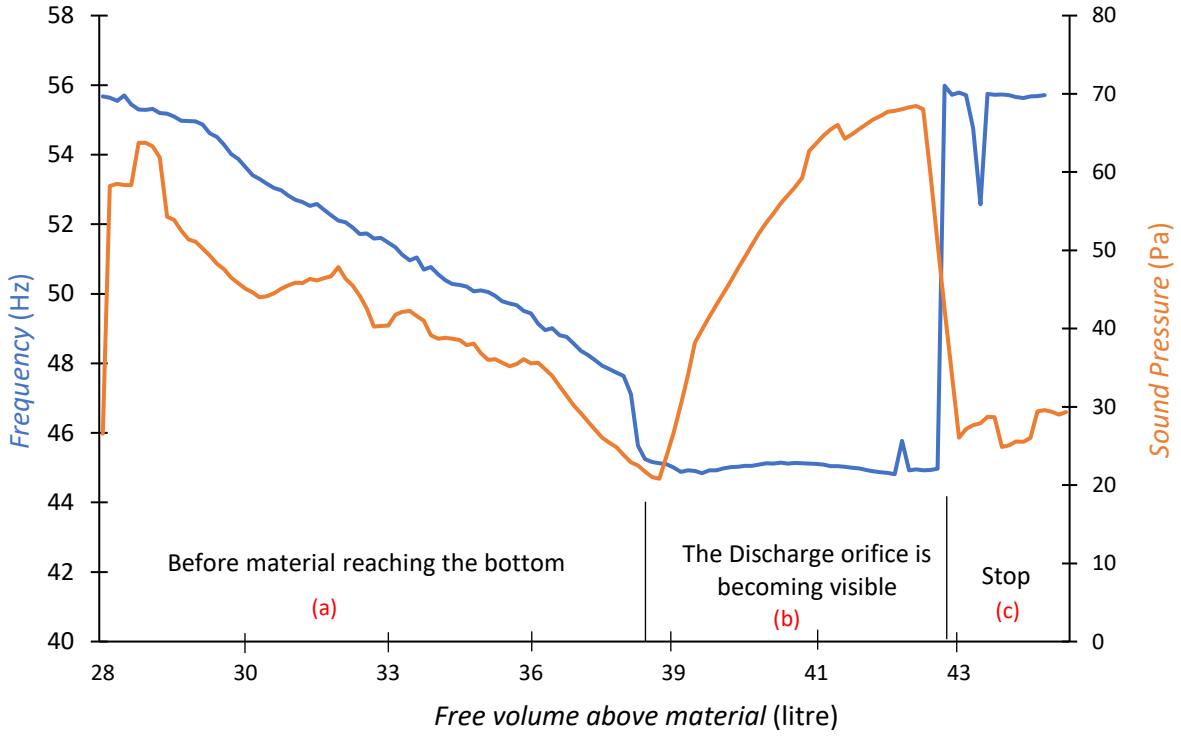


Figure 4-22: *Resonance frequency and the sound pressure change of the 50-litre vessel. The sample under discharge is agricultural lime (AL1).*

The discharge orifice started to uncover from the material as the free volume increased to region (b), and the particles still flowed through it. In region (b), the bottom orifice gradually became visible inside the vessel. The dominant frequency was about 45 Hz, nearly unchanged up to 42 litres of empty

volume. It is while the chamber volume was changing. Opening the second port at the bottom caused an acoustic energy leak from the system and lowered the resonance quality, recording two separate peaks in power spectral density analysis. The first one was around 45 Hz, and the second resonance peak was roughly at 55 Hz, which was almost constant in frequency, but its amplitude was increasing (not shown in the figure) and dominated the 45 Hz peak when the vessel's empty volume entered region (c). In region (c), sound pressure gradually increased as the system became a dual port resonator with a resonance frequency of 55 Hz. The third region, "Stop", is where the discharge almost stopped, and the discharge orifice was fairly open. Here, the resonance peak at 45 Hz disappeared.

As shown in Figure 4-23, plotting resonance frequency f versus the free volume to the power of negative two V_E^{-2} provided a line fit to correlate resonance frequency to the free volume of the resonator. This line fit, shown in Figure 4-23 as an example, can be used to correlate volume to resonance frequency statistically in different resonators and test materials.

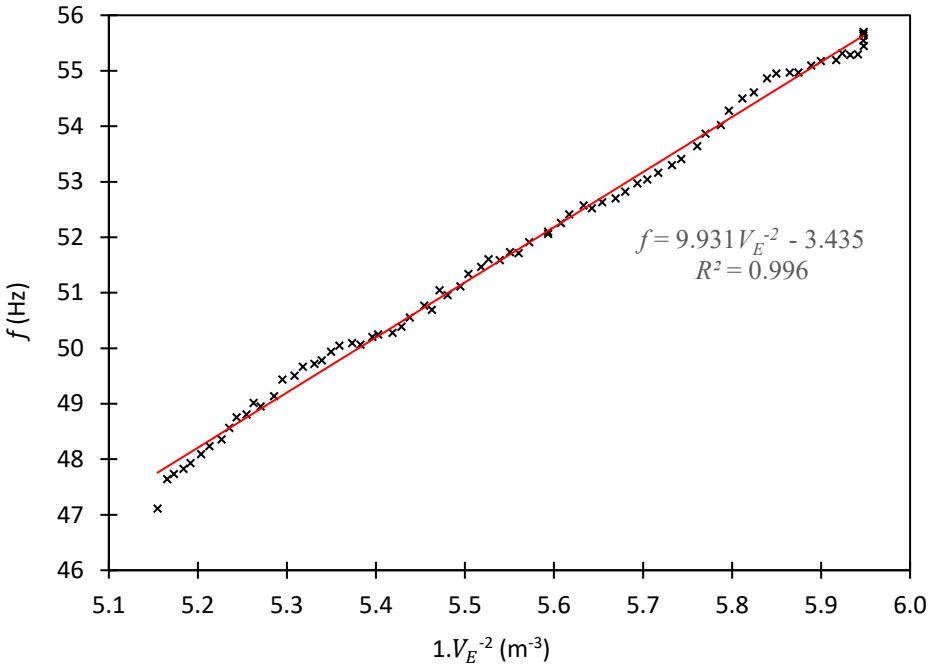


Figure 4-23: *Linear fit of resonant frequency versus* $1.V_E^{-2}$.

The line fit in Figures 4-23 was used to estimate the fill volume of the 50-litre vessel for a second discharge run. The resonance frequency was used to estimate fill volume using the line fit. The results are plotted in Figure 4-24. The maximum deviation between the actual volume and the acoustically estimated volume was 1.2 litre, which was ±1.5%V_0 (±1.5% of the vessel capacity).

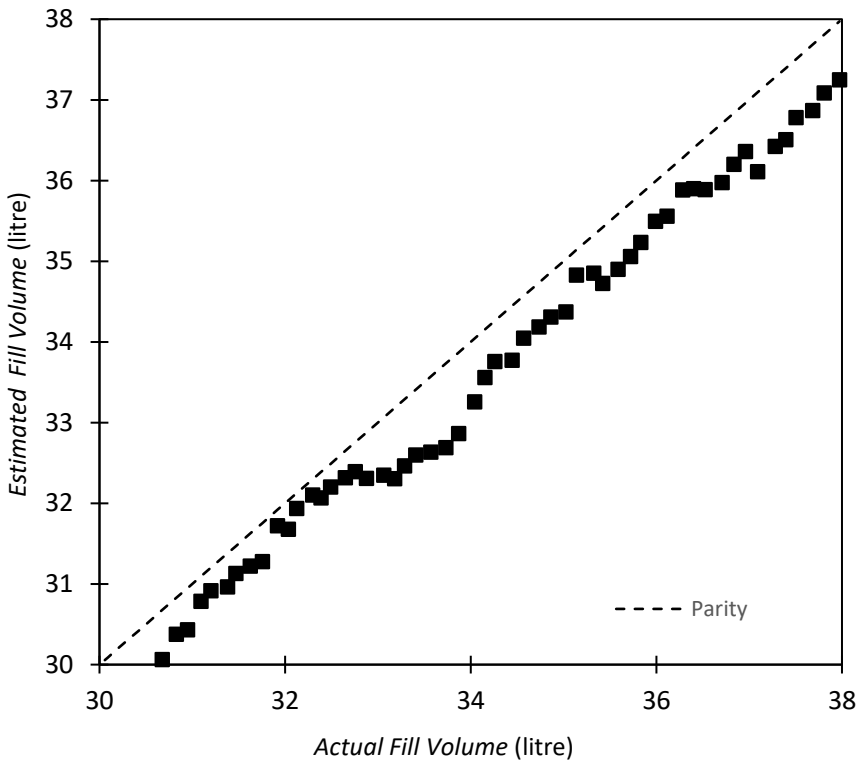


***Figure 4-24**: Acoustically measured fill volume of the 50-litre vessel while discharging agricultural lime. The dashed line is parity.*

Figure 4-25 demonstrates the dynamic discharge test results for mustard. Four regions are marked in the graph. As the particle size diameter of the mustard seeds is large enough for the sound wave to penetrate to the bottom of the material, a sudden drop in the sound pressure was detected as soon as the tape covering the orifice was removed. The detected dominant peak in power spectral measurements remained relatively constant throughout the discharge process until the hopper empty volume decreased to 47 litres, with the resonance frequency jumping to 56 Hz. At this point onward, region (d), there is no further material discharge, and the system is resonating as a double port Helmholtz Resonator. However, the quality factor is not as high in similar conditions for the agricultural lime as the free volume in the porous bulk of mustard seeds damped resonance. In other words, the bulk of mustard particles acts as a muffler. In region (b), the resonance frequency is nearly constant, and the sound pressure gradually increases as the material is discharged.

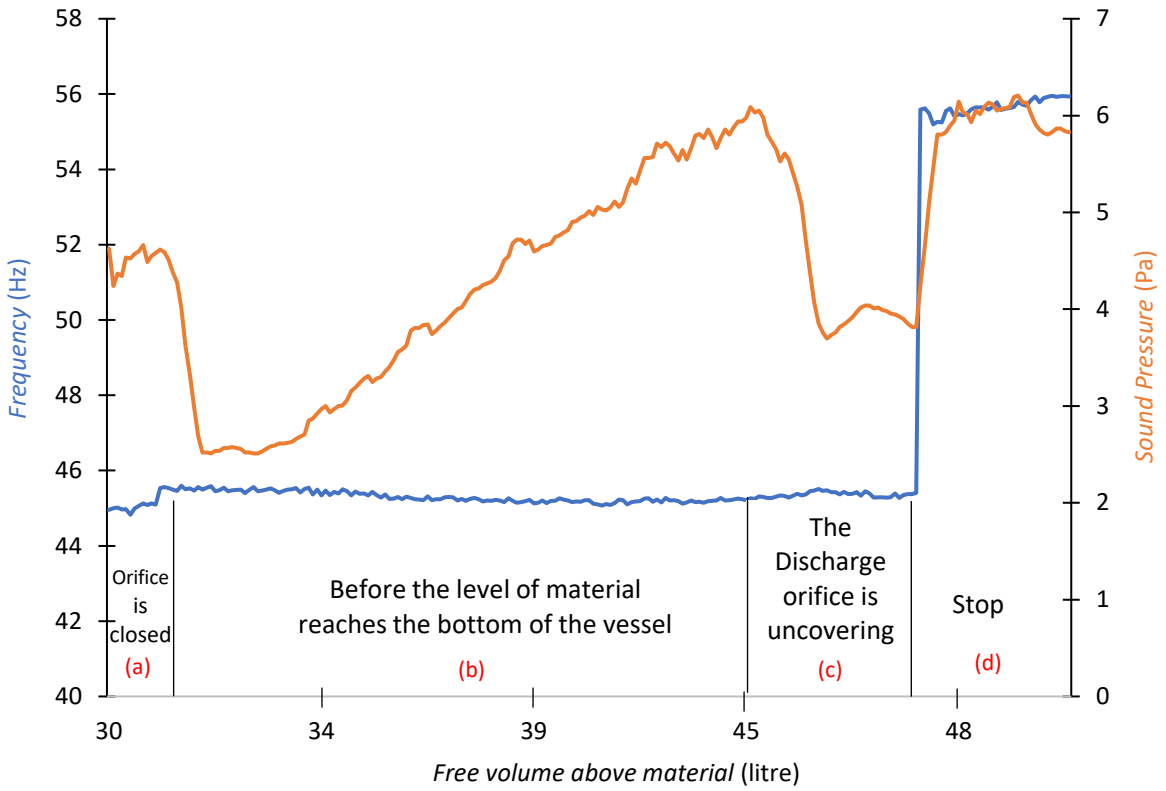


***Figure 4-25**: Resonance frequency and sound pressure tracking of mustard seeds discharged from the 50-litre vessel.*

As mentioned in Section 4.3.4, the resonance frequency for the tests on the 50-litre resonator is measured using the Undriven Method (Section 4.3.1). The method failed to track the resonance frequency of the vessel while discharging a sample of mustard seeds. The observed power peak was at ~45 Hz throughout the discharge. Considering that the empty volume of the system was changing, the constant recorded frequency was not associated with the Helmholtz Resonance frequency of the system. The Undriven resonance frequency hunting method failed to track resonance frequency as the empty volume changed. The control software generated chirps around 43 Hz, the detected peak in the spectral analysis of the resonator response, and a new location for resonance was not observed. The response sound amplitude to the steady excitation centred at 43 Hz consistently changed with system volume, as shown in region (b) of Figure 4-25. This observation was highly significant for this study and triggered the development of a model for sample volume estimation from sound pressure level, as provided in Chapter 7.

4.4.2. Resonant frequency detection in the topdressing hopper

Figures 4-26 shows the dynamic discharge test result for agricultural lime from the topdressing Hopper. The resonance frequency was detectable and gradually increased with empty volume until the hopper was almost three-quarters empty. The discharge gate became visible inside the hopper at a free volume of around 1,600 litres. The detectable resonance frequency fluctuated in this region in the 35-55 Hz range. The resonance frequency trend reverses From the three-quarter empty volume until the discharge cease of agricultural lime. In this region, the secondary port, the discharge gate, was uncovered from the material, but there were flows from the sides of the discharge gate.

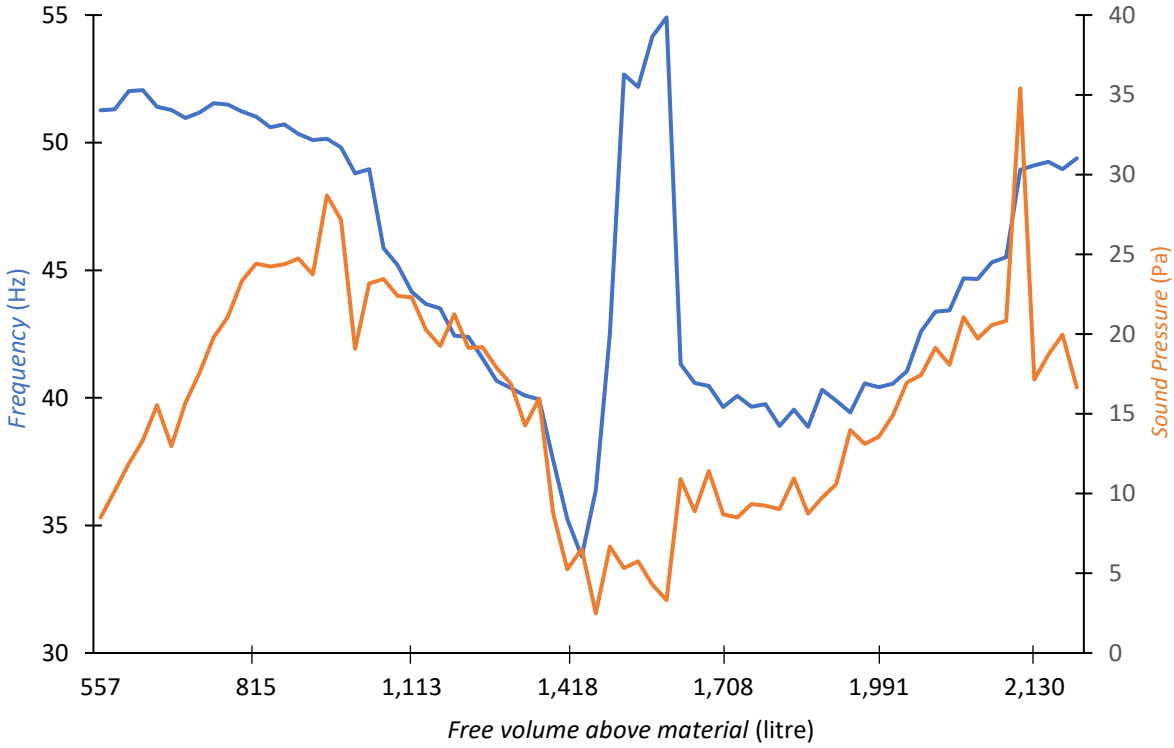


Figure 4-26: *Resonant frequency change of the topdressing aeroplane hopper in dynamic discharge test for agricultural lime.*

Figures 4-27 shows the dynamic discharge test for urea from the topdressing hopper. The resonance frequency was detectable, up to the point that the hopper was nearly three-quarters empty. Fluctuations and the relatively steady resonance frequency in the 700-1,100 litre region made it difficult to associate the resonance frequency with the hopper fill volume. The secondary port became visible as the empty hopper volume approached 1,400 litres. The discharge gate at the bottom of the vessel appeared, and a second resonance peak was detected at ~60 Hz. Similar to the tests on the agricultural lime, where the second port in the form of the discharge gate was introduced to the system, the acoustic response of the hopper started to fluctuate.

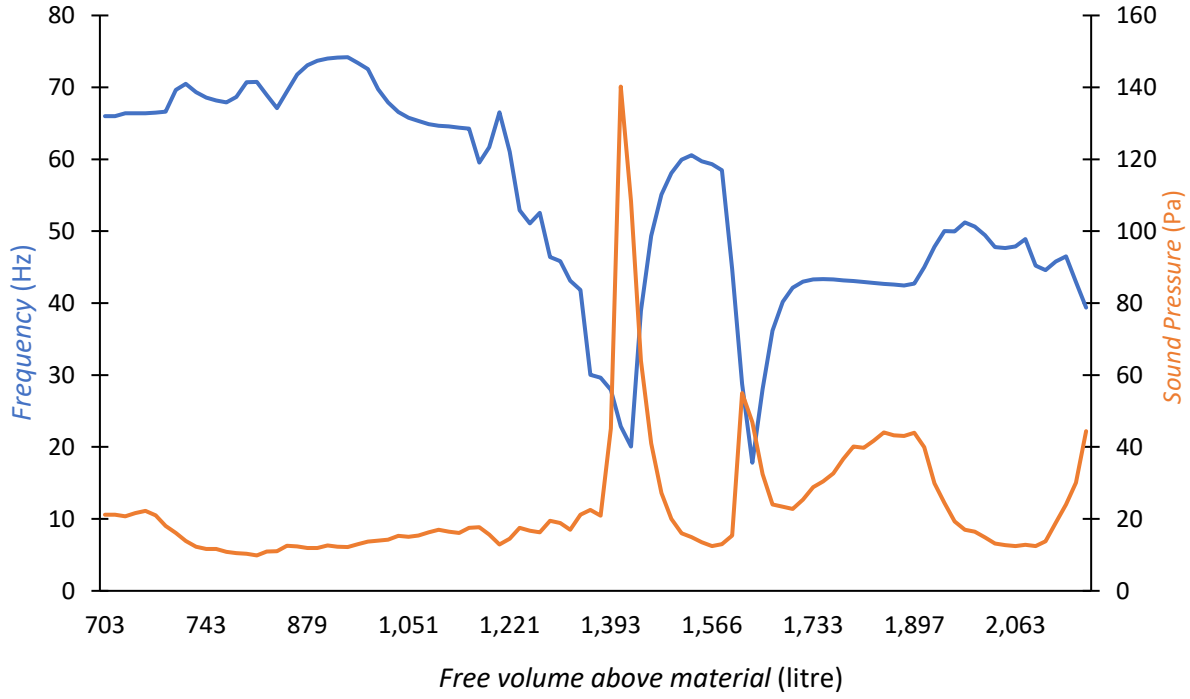


Figure 4-27: *Resonant frequency change of the topdressing aeroplane hopper in dynamic discharge test for urea.*

4.4.3. Testing for non-linearities in the lab-scale resonator

Figure 4-28 plots the water volume measurement results in the 3-litre resonator using Undriven Resonance Frequency Hunting.

The results show a good agreement between volume estimations using Classical Helmholtz Resonance equation and the water volume. As the resonator free volume changed, geometrical non-linearities affected volume measurement accuracy, reducing the port length extension factor Δl when the water level reached the port internal opening. Error *D% (See Error Analysis Equations Section)* from the actual volume is represented in Figure 4-29. As shown in the Figure, a second-order polynomial fits the deviations from actual values for the resonator calibration.

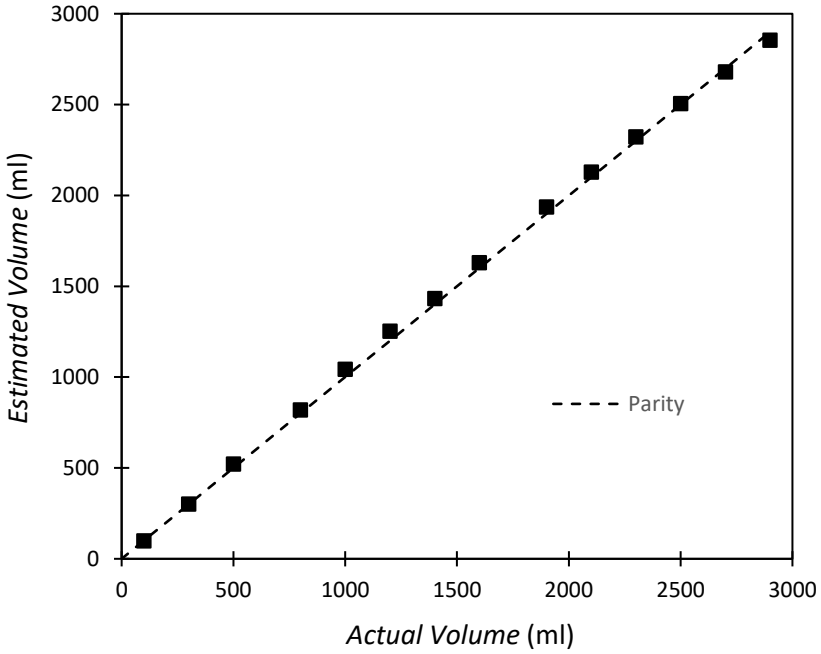


Figure 4-28: *Water volume measurement in the 3-litre resonator using Undriven Resonance Frequency Hunting.*

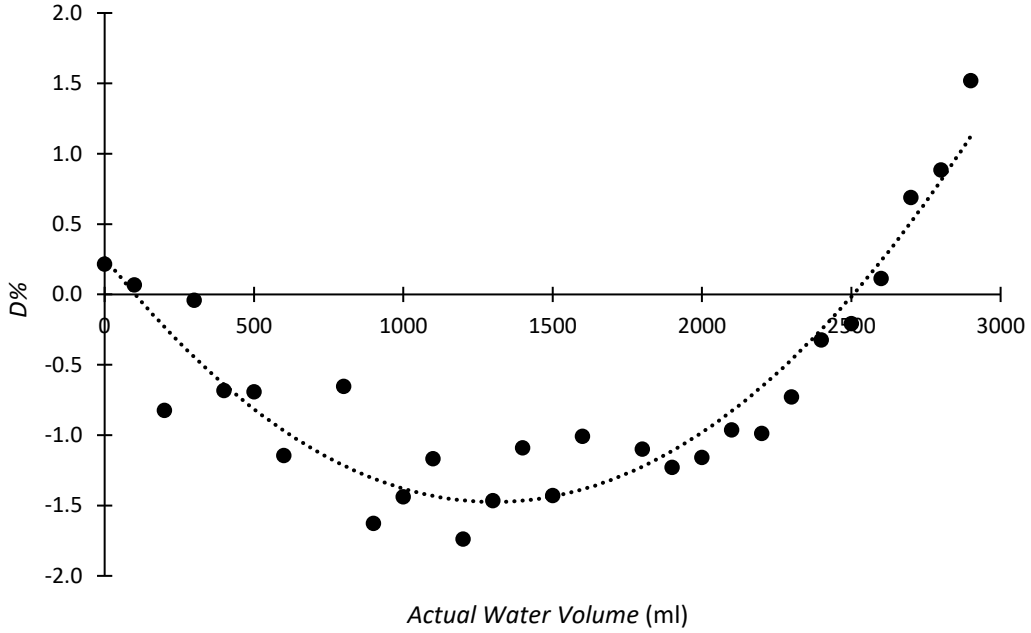


Figure 4-29: *Volume estimation error D% versus fill levels of the three-litre resonator.*

4.4.4. Comparing ports and resonance hunting methods

Resonance frequency response results for different port lengths are presented in Figures 4-30. The abscissa in the charts denotes the Fill Factor (*FF*) or the water level in the resonator cavity. A Fill Factor of 0 denotes the empty state of the resonator, and a Fill Factor of 1 denotes the state in which the resonator cavity is fully occupied with the sample.

All three resonance frequency hunting methods enabled hunting resonance responses throughout the experiments. Results from three different methods of resonance frequency hunting, namely, Undriven, Driven and Transfer Function Methods (TF), agreed with each other with a deviation of less than 1% throughout all Fill Factors for 51, 250, 500 and 1000 mm.

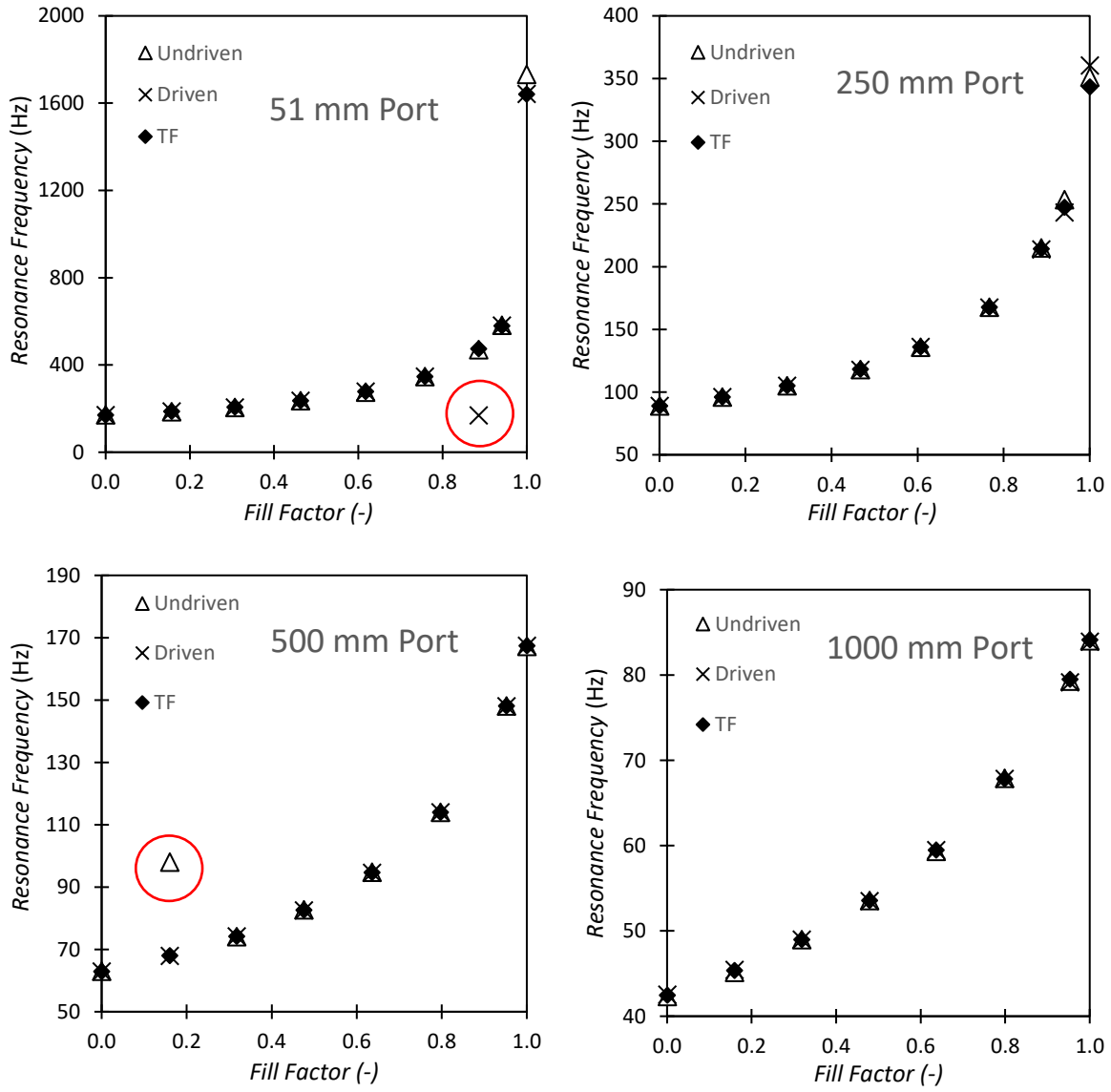


Figure 4-30: *Resonance response of the 2-litre resonator with various port lengths. The resonance frequencies were hunted using Undriver, Driven and Transfer Function (TF) methods.*

Figure 4-30 shows that two outliers, shown using red circles, were recorded for the 51 mm and 500 mm ports. An outlier for the 51 mm Port was recorded at the Fill Factor ~0.9 for the Driven method. The repeated tests in that Fill Factor resulted in recording the same outlier of 169 Hz. This outlier could be due to an external noise on the microphone setup or a nonlinearity in the microphone's frequency response. The other outlier was recorded for the Undriven method in the 500 mm port at Fill Factor of about 0.2. The outlier was 100 Hz, which could be a harmonic of the main hum noise. When hunting for the resonance frequency using the Transfer Function method, no outliers were observed in the repeated tests.

Table 4-3 provides the approximate frequency response of the 2-litre resonator. The response Resolution was calculated using $Span/V_c$, where *Span* is the resonance frequency range of the resonator, the frequency at *Fill Factor=1* minus the resonance frequency at *Fill Factor=0*. The port length had a negative correlation with the frequency response resolution. The resonator's minimum and maximum resonance frequencies negatively correlated with the resonator port length.

Table 4-3: *Frequency response of the 2-litre resonator.*

Port Length (mm)	Resonance Frequency At Fill Factor = 0 (Hz)	Resonance Frequency At Fill Factor = 1 (Hz)	Span (Hz)	Resolution (Hz/ml)
51	170	1730	1560	0.8
250	89	353	254	0.14
500	62	167	105	0.05
1000	40	82	42	0.02

In Classical Helmholtz Resonance, Equation 1-3 $f = \frac{c}{2\pi}\sqrt{\frac{S_p}{V_c \mathrm{l}}}$, where cavity volume V_c approaches zero, resonance frequency approaches infinity, which contradicts the experimental results. When cavity volume approaches zero, the detected resonance frequency approaches the quarter wavelength resonance of the port. The quarter wavelength resonance frequency f of a port with one side closed, and the other side open to the environment with length l is:

$$f = \frac{c}{4l} \qquad 4\text{-}39$$

The quarter wavelength resonance frequency of the 51, 250, 500 and 1000 mm ports at room temperature was ~1681 Hz, ~343 Hz, ~171 Hz and ~85 Hz, respectively, which are in agreement with

the recorded resonance frequencies for all ports using all three resonance hunting methods when the Fill Factor was 1.

The results of water volume estimation using the classical Helmholtz Resonance model are presented in Figure 4-31.

As shown in Figure 4-31 (a), using the 51 mm port, volume estimation results from all three resonance hunting methods of resonance frequency hunting were highly linear (R^2>0.99). The volume estimation error was maximised at the Fill Factor of 0.94, where the sample volume was underestimated for 48 ml, an error of *D%*=2.

As shown in Figure 4-31 (b), water volume estimation using the 250 mm port resulted in the same agreement between different hunting methods as for the 51 mm port. The trends were highly linear. However, the estimated volume values were slightly lower than the actual values. This deviation increased with higher Fill Factors, reaching a maximum of about 130 ml underprediction at a Fill Factor of 0.94, equivalent to an error *D%* of almost 7.

Doubling the port length almost doubled the maximum absolute deviation, as shown in Figure 4-31 (c). In the case of the 500 mm port, despite having a high agreement between the different resonance frequency hunting methods, the results were offset. A linear offset of the estimated volume from the actual volume with a slope of 0.89 was recorded for the 500 mm port. This slope resulted in a maximum error *D%* of 14 when the Fill Factor approached 1.

By inspecting Figure 4-31 (d), which presents data for the 1000 mm port, it is evident that doubling the port length from 500 mm to 1000 mm increased the maximum error, *D%*, to 25, a large error from parity. Similar to the results with other ports, various resonance frequency hunting methods yielded roughly identical results for the 1000 mm port.

The high deviation margins for the more extended ports, especially for the 500 mm and 1000 mm ports, can be explained; As mentioned in Section 4.1.1, the scope of availability for the classical Helmholtz Resonance model is the region where the resonator dimensions are marginally smaller than the resonance wavelength. Therefore, ports longer than 250 mm result in sample volume estimations with a deviation from the actual volumes.

For all the ports, the highest linearity as an indicator of measurement precision was obtained using the Transfer Function method with R^2 = 0.999. This linearity is obtained with the sacrifice of measurement speed. The total time for one volume measurement using the undriven method was 0.7 s, while this figure was 5 and 10 seconds for the Driven and Transfer Function methods, respectively.

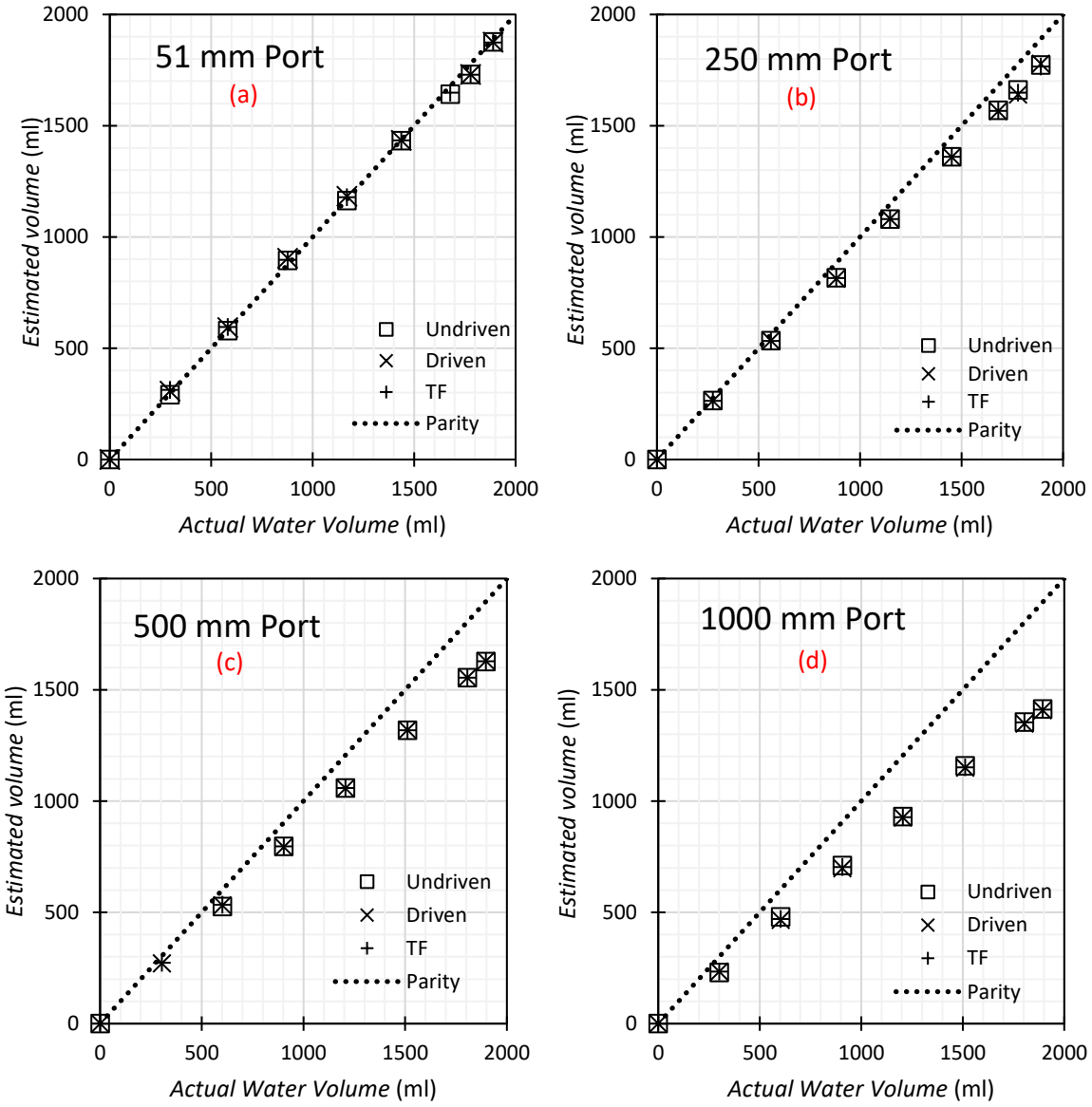


Figure 4-31: *Water volume estimation using Classical Helmholtz Resonance model in the 2-litre resonator with 51, 250, 500 and 1000 mm ports. Volumes were estimated from three different resonance frequency hunting methods.*

Figure 4-32 demonstrates the error *D%* of the estimated Fill Factor using Classical Helmholtz Resonance model from the actual Fill Factor based on cavity volume, which was calculated by dividing the volume deviation by the empty cavity volume of the resonator. Negative numbers are associated with over-estimation of the sample volume and vice versa. The resonance frequencies for volume measurement error analysis in Figure 4-33 were detected using the Transfer Function method. This figure shows that the error *D%* in water volume estimation increases with port length. For the 250, 500 and 1000 mm ports, *D%* increases with the Fill Factor.

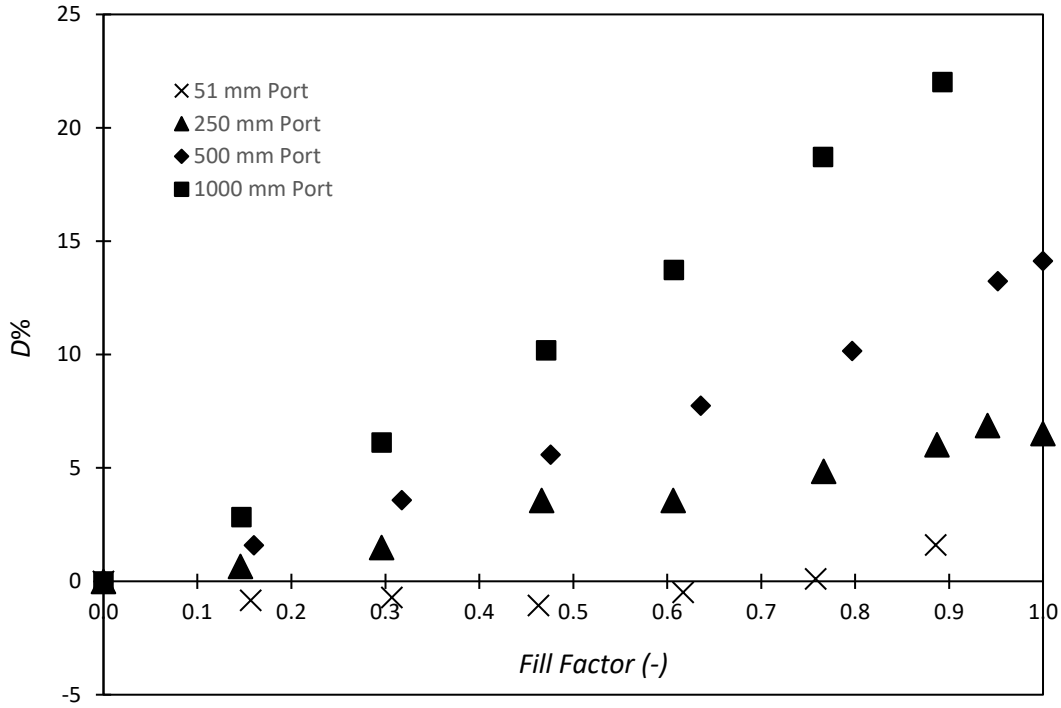


Figure 4-32: *Error D% of water sample volume estimation in the 2-litre Helmholtz Resonator with various port lengths.*

The resonance wavelength λ and volume V_c can be correlated using Equation 4-40, which is the classical Helmholtz Resonance model algebratically manipulated by combining with $c = \lambda f$ (See Basic Equations).

$$\lambda^2 = \frac{1}{\alpha^2} V_c \qquad \textit{4-40}$$

Equation 4-40 establishes a linear relationship between cavity empty volume and square of resonance wavelength. It also estimates a zero resonance wavelength when cavity volume approaches zero. As the resonator port length scales up, it exceeds the scope of Classical Helmholtz Resonance model and results in a resonance wavelength offset from the estimated resonance wavelength. The comparison between the estimated λ^2 and the experimentally obtained values are demonstrated in Figure 4-33.

As shown in Figure 4-33, the experimental values of λ^2 for the 51 mm port agree with the estimated values from the model. For longer ports, experimental and estimated values are roughly equal in slope but demonstrate a constant offset of each other. This offset value was equal to the Y-intercept of the experimental values and was roughly 0.04, 1, 4 and 16 m^2 for the 51, 250, 500 and 1000 mm ports. This observation is further explained in the next chapter to validate a new model for Helmholtz Resonance of resonators with long ports.

As the resonator Fill Factor increased, the magnitude of the resonance amplitude relative to the excitation amplitude in resonance frequency slightly fluctuated.

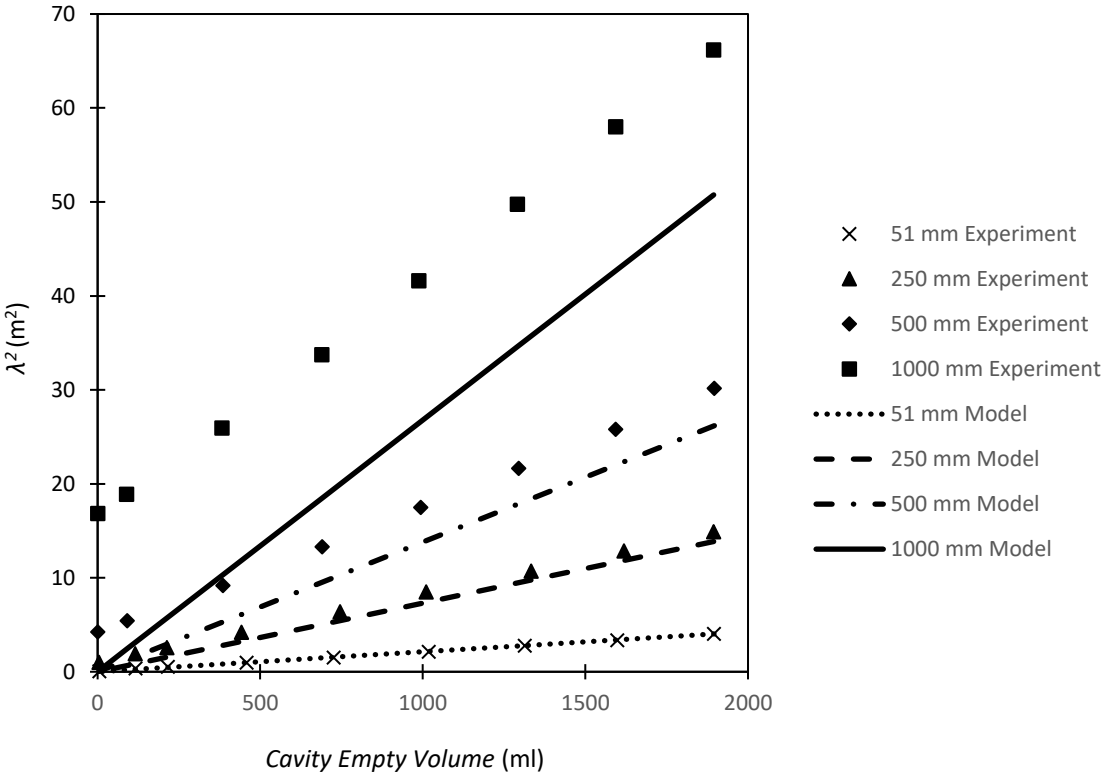


Figure 4-33: *Resonance Wavelength squared vs. cavity empty volume for various port lengths. "Model" refers to the estimated values using the classical Helmholtz Resonance Model.*

The magnitude of the Transfer Function $|H(f)|$, as defined in Section 4.3.3, a parameter in Equation 4-26, for different fill levels is presented in Figure 4-34. The data on Transfer Function magnitude in this figure indicate the system's resonance response strength at various Fill Factors.

Practically, a Transfer Function magnitude of *X* at resonance frequency *F* signifies that at frequency *F*, the sound amplitude sampled by the microphone at the root of the resonator's port was *X* times the amplitude sampled from the microphone in front of the loudspeaker.

Figure 4-34 shows that the transfer function magnitude at resonance peaks for 51, 250, 500 and 1000 mm long ports, despite fluctuations, had an average value of 3.6. No positive or negative trend was found for any tested ports. In other words, the transfer function magnitude at resonance was roughly constant and did not show a trend with port length or resonator fill factor.

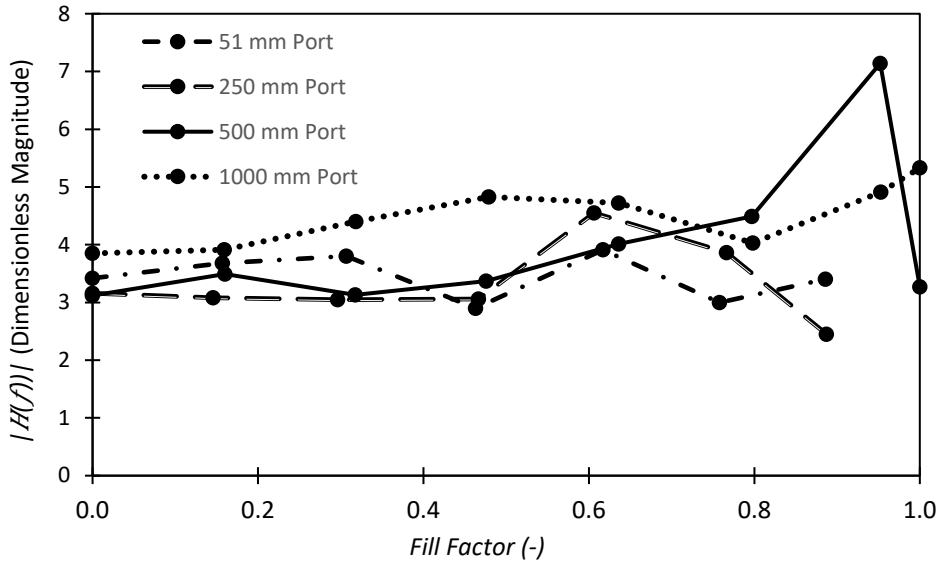


Figure 4-34: *Transfer Function magnitude change versus resonator fill factor with different ports under study.*

4.4.5. Static volume measurement tests on particles

The detailed resonance frequency hunting for various samples in the 2-litre resonator with various port lengths of 51, 250 and 1000 mm are presented in this section.

Figure 4-35 compares different resonance frequency hunting methods in all ports on the large marble sample. The experiments on the sample small marbles (SMB), not shown here, had similar results regarding the agreement of different resonance hunting methods.

By inspecting Figure 4-35, it is evident that all three resonance frequency hunting methods maintained an agreement of less than 1%. The same agreement between different methods for resonance hunting was observed for water (not shown here). The resonance frequencies were detected regardless of the fill factor of the resonator. The frequency variation range was 60, 30 and 10 Hz for 51, 250 and 1000 mm ports. Shorter ports demonstrate higher sensitivity to chamber volume change regarding resonance frequency response resolution.

As shown in Figure 4-35, resonance frequency increased roughly linearly with sample volume inside the resonator.

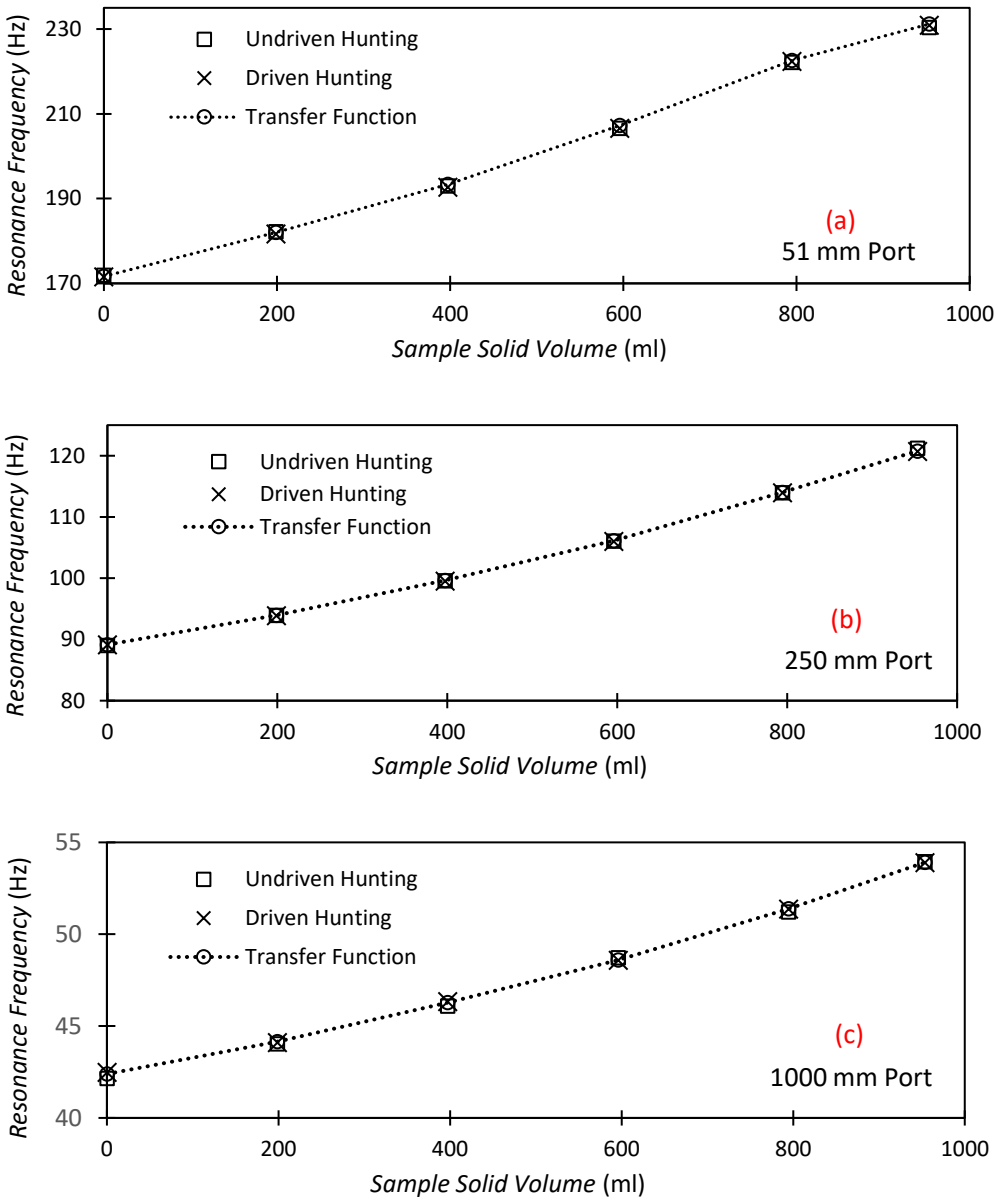


***Figure 4-35**: Resonance Frequency hunted for large marble Sample (LMB) vs sample volume. Graphs from top to bottom are for 51, 250 and 1000 mm ports.*

Figure 4-36 shows the results of resonance frequency hunting for ball bearings with a mean particle diameter of 3.175 mm. Similar trends and resonance hunting capabilities were observed when conducting experiments on mustard seeds with a mean particle diameter of ~2 mm.

By inspecting Figure 4-36 (a), it is evident that when using the 51 mm port, the undriven method failed to detect resonance frequency for Fill Factors higher than *FF*=0.4 for ball bearings; this was even lower and at *FF*=~0.2 for mustard seeds.

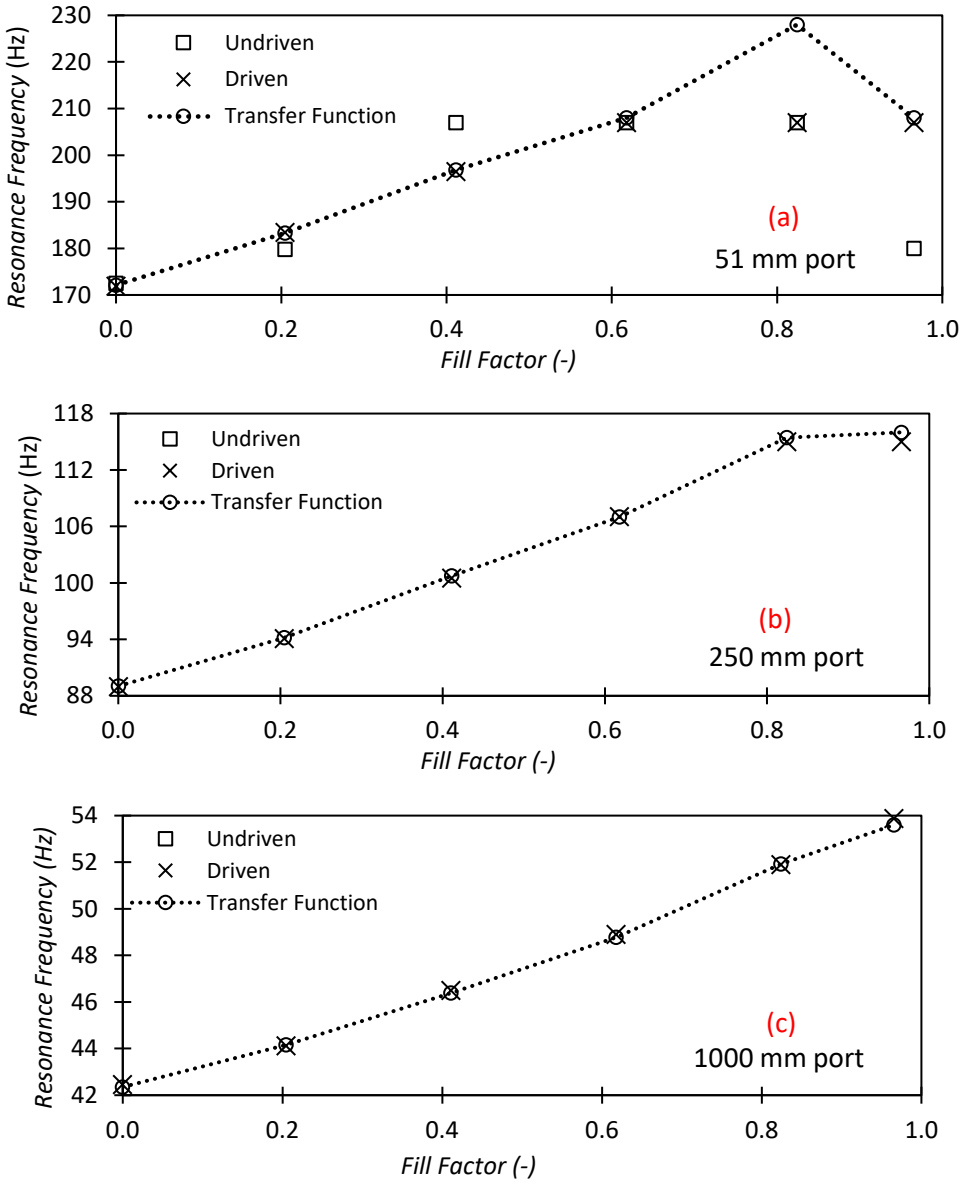


***Figure 4-36**: Resonance Frequency hunted for ball bearings (BB) sample vs Fill Factor. Graphs from top to bottom are for 51, 250 and 1000 mm ports. The Sample is loose-poured.*

Upon inspecting Figure 4-36 (a), it is evident that the Transfer Function method effectively identified the resonance frequency up to Fill Factors of 0.65 and 0.8 for mustard seeds and ball bearings samples, respectively. This demonstrates its higher precision in detecting resonance frequencies when using the 51 mm port compared to other methods.

Upon inspecting Figure 4-36 (b), it is evident that Using the 250 mm port compared to the 51 mm port, the maximum Fill Factor at which resonance frequency was detectable using all methods increased from ~0.6 to ~0.8.

By inspecting Figure 4-36 (c), it can be seen that for the 1000 mm port, resonance frequency was detectable regardless of the Fill Factor, and various resonance hunting methods yielded roughly identical results.

Figure 4-37 plots the volume estimation results using Equation 4-32 for ball bearings (a) and large marbles (b) versus the actual volume. These measurements are conducted using the 51 mm port. As observed in the previous section (Section 4.4.4), the classical Helmholtz Resonance model cannot accurately predict cavity volume when using 250, 500, and 1000 mm ports due to the geometrical limitations of the model's scope. Therefore, this section provides sample volume estimations using the classical Helmholtz Resonance model when only the measurements are conducted using the 51 mm port.

Figure 4-37 (a) shows that the transfer function method enabled resonance frequency hunting at a higher fill factor level compared to the driven and undriven methods. The estimated volumes of the ball bearings sample were slightly underestimated, with a maximum deviation *D%* of 7%. The same volume deviation was observed for the mustard seeds sample when tested using the 51 mm port. The maximum deviation *D%* for mustard seeds was 11% at the highest achievable Fill Factor of 0.65 using the Transfer Function Method. Higher than this Fill Factor, resonance frequency was undetectable.

Comparison of graphs (a) and (b) in Figure 4-37 reveals that when using a short port, volumetry via Helmholtz Resonance is more feasible and practical for larger samples, such as large marbles with a mean particle diameter of 25 mm, compared to smaller samples like ball bearings, which have a mean particle diameter of approximately 3 mm.

The experiments conducted on samples with a mean particle diameter smaller than 15 mm demonstrated that using a short port, such as the 51 mm port, made it difficult to detect the resonance frequency. Furthermore, at higher Fill Factors of the resonator, detection became impossible. The difficulty in resonance frequency hunting of powders supports observations of Webster (2010), who reported the same limitation with the use of the Helmholtz Resonance principle for the volumetry of powders.

Using the Classical Helmholtz Resonance model, the calculated sample volumes demonstrated an underprediction of the actual volume. The observation of the deviation of calculated sample volumes from actual volumes agrees with the results of Inoue et al. (2021). They attributed the observed volume underprediction to the configuration of their resonator, which was a double resonator type with a port placed between two cavities. They assumed that this resonator configuration was the reason for the observed deviations in volume estimation. In contrast to the interpretations made by

Inoue et al., the results of this thesis, where a standard resonator with one cavity is used, suggest that the powder bed causes a deviation in solid volume estimation regardless of the resonator type port length and resonance frequency hunting method.

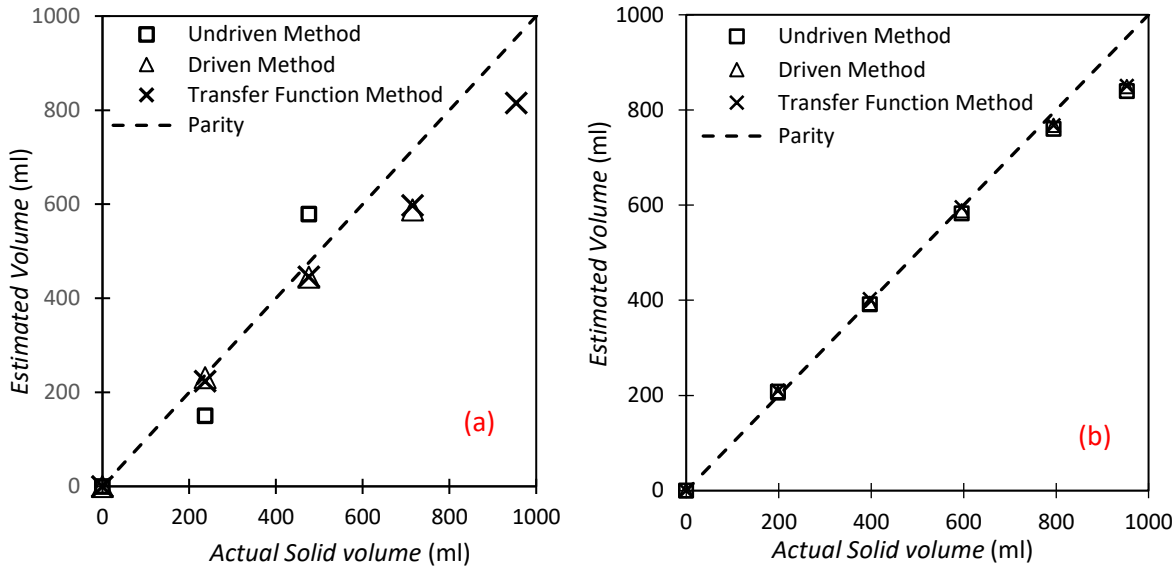


Figure 4-37: *Solid sample volume estimation using the 2-litre resonator with the 51 mm port attached. (a): ball bearings BB, (b): large marbles LMB.*

Figure 4-38 shows the results of resonance frequency hunting using various port lengths when the resonator was filled with the fine ballotini sample (B250), typical for the coarse ballotini sample, regarding the maximum achievable fill factor for different ports. Figure 4-38 demonstrates resonance frequency hunting when the sample inside the resonator has a loose-poured structure.

By inspecting Figure 4-38 (a), it can be seen, similar to observations made for the mustard seeds and ball bearings samples, respectively, the resonance hunting systems had difficulty detecting the system's resonance response for ballotini B250 samples with a mean particle diameter of 0.24 mm. This was particularly the case when the resonator's port was 51 mm long.

As shown in Figure 4-38 (b), when using the 250 mm port, the maximum resonance frequency hunting Fill Factor for both the Undriven and Driven methods was ~0.88. At higher Fill Factors, these methods missed the resonance frequency. In contrast, the Transfer Function method detected the resonance frequency with no limit.

Inspecting Figure 4-38 (c), when using the 1000 mm port, all three resonance frequency hunting methods tracked changes in the resonance frequency with changes in the fill factor. However, at Fill Factors exceeding 0.65, the recorded resonance frequencies in each method were slightly offset.

Specifically, at a Fill Factor of 1, the Undriven, Driven, and Transfer Function methods recorded resonance frequencies of 60 Hz, 56 Hz, and 68 Hz, respectively.

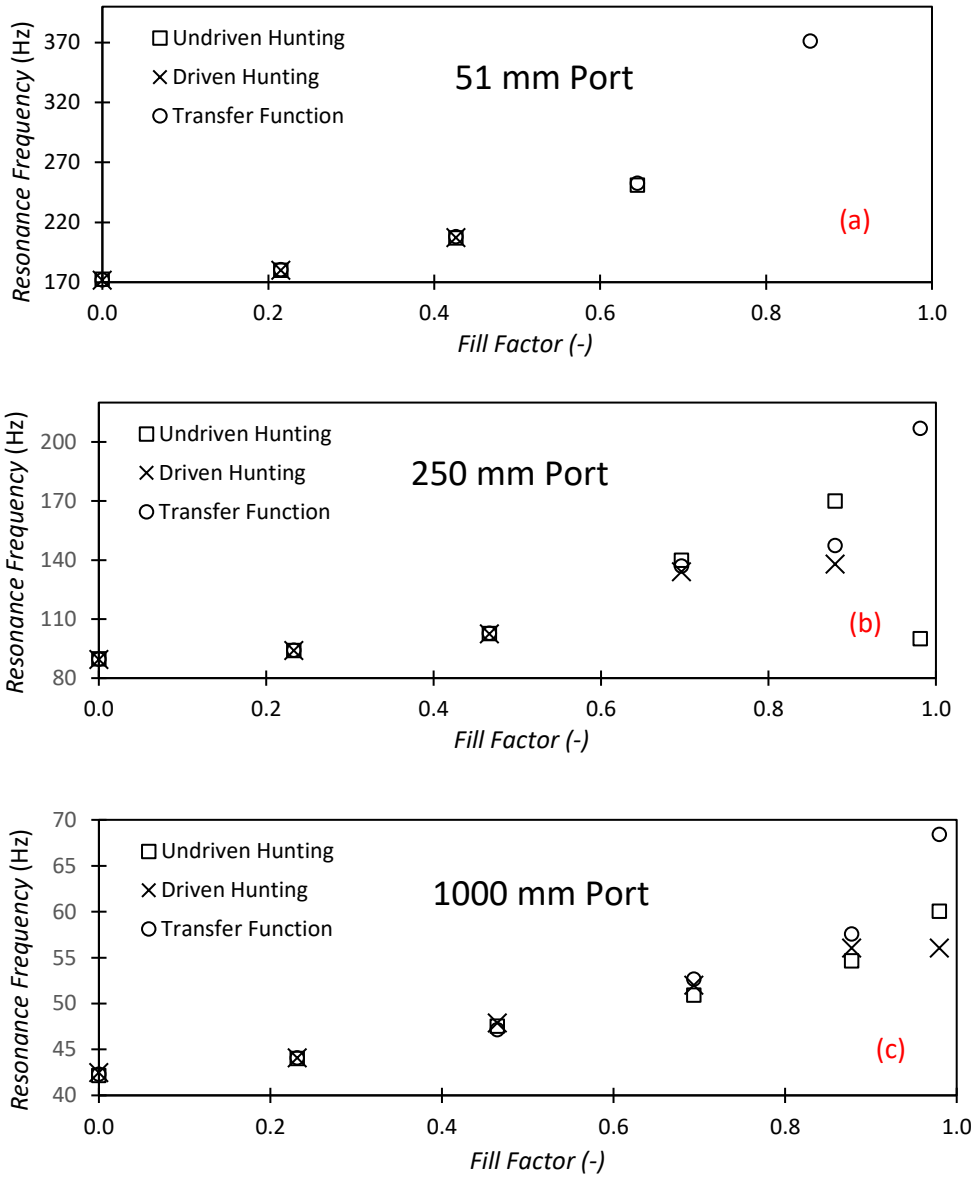


Figure 4-38: *Resonance Frequency hunting for fine ballotini Sample vs Fill Factor. Graphs from top to bottom are for 51, 250 and 1000 mm ports. The Sample is loose-poured.*

For the fine sand (FS) sample (Graph not provided), when using 51 mm, resonance frequency was more straightforward to hunt in terms of finding a distinct resonance peak in the power spectral density graph. It could be due to lower acoustic absorption by the bulk of the fine sand sample due to the very packed and impenetrable structure. The agricultural lime sample exhibited results similar to fine sand regarding ease of resonance frequency hunting in the 51 mm Port, where resonance frequency was recorded up to a fill factor of 0.8 for undriven and transfer function methods.

The resonance-damping effect of powders

An experiment was conducted to investigate the effect of sample volume on resonance quality dampening when using the 51 mm port. In this experiment, a detailed scan of the recorded sound amplitude for a range of frequencies was conducted. Mustard seeds were added layer by layer, and the mass was recorded. The bed packing was loosened using the perforated plate method described in section 4.3.8. The results are plotted in Figure 4-39. The resonator response to the excitation tone falls short of a detectable amplitude at Fill Factor 0.54 and higher. From this Fill Factor, the response to the range of frequencies from 145 Hz to 160 Hz was almost flat, with three maxima with almost equal amplitudes. This Figure demonstrates the dampening effect of powders on resonance response due to sound absorption. The Fill Factor of 0.45 was the Maximum Fill Factor at which resonance frequency hunting was possible.

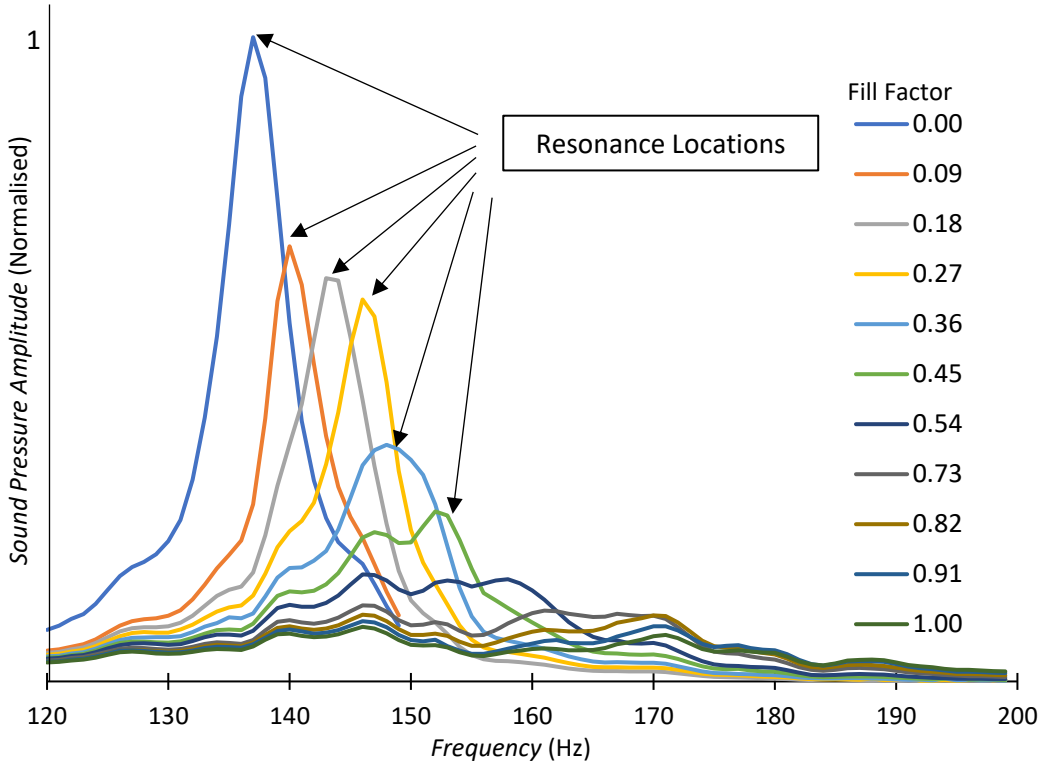


***Figure 4-39**: Resonance amplitude decay versus resonator Fill Factor. The mustard seeds sample was loosely poured into the 3-litre resonator with a 51 mm port.*

Table 4-4 provides the maximum Fill Factors at which resonance frequency was detectable (Maximum Fill Factor) for various samples and port lengths. At Fill Factors greater than those shown in the table, the resonance frequency peak was undetectable due to the flat response of the microphone signal in the frequency domain.

Table 4-4 indicates that the maximum Fill Factor increased with increasing port length. The sample mean diameter also appears to be a governing factor in the resonance frequency hunting capability. For the 1000 mm port, a maximum Fill Factor of 1 was achievable for all the sample tests. Among the three resonance frequency hunting methods, the Transfer Function method detected resonance frequency at higher Fill Factors.

Table 4-4: *Maximum Fill Factor at which resonance frequency was possible to hunt (MFF).*

		***Port Length* (mm)**									
		51			**250**			**1000**			**mean diameter (mm)****
	Hunting Method***	**UM**	**DM**	**TF**	**UM**	**DM**	**TF**	**UM**	**DM**	**TF**	
		Maximum Achievable Fill Factor									
***Sample* (Packing*)**	**AL1 (LP)**	0.8	0.6	0.8	1	0.85	1	1	1	1	**0.06**
	AL1 (T)	0.6	0.6	0.8	0.85	0.85	0.85	1	1	1	
	FS (LP)	1	0.6	1	0.85	1	1	1	1	1	**0.11**
	FS (T)	1	0.6	1	0.85	0.85	0.85	1	1	1	
	B250 (LP)	0.65	0.43	0.85	0.7	0.7	0.9	0.8	0.9	1	**0.24**
	B250 (T)	0.19	0.19	0.19	0.67	0.67	0.84	0.8	0.9	1	
	B710 (LP)	0.22	0.42	0.42	0.59	0.59	0.6	1	1	1	**0.67**
	B710 (T)	0.21	0.4	0.58	0.57	0.57	0.57	1	1	1	
	MS (LP)	0.43	0.65	0.65	0.83	0.83	83	1	1	1	**1.98**
	MS (T)	0.24	0.4	0.58	0.57	0.57	0.57	1	1	1	
	BB	0.2	0.41	0.41	0.82	0.82	0.8	1	1	1	**3.175**
	SMB	0.9	0.9	0.9	1	1	1	1	1	1	**15.97**
	LMB	1	1	1	1	1	1	1	1	1	**24.76**

* (LP): Loose Poured Packing, (T): Tapped Packing ** D[3,2] diameter for powders. UM: Undriven Method, DM: Driven Method***, TF: Transfer function Method. AL1: agricultural lime, FS: fine Sand, B250 & B710: ballotini, MS: Mustard seeds, BB: ball bearings, SMB & LMB: marbles

The observation of ease of resonance frequency hunting using the very long port (1000 mm) when the resonator was filled with powders could have two possible explanations. The long port provides resonance with a higher-quality factor, or the long port lowers the range of resonator resonance frequency to a range that powders tend to absorb less acoustic energy. These two hypotheses were examined through experimentation and discussed later in this chapter.

Effect of packing

Bed packing, loose poured (LP) or tapped (T), slightly shifted resonance frequency. Figure 4-40 demonstrates resonance location regarding wavelength squared for fine sand (FS), ballotini (B250) and mustard seeds (MS). The resonance frequencies in Figure 4-40 are detected using the Transfer Function method.

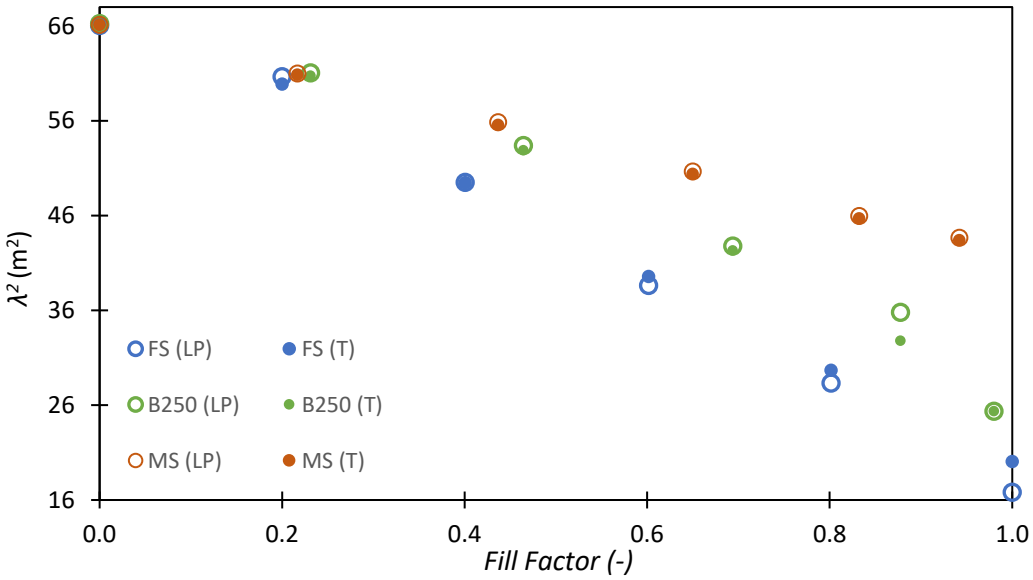


Figure 4-40: *Effect of bed packing on resonance shift.*

The tapped beds had lower resonance wavelengths or higher resonance frequencies for open pore samples, including mustard seeds and ballotini. For fine sand (FS) with very fine pores, tapping caused a decrease in resonance wavelength up to Fill Factor ~0.4, and the trend reversed up to Fill Factor 1. More packing lowered the occupied space of the cavity; the higher empty cavity volume in the resonator manifested into a higher resonance wavelength, as is the case for fine sand from Fill Factor 0.4 onwards. This observation of dual behaviour in terms of resonance frequency shift based on bed packing prompted an experiment to investigate acoustic pressure transmission loss in the bed of particles.

Acoustic Pressure Transmission Loss

Two samples, namely ball bearings, an open-pore sample with large particles, and fine Sand, a closed-packed sample with very fine particles, were tested for transmission loss. The samples had loose pour packing. The resonance frequency and amplitude were recorded from both the top and bottom of the bed of samples in the resonator.

When the resonator was empty, the resonance frequencies from the top and bottom of the resonator cavity were almost equal (within ±0.01 Hz of each other). The bed of samples caused a slight deviation in resonance frequencies recorded from the top and bottom. This deviation was negligible in the ball bearings (a) bed compared to fine sand (b), as shown in Figure 4-41.

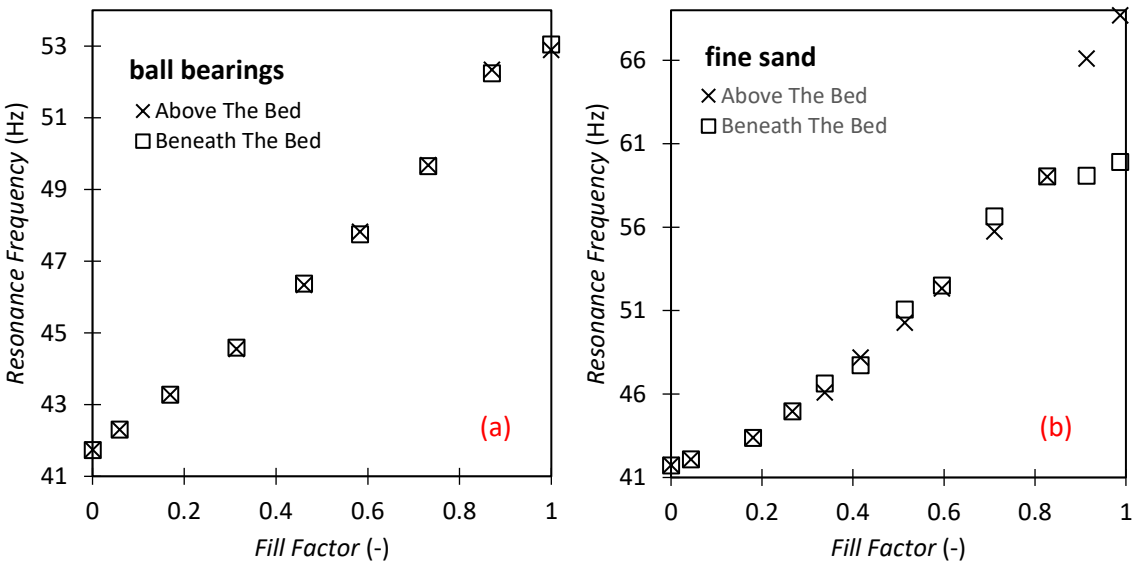


Figure 4-41: *Comparison of resonance frequencies hunted using the Driven method from above and beneath the ball bearings bed (a) and fine sand bed (b).*

In Figures 4-42, the ordinate of the graphs is the resonance amplitude for various fill factors divided by the resonance amplitude of the empty resonator. Inspecting Figure 4-42 it can be seen that increasing a resonator fill factor results in a drop in resonance amplitude.

As shown in Figure 4-42 (b), the investigation of Transmission Loss through the bed of fine sand revealed that resonance amplitude dropped more than a thousand folds after a depth of ~20 mm or a Fill Factor of ~0.2.

By Inspecting Figure 4-42, It can be assumed that for fine sand, a sample with fine and packed particles, the acoustic pressure does not reach the bottom of the resonator to bounce back up and contribute to the elasticity of the air inside the resonator. This constitutes a transmission loss, and the bed behaves like a solid. In contrast, the ball bearings sample passed acoustic pressure to the bottom of the bed, and the resonance amplitude sampled by the microphones above and beneath the bed was comparable for different fill factors.

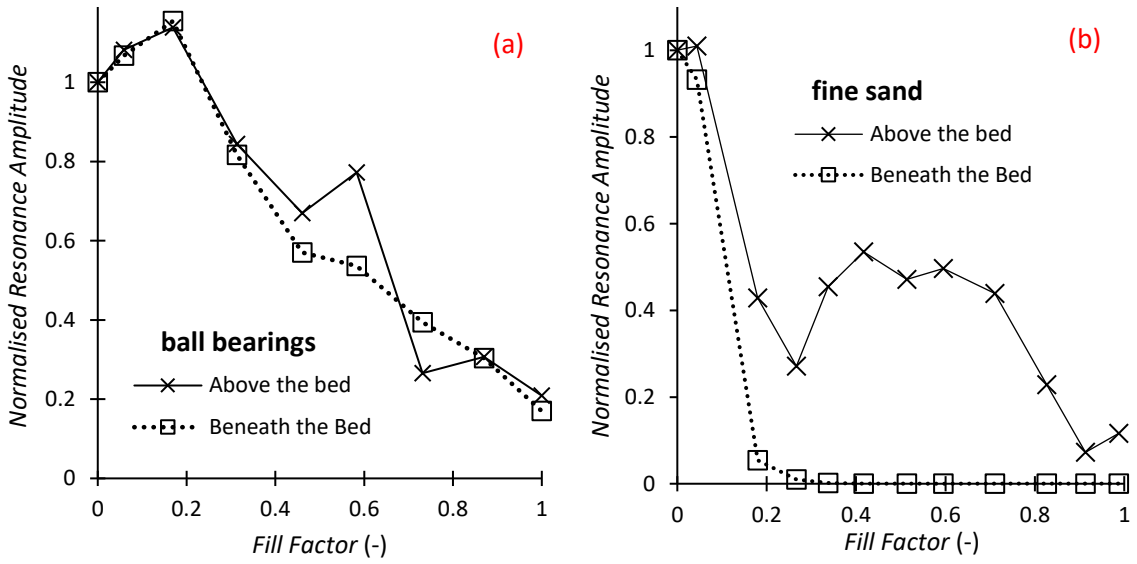


Figure 4-42: *Normalised resonance amplitude comparison for the resonance frequencies hunted from above and the bottom of the bed of ball bearings (a) and fine sand (b) samples.*

Powder solid volume estimation from line fitting

When rearranging the Classical Helmholtz Resonance equation in the form of resonance wavelength (See Basic Equations), a linear relationship between the resonator's occupied volume and wavelength squared λ^2 was established and demonstrated through experimentation, as depicted for the water sample in Figure 4-31. A similar trend was observed for the powder volume measurement. Because of the highly linear relationship between a sample volume and the hunted resonance frequencies, linear fits can help estimate sample volume from the resonance frequency. Solid volume was correlated to the resonance wavelength squared for all tested samples, as presented in Table 4-5. As the table provides, the Mean Deviation *MD%* (See Section Error Analysis Equations at the beginning of the thesis) between volume estimation using the line fit and the actual values obtained by weighing negatively correlated to the linearity of the trend in terms of R^2. The line fittings were obtained through repeated experiments on the 2-litre resonator with the 1000 mm port attached, and resonance frequencies were identified using the Transfer Function method. Therefore, the scope of validity is limited to experimental conditions accordingly.

Table 4-5: Sample Volume as a function of resonance wavelength through experimental line fitting.

Sample	Line Fit parameters* (V_s in ml, λ^2 in m²)	R^2	*MD*%
agricultural lime (AL1)	$V_s = -20.638\lambda^2 + 1402.5$	0.996	0.79
fine sand (FS)	$V_s = -24.146\lambda^2 + 1661.7$	0.992	1.23
fine ballotini (B250)	$V_s = -27.219\lambda^2 + 1907.5$	0.964	3.25
coarse ballotini (B710)	$V_s = -51.1\lambda^2 + 3393.3$	0.998	0.82
mustard seeds (MS)	$V_s = -47.191\lambda^2 + 3124.5$	1.000	0.28
ballBearings (BB)	$V_s = -44.085\lambda^2 + 2906.0$	0.999	0.59
small marble (SMB)	$V_s = -37.675\lambda^2 + 2490.9$	1.000	0.13
large marble (LMB)	$V_s = -38.693\lambda^2 + 2562.0$	1.000	0.23

4.4.6. Dynamic resonance hunting using the 3-litre lab-scale resonator

The dynamic test results for samples BMS and AL2 are presented in Figure 4-43. The linearity of the change in resonance wavelength throughout the discharge process was investigated by fitting a line with R^2 values in the figure. The total discharge time was 60 and 180 seconds for samples AL2 and BMS, respectively. The resonance wavelength decreased as the material discharged.

After opening the discharge orifice, both samples' resonance frequencies significantly increased. The detected resonance frequency ranged from 175 Hz to 185 Hz for both samples BMS and AL2 during discharge. Comparing this range with the resonance frequency range of the system in a static setup, when the bottom orifice was closed and the material was steady, showed a five-fold increase in resonance frequency. This increase could be due to the complex effects of material reformation in the resonator and the introduction of air leakage from the bottom of the resonator.

In the discharge tests, the resonator's Fill Factor impacted the resonance frequency hunting's practicality, similar to static tests, as seen in Table 4-4. For the agricultural lime sample, resonance frequency hunting was impossible for Fill Factors above 0.75 (2500 g of the loaded 3275 g). For the sample black mustard seeds, this figure was 0.85 (1600 g of the loaded 1880 g).

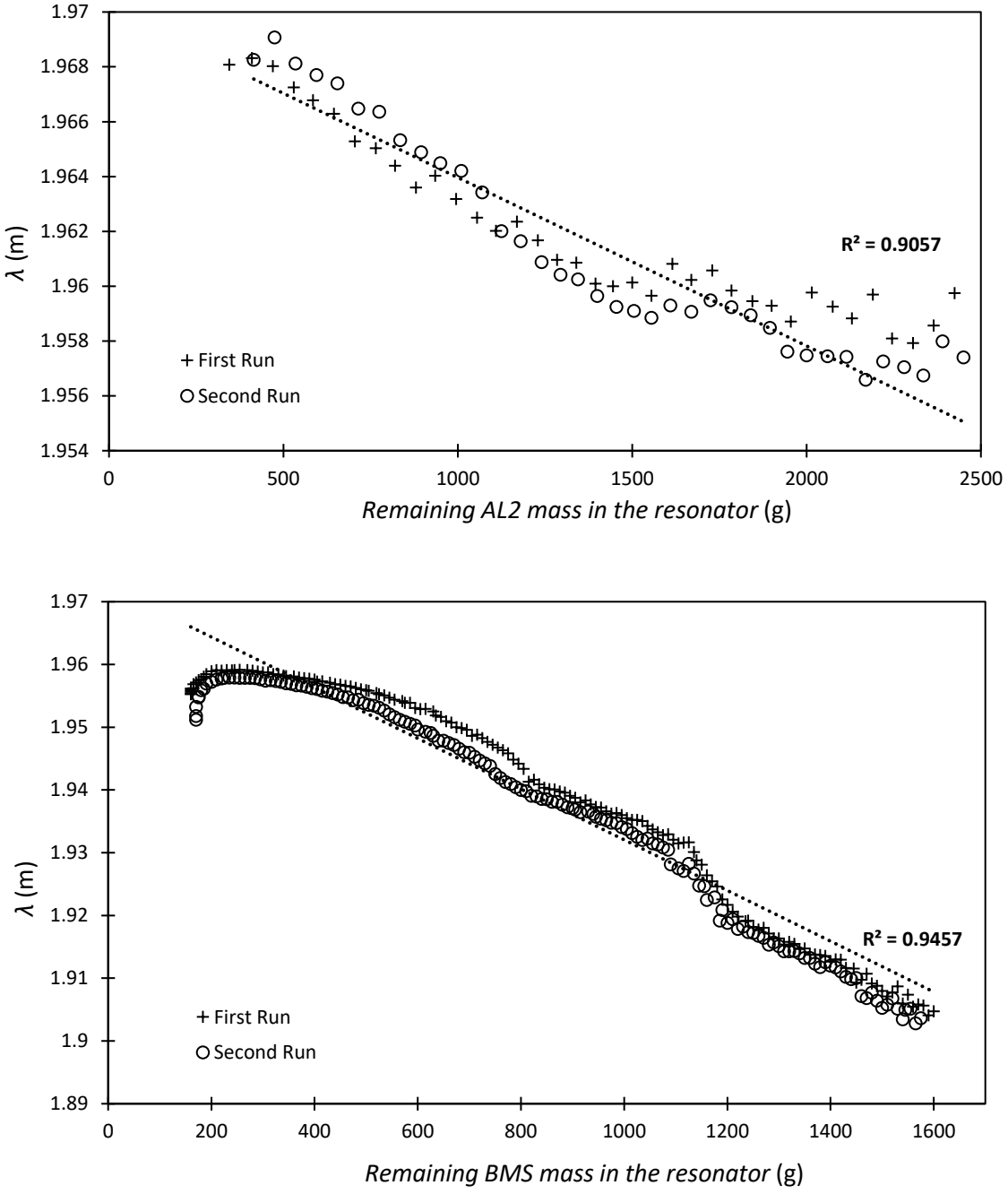


***Figure 4-43**: Dynamic tests on resonance wavelength tracking for 3270 g of AL1 sample (Top) and 1880 g of BMS sample (Bottom). The data points appear in both graphs from the right side to the left.The dotted lines are line-fits.*

4.4.7. Port length effect on the resonance quality

Undriven Resonance

Figure 4-44 demonstrates the results of the undriven response of the 2-litre resonator. This Figure shows the resonance response after the subwoofer set drove the resonator at 25% of its nominal power, which was 1500 W. This speaker power resulted in resonance amplitudes with reference pressure 20 uPa of 132 dB at 171.7 Hz, 137.6 dB at 89.9 Hz, and 124 dB at 42.5 Hz for 51, 250, and 1000 mm ports, respectively.

The decay lines were generated as described in Section 4.1.4. Amplitude Maxima A_M is the peak location of resonance amplitudes from the left-hand side graphs (a, b and c) of Figure 4-44. The right-hand side graphs of Figure 4-44 (a*, b*, and c*) demonstrate that the resonator response logarithmic decay had a linear trend (R^2=1). The damping ratio of the resonator for each port was calculated using Equation 4-15 ($ln(x) = -\zeta\omega_n t$) from the calculated slopes. The damping ratio for ports 51, 250 and 1000 mm was 0.0107, 0.0093 and 0.0129, respectively, showing a highly underdamped resonance for all ports.

The quality factor of the resonator from undriven resonance for each port was calculated using Equation 4-16 ($Q = 1/(2\zeta)$). Repeated experiments with 20 iterations showed that ports 51, 250 and 1000 quality factors were 46.5, 52.7 and 35.0, respectively.

The effect of speaker power on resonator quality in undriven resonance was investigated through repeated experiments in the range of 10% to 100% of the speaker power, which resulted in Sound Pressure Level variations from ~80 to ~125 dB (reference pressure: 20 uPa). According to the results for all ports, the quality factor from undriven response fluctuates around its mean value with no dependency on the power of the speaker sound in the tested range.

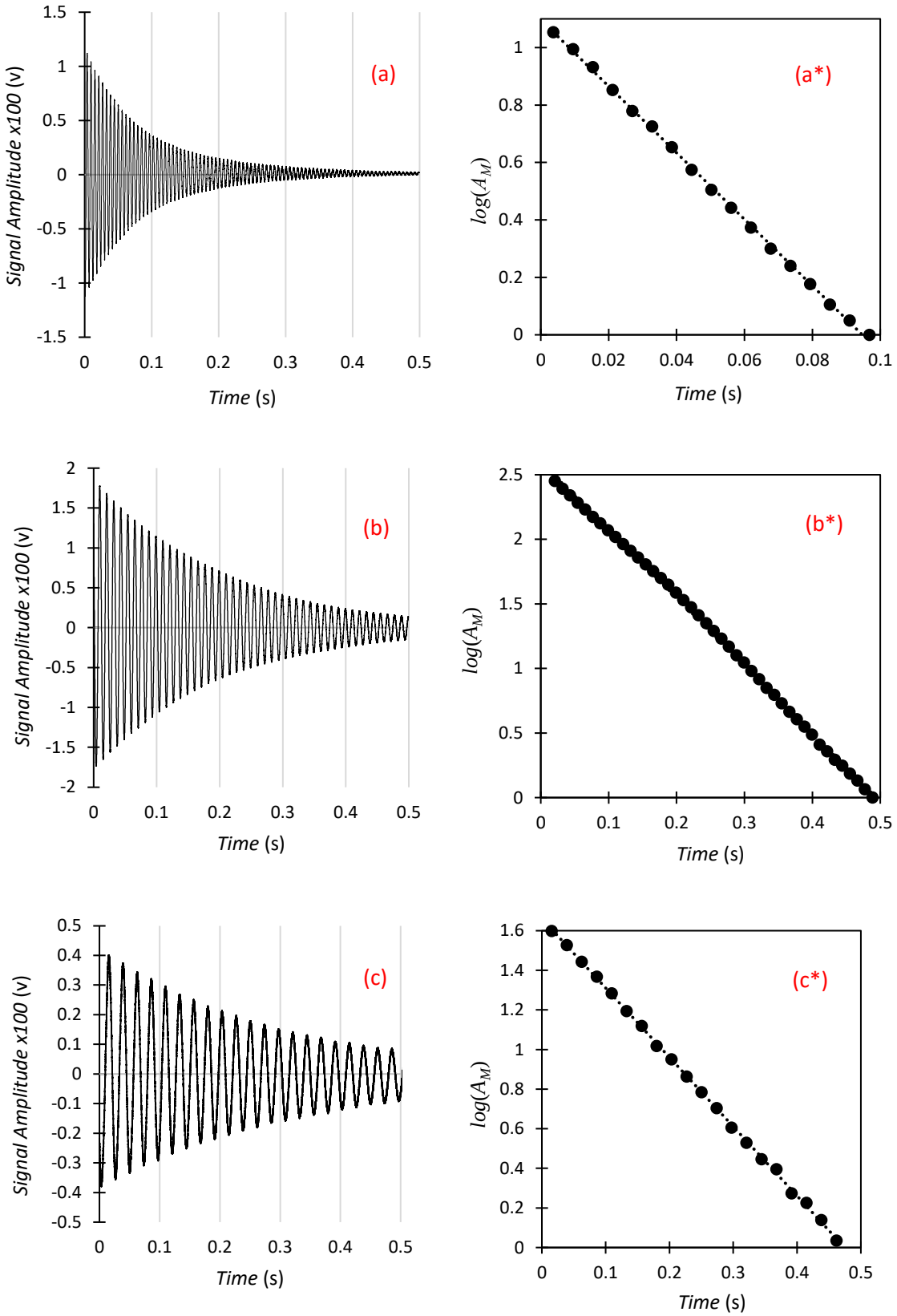


***Figure 4-44**: Signal Response from the 2-litre resonator equipped with the 51 mm port (a), 250 mm port (b) and 1000 mm port (c). The Graphs on the left show microphone port response, and the graphs on the right show logarithmic decay lines with associated line fit.*

Driven Resonance

The second method used to test the resonator quality factor was the power spectral density graph in Driven Resonance mode described in Section 4.1.5.

Figures 4-45 and 4-46 show the port microphone signal and power spectral density graph in driven resonance, respectively. The resonator's port length, as shown in Figures 4-45 and 4-46, where its response is sampled, is 1000 mm, and the cavity volume is 2 litres. As shown in Figure 4-45, the resonance reaches its maximum of around 1.7 seconds after the initiation of excitation by chirp. At this point, the excitation frequency was around 42 Hz.

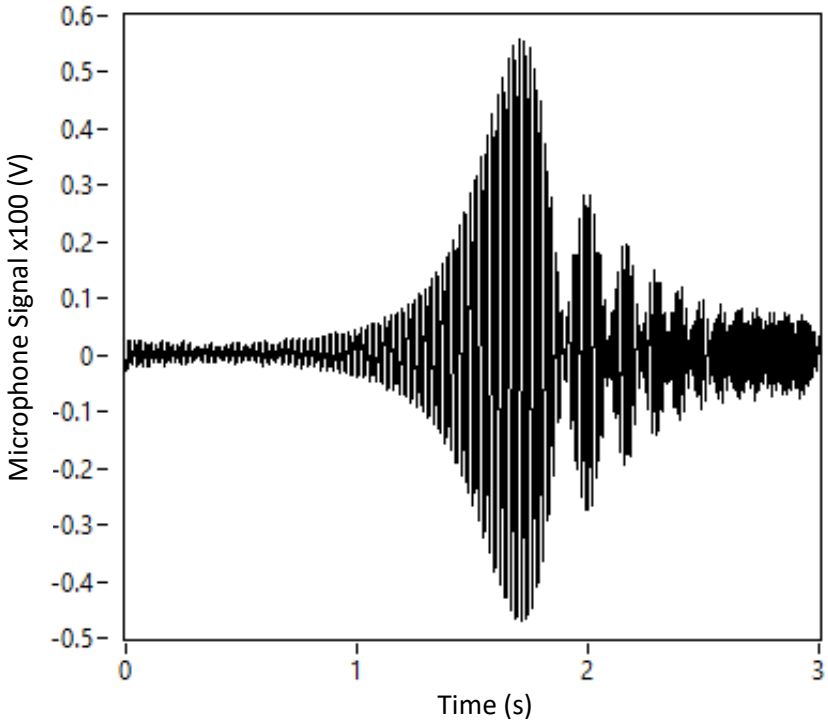


Figure 4-45: *Port Root Microphone signal, 1000 mm Port, Driven Resonance.*

The signal shown in Figure 4-46 is the response signal to a continuous driving chirp starting at 30 Hz (Time = 0 s) and ending at 60 Hz (Time = 3 s). At nearly 1.7 seconds from the start of the chirp, the resonance within the port reaches a maximum amplitude of roughly 0.5 V.

Figure 4-46 shows the power spectral density graph of the signal in Figure 4-45. The resonance frequency was a distinctive peak at 42.5 Hz. The harmonics of the resonance frequency are also visible in the figure as multiples of the resonance frequency at ~85 Hz, ~127.5 Hz and the rest of harmonics.

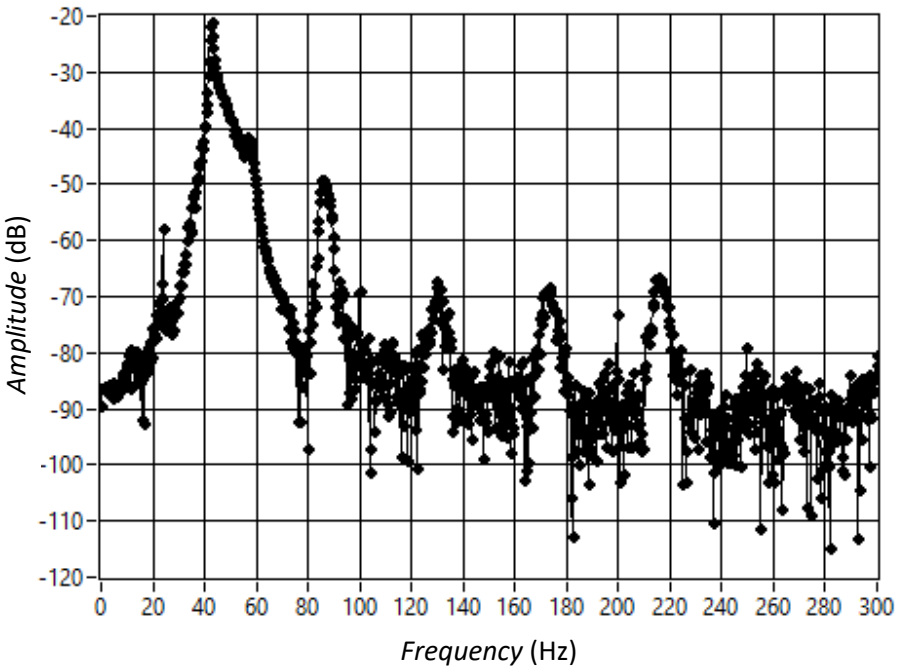


Figure 4-46: *Power Spectral Density of Driven Resonance Signal. 2-litre resonator with 1000 mm Port.*

Figure 4-47 presents the results for the Driven Quality Factor from power spectral density, measured across various Sound Pressure Levels (SPL) for 51, 250 and 1000 mm ports. The ordinate is the Quality Factor, and the abscissa is the mean SPL (reference pressure: to 20 uPa) at the opening of the resonator port.

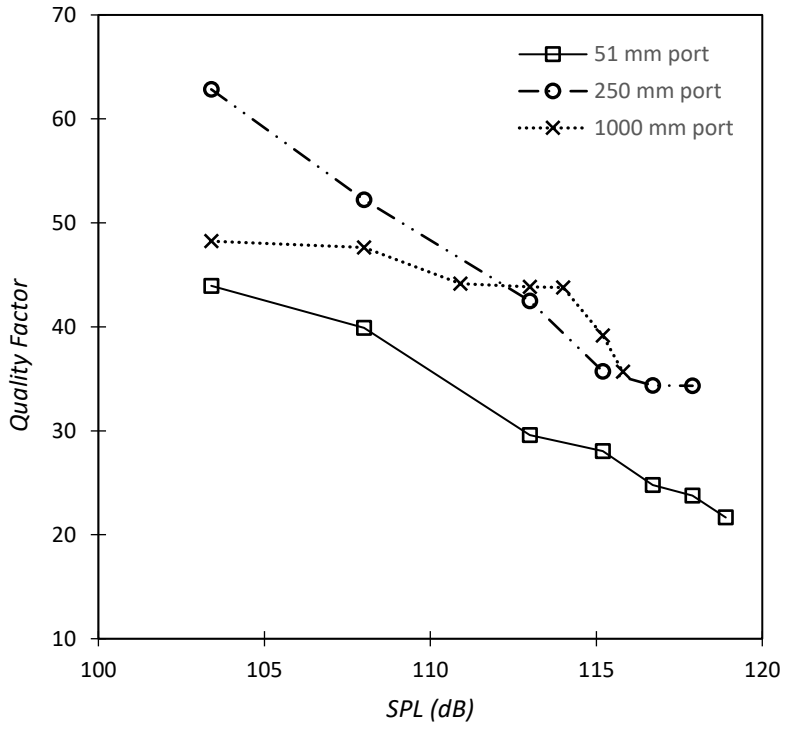


Figure 4-47: *Quality factor for driven resonance vs Sound Pressure Level (SPL).*

As is shown in Figure 4-47, adjusting loudspeaker power, which manifested in changing incident sound SPL, resulted in variation in the driven quality factor. Overall, there was a negative correlation between the resonance quality factor and incident sound pressure level for individual ports; the resonance quality factor decreases with increasing incident sound pressure level. The observed trend was consistent across different setups, including the use of 170 mm and 500 mm ports, as well as with 1-litre and 3-litre resonators. In all cases, the overall trend indicated that an increase in sound pressure level at the port opening leads to a decrease in the quality factor when the resonators are in driven resonance.

Driven Resonance – Quality from Transfer function phase shift

The third method to evaluate quality factors was using phase shift from the Transfer Function method. Typical to 51 and 250 mm ports, the phase shift between the driver microphone signal and the 1000 mm port microphone signal is demonstrated in Figure 4-48.

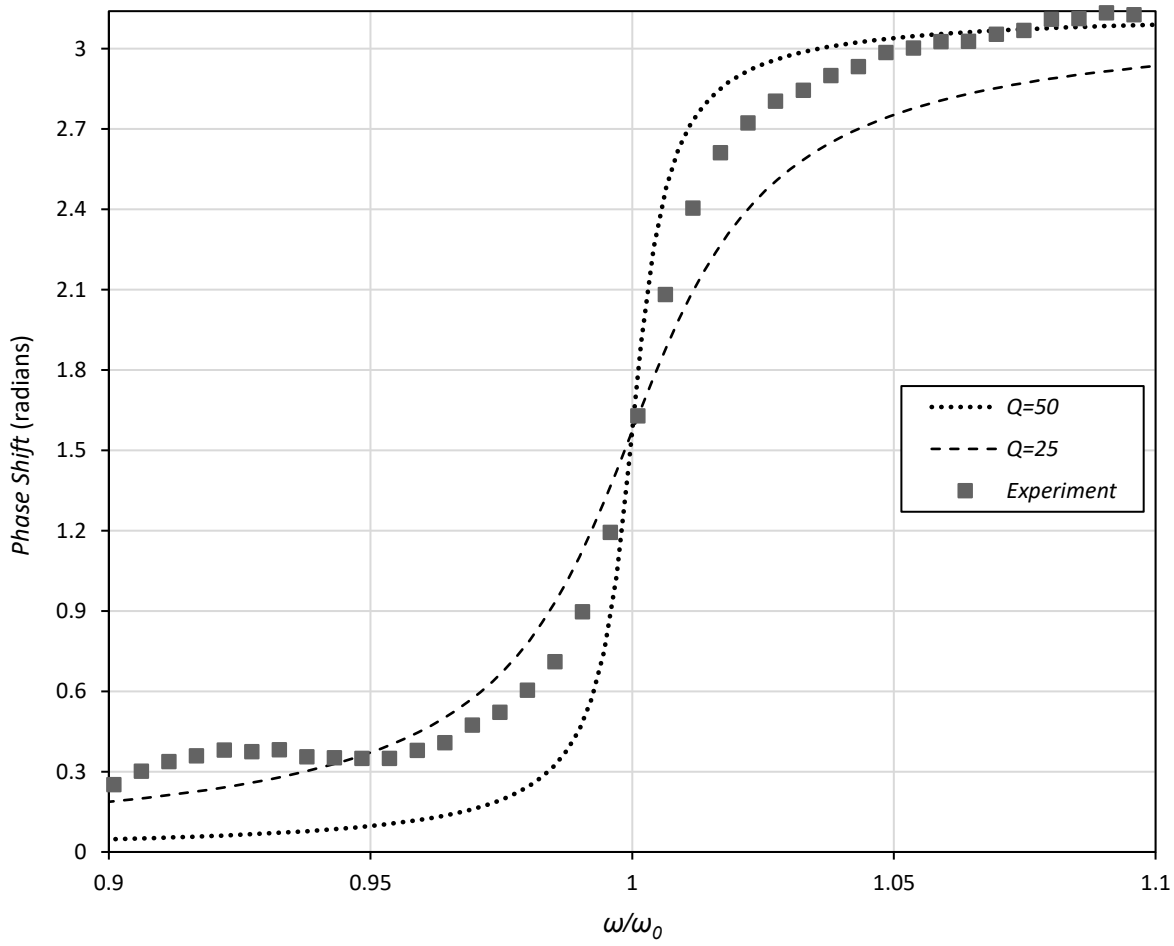


Figure 4-48: *Phase shift between the driver and the resonator port microphone signals.*

In Figure 4-48, F/F_0 is the ratio of the driving frequency to the resonance frequency. The phase shift between the driver and resonance signal approaches π/2 radians when F/F_0 approaches 1. The measured phase-shift data points lie between the estimated phase-shift profile of Q=25 and Q=50. In the results demonstrated in Figure 4-48, the speaker power was set at 0.25, and the quality factor from the driven spectral analysis was 42.

4.4.8. Effect of powders on quality factor

Resonance quality for various samples was measured using Undriven and Driven methods. For both methods, the speaker power was set at 25%.

Figure 4-49 shows the trend in resonance quality factor for agricultural lime and water samples for various Fill Factors of the resonator measured using the Driven method from spectral analysis using Equation 4-22. For Water, the variation of the resonator Fill Factor did not result in a positive or negative trend for the Quality Factor. With some fluctuations, the quality factor fluctuated between 40 to 50. Filling the resonator with agricultural lime up to a Fill Factor of 0.1 resulted in a sharp drop in Quality Factor from 45 to 30. From that point onwards, the resonance quality factor remained in channel 30 with some fluctuations, similar to water. The Fill Factor of 0.1, equivalent to a sample depth of 12.3 mm, could be the depth of the sample that resonance pressure waves penetrated and decayed.

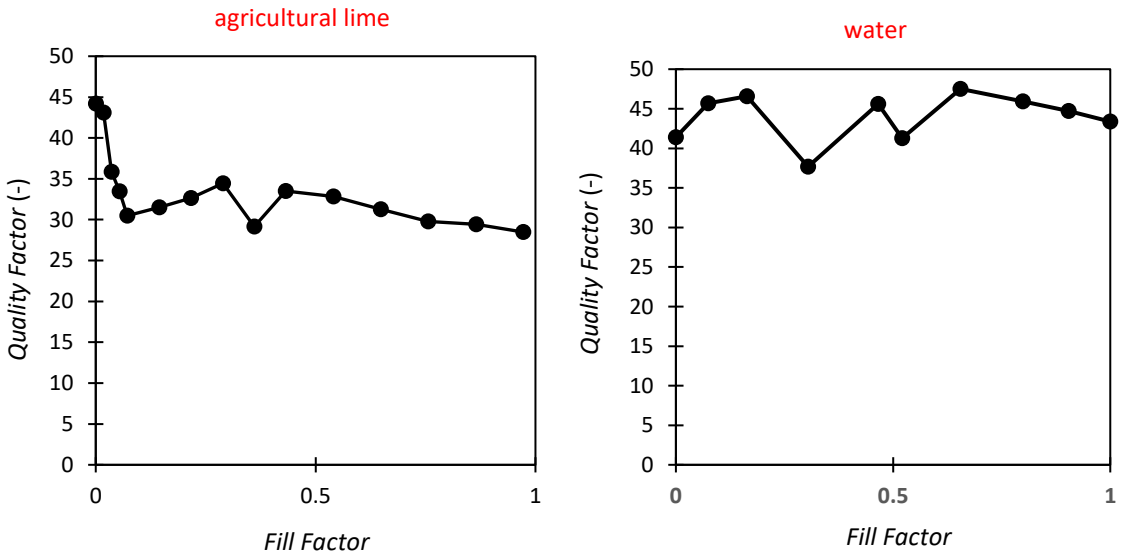


Figure 4-49: *Quality factor comparison between water and agricultural lime samples.*

The tested samples showed a decline in resonance Quality Factor with increasing resonator Fill Factor. The results are presented in Figure 4-50. These results are typical for polyethylene small and large (PE1, PE2) and mustard seed (MS) samples, which also show a steady decline in quality factor as the resonator fill factor increases.

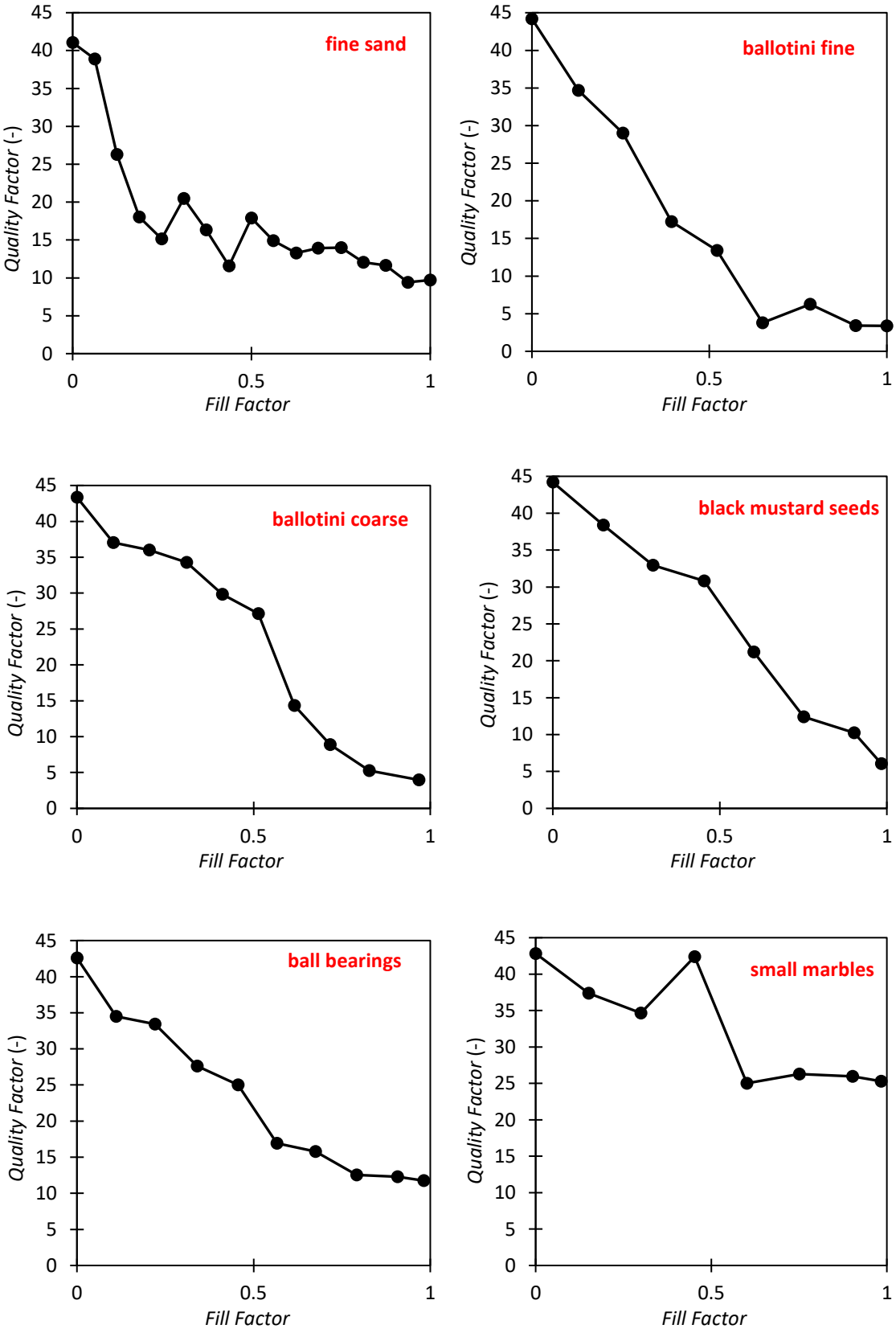


Figure 4-50: *Resonance Quality vs Fill Factor for the six samples mentioned in the graphs.*

In Undriven resonance, the quality factor was calculated from the signal decay line (Section 4.1.4). The results were in agreement with Driven resonance frequency hunting. Typical for all samples, Figure 4-51 shows the agreement between the two methods of resonance frequency hunting for the ball bearings sample.

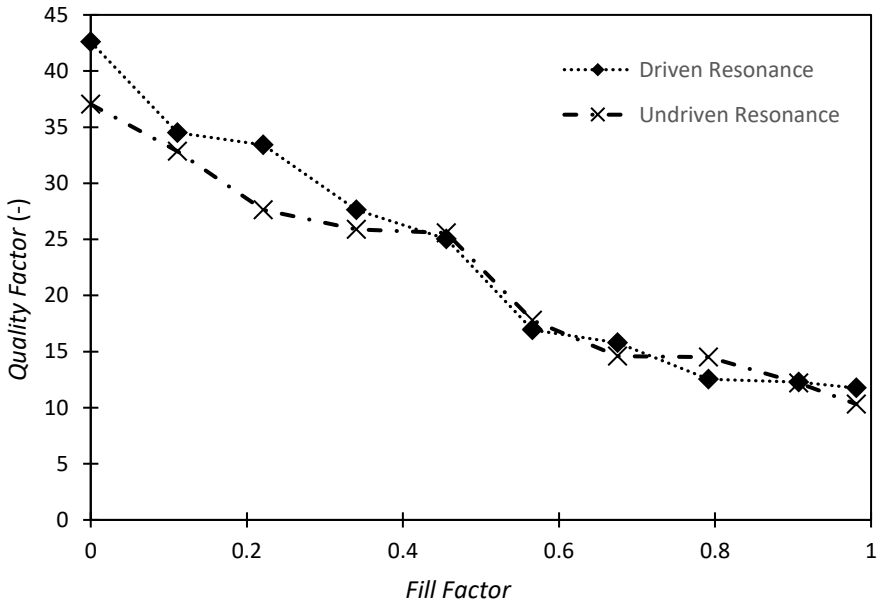


Figure 4-51: *Resonance quality measured using Undriven and Driven methods Fill Factor. The test sample was ball bearings (BB).*

The minimum Quality Factor for open pore samples was obtained at Fill Factor 1. Comparing the particle mean diameter to the Quality Factor at Fill Factor 1 is shown in Figure 4-52. As shown in Figure 4-52, the minimum resonance quality factor increased in a linear fashion with the increase in the mean particle diameter.

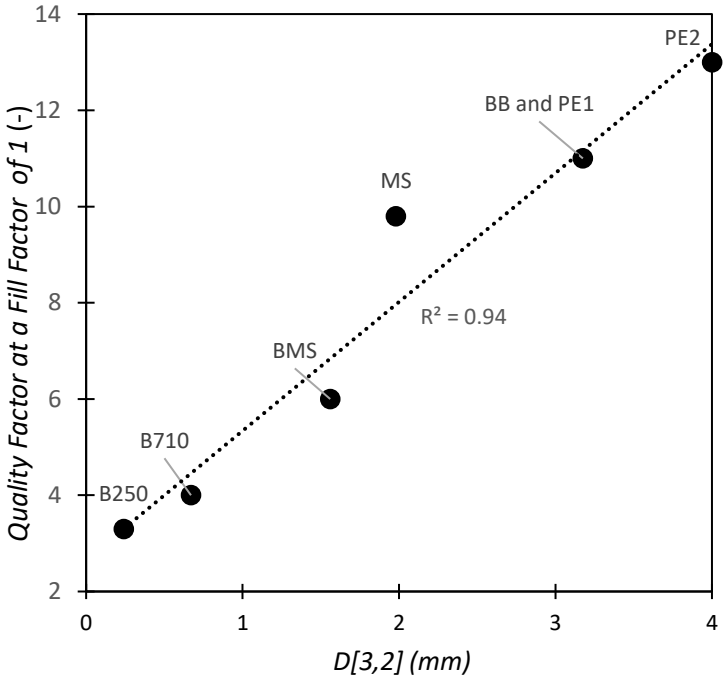


Figure 4-52: *Driven Resonance Quality Factor when the resonator is full of samples vs sample particle diameter.*

The driven resonance phase shift of fine sand sample is provided in Figure 4-53. The experiment on other test materials resulted in obtaining graphs similar to what is shown in Figure 4-53. The graph shows the phase shift between the driving and resonator microphone signals, as discussed in Sections 4.1.5 and 4.3.3. The resonator was filled with fine sand to the top with a loose poured packing. In the figure, the abscissa is the driving chirp frequency ω divided by the resonance frequency ω_0, and the ordinate is the Phase Shift φ in radians between the two signals from the driver and the resonator microphones. As is shown in Figure 4-53, when the driving chirp frequency approaches resonance frequency (ω/ω_0=1), the phase shift approaches π/2 radians. Theoretical phase shifts for Quality Factors 8, 10, 12, and 17 are estimated using Equations 4-23 and plotted in Figure 4-53. The measured phase shift lies between the theoretical Quality Factors of 8 and 12. For this load of fine Sand, the quality factor from Undriven resonance was 9.7, which agrees with the quality factor obtained from the phase shift.

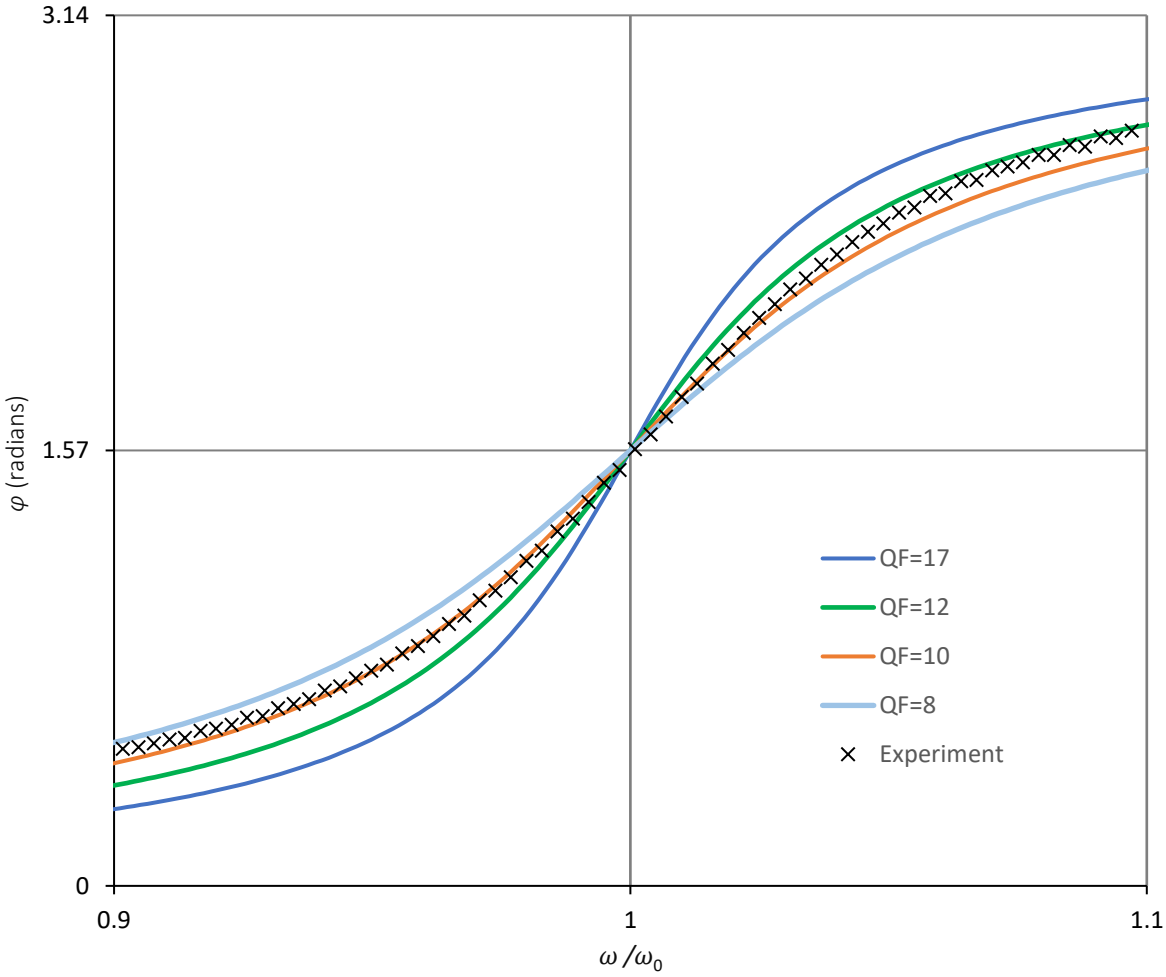


Figure 4-53: *Phase Shift between driver and resonator signal vs resonance frequency for the 2-litre resonator, fine sand (FS) at a Fill Factor of 1.*

The effect of air leakage from the resonator cavity (with the 51 mm port) on resonance quality was measured. Opening a pinhole with a diameter of 2 mm in the bottom of the resonator affected the resonance frequency and Quality Factor, as seen in Table 4-6. The data in Table 4-6 are averages of 20 measurements.

Table 4-6: *The effect of air leak in the resonator on resonance hunting parameters.*

Hunting Method	**Undriven**		**Driven**		**Transfer Function**	
Parameter	**Resonance Frequency (Hz)**	**Damping Ratio (-)**	**Resonance Frequency (Hz)**	**Quality Factor**	**Resonance Frequency (Hz)**	**Quality Factor**
Without Hole	171.47	0.0096	171.06	36.93	172.13	25.47
With Hole	170.38	0.0098	170.40	37.31	171.50	30.70
Variation (%)	0.63	-1.89	0.38	-1.02	0.37	-20.64

4.4.9. Acoustic Energy Absorption tests

The results of sound Absorption coefficient measurements can be divided into sub-categories of sub-millimetre powders and powders with particles larger than 1 mm in diameter. In this section, depth refers to the depth of the sample holder, which is equivalent to sample thickness.

Powders with particles smaller than 1 mm

The finest powder tested for sound absorption was fine Sand, with the results in Figures 4-54. As shown in the figure, sound absorption increases slightly with incident frequency.

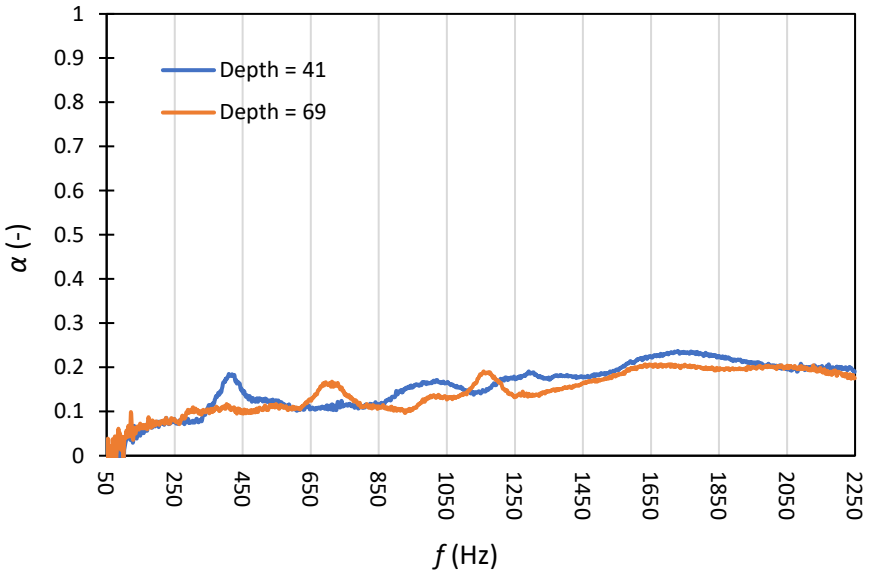


Figure 4-54: *Normal Incident Sound Absorption for fine sand (FS) Sample. The depth unit is mm.*

For fine Sand, the maximum absorption occurs at 1729 Hz and 1680 Hz for bed Depths of 41 mm and 69 mm, respectively, with a shift of almost 50 Hz for the Maximum Absorption Peak. Considering an excellent sound absorber as a material that absorbs more than 90% of the incident sound energy, this sample, with a maximum sound absorption coefficient of less than 0.3, was not an excellent sound absorber.

Like fine sand, fine ballotini (B250) was not a good sound absorber, with the results shown in Figure 4-55. Increasing the sample thickness from 41 mm to 69 mm resulted in a slight decrease in sound absorption for frequencies higher than 250 Hz. For lower frequencies, the thicker bed had higher sound absorption.

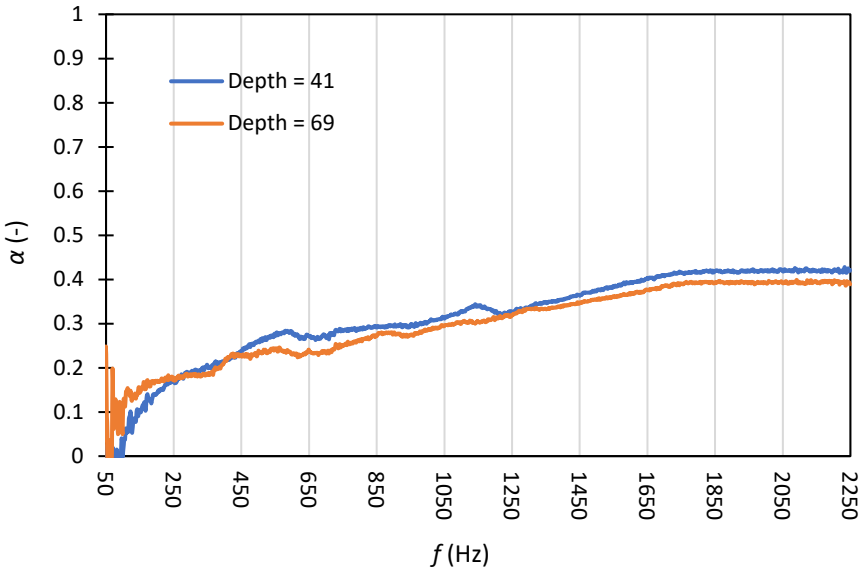


Figure 4-55: *Normal Incident Sound Absorption for fine ballotini (B250) Sample. The depth unit is mm.*

Compared with fine sand and fine Balotini, large ballotini (B710) had higher sound absorption coefficient peaks at ~650 Hz and ~1180 for the 41 mm and 69 mm bed depths, respectively (Figure 4-56). Increasing sample depth from 41 to 69 mm shifted the sound absorption peak by ~530 Hz. For the B710 sample, the increase in depth from 41 to 68 mm reduced sound absorption peak height but shifted it towards lower frequencies. For the 68 mm bed, the sound absorption profile was roughly flat for frequencies higher than ~650 Hz.

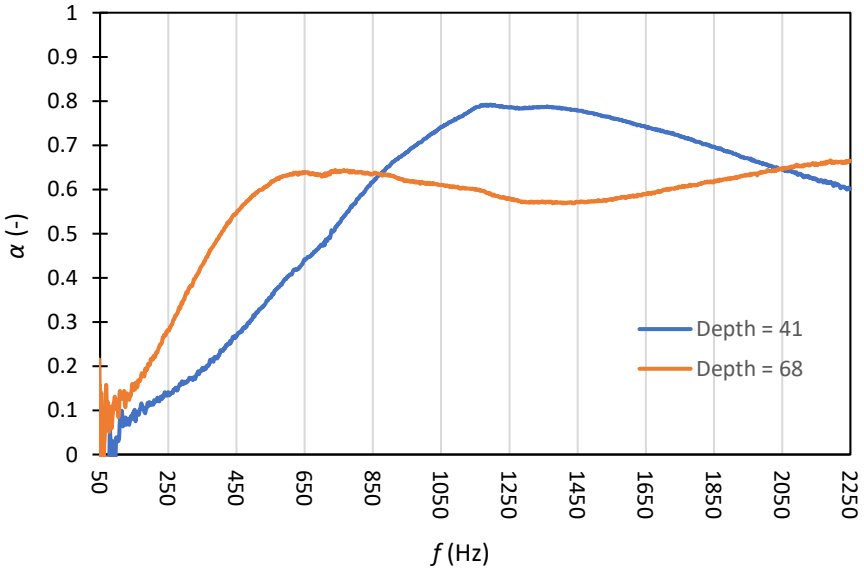


Figure 4-56: *Normal Incident Sound Absorption for coarse ballotini (B710) Sample. The depth unit is mm.*

Powders with particles larger than 1 mm

For samples with a mean particle diameter larger than 1 mm, the sound absorption peak location was primarily influenced by sample depth, and narrower peaks were observed. Sound absorption measurement results for black mustard seeds, typical for mustard seeds, are shown in Figure 4-57.

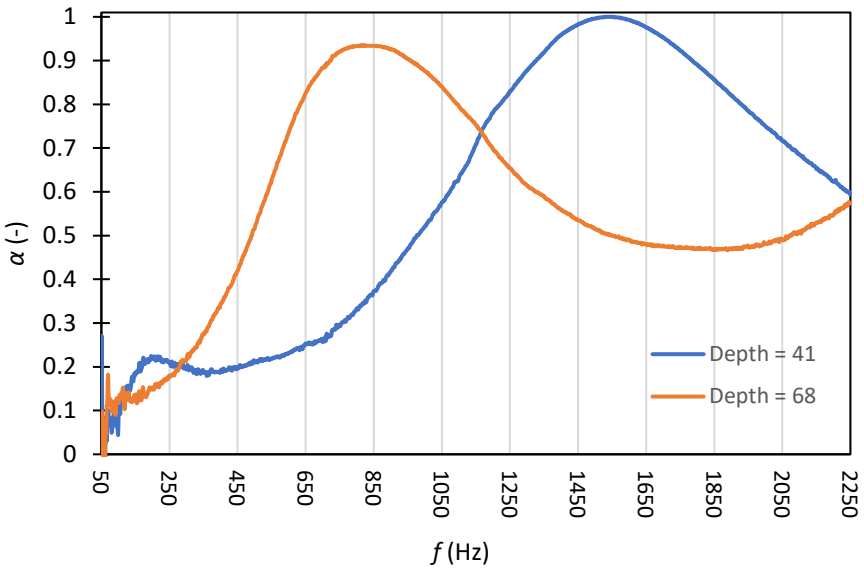


Figure 4-57: *Normal Incident Sound Absorption for black mustard seeds (BMS) Sample.*

Unlike fine samples (FS, AL2, B250 and B710), black mustard seeds had much higher sound absorption for the entire frequency range. This sample demonstrated two distinct sound absorption peaks at ~1540 and ~825 Hz for 41 and 68 mm bed depths. Increasing the bed depth recorded the absorption peak by almost 715 Hz.

Figure 4-58 shows normal incident sound absorption test results for ball bearings, typical for polyethylene samples. All of the three following features were observed for samples ball bearings (BB), small PolyEthylene (PE1) and large PolyEthylene (PE2) samples, which have a mean particle diameter larger than 3 mm:

1: Having a peak with almost perfect sound absorption $\alpha>0.9$,

2: Having peak locations distinctively apart for different bed thicknesses and,

3: Shifting sound absorption profile towards lower frequencies for a thicker bed.

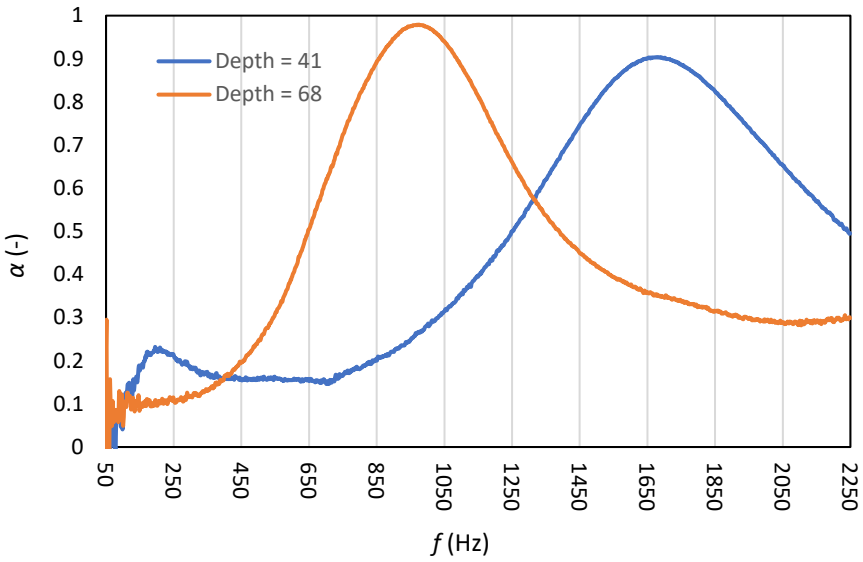


Figure 4-58: *Normal Incident Sound Absorption for ball bearings (BB) Sample.*

4.4.10. Compression uniformity

Compression Uniformity in this section is expressed in phase mismatch between the signal from top and bottom microphones in the 2-litre resonator chamber.

The signal phase mismatch between the top and bottom microphone at resonance when the resonator was empty was measured 15 times. The phase mismatch between the two microphones was almost 0.14 degrees, equivalent to a 9.7×10^{-6} second shift in the zero-crossing time of the signals. This very low time difference between pressure wave zero crossing of the resonator cavity top and bottom sections results from the uniform compression, as it was an assumption in the classical Helmholtz Resonance model (Lord Rayleigh, 1916).

The presence of powders in the resonator causes a delay in pressure wave zero-crossing between the top and bottom of the powder bed inside the resonator. The pressure fluctuations in the bottom and top of the resonator cavity were not simultaneous. In this study, this observation is referred to as Compression non-uniformity.

The results can be divided into two sub-categories: Samples that cause a moderate phase shift (<10 degrees) between the top and bottom pressure signals, including mustard seeds (MS), black mustard seeds (BMS), large polyethene (PE2) and small polyethylene (PE1), which have a particle diameter of more than 1 mm and samples which caused a high phase shift (>10 degrees) between the top and bottom pressure signals including fine sand (FS), small ballotini (B250) and coarse ballotini (B710) which have particles with the diameter smaller than 1 mm. The Phase Shift for agricultural lime

(AL2) sample was not detectable. For this sample, the signal shape in the bottom microphone was heavily distorted, and zero crossing was not detectable for a bed thickness larger than 39 mm.

Signal Phase mismatch results for the samples with moderate phase shift are presented in Figure 4-59.

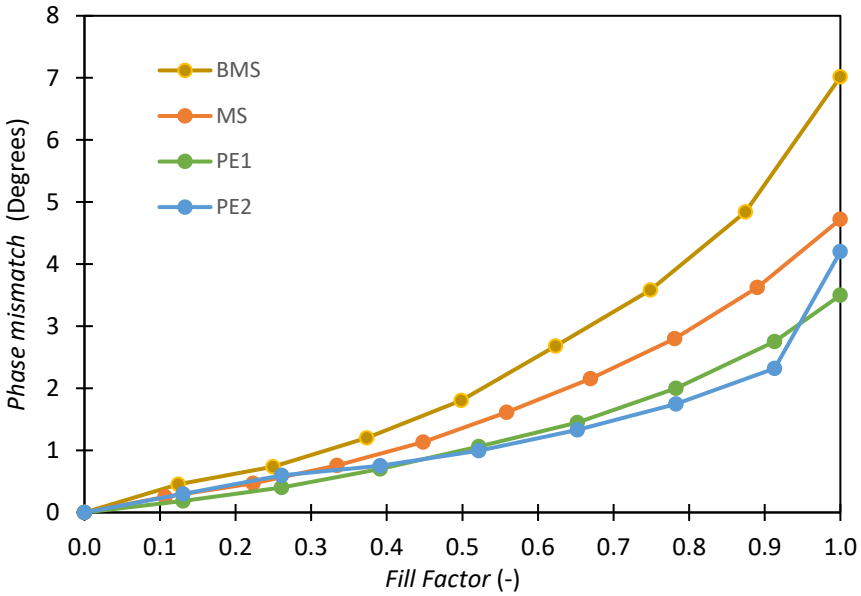


Figure 4-59: *Pressure signal phase mismatch between up and down sections of the resonator vs. Fill Factor for samples with particle diameter larger than 1 mm.*

As shown in Figure 4-59, putting a sample with particle diameters larger than 1 mm into the resonator resulted in a phase shift in the pressure signal. Resonator Fill Factor had a direct relationship with phase mismatch for all samples. On average, the samples with larger particle diameters had lower phase mismatch. Samples with smaller particles caused a high compression non-uniformity.

Figure 4-60 shows signal phase mismatch results for samples with particle diameters smaller than 1 mm. Increasing the Fill Factor for each sample increased the signal phase mismatch. Similar to samples with a mean particle diameter larger than 1 mm, samples with a higher mean particle diameter resulted in a lower phase mismatch. In the most extreme case, when the resonator was filled with the sample fine sand (FS), which has the finest particles among the samples under test, a phase mismatch of π radian between the pressure signals from the top and bottom sections of the resonator was observed. In terms of compression non-uniformity, this high level of phase mismatch means that when the air inside the cavity at the top section of the bed was under compression, the air at the bottom of the bed was under expansion, which is further discussed in Section 4.5.11.

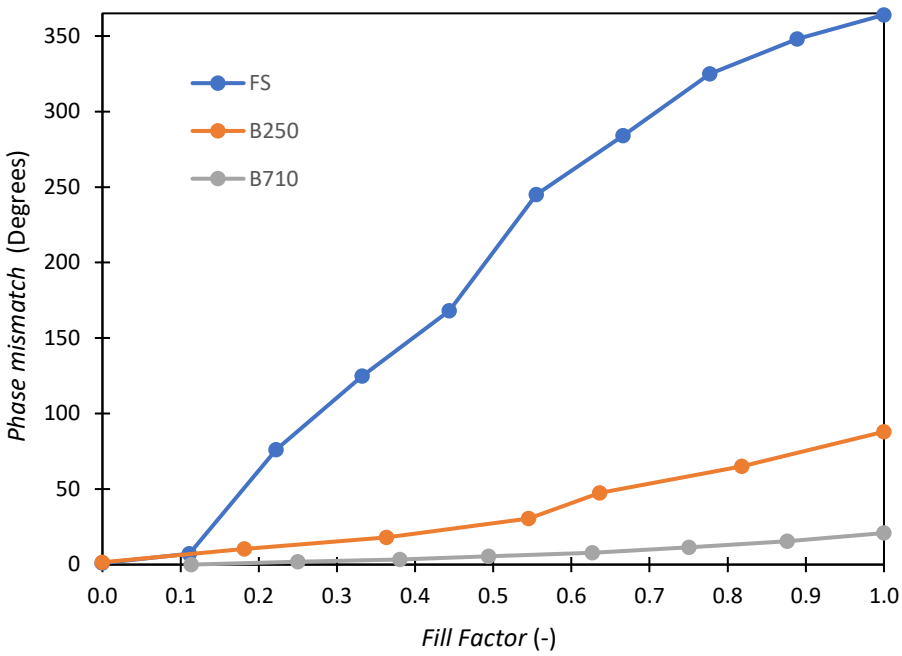


***Figure 4-60**: Pressure phase mismatch between top and bottom of the powder bed versus Fill Factor for samples with particle diameter smaller than 1 mm.*

4.4.11. Sound wave penetration speed

Before measuring the time of flight of sound in the samples, an experiment was designed to verify the measurement method.

Two sets of tests in the empty chamber, each with nine replications, were performed for validation. Each test set was performed with a spacer between the loudspeaker and the chamber. The first experiment was performed by adding one spacer, and the second experiment was performed by adding two spacers between the loudspeaker and the chamber. The spacers were duct tape rolls with heights of 47.2±0.5 mm and 50.5±0.5 mm. Figure 4-61 shows the experimental setup for verification of the method. The time of flight of the 150 Hz monotone wave was measured with and without the spacers. The speed of sound was estimated based on the temperature of the cavity (See Basic Equations). The added travel distance with the spacers was estimated by multiplying the speed of sound by the time of flight difference ($\Delta TOF \times c$). According to the results, the added travel distance was estimated to be 47.68 mm and 97.91 mm for one and two duct tape rolls, respectively. The estimated added travel distance of the wave for both experiments was within the uncertainty of the actual spacer(s) height(s), shows the agreement and verifies the experimental method for time of flight measurement.

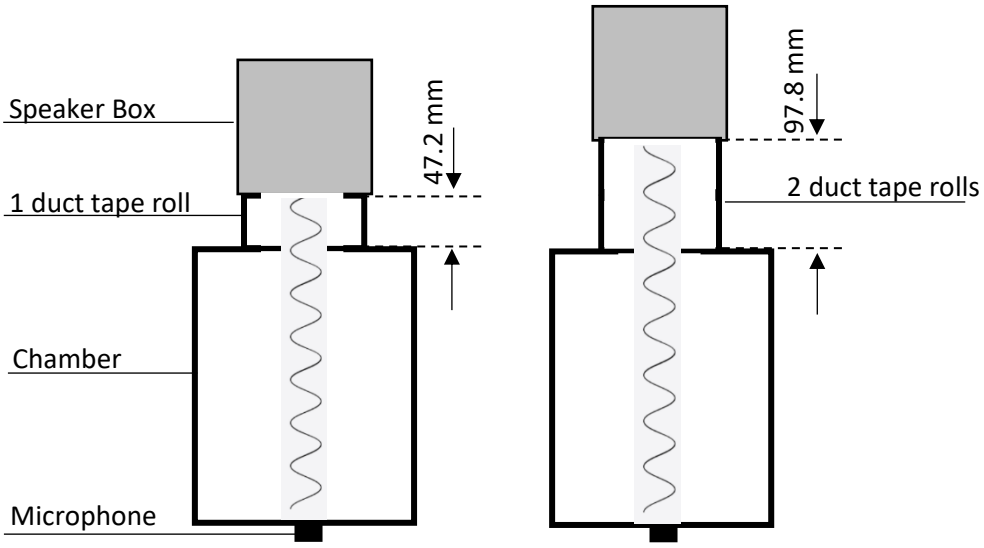


***Figure 4-61**: Verification of the speed of sound measurment apparatus by adding one (Left) and two (Right) spacers.*

Figure 4-62 shows how the sound flight time was measured for the sample black mustard seeds (BMS) as an example for all samples.

As is shown in Figure 4-62 (a), TOF_1 for when the cavity was empty was recorded at 1.2782 ms. The sound flight time when the cavity was filled with the black mustard seeds sample (TOF_2) was recorded at 1.5299 s, an increase of 0.2517 ms (Figure 4-62, b). The effective sound wave travel length (L'), acoustic tortuosity (α_0) and sound wave penetration speed (v) for samples fine sand (FS), agricultural lime (AL2), ballotini (B250), black mustard seeds (BMS), mustard seeds (MS), ball bearings (BB), small polyethylene (PE1), large polyethylene (PE2), small marbles (SMB) and large marbles (LMB) were calculated, and the results are presented in Table 4-7.

***Table 4-7**: Sound propagation analysis.*

	Sample									
	FS	**AL2**	**B250**	**BMS**	**MS**	**BB**	**PE1**	**PE2**	**SMB**	**LMB**
L'**(mm)**	255	259	259	274	276	270	262	249	224	219
α_0	1.36	1.38	1.37	1.46	1.47	1.43	1.39	1.32	1.19	1.17
v**(m.s^{-1})***	253	249	249	235	234	239	246	259	288	294

* Lab temperature for these experiments was kept at 23.3±0.2 °C, and the speed of sound in the air was estimated to be 345 m.s^{-1s}.

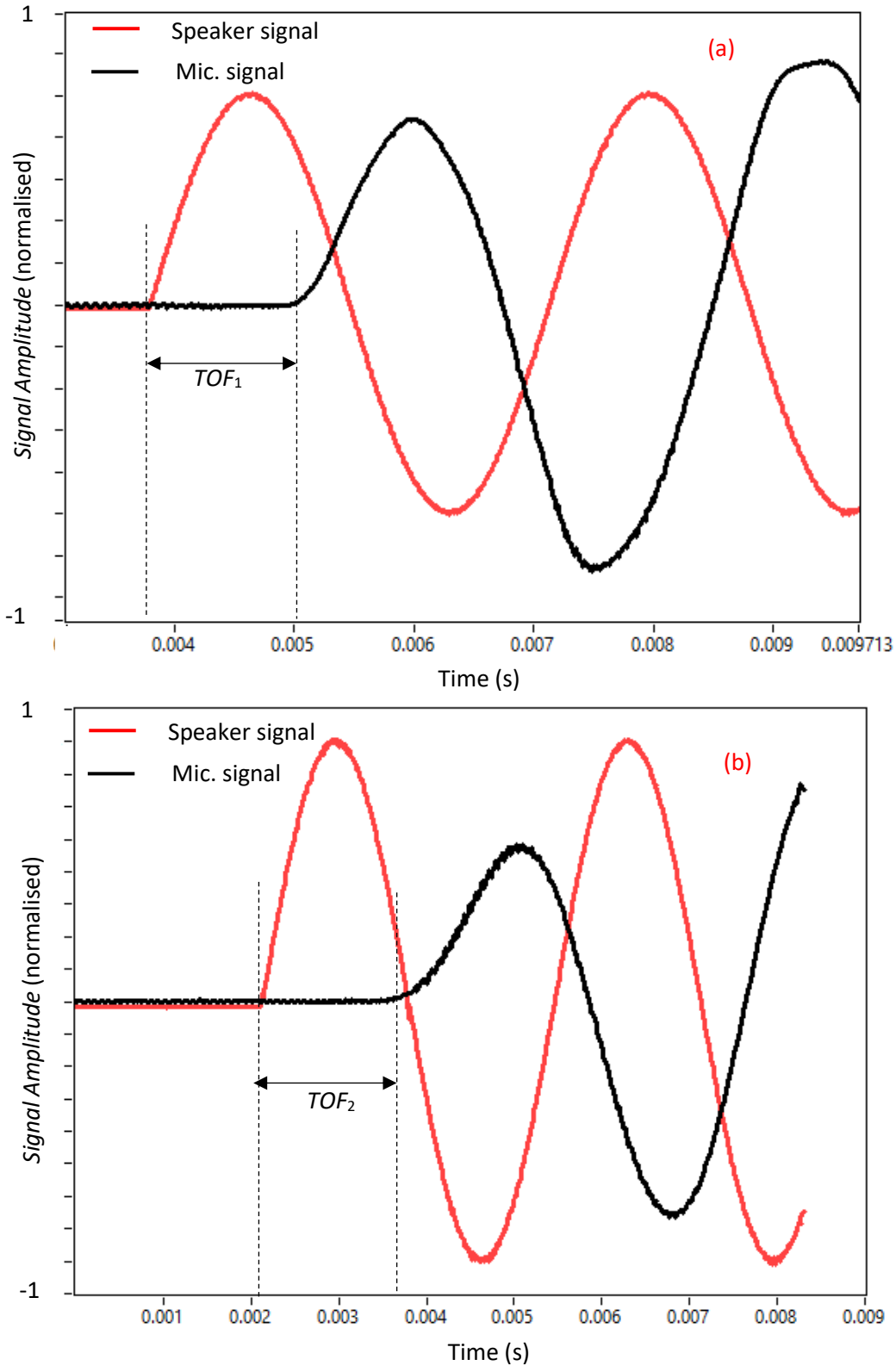


Figure 4-62: *Time of flight measurement when the cavity was empty (a) and when the cavity was filled with black mustard seeds (b).*

The highest tortuosity was recorded for the mustard seeds (MS), followed by the black mustard seeds (BMS). The lowest tortuosity was for the large marble sample. The speed of sound penetration for all samples was significantly (>10 %) lower than the speed of sound in the air. This deviation is due to the tortuose travel path of the particle bed. The highest sound propagation speed was 294 $m.s^{-1}$ for the large marble sample, and the lowest was 234 m.s-1 for mustard seeds. The very fine samples, including fine sand, ballotini, and agricultural lime (*D[3,2]*<0.5 mm), had relatively higher sound penetration speeds in comparison with mustard seeds samples with much larger particles (*D[3,2] = 1.98* mm). The measured tortuosity of the fully spherical sample ball bearings (BB) was 1.43, which is in agreement with the reported value of tortuosity for fully spherical particles in the range of 1.2 mm to 5 mm particle diameter by Comiti & Renaud (1989). They reported a range of 1.40 to 1.44 for similar particles.

4.5. Discussion

4.5.1. Resonant frequency hunting in the 50-litre vessel

The experiments on the 50-litre discharge vessel showed two distinct acoustical responses for the tested samples: Mustard seeds and agricultural lime. The resonance of the vessel was hunted using Undriven method.

In discharge tests on the agricultural lime sample (AL1), a cohesive sample containing dust, the resonance frequency variation was detectable throughout the discharge. The resonance frequency decreased with the sample mass in the vessel. A linear statistical fit made it possible to estimate sample volume every 0.7 seconds with a deviation of ±1.5% of the resonator full scale. When the sample level reached the bottom of the resonator, making the control orifice visible from inside the vessel, the resonance frequency could not be determined accurately. The hunted frequency, the frequency bin with the highest amplitude in power spectral analysis, remained constant regardless of the volume change inside the vessel. However, while the system was excited with a chirp with a constant frequency range, the sound pressure inside the vessel changed as the volume of material inside the vessel varied.

For the mustard seeds (MS), an open-pour free-flowing sample, it was challenging to track resonance frequency change with the mass of the material inside the vessel. The undriven resonance hunting method detected a constant frequency peak and continued exciting the vessel around the hunted frequency of 45 Hz. In response to the fixed excitation chirp, the sound pressure linearly increased with the decrease in the sample volume inside the vessel.

The data from the discharge of mustard seeds was insufficient to understand the acoustical response of the vessel during material discharge. The inability to hunt the resonance frequency with the change in the vessel volume guided the research into the lab-scale resonator tests on powders. The resonance frequency of the vessel was not successfully hunted when containing mustard seeds, which is typical for open-pour powders. A critical observation in this experiment was the signal amplitude change when the vessel was excited continuously with a constant driving frequency. The measured signal amplitude was a function of the amount of material inside the resonator. This observation prompted further investigation, reported in Chapter 7, where a method is introduced for real-time sample volume estimation based on microphone signal amplitude.

4.5.2. Resonant frequency detection in the Airplane hopper

The results of the dynamic discharge test from a topdressing aeroplane were similar to the experiments on the 50-litre vessel in terms of acoustical response to samples with low and high mean particle diameters. The resonance frequency fluctuated when the material level went below a certain level where the discharge gate became visible. This peak frequency fluctuation could be due to air ingress from the bottom of the hopper and the introduction of the discharge gate as a secondary port. Inspecting Figure 4-26, during the discharge of the urea powder, in the region where the detected frequency peak, hence, the excitation chirp frequency, remained constant –between 1700 to 1850 litre of empty volume in the hopper – there was a noticeable trend between sound pressure level and the free volume of the hopper.

The results of the preliminary experiments on the topdressing hopper suggested that it is difficult to reliably detect resonance frequency for urea, an open pore material. However, the sound pressure and the fluctuations in frequency can help detect clogging in the hopper. A sudden increase in the resonance frequency was observed when the discharging material uncovered the hopper's discharge gate. Conducting repeated experiments could be beneficial in developing experimental models. These models would link the volume occupied in the hopper with the tracked resonance frequency and sound pressure level for various sample resonance non-linearities in the lab-scale resonator.

4.5.3. Resonance non-linearity in the 3-litre resonator

A series of experiments was conducted to better understand the resonance frequency hunting method's limitations and assess the feasibility of measuring powder sample volume in a controlled lab environment.

Water calibration and resonance frequency hunting results in the 3-litre resonator show that the Undriven Resonance Hunting method can hunt the resonator resonance frequency when filled with water up to the maximum Fill Factor of 1. Repeated experiments showed a non-linear deviation between the actual and estimated water volumes. The results from Section 4.4.3 suggest that sample fill level in the cavity causes non-linearity in volume estimation with a repeatable pattern. A maximum deviation of -1.6 % of the full scale was recorded at a Fill Factor of 0.4. At Fill Factors higher than 0.8, the deviation reversed, maximising at Fill Factor 1 with a deviation of +1.6 %. A 2nd order polynomial could be used for calibration to improve the accuracy of water volume estimation; however, to prevent confusion in interpreting the results, this research does not focus on accuracy improvement using data fitting by calibration and mainly focuses on the physics and reporting the non-linearities.

4.5.4. Comparing ports and resonance hunting methods

In these experiments, water was used to set the free volume of the resonator. The idea was to compare the efficiency of using different resonance hunting methods, namely, Undriven, Driven, and Transfer Function, for resonance hunting over the full range of resonator Fill Factors. This set of experiments was conducted on various port lengths of 51, 250, 500 and 1000 mm.

According to the results, resonance frequency was detectable across all Fill Factors, using port lengths ranging from 51 mm to 1000 mm. The detected resonance frequencies obtained using the Undriven, Driven, and Transfer Function methods agreed well. The Transfer Function method provided more consistent results regarding repeatability and precision. Unlike the Undriven and Driven methods, no outliers were recorded using the Transfer Function method. This observation might be attributed to the Transfer Function method's capability for noise cancellation based on signal Coherence data. The Transfer Function method also addressed the non-linearities in signal response when using identical microphones, which could explain its more consistent results.

For the 51 mm port, there was a good agreement between the estimated and actual water volumes, with a mean error *MD%* of ($0.2\%V_0$) and a maximum error of 1.6 %.

Increasing the port length to 250 mm resulted in a linear deviation between the estimated and actual volumes. There was a direct relationship between port length and the deviation. The scope of availability of Classical Helmholtz Resonance can explain this deviation. The classical Helmholtz Resonance model assumes that the resonator dimensions are much smaller than the resonance wavelength.

The experimental results confirm that the ports 250 mm and longer are out of the scope of validity for the classical Helmholtz resonance. The results from this section are further investigated in the next chapter and are used to validate a proposed algebraic equation for sample volume estimation when using ports with lengths comparable to resonance wavelength.

A resonator's working frequency range is a function of the resonator port length. More extended ports resulted in resonance at lower frequencies. By adjusting the resonator port, one can adjust the working frequency range of the resonator to a desirable range depending on the application.

Resonance resolution, defined as the resonator working frequency range divided by resonator cavity volume with the unit of $Hz.ml^{-1}$, had a negative relationship with resonator port length; increasing port length decreases resonance resolution. Resonance frequency variation did not have a linear relationship with volume change. At higher Fill Factors, resonance resolution increases with the power of two of the volumes.

The classical Helmholtz Resonance model was rearranged of resonance wavelength-squared λ^2 to form a linear relationship between λ^2 and cavity volume. By inspecting Figure 4-33, it can be seen that λ^2 had a highly linear relationship with resonator cavity volume for all port lengths. For the 250, 500 and 1000 mm ports, referred to as long ports, the line fit between λ^2 and cavity volume had a constant offset from the estimated values from the classical Helmholtz. This observation is thoroughly investigated further in the next chapter.

4.5.5. Static volume measurement tests

The results of static tests revealed that for samples with particle diameters smaller than 5 mm and larger than 0.25 mm, there was a limitation on the maximum achievable resonator Fill Factor where the resonance frequency could be measured. This limitation was a function of the average particle diameter: the smaller the diameter, the lower the achievable Fill Factor for volume measurement. This observation aligns with Webster's (2010) report on the limitation of the resonator Fill Factor for resonance frequency measurements in powder samples. The achievable Fill Factor increased when the resonator was filled with samples containing very fine particles and packed beds, such as fine sand and agricultural lime, with average particle diameters of less than 0.25 mm. For fine sand, resonance frequency could be measured up to a Fill Factor of 1 for both tapped and loose-poured beds, which is thought to be due to the bed acting as a barrier, reducing the damping effect of the bed.

The initial experiments utilized a 51 mm port. The challenges in maximizing the resonator Fill Factor raised questions about the possibility of achieving higher Fill Factors with successful resonance frequency detection. Efforts to explore various resonance hunting methods and employ longer ports to reduce the resonance frequency were driven by trying to achieve a Fill Factor of 1 in the resonator containing powders.

The samples for which the achievable Fill Factor was limited include agricultural lime, ball bearings, fine and coarse ballotini and mustard seeds. Using the Transfer Function method, the achievable Fill Factor of the 2-litre resonator increased by ~30%, which is thought to be due to the efficiency of the transfer function method in resonance frequency isolation.

Another approach to achieve a Fill Factor of 1 involved using a relatively long port (1 meter; almost eight times longer than the resonator cavity) attached to the 2-litre resonator. When employing a 1 m long port and using the Transfer Function Method for frequency hunting, there were no limitations on the resonator Fill Factor for the tested samples. The primary reasons suggested for this observation include (a) the increased quality factor of the resonance when the port length is extended and (b) the

use of longer ports, which lowered the resonance frequency of the resonator to a range wherein the samples absorbed less acoustic energy. Reason (a) is refuted in Section 4.5.8, while reason (b) is discussed in Section 4.5.10.

4.5.6. Dynamic resonance hunting using the 3-litre lab-scale resonator

These tests were conducted using Driven Resonance Frequency hunting. Earlier tests on the 50-litre vessel and the topdressing hopper were conducted using the Undriven Method. Initial attempts for resonance frequency hunting during material discharge in the lab-scale resonator using the Undriven Method failed. Due to the lack of resonance quality, the computer software could not track resonance frequency using the undriven method. For Driven Resonance frequency hunting, measurement duration was reduced to 1 s from 5 s. For Fill Factors up to 0.75 and 0.85 for agricultural lime (AL2) and black mustard seeds (BMS), the driven method could track resonance frequency change while the sample was discharged. The repeated experiments showed good agreement between the results.

Opening the control orifice to initiate discharge increased the resonance frequency by 500%. Several factors can contribute to this frequency shift in such a highly dynamic system, including rearranging samples in the resonator while discharging, air ingest through the bottom orifice and enabling the discharge orifice as a secondary port to the resonator. However, the experiment was repeatable. For a specific test material, the repeated runs resulted in the same recorded resonance wavelength with a deviation of ±0.15%. Repeated experiments can be used to correlate the resonance wavelength during discharge and the amount of material inside the resonator for rapid fill volume and flowrate measurement.

4.5.7. Port length effect on the resonance quality

As discussed in sources including Kinsler et al. (2000) and Blackstock (2000), the following equation estimates the Quality factor of a Helmholtz Resonator:

$$Q = 2\pi\sqrt{\frac{l^3 V_c}{{S_p}^3}} \qquad \textit{4-41}$$

which describes a direct relationship between port length (l) and Quality Factor (Q). The results of this section demonstrate a discrepancy between the experimental result and this theoretical model for Quality Factors. This disagreement between experimental data and the theoretical model presented in Equation 4-41 was also reported by Webster (2010).

The resonance quality factor was measured using three methods: Undriven resonance decay rate analysis, full width at half maximum in the driven method spectral analyses, and phase shift of transfer

function analysis. When using the Undriven Method for resonance hunting, increasing the port length from 51 mm to 1000 mm reduced resonance quality by up to 25%.

The Resonance Quality from the driven resonance was highly dependent on the driver amplitude *(This observation is highly significant in developing the experimental results of Chapter 7).* As measured by the Driven Resonance hunting method, the resonance quality decreased with an increase in driver sound amplitude. In other words, the resonator's quality factor is a function of the speaker power and distance to the port opening. A similar observation was reported by Komkin et al. (2017)., who reported that sound attenuation by a Helmholtz Resonator is a function of incident sound and frequency. Increasing incident sound pressure levels resulted in a broader absorption, and vice versa; lower sound pressures resulted in narrower and higher attenuations.

By inspecting Figure 4-48, the phase-shift graph generated using the Transfer Function method, the resonance occurred near the phase shift of $\pi/2$ radians, as estimated using Equation 4-23 (Section 4.1.5). This observation contradicts the assumption by Webster (2010) on the approach of Phase Shift to zero when the driving frequency approaches the system's natural frequency. The resonance quality was assessed by plotting the experimental data points against the theoretical estimation graph of quality factor curves, as seen in Figures 4-53.

As discussed in Section 4.5.6, using the 1000 mm port allowed resonance frequency detection for all samples and all fill factors. Port length affects resonance frequency and quality (Blackstock, 2000; Kinsler et al., 2000; Webster, 2010).

Two hypotheses to explain detecting resonance frequency at Fill Factor 1 for all samples using the 1000 mm port are (a) the longer port results in a higher resonance quality factor to obtain a distinct resonance peak in spectral analysis and (b) the longer port results in a lower resonance frequency range at which sound absorption by the powder bed is minimised. The results of this section reject the hypothesis that assumed the 1000 mm port is associated with a higher quality factor in comparison with the 51 mm port (Hypothesis (a) rejected); thus, hypothesis (b) is favourable. As explained in Section 4.5.5, for the 2-litre resonator, the 1000 mm port, compared to the shorter ports, takes the resonance frequency range from hundreds of Hz to frequencies under 80 Hz for all fill factors at room temperature. The energy acoustic absorption is minimal in this region, as discussed in section 4.5.10.

4.5.8. Effect of powders on quality factor

The relationship between cavity volume and resonance quality was examined using water to adjust the resonator cavity volume. Despite fluctuations, the resonance quality remained stable irrespective of the resonator free volume when filled with water.

Increasing the resonator Fill Factor for powder samples decreased the resonance quality factor. The fine sand and agricultural lime (AL1) samples with very low mean particle diameter resulted in resonances with higher quality factors than samples with relatively larger particles up to 3 mm. As the results for static sample volume measurement (Section 4.4.6, Table 4-4) suggest, a maximum Fill Factor of 0.8 and 1 was achievable for samples AL1 and FS, respectively, when using the 51 mm port. The higher resonance quality explains reaching higher Fill Factors with the very fine samples.

Inspecting Figure 4-50, filling the resonator with samples having relatively larger particles, including fine ballotini (B250), coarse ballotini (B710) and mustard seeds (MS), was associated with lower achievable Fill Factors, as seen in Table 4-4. Such samples, which had a substantial decline of quality factor with increasing fill factor, were the hardest to detect resonance frequency.

For samples with an average particle diameter larger than 0.2 mm, there was a linear relationship between the lowest recorded resonance quality and particle diameter. The results of this section suggest that the resonance quality factor is a function of the volume of powders inside the resonator and can be used as a fill factor indicator. This observation is further investigated in Chapter 6, where a semi-empirical model for sample volume measurement is introduced.

4.5.9. Acoustic Energy Absorption Tests

The results of this section verify that all of the tested powder samples tend to absorb less acoustic energy in the lower ends of the tested frequency spectrum (50-2250 Hz). The sound absorption coefficient of ~70 mm thick bed of all samples resulted in values less than 0.03 for frequencies lower than 100 Hz, which covers the resonance range of the resonator when the 1000 mm port is used. For the 51 mm port, the resonance frequency range of the resonator was between 170 Hz and 17,000 Hz. Powder samples had absorption peaks of almost 1 (Perfect Absorption) in this range. This high level of sound absorption explains the limited achievable Maximum Fill Factor when testing for resonance frequency using the shorter ports (51 and 250 mm). This observation explains the hypothesis in Section 4.5.5, which assumes that “The 1000 mm port reduces the resonance frequency, which decreases sound absorption, leading to higher achievable Fill Factors”. The fine sand and agricultural lime samples had no sound absorption peak in the incident sound frequency range. The observed low

sound absorption using these samples can explain the higher achievable Fill Factors when using the 51 mm port compared to other powder samples (Section 4.4.6).

The peaks in the sound absorption coefficients spectrum of the tested samples occurred in the frequencies where almost all of the incident acoustic energy is absorbed. The literature describes this absorption as perfect because of quarter wavelength absorption (Okudaira et al., 1993; Seddeq, 2009; Viet Dung et al., 2019). The frequency location of these peaks depends on sample depth and tortuosity (Horoshenkov & Swift, 2001).

Tortuosity, α_0, for the samples with distinctive sound absorption peaks was estimated by dividing the quarter wavelength that was perfectly absorbed by the apparent sample depth using the following equation:

$$\alpha_0 = \frac{L'}{L} = \frac{0.25\frac{c}{f_{\widehat{\alpha}}}}{L} \qquad 4\text{-}42$$

where L is the sample depth in the impedance tube and $f_{\widehat{\alpha}}$ is the location of the absorption peak in the frequency domain. The tortuosity of the samples ball bearings, black mustard seeds, mustard seeds, large polyethylene, and small marbles was estimated using Equation 4-42 to be 1.25, 1.52, 1.43, 1.33, and 1.21, respectively. From Equation 4-42, the depth at which Quarter-Wavelength absorption, $L_Q$occurs in an open−pore sample can be estimated as:

$$L_Q = \frac{\lambda_L}{4\alpha_0} \qquad 4\text{-}43$$

where λ_L is the resonance wavelength of the Helmholtz Resonator at Fill Factor 1 for the specific sample. When designing a resonator for powder volume estimation, it's essential to ensure that the resonator depth (L) is significantly smaller than L_Q ($L << L_Q$). Applying design equation 4-43 to all the open-pore samples tested in the 2-litre resonator with the 1000 mm port, the resonator depth was found to be less than 0.15 times the depth at which quarter-wavelength absorption occurs ($L<0.15L_Q$).

Horoshenkov & Swift (2001) suggest that flow resistivity affects the height of the sound absorption peak. The results of this section confirm this. Test material with a higher permeability demonstrated sound absorption peaks with lower heights. Agricultural lime, fine sand and fine ballotini, the samples with the lowest permeability among all samples, had absorption peaks much shorter than the samples with higher permeabilities.

4.5.10. Compression uniformity test

The presence of powders inside the resonator caused non-uniform compression within the resonator. Figure 4-63 depicts the compression non-uniformity in an instance of time. Consider a mass of air in the port of the resonator that oscillates. Maximum compression, shown in red, occurs at the end of the port air mass travel into the resonator, as shown in Figure 4-63 (a). Maximum expansion, shown in blue, occurs when the elasticity of the air inside the cavity pushes the mass of the air in the port out of the resonator to a maximum point, as shown in Figure 4-63 (b). When the 2-litre resonator was filled with fine sand, a phase mismatch of almost π radian between the top and the bottom pressure wave signals was observed. This phase mismatch is shown in the bottom part of Figure 4-63. At the instance when the air at the top of the resonator cavity was undergoing compression, the air at the bottom was expanding and vice versa. This non-uniformity in air compression inside the cavity violates the assumption of almost uniform compression in the classical Helmholtz Resonance model. This observation can explain the deviation between actual sample volume and estimations from classical Helmholtz Resonance that Inoue et al. (2021) and Webster (2010) observed. Inoue et al. reported a deviation of up to 58%, and Webster reported a significant deviation between the actual sample volume and the estimated volume using Helmholtz Resonance.

Samples with higher permeability caused a lower compression non-uniformity in the resonator and vice versa; the lower the permeability, the more significant the phase mismatch. For example, the samples coarse ballotini B710 (K=256 darcy), fine ballotini B250 (K=55 darcy) and fine sand FS (K=11 darcy) had the pressure signal phase mismatch of up to 21, 88 and 364 degrees, respectively. This observation suggests that compression non-uniformity in the resonator is a function of the static air flow resistivity of the bed of particles.

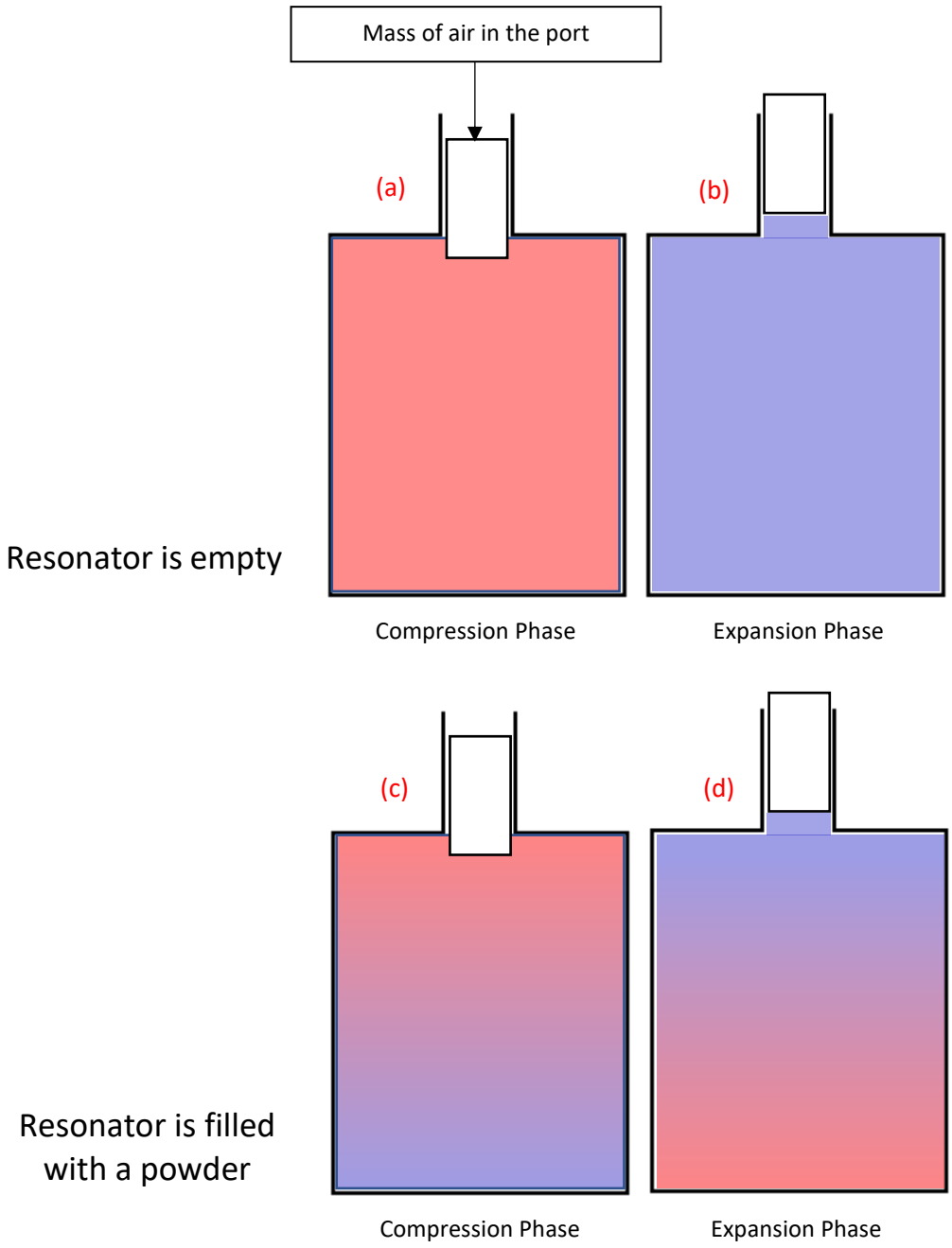


***Figure 4-63**: Non-uniformity in air compression for when the resonator is empty (Top) and for when the resonator is filled with powders samples (Bottom).*

4.5.11. Sound wave penetration speed

A method was proposed to measure the speed of sound in a bed of particles. Because the sound wave was captured in the air phase of the bed of particles, the delay in sound transfer through the bed was correlated to sample tortuosity. Sound wave penetration speed in the bed of particles was significantly lower than the speed of sound in the air. It can be explained by the tortuose path that sound waves take when travelling through the bed of particles. Unlike compression non-uniformity

correlated to the permeability of the sample beds, the speed of sound penetration was neutral to permeability and was related to bed voidage and, to a lesser extent, to sample particle diameter. The mustard seeds sample with the lowest bed voidage (0.29) had the highest tortuosity (1.47).

For the samples FS, AL2, B250, BMS, MS, BB, PE1 and PE2, the penetration speed of sound ranged from 234 to 259 $m.s^{-1}$, a variation of a maximum of 10%, correlated to the variation of sample tortuosity (Table 4-7).

No correlation was observed between the speed of sound penetration into the bed of particles and resonance hunting parameters, including quality factor, the maximum achievable fill factor, and deviation between estimated and actual sample volume.

The estimated tortuosities in this section were close to the estimates made using the impedance tube (section 4.5.9) with an average deviation of 2%.

4.6. Summary

When a powder mass is put into the cavity of a resonator, the resonance frequency is associated with the volume that the powder sample occupies from the cavity. To perform a volume measurement using the Helmholtz Resonance principle, a Helmholtz Resonator containing a sample must be acoustically excited to hunt for resonance frequency. This excitation can be performed in two main methods: Undriven and Driven. Undriven excitation refers to exciting the resonator with a short burst of acoustic energy and immediately removing the excitation force. Driven excitation refers to exciting the resonator continuously by a sinusoidal wave. A Helmholtz Resonator can be considered analogous to a Mass-Spring-Dashpod resonator, and the governing equations for natural frequency location are identical. In an Undriven resonance, the decay of resonance amplitude follows the logarithmic resonance decay of a mass-spring-dashpot system.

There are challenges to overcome in a resonator cavity containing a powder sample. The main challenge arises from the sound-absorptive nature of powders. The sound absorption in powders limits the maximum Fill Factor of a resonator at which the resonance frequency can be hunted.

A resonance hunting method known as the Transfer Function method was detailed. This method involves extracting the resonance frequency from the magnitude of the transfer function between two microphones: one positioned in front of the driver speaker and the other inside the resonator port. It has been employed for noise cancellation and to compensate for non-linearities in both the microphones and the loudspeaker. As a result, there is an enhanced sensitivity to the resonance frequency. Utilizing this method has led to an increase in the achievable Fill Factor in the resonators for various powders, and it has also improved the repeatability of measurements compared to the traditional single microphone method.

The ultimate solution for achieving the Fill Factor of 1 for all powder samples under study was to use a radically long port, which was 1 m long, eight times longer than the resonator cavity. Replacing the 51 mm port with a 1000 mm port shifted the resonance range (depending on the Fill Factor) of the 2-litre resonator from 170-1700 Hz to a frequency range of 40-80 Hz.

An impedance tube was designed to measure the powder samples' sound absorption coefficient (α). All samples had a minimal sound absorption (α<0.03) for sound frequencies under 100 Hz at a bed thickness of up to 70 mm. Minimal sound absorption in frequencies below 100 Hz justifies using a long port to lower the resonator's resonance frequency range.

The 1000 mm port made it possible to hunt resonance for all samples, but the dimensions of the resonator with this port fall out of the scope of availability of the classical Helmholtz Resonance model;

therefore, estimation of sample volume based on resonance frequency requires an alternative model which estimates sample volume inside a resonator with a port with the length comparable to resonance wavelength. This requirement was one of the research problems addressed in Chapter 5.

Dynamic discharge tests were conducted on a lab scale resonator, a 50-litre vessel and a topdressing hopper. Resonance amplitude and frequency were correlated to the amount of material inside the resonator. As the material discharged, the resonance frequency increased. For samples with large particles, the sound pressure amplitude negatively correlated with the amount of material, with a significant fluctuation when the material level discharges to the orifice level.

The sample particle size and the Fill Factor govern resonance quality when filled with powders. The resonance quality decreased with increasing the amount of powder sample inside the resonator.

When a resonator was filled with powders, air compression inside the cavity became non-uniform, which violates the assumption of uniform compression in a Helmholtz Resonator and, hence, takes resonance out of the scope of the Classical Helmholtz Resonance model. This non-uniformity in the compression inside the resonator explains the deviation between the estimated and actual sample volumes. Chapter 6 discusses this deviation between the actual and estimated powder sample volumes and proposes a model for minimising it.

Chapter 5 Extended Helmholtz Resonance model

5.1. Introduction

As discussed in the previous chapter, it is not easy to make a Helmholtz Resonator resonate when filled with specific powder samples (see Sections 4.4.6 and 4.5.6). This is due to the high sound absorption of some powder samples (see Section 4.4.10). This limitation results in a limited Fill Factor for each sample to perform resonance hunting. It was observed that this limitation occurs with short ports, and using a 1-meter-long port resolved the limitation. More extended ports were suggested to shift the resonance frequency to lower regions where powder samples do not absorb minimal acoustic energy.

The classical Helmholtz Resonance model is developed, assuming the resonator dimensions are smaller than 1/16 of the resonance wavelength. This assumption is violated when using a comparatively long port (a port longer than 1/16 of the resonance wavelength), which is of interest in overcoming the mentioned limitation in reaching high Fill Factors. As discussed in Section 4.5.5 (water calibration), the classical Helmholtz Resonance equation resulted in up to a 25% error from the actual water volume when the 1000 mm port was used.

This chapter presents an algebraic equation for estimating sample volume using Helmholtz Resonance with an extended port. This model approximates the transcendental generalized Helmholtz Resonance model by Tang & Sirignano (1973) in an algebraic form, enabling the estimation of sample volume based on the resonance wavelength of a Helmholtz Resonator. The primary advantage of the model introduced in this chapter over the generalised Helmholtz Resonance model lies in its simplicity. It offers a direct estimation of the sample volume, eliminating the need to combine chamber dimensions and bypassing the requirement for numerical analysis.

The trigger for the development of this model was the observed linear offset between actual resonator cavity volume and estimations from the classical Helmholtz Resonance model presented in Chapter 4, Section 4.4.4.

5.2. Model Development

Some of the equations introduced in previous chapters are being reintroduced in this chapter to maintain consistency in the text structure.

Tang & Sirignano (1973) proposed a model that combined the continuity and momentum equations in various regions of a Helmholtz Resonator. They derived the following transcendental expression for the resonance location based on resonator dimensions:

$$tan(k_r l) \times tan(k_r L) = \frac{S_p}{S_v} \qquad 5\text{-}1$$

where L is the cavity length, S_v is the cavity cross-sectional area and k_r is the resonance wavenumber. Hereafter, the transcendental equation refers to the model in Equation 5-1.

In a similar study, Selamet et al. (1994) examined the transmission loss of a Helmholtz Resonator attached to a tube. They modelled the resonator using a one-dimensional wave propagation equation in various regions of the resonator, assuming a fixed reservoir volume. The results of their study confirmed the transcendental model (Equation 5-1).

Panton and Miller (1975) approximated the transcendental equation for the case of a Helmholtz Resonator with an extended cavity, where the cavity length L is comparable to or larger than the resonance wavelength) and proposed the following model:

$$\omega_0 = c\left(\frac{S_p}{lV_c + \frac{1}{3}L^2 S_p}\right)^{0.5} \qquad 5\text{-}2$$

where ω_0 is the angular resonance frequency. They estimated an error of less than 10% for locating the resonance frequency based on resonator dimensions for most practical applications.

The model proposed in this chapter builds upon the previous works of Tang and Sirignano (1973), Panton & Miller (1975), and Selamet et al. (1994) for correlating the resonance wavelength to the resonator volume. The theoretical approach for developing this model involves linearizing and approximating the transcendental equation by substituting the cavity dimensions with the volume V_c.

The first assumption is that the length of the chamber is short enough to fulfil the condition $k_r L \ll 1$ then, in Equation 5-1, $\tan(k_r L)$ can be replaced by $k_r L$, simplifying it to:

$$k_r L\, tan(k_r l) = \frac{S_p}{S_v} \qquad 5\text{-}3$$

The resonator cavity volume is:

$$V_c = LS_v \qquad 5\text{-}4$$

Wavenumber and wavelength are related to each other using the following:

$$k_r = \frac{2\pi}{\lambda} \qquad 5\text{-}5$$

where λ is the wavelength.

Rearranging 5-3 based on 5-4 and 5-5 gives:

$$cot\left(\frac{2\pi l}{\lambda}\right) = \frac{2\pi V_c}{\lambda S_p} \qquad 5\text{-}6$$

Applying a Taylor series expansion of the left side of 5-6 gives:

$$cot\left(\frac{2\pi l}{\lambda}\right) = \frac{\lambda}{2\pi l} - C_{res} = \frac{2\pi V_c}{\lambda S_p} \qquad 5\text{-}7$$

where $C_{\text{res}} = \left[\frac{2\pi l}{3\lambda} + \frac{(2\pi l)^3}{45\lambda^3} + \frac{2(2\pi l)^5}{945\lambda^5} + \cdots\right]$ is the subsequent terms in the expansion after $\frac{\lambda}{2\pi l}$.

Assuming a relatively large wavelength and taking C_{res} out of 5-7 (C_{res}=0), Equation 5-7 becomes:

$$\lambda^2 = \frac{4\pi^2 V_c l}{S_p} = \frac{V_c}{\alpha^2} \qquad 5\text{-}8$$

which is the Classical Helmholtz Resonance model (See Basic Equations).

Multiplying Equation 5-7 by $2\pi l\lambda$ gives:

$$2\pi l\lambda \times cot\left(\frac{2\pi l}{\lambda}\right) = \lambda^2 - \acute{C}_{Res} = \frac{V_c}{\alpha^2} \qquad 5\text{-}9$$

where:

$$\acute{C}_{Res} = 2\pi l\lambda C_{res} = \left[\frac{(2\pi l)^2}{3} + \frac{(2\pi l)^4}{45\lambda^2} + \frac{2(2\pi l)^6}{945\lambda^4} + \cdots\right] \qquad 5\text{-}10$$

The term $\acute{C}_{Res}$ is a function λ and l: $\acute{C}_{\text{res}} = f(\lambda(m)\ ,\ l(m))$ with the dimension m^2.

Both λ and l have the same dimension and magnitude of m. It is assumed that resonance wavelength in a resonator with a very small cavity is a function of port length: $\lambda = f(l)$. With this assumption, $\acute{C}_{Res}$ can be approximated solely based on the port length, as depicted in Figure 5-1, and represented as:

$$\acute{C}_{Res} \sim f(l) \qquad 5\text{-}11$$

From the boundary condition that the cavity volume approaches zero, the term $\frac{V_c}{\alpha^2}$ in the right-hand side of 5-9 vanishes, and the following expression can be derived:

$$\acute{C}_{res} = \lambda_0^2 \qquad 5\text{-}12$$

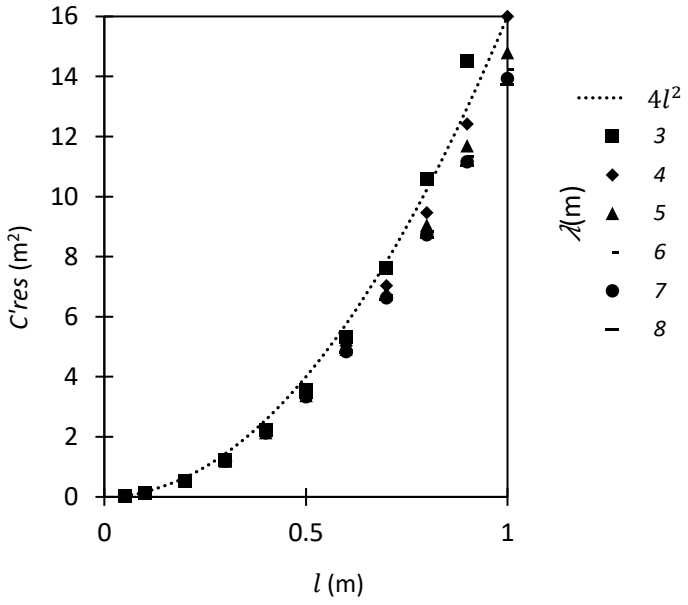


***Figure 5-1**: Numerical approximation of $\acute{C}_{res}$ to $(4l)^2$ for a range of port lengths (l) and wavelengths (λ).*

To have a zero value on the left side of 5-9, *cot (2πl/λ)* must equal zero. Hence:

$$\frac{2\pi l}{\lambda_0} = \frac{(2n-1)\pi}{2} \qquad 5\text{-}13$$

where *n* is an integer. For the first harmonic (*n=1*), 5-13 reduces to:

$$\lambda_0 = 4l \qquad 5\text{-}14$$

Putting Equation 5-14 into Equation 5-12 and rearranging Equation 5-9, a model for Helmholtz Resonance for a resonator with a small cavity compared to resonance wavelength can be proposed as follows:

$$\lambda^2 = \frac{V_c}{\alpha^2} + (4l)^2 \qquad 5\text{-}15$$

Hereafter, Equation 5-15 is referred to as the Extended Helmholtz Resonance (EHR) model, which is the classical Helmholtz Resonance model rearranged for wavelength (Equation 5-8) with the added term $(4l)^2$.

Figure 5-2 shows a numerical comparison between the transcendental equation (Equation 5-1), plotted using solid lines, and the extended Helmholtz resonance model plotted using dots. For the generation of Figure 5-2, both models were plotted as a function of port length with other parameters

fixed. The numerical comparison in Figure 5-2 is based on three cavity volumes of 2, 3 and 10 litres. The cavity cross-sectional area for all three volumes is the same and was chosen to be equal to the cross-sectional area for the cavity of the resonator used for the experiments in this section (S_v= 0.0153 m^2). Chamber length to chamber diameter (*L/D*) for the three cavity volumes of 2,3 and 10 litres is roughly 0.9, 1.4 and 4.6, respectively. The constant port diameter for all plots is 0.044 m, the physical port diameter of the resonators tested in this chapter.

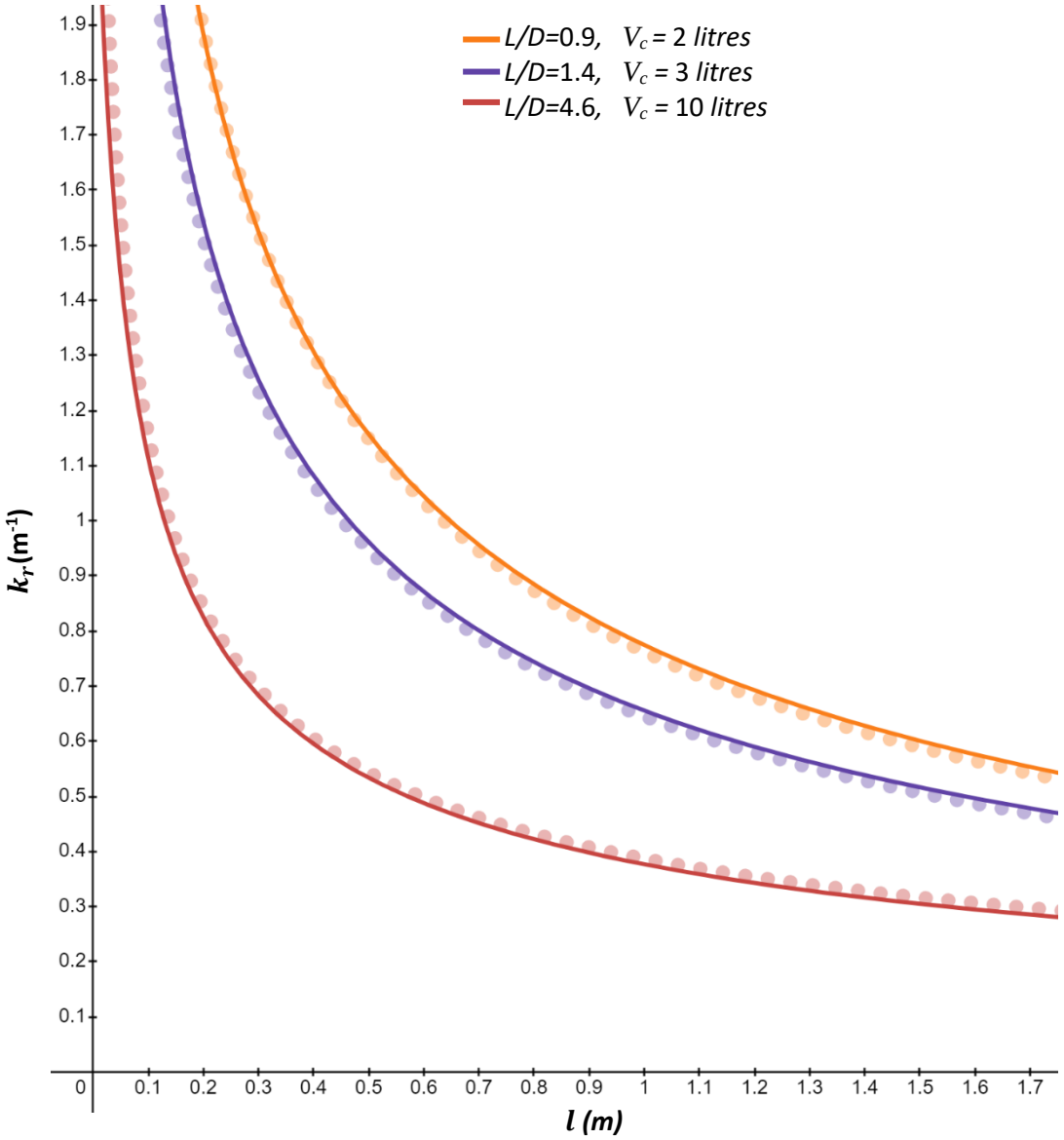


Figure 5-2: *Comparision of the estimated wavenumber* $\boldsymbol{k_r}$ *versus port length l generated using the the transcendental equation (**solid lines**) and the Extended Helmholtz Resonance Model (**dots**).*

As is shown in Figure 5-2, the transcendental model (Equation 5-1) is in agreement with the extended Helmholtz Resonance model for resonator volumes 2, 3 and 10 litres with a maximum deviation of less than (1%).

Interestingly, the first term on the right-hand side of Equation 5-15 ($\frac{V_c}{\alpha^2}$) and the second term $(4l)^2$, represent the resonance wavelength squared for the classical Helmholtz Resonance model and the port as a quarter-wavelength resonator, such as an organ pipe, respectively. This model provides an algebraic solution for correlating the cavity volume to the resonance wavelength, and it can also be applied to resonators with longer ports, provided that the dimensions of the chamber are smaller than the resonance wavelength.

Extended Helmholtz resonance model, Equation 5-15, can be rearranged in terms of frequency to give Equation 5-16:

$$f = \frac{c}{2\pi}\sqrt{\frac{S_p}{lV_c + \frac{4l^2 S_p}{\pi^2}}} \qquad \textit{5-16}$$

Table 5-1 summarises three algebraic equations for resonance location in a Helmholtz Resonator based on cavity volume and port geometry.

Table 5-1*: Comparison of three algebraic equations of Helmholtz Resonance and their scope.*

Name	Model	Scope
Classical Helmholtz Resonance (Helmholtz, 1877)	$f = \frac{c}{2\pi}\sqrt{\frac{S_p}{lV_c}}$	Resonators with small dimensions compared to the resonance wavelength
Modified Helmholtz Resonnace (Panton & Miller, 1975)	$f = \frac{c}{2\pi}\sqrt{\frac{S_p}{lV_c + \frac{1}{3}L^2 S_p}}$	Resonator with small port compared to the resonance wavelength
Extended Helmholtz resonance (EHR) model that this thesis proposes	$f = \frac{c}{2\pi}\sqrt{\frac{S_p}{lV_c + \frac{4l^2 S_p}{\pi^2}}}$	Resonator with small cavity compared to the resonance wavelength applicable to short and long ports

A method based on the extended Helmholtz resonance model is now introduced to estimate the volume of a sample inside the resonator. By taking two consecutive resonance frequency measurements and calculating wavelengths using $\lambda = c/f$, when the resonator cavity is empty, *State* 0, and when it contains a sample with the volume V_s, *State* 1, Equations 5-17 and 5-18, are written for both states:

$${\lambda_0}^2 = \frac{V_c}{\alpha^2} + (4l)^2 \qquad \textit{5-17}$$

$${\lambda_1}^2 = \frac{V_c - V_S}{\alpha^2} + (4l)^2 \qquad \textit{5-18}$$

Dividing Equation 5-18 by 5-17 and with some algebraic manipulation:

$$V_s = V_c\left(1 - \frac{{\lambda_1}^2 - (4l)^2}{{\lambda_0}^2 - (4l)^2}\right) \qquad 5\text{-}19$$

When using Equation 5-19 for sample volume estimation, the geometrical values required for sample volume measurement are reduced to the empty volume of the cavity and the physical port length.

5.3. Experimental Data

The data used for experimental analysis of the model expressed as 5-19 were those obtained by the method explained in Chapter 4, Sections 4.3.7 and 4.3.8. The results are presented in Chapter 4, Sections 4.4.4 and 4.4.5. To keep the text coherent, a briefing of the materials, methods, and samples used for the generation of the experimental data of this chapter is presented.

The Resonator as detailed in Chapter 4, Section 4.2.1: Small Scale Resonator

The resonator used was the 2-litre resonator introduced in Chapter 4, Section 4.2.1. Four-port lengths of 51 mm, 250 mm, 500 mm, and 1000 mm were used for the water model verification. Experiments on powder and particle samples were conducted on all ports except the 500 mm port.

Resonance frequency hunting as detailed in Chapter 4, Section 4.3.3: Resonance Hunting Method 3, Transfer Function

The resonance frequency hunting was conducted by locating the peak magnitude of a transfer function between the reference signal (the microphone in front of the speaker) and the resonance signal (the microphone inside the port).

Test material as detailed in Chapter 4, Section 4.2.11, Samples

The resonator cavity volume was adjusted using incremental additions of reverse osmosis (RO) water with known mass. The exact empty volume of the resonator cavity after adding water was used for model verification. Solids and powders that were used for volume measurement using the proposed model were large marbles (LMB), small marbles (SMB), ball bearings (BB), mustard seeds (MS), coarse ballotini (B710), fine ballotini (B250), fine sand (FS) and agricultural lime (AL1).

Experimental Procedure as detailed in Chapter 4, Sections 4.3.7 and 4.3.8

Water calibration tests were conducted to verify the proposed model for each port connected to the 2-litre resonator. Water was added in 300 ml increments until the resonator cavity was filled. The resonance frequency and ambient temperature were recorded, and the predicted water volumes, calculated using Equation 5-19, the extended Helmholtz resonance model adopted for volume determination, were compared to the actual water volumes.

For sample volume estimation, the samples were added to the 2-litre resonator with the 1000 mm port attached in increments of approximately 400 ml until the resonator was filled to its maximum capacity. A Perspex perforated plate with a handle attached to its centre (Chapter 4, Section 4.3.8. Drawing available in Appendix E) was placed at the bottom of the resonator before loading powder samples. The powder samples, MS, B250, B710, FS, and AL1, were poured onto the perforated plate, and the perforated plate was gently pulled out to create loose packing in the sample. The resonator port was then fixed to the resonator and secured with four bolts. After measuring the resonance frequency, the port was removed, and the resonator was mounted on a tapping machine. The machine was fitted with a 5 kg tapping plate that dropped 10 mm 90 times per minute; the resonator was tapped 120 times. The port was then reattached to the resonator, and the resonance frequency was measured again for the tapped sample.

5.4. Results

5.4.1. Model Verification

Figure 5-3 shows the estimated resonator fill factor *FF*, the ratio of occupied volume to resonator volumetric capacity, based on the classical and extended models. Resonator Fill Factor refers to the volume of water in the resonator compared to the cavity volume.

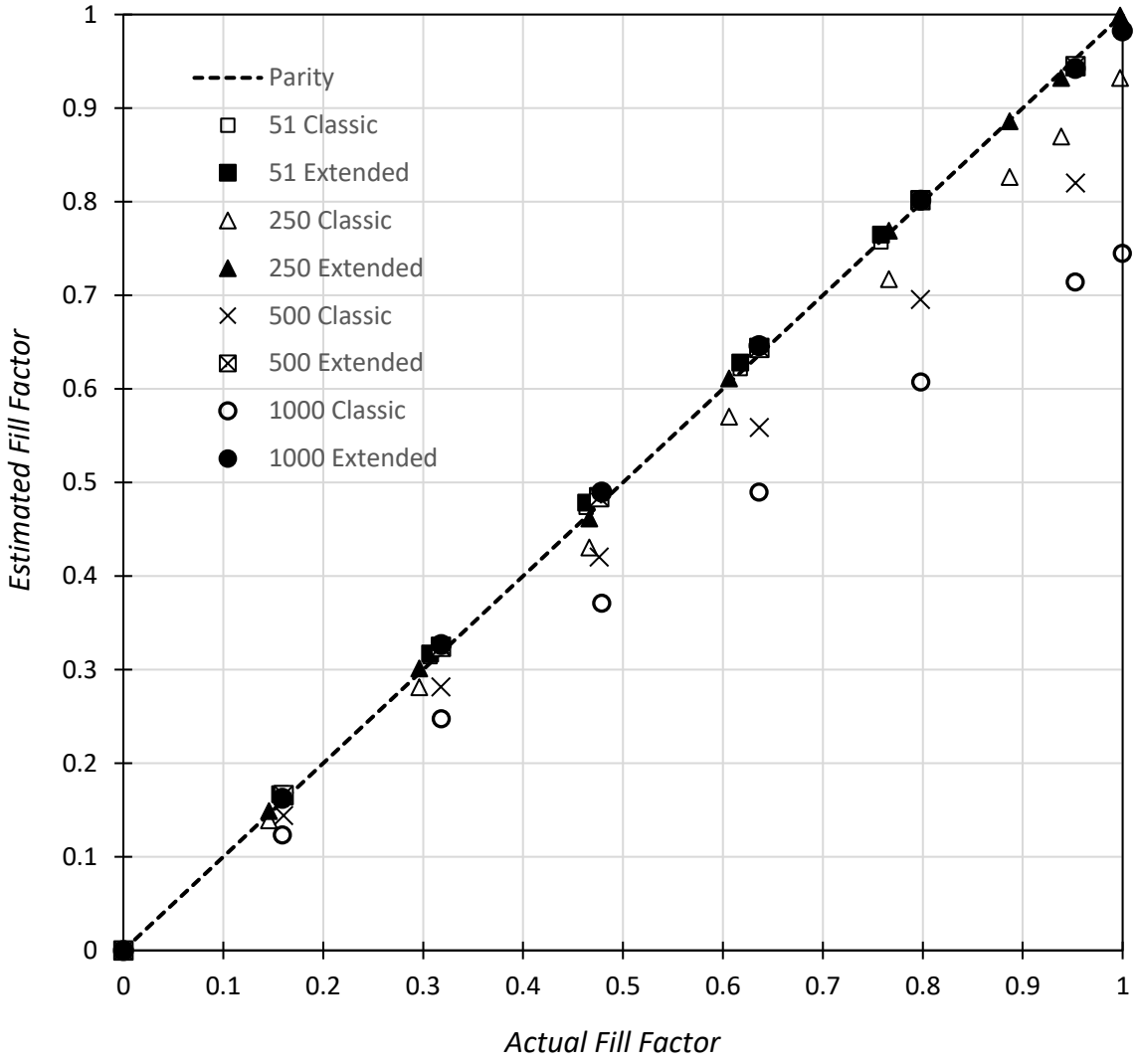


Figure 5-3: *Comparison of estimated fill factor versus actual fill factor. The numbers in the chart legend represent port lengths in millimetres. "Classic" refers to the classical Helmholtz Resonance model, and "Extended" refers to the extended Helmholtz Resonance model.*

Figure 5-4 compares the $MD\%$ from the actual volume for the Classical Helmholtz Resonance model, the extended model using Equation 5-19 and the transcendental equation (Equation 5-1). The mean deviations are calculated based on the percentage of the cavity volume and calculated using: $MD\% = \frac{100}{n}\sum\frac{|V_A - V_E|}{V_0}$ where V_A is the actual volume, V_E is the estimated volume, V_0 is the cavity

volume, and n is the number of measurements. The error bars represent one Standard Deviation (*SD*) of estimated values from the actual values. When using the classical Helmholtz Resonance model, $MD\%$ increased point length. The maximum deviation was recorded for the 1000 mm port using Classical Helmholtz Resonance model. The volume estimation using this port resulted in a $MD\%$ of 13%. Conversely, the classical model recorded the minimum mean deviation of 0.61% when using the 51 mm port, the shortest.

The mean deviation for the transcendental equation remained below 1%, except for the 51 mm port, which reached 2.6%.

The proposed model in the study maintained a mean deviation of 1% for all four ports. While the extended model is an approximation of the transcendental equation, the experimental data recorded a comparatively higher accuracy (99 % vs. 97.4 %). The extended model negates the need to measure the port extension factor (Δl). For the transcendental equation, the value of the port extension factor was calculated using 8a/3π+0.6a equivalent to 0.0318 m (See Chapter 4, Section 4.1.1), which was the best fit for this port in agreement with Webster's (2010) measurement.

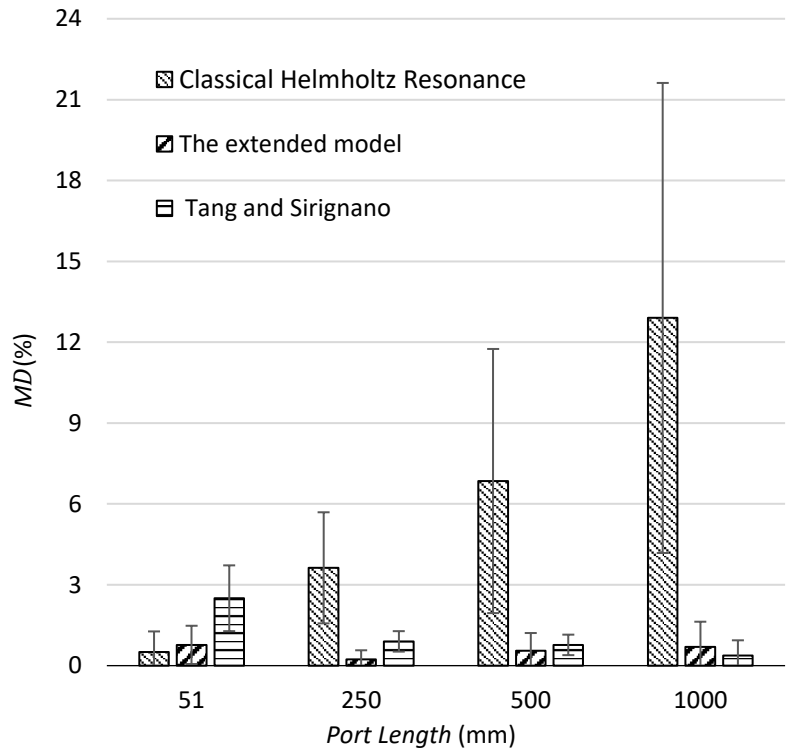


Figure 5-4: *Average deviation of the estimated volume from the actual volume based on the experimental data for various models.*

Figure 5-5 is a plot of wavelength squared versus cavity volume. The estimations using the extended model are plotted using lines, and the experimental observations are plotted using markers.

As shown in Figure 5-5, the estimated resonance wavelengths agree with the experimental data, and the results are highly linear ($R^2 \cong 1$) supporting the extended model's validity in the experimental scope.

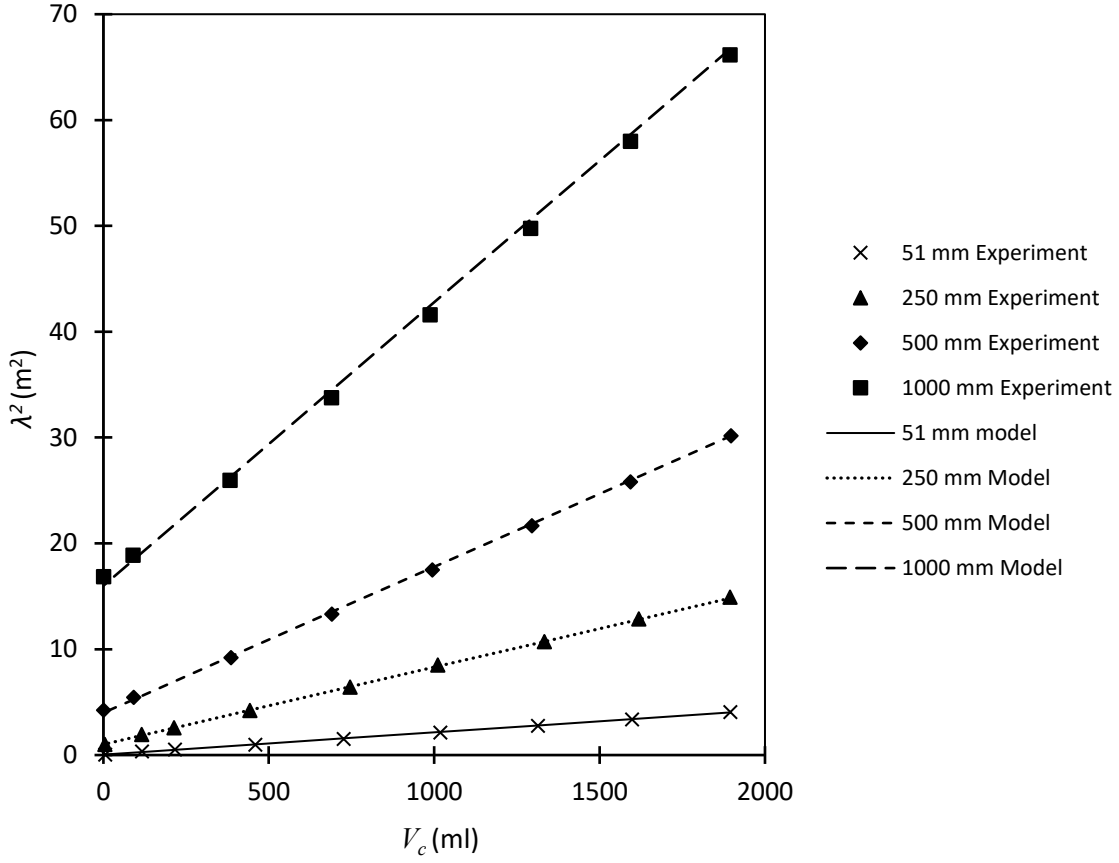


Figure 5-5*: Resonance Wavelength squared vs cavity empty volume for various port lengths. "Model" refers to the extended Helmholtz resonance model. The "# mm"s in the legend are port lengths.*

5.4.2. Solids and powders volume measurement

Figure 5-6 shows volume estimation using the extended model for the powder and solid samples in the 2-litre resonator with the 1000 mm port. The estimated sample solid volume V_S based on the extended model and the actual sample solid volume V_A are plotted against each other. The volume of samples with fine particles was generally overestimated as the data points are above the parity line. These samples include fine sand (FS), agricultural lime (AL1), and fine ballotini (B250). Conversely, the solid volume of samples with larger particles, including coarse ballotini (B710), ball bearings (BB), mustard seeds (MS) and marble samples, was underestimated as the data points are beneath the parity. For large marble (LMB), sample volume was predicted accurately with a mean deviation of 0.15%.

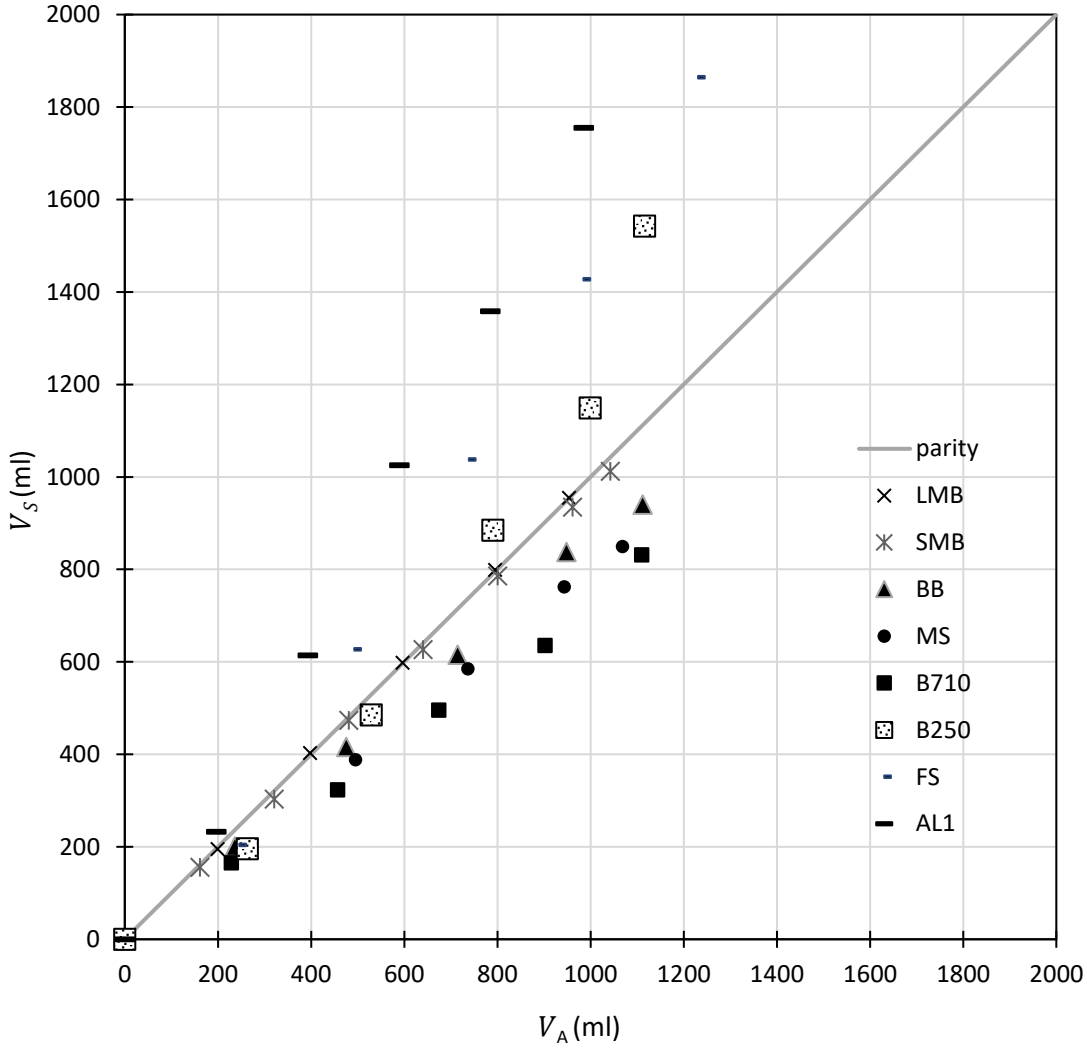


***Figure 5-6**: Estimated solid volume V_S vs actual solid volume V_A.*

Figure 5-6 shows a deviation between the estimated and actual solid volume for all samples except for large marble. The arbitrary parameter Depth Penetration Factor (*DPF*) is defined in Equation 5-20 to discuss this deviation. Parameter *DPF* quantifies the effective sample bed depth at which the void fraction of the sample is involved in cavity pressure fluctuations:

$$DPF = \frac{(V_s - V_b)}{\phi V_c} \qquad 5\text{-}20$$

where V_b is the sample bulk volume, and ϕ is the percentage of bed voidage. Consider the resonator filled with a sample (Fill Factor=1). In this resonator, when the particles in the bed are tightly packed, effectively acting as a barrier to the penetration of pressure waves, the *DPF* is 0. In such a scenario, the void volume of the sample isn't measured, and the estimated sample volume matches the sample's bulk volume. A *DPF* of 1 suggests that the sample's void volume is precisely measured,

resulting in an estimated sample volume equivalent to the sample's solid volume. In Figure 5-6, samples below the parity line have DPF values exceeding 1, which is physically impossible. It underscores a non-linearity when performing volume measurements on samples falling in this group. These samples have average particle diameters ranging from larger than 0.5 mm to smaller than 15 mm. The estimated solid volume using the extended model is less than the actual volumes for these samples.

In contrast, the solid volume was overestimated for samples with an average particle diameter of 0.25 mm or less with a *DPF* value less than 1. The large marble (LMB) sample was the sole one with a *DPF* of 1. Table 5-2 lists the *DPF* values. As the table provides, tapped packing reduced the *DPF* for all powder samples.

Table 5-2: *Depth Penetration Factor for selected tapped and loosely packed materials.*

Material	Loose Poured	Tapped	Volume Estimation (D% at FF=1)
	Depth Penetration Factor (DPF)		
agricultural lime (AL1)	0.17	0.13	Over**(+40)
fine sand (FS)	0.28	0.19	Over(+33)
ballotini (B250)	0.73	0.51	Over (+22)
ballotini (B710)	1.44	1.34	Under** (-15)
mustard seeds (MS)	1.7	1.69	Under (-12)
ball bearings (BB)	1.22	NA	Under (-10)
small marbles (SMB)	1.02	NA	Under (-1.5)
large marbles (LMB)	1	NA	Exact** (±0.5)

**NA: Not Applicable **Over: The estimated values were greater than the actual values; Under: The estimated values were less than the actual values; Exact: The estimated values agreed with the actual values.*

Figure 5-7 illustrates the relationship between the estimated cavity void fraction and Fill Factor *FF* for various loads of the material inside the resonator. This figure intends to represent the estimated voidage of the bed for various fill factors. In Figure 5-7, the ordinate is the void fraction of the cavity, which is $1 - V_S/V_c$ where V_S is the estimated sample volume using the extended Helmholtz resonance model. The abscissa is the actual fill factor of the resonator.

The diagonal lines represent the estimated voidage. When loading water in the resonator, voidage is null, as shown in Figure 5-7, where the data points of water are located on the *φ=0* line. For the sample of ballotini B710, the estimated voidage was the highest among all the tested materials. For ballotini B710, the estimated voidage ranged between 50% and 60%.

The deviation from the actual values of voidage grew as the fill level increased.

The DPF value of each sample, as outlined in Table 5-2, was correlated to the voidage estimations. For samples with a *DPF* greater than 1, the estimated voidage was higher than the actual voidage; conversely, voidage was lower than actual values for those with a *DPF* less than 1.

In Figure 5-7, inspecting the data points around the diagonal line $\varphi=0$ and close to *FF=1*, including the tapped fine sand FS, ballotini B250 and agricultural lime, reveals that the voidage is estimated to be nearly zero, which is not physically accurate. This observation suggests that the estimated values for the volume of these samples were close to the sample bulk volume. These powder samples had the finest particles among all the samples.

The samples near the higher diagonal lines had mean particle diameters larger than 1 mm, and the estimated volumes reflected the sample's solid volume.

For small marbles (SMB), the estimated bed voidage closely matched the actual value of 43%. The estimated volume was roughly equal to the actual sample volume for this test material.

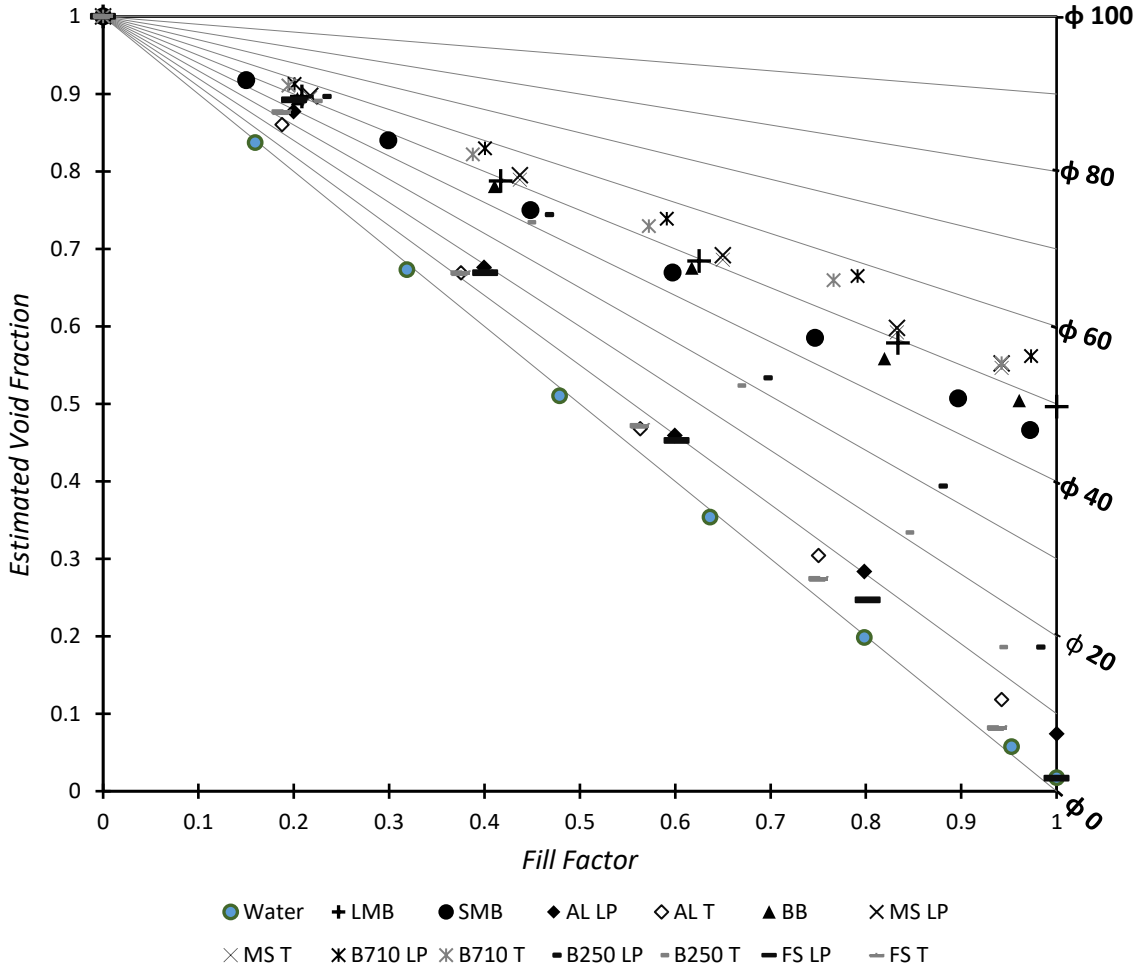


***Figure 5-7**: Volume fraction of the samples vs. Fill Factor of the resonator. The diagonal lines represent the estimated void fraction.*

As shown in Table 5-3, the deviation of the estimated solid volume from the actual solid volume decreased with increasing particle diameter. The maximum deviation of sample volume from the actual value was calculated using the following:

$$D\% = \left|\frac{100(V_S - V_A)}{V_C}\right| \qquad 5\text{-}21$$

where $D\%$ is the percentage of deviation between the estimated volume and bed solid volume based on vessel capacity.

Table 5-3: A comparison between particle diameter and volume deviation from the parity.

Sample	D[3,2] (mm)	$D\%$
LMB	24.76	<1
SMB	15.97	2
BB	3.175	10
MS	1.98	17
B710	0.67	15
B250	0.24	22
FS	0.11	33
AL1	0.06	41

5.5. Discussion

5.5.1. Model Verification

The Experimentally estimated cavity volumes agreed with the estimated values from the extended Helmholtz Resonance model. The average disparity between the model and the experimental observation remained under 1%V_0 (percentage of vessel capacity) for all port lengths from 51 mm to 1000 mm. Disparities at different Fill Factors followed a normal distribution.

The extended model was also verified using the 3-litre resonator with the 1000 mm port. The results suggest that the proposed model is valid for the scope of experiments conducted in this study.

In calculating sample volume using the extended model, the highest accuracy was obtained using the actual physical port length in the organ pipe term of the model $(4l)^2$. Consequently, when calculating sample volume using Equation 5-16, which is the extended model based on resonance frequency, the highest agreement of ±0.1% with the experimental observation was obtained when a port length extension of $\Delta l = 0.0318$ mm, as discussed in Section 4.1.1, was introduced to the model in the following order:

$$f = \frac{c}{2\pi}\sqrt{\frac{S_p}{(l+\Delta l)V_c+\frac{4l^2S_p}{\pi^2}}} \qquad 5\text{-}22$$

The Extended Helmholtz Resonance model extends the Classical Helmholtz Resonance model, enhancing its validity for resonators with longer ports. For a very short port, the term $\frac{4l^2S_p}{\pi^2}$ in the denominator of Equation 5-22 vanishes, reducing it to the classical Helmholtz Resonance model.

All results presented in this chapter were obtained without the use of any statistical correction methods. For consistency with the rest of the study, the duration of resonance hunting was maintained at 10 seconds, as introduced in Chapter 4, Section 4.3.3. Nevertheless, when using the extended Helmholtz resonance model, the accuracy of sample volume measurement can be theoretically improved by extending the duration of resonance frequency hunting. Additionally, statistical correction factors can be utilized to compensate for non-linearities, as detailed in Chapter 4, Section 4.4.3.

5.5.2. Solids and powders volume measurement

The solid volume of marble samples with particle diameters >15 mm was measured accurately using the extended Helmholtz resonance model. For the large marble sample, volume estimation accuracy was comparable with the accuracy of measuring water volume, <0.5%V_0 up to a Fill Factor of 0.9.

The estimated volumes obtained using the extended model for beds with particle diameters less than 0.5 mm, which include fine sand, agricultural lime, and fine ballotini, closely matched the bed bulk volume. For instance, for the agricultural lime sample (AL1) in a tapped condition, the estimated volume agreed with the sample's bulk volume, exhibiting a maximum deviation of 7% from the Bulk Volume. Comparable figures for fine sand and fine ballotini samples were 10% and 20%, respectively. The samples with a mean particle diameter of less than 0.5 mm exhibited similar acoustical properties, as observed and discussed in the previous chapter. In the results of the Acoustic Absorption Tests (Chapter 4, Section 4.4.9), these samples did not exhibit quarter-wavelength absorption peaks, indicating that the acoustic energy could not penetrate the bottom of the bed and reflect to form a quarter-wavelength absorber.

Furthermore, in the Compression Uniformity Tests (Chapter 4, Section 4.4.10), these samples caused the maximum non-uniformity in pressure distribution within the resonator cavity. Another common characteristic of these samples is their lower permeability values compared to others. The permeability values for fine sand, agricultural lime (AL1), and fine ballotini were 11, 15, and 55 Darcy, respectively, whereas other samples had permeabilities higher than 250 Darcy. Additionally, the

extended model tended to overestimate the solid volume of samples with average particle diameters of less than 0.5 mm.

This study intentionally avoids statistical fitting and, instead, concentrates on the physics of the problem. However, using statistical calibration from Figure 5-6 to account for non-linearities offers an approach to estimating the volume of samples with fine particles. For instance, a 3rd-order polynomial curve fitting for the fine sand sample can correlate the bulk volume based on resonance wavelength, achieving an R^2 larger than 0.95. The curve fitting takes resonance wavelength as input and correlates it to the sample volume. For fine sand, a count of five repeated tests led to sample volume estimates with a maximum deviation of 0.9% between repetitions, provided that the sample's packing was consistently maintained using the perforated plate.

For samples with an average particle diameter higher than 0.5 mm, solid volume was underpredicted for all Fill Factors with a linear deviation offset from the actual values (See Figure 5-6). This underprediction means the estimated sample volume was lower than the solid phase volume. The results of the Compression Non-Uniformity tests in Chapter 4 might explain the deviations between the estimated volume and actual solid volume. All the samples in this category caused non-uniformity in air compression inside the resonator, effectively violating the assumption of uniform compression in a resonator established in a resonator with a small chamber.

5.6. Summary

As outlined in the preceding chapter, Section 4.5.5, determination of the resonance frequency of a lab-scale resonator filled with powder samples becomes challenging, if not unfeasible, for specific samples unless the longest tested port, a 1000 mm long port, is utilized. However, with this long port, the resonator no longer conforms to the parameters of the Classical Helmholtz Resonance model. In this chapter, the extended Helmholtz resonance model was developed to enhance the Classical Helmholtz Resonance model. This revised model presupposes that the resonator cavity size is significantly smaller (less than 10%) than the resonance wavelength. Yet, it remains relevant when the port length is on par with the resonance wavelength. The advantage of the EHR model is a continuum of calculable resonance wavelengths based on the cavity volume with no theoretical limit on the port length.

The model was experimentally verified in the 2-litre resonator using four distinct port lengths: 51 mm, 250 mm, 500 mm, and 1000 mm. The experimental results aligned with the estimations from the extended Helmholtz resonance model, with a maximum error of 1%, unadjusted for non-linearities.

The extended Helmholtz resonance model was also used to estimate the sample volume of solids and powders. The solid volume of the large marble sample, with an average diameter of 25 mm, was estimated with a maximum error of $0.3\%V_0$, regardless of the number of marbles in the resonator. For very fine samples, including fine ballotini, agricultural lime, and fine sand, the estimated volumes were closer to the bulk volume of the sample bed. However, there was a maximum deviation of 20% between the bulk volume of the bed and the estimated volume. In this group, the deviation between the estimated and actual sample volumes linearly increased with the Fill Factor for each sample.

In contrast to fine samples, estimating solid volumes of samples with particle diameters larger than 0.5 mm resulted in values lower than the actual solid volume. For the bed of powders with a mean particle diameter higher than 0.5 mm, solid volumes were underestimated for all Fill Factors. The observed underestimation can be explained by the non-uniform compression in the resonator, as discussed in the previous chapter. Non-uniformity in compression violates the assumption that the resonator cavity must be less than 10% of the resonance wavelength.

The next chapter introduces and discusses a semi-empirical model for estimating the solid volume of powders based on the Enhanced Helmholtz Resonance model.

5.6.1. Summary of the Models developed in this chapter

$$\lambda^2 = \frac{V_c}{\alpha^2} + (4l)^2$$

Extended Helmholtz Resonance (EHR) model

λ: Resonance wavelength (m)

V_c: Cavity Volume (m^3)

α: Resonator geometrical constant ($m^{0.5}$)

l: port length (m)

Suggested scope of validity:

- A resonator with chamber dimensions smaller than 10% of the resonance wavelength

$$V_S = V_c(1 - \frac{\lambda_1^2 - (4l)^2}{\lambda_0^2 - (4l)^2})$$

Sample volume from the extended Helmholtz resonance model

V_S: Sample volume (m^3)

V_c: Cavity volume (m^3)

λ_0: Resonance wavelength of the empty resonator (m)

λ_1: Resonance wavelength of the resonator containing the sample (m)

l: Resonator port length (m)

Suggested scope of validity:

- A resonator with chamber dimensions smaller than 10% of the resonance wavelength

- Liquid or solid samples with an average diameter larger than 15 mm

Chapter 6 A semi-empirical model for solid volume measurement in a Helmholtz Resonator containing a powder with a random size distribution

6.1. Introduction

In Chapter 4, specifically in Section 4.4.5, a direct correlation was noted between the port length and the maximum Fill Factor of powders at which the resonance frequency was detectable. Extending a Helmholtz Resonator port length makes resonance frequency hunting in a resonator filled with powders more feasible, especially when aiming for higher resonator Fill Factors. As the resonator port length approaches the resonance wavelength, the extended Helmholtz Resonance model, developed in Chapter 5, becomes applicable for estimating the sample volume based on the resonance wavelength. The proposed model accurately estimated the large marble Sample (LMB) volume regardless of the number of marbles inside the resonator.

However, the proposed model was unsuccessful in accurately estimating the solid volume of the powder samples. The discrepancy between estimated and actual values varied for the different test materials. The bed solid volume was underestimated for samples with particle diameters larger than 0.5 mm. Conversely, the bed solid volume was overestimated for samples with very fine particles with $D[3,2]$<0.25 mm.

For a specific powder sample with known particle size distribution, a Helmholtz Resonator can be calibrated by plotting resonance frequency versus various resonator Fill Factors and statistical means (Curve Fitting). The resonator can estimate the specific sample's solid volume using the calibration data.

With the available models and methods, it is not practical to estimate the solid volume of a powder with a random packing and particle size distribution using the Helmholtz Resonance method. This limitation is the problem that this chapter addresses.

In a Helmholtz Resonator, the resonance frequency change is governed by two main factors: the volume of the cavity occupied by the sample and the effect of the powder sample on resonance response. It was observed that powders changed the damping ratio of the resonator (Chapter 4, Section 4.4.8) and introduced non-uniformity in pressure distribution within the resonator cavity (Chapter 4, Section 4.5.10).

The quality factor of resonance was observed to change when a powder sample was placed inside the resonator cavity. This change in the quality factor is influenced by both the quantity and type of the powder sample. Consequently, the resonance wavelength and quality factor, as two key variables of resonance, can be utilized as indicators to determine the solid volume of a powder sample within a resonator.

This chapter introduces a semi-empirical model that modifies the extended Helmholtz resonance model for cavity volume determination introduced in Chapter 5. The Quality Wavelength Resonance (QWR) model, a semi-empirical model, aims to estimate the solid volume of a powder whose physical properties, like particle diameter and voidage, are unknown. It uses the resonance wavelength and quality factor as key parameters.

6.2. Experimental Data

The experimental data used in this chapter were obtained using the methods described in Chapter 4, Section 4.3.11. However, to keep the consistency of the text in this chapter, the method is concisely described.

The resonator was the 2-litre lab-scale resonator with the 1000 mm port described in Chapter 4, Section 4.2.1. The samples were small marbles (SMB), small polyethylene (PE1), large polyethylene (PE2), ball bearings (BB), mustard seeds (MS), black mustard seeds (BMS) and coarse ballotini (B710). The samples were loaded into the resonator with increments of approximately 300 ml, bulk volume. Each load of the samples was loaded onto the perforated plate (Introduced in Chapter 4, Section 4.3.8; Drawing available in Appendix E), and the plate was gently pulled up for a repeatable loose packing. The resonance frequency was measured for each load, and the quality factor was calculated. The resonance frequency for various samples was hunted using Transfer Function method as described in Chapter 4 Section 4.3.3. The resonance Quality Factor was measured using the driven resonance spectral analysis by dividing the resonance frequency by Full Width at Half Maximum (See Chapter 4, Section 4.1.5, Equation 4-22). Ambient Temperature (Chapter 4, Section 4.2.7) was used to calculate the sound speed for the resonance wavelength from the resonance frequency.

6.3. Model Development

The difference between the estimated solid volume of a powder sample and the actual values obtained using a specific gravity bottle was assessed. Figure 6-1 shows the estimated solid volume V_S of different samples versus the actual solid volumes V_A. Estimated solid volumes were obtained using the extended Helmholtz Resonance model, which was introduced in Chapter Four $V_S = V_c(1 - \frac{{\lambda_1}^2 - (4l)^2}{{\lambda_0}^2 - (4l)^2})$. Actual solid volume V_A was calculated from the sample mass divided by its solid density. As is shown in Figure 6-1, the slopes of deviation between the actual and estimated volumes for all samples are highly linear ($R^2 > 0.99$).

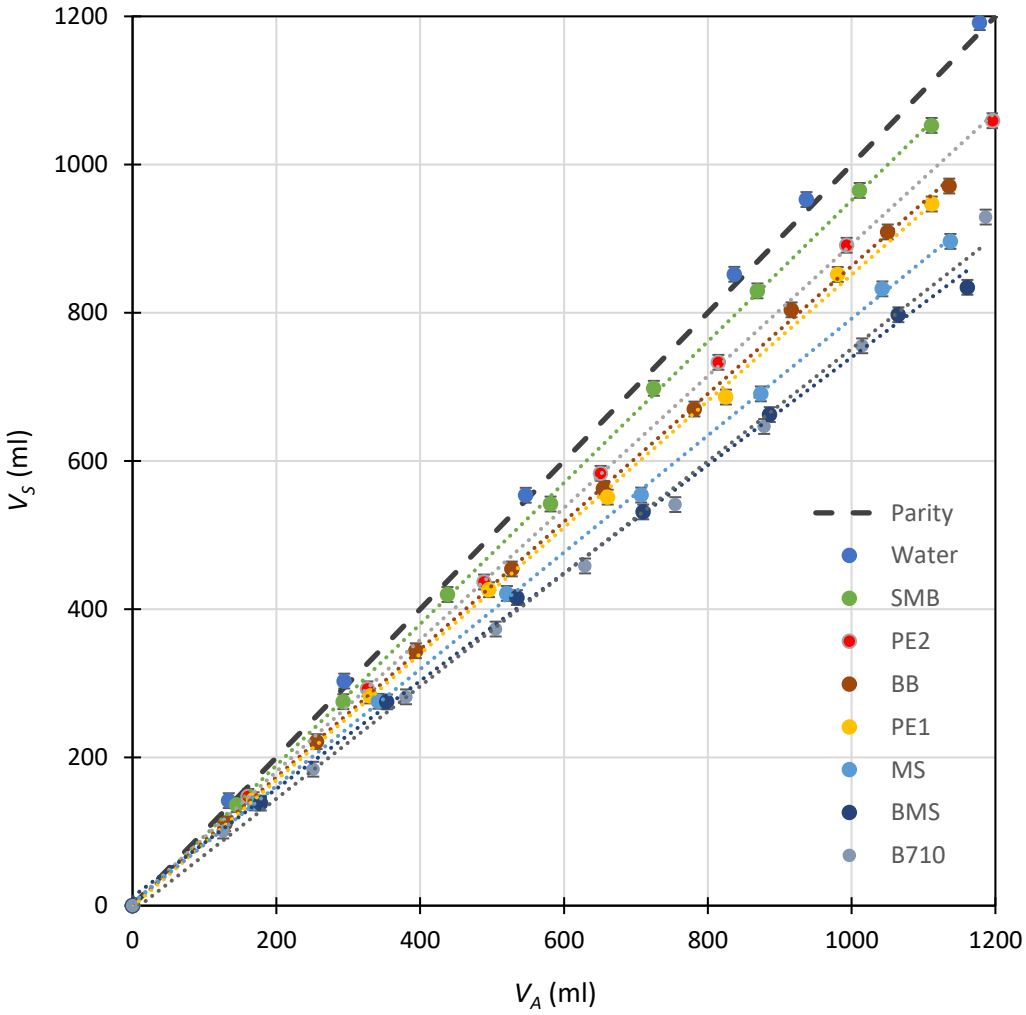


Figure 6-1: *Estimated sample volumes V_S vereses the actual values V_A* with trendlines.

In Figure 6-1, the linear trend of the results for each sample has a slope with the parity line. This slope governs the following equation for each data point of a sample:

$$\frac{V_A - V_S}{V_A} = \sigma \qquad 6\text{-}1$$

where σ is the Deviation Index, a dimensionless constant dedication to each sample. Since the solid volume of all powder samples with a mean diameter >0.25 mm was underestimated from the actual values, σ is between 0 and 1.

If the estimated solid volumes for a sample all lie on a straight line, σ remains constant; however, due to the slight non-linearity depending on the resonator Fill Factor, an average σ can be calculated for all the data points of a sample in Figure 6-1. Table 6-1 shows the averaged Deviation Index $\bar{\sigma}$ for all the samples.

When the estimated solid volumes for a sample consistently align on a straight line, σ remains constant. However, owing to a slight non-linearity influenced by the resonator Fill Factor, an average σ can be derived from all the data points of a sample, as illustrated in Figure 6-1. Table 6-1 presents the averaged Deviation Index $\bar{\sigma}$ for all the samples.

Table 6-1: *Deviation Index of the samples tested.*

Sample*	$\bar{\sigma}$	Standard Deviation
ballotini (B710)	0.265	0.025
mustard (BMS)	0.240	0.020
mustard (MS)	0.210	0.011
polyethylene (PE1)	0.150	0.012
ball bearings (BB)	0.137	0.006
polyethylene (PE2)	0.105	0.002
marbles (SMB)	0.051	0.010

*Sorted by particle size from small to large

As shown in Table 6-1, the samples with fine particles like ballotini with a Sauter mean diameter of 0.67 mm have the highest deviation. The sample particle size increases, and the deviation index decreases. As shown in Figure 6-1, all the samples had a highly linear trend, with a maximum standard deviation of 0.025 for sample ballotini B710, as shown in Table 6-1.

Combining Equation 6-1 with the Enhanced Helmholtz Resonance model introduced in the previous chapter (Equation 5-19) gives:

$$V_A = \frac{V_c}{1-\bar{\sigma}}\left(1 - \frac{\lambda_1^2-(4l)^2}{\lambda_0^2-(4l)^2}\right) \qquad 6\text{-}2$$

The next step in model development was to estimate $\bar{\sigma}$ from the resonance characteristics of the resonator containing the powders.

As discussed In Chapter 4 Section 4.4.8, it was observed that the rate of change in resonance quality factor with the change of resonator fill factor was specific for each sample and was correlated to sample particle size distribution as shown in Figures 4-54 and 4-55. The relationship between resonance quality factor and resonance wavelength squared can be approximated by a line fit with the slope being the rate of change of quality factor per change of wavelength squared. Typical for other samples, Figure 6-2 shows the change of quality factor with resonance wavelength squared. The slope of the line fit in Figure 6-2 was specific for each sample.

Table 6-2 represents the rate of change (ε) of the Quality Factor with squared resonance wavelength for all tested samples. R^2 values are also presented in the table as an indicator of linearity.

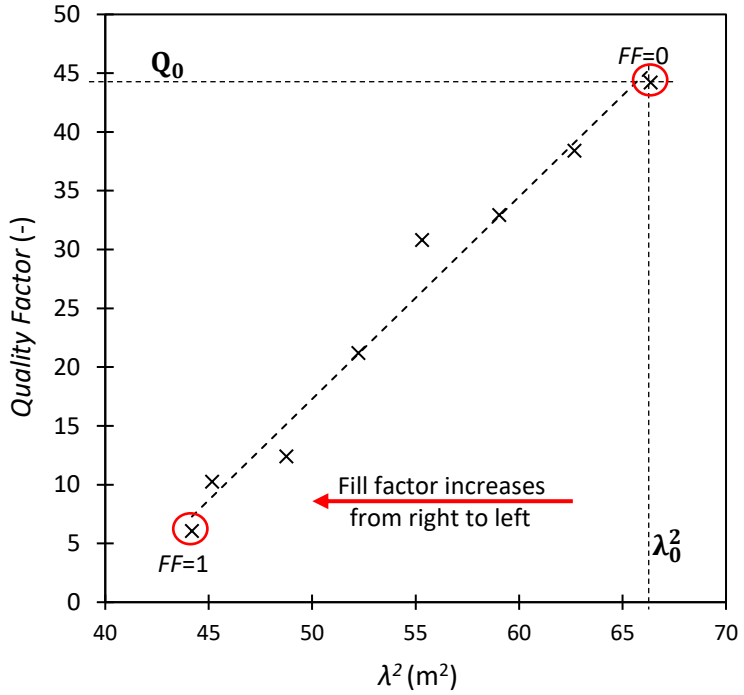


Figure 6-2: *The linear trend (Dashed Line) of resonance quality factor change based on resonance wavelength squared for different Fill Factors of the resonator. The test sample is black mustard seeds (BMS).*

Table 6-2: *Rate of change of quality factor with resonance wavelength squared.*

Sample	ε (m^{-2})	R^2
ballotini (B710)	1.80	0.93
mustard (BMS)	1.72	0.97
mustard (MS)	1.52	0.95
polyethylene (PE1)	1.17	0.89
ball bearings (BB)	1.19	0.94
polyethylene (PE2)	1.02	0.88
marbles (SMB)	0.69	0.73

From Figure 6-2, the rate of change of the Quality Factor Q with resonance wavelength squared λ^2 is the slope of the line (ε) can be expressed as:

$$\varepsilon = \frac{Q-Q_0}{\lambda^2-\lambda_0^2} \qquad 6\text{-}3$$

where Q_0 and λ_0 are the Resonance Quality Factor and Resonance Wavelength (m) of the resonator when the resonator cavity is empty. These values are constant for a resonator (subjected to a constant driving amplitude for driven resonance, as discussed in Chapter 4, Section 4.4.7 and 4.5.7).

For the 2-litre resonator with the 1000 mm port, the values of Q_0 and λ_0 were 43±1 and 8.13±0.01 m respectively.

The next step in model development was to correlate the averaged deviation index ($\bar{\sigma}$) to the rate of change of the Quality Factor ($\boldsymbol{\varepsilon}$). Figure 6-3 shows the relationship between these two parameters, approximated by a linear fit.

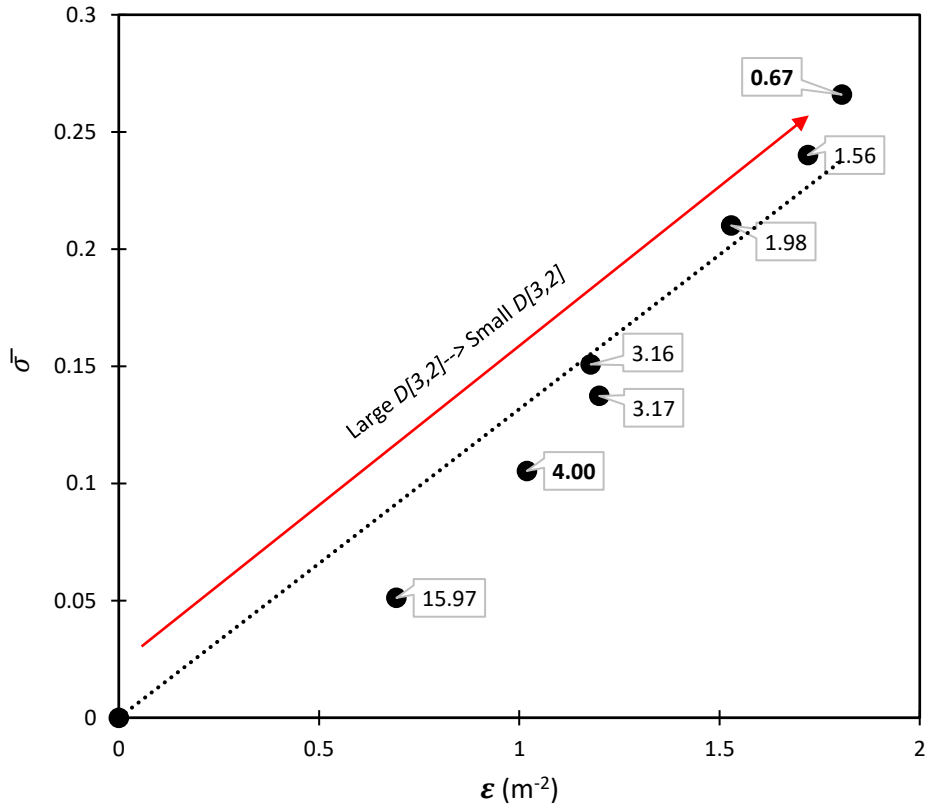


Figure 6-3: *The linear relationship between the Deviation Index ($\bar{\sigma}$) and the rate of change of the Quality Factor ($\boldsymbol{\varepsilon}$). Data labels are d[3,2].*

The line equation of the linear fit in Figure 6-3 is:

$$\bar{\sigma} = \Omega \times \varepsilon \qquad 6\text{-}4$$

where Ω is the slope of the line (m^2) with the line intercept set to zero. The obtained constant Ω for the resonator used in this study was 0.1317 $m^{2,}$ as shown in Figure 6-3 line equation.

Combining 6-4 and 6-3 and putting them into 6-2 gives the model, which is referred to as Quality Wavelength Resonance (QWR):

$$V_A = \frac{V_c}{1-\Omega\frac{Q_1-Q_0}{\lambda_1^2-\lambda_0^2}}\left[1-\frac{\lambda_1^2-(4l)^2}{\lambda_0^2-(4l)^2}\right] \qquad 6\text{-}5$$

which is the semi-empirical model for the estimation of a powder sample solid volume V_A. The slope of the line Ω is assumed to be constant for a resonator for the range of particle sizes tested for deriving it. Port length l, empty resonator resonance wavelength λ_0, empty resonator resonance quality factor Q_0 and resonator cavity volume V_c are constants. The only input parameters for sample solid volume estimation are λ_1 and Q_1 which are the hunted resonance wavelength and the calculated resonance quality factor from spectral analysis.

6.4. Model Verification

The hunted resonance wavelength of the samples was used to calculate sample solid volumes using Equation 6-5. Figure 6-4 shows the solid volumes from weighing V_W vs sample volumes calculated using the model V_A.

As shown in Figure 6-4, the estimated volumes of the samples are centred around parity with an average deviation from parity of 1.2%V_0 (1.2% of the resonator capacity). The standard deviation of the error from the average was 2.14%V_0. The maximum deviation from the actual solid volume was 4%V_0 of overestimation and was recorded for 655 ml of the ball bearings (BB) sample. In comparison, when estimating the volume based on just resonance wavelength using the extended Helmholtz resonance model introduced in the previous chapter (The results in Figure 6-1), the maximum deviation was -17%V_0 recorded for the ballotini sample (B710) with an average absolute deviation of 5.7%V_0.

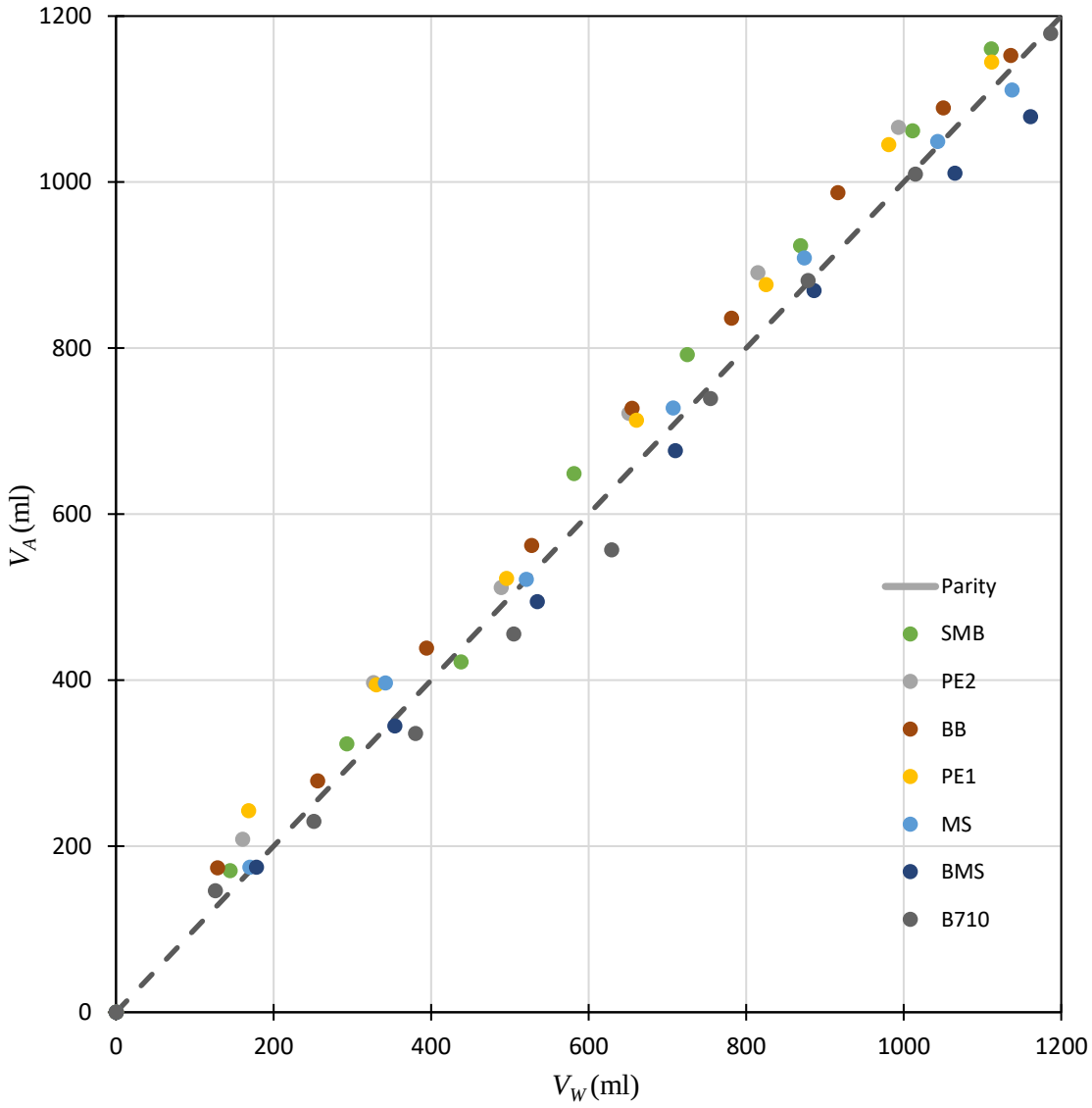


Figure 6-4: *Estimated sample solid volume from the QWR model vs actual volume from weighing.*

As shown in columns A, B, C and D of Table 6-3, multiple mixed samples were prepared and loaded into the resonator to validate the model for estimating the solid volume of a sample with random particle size distribution. The mixed samples were prepared by rotating the resonator containing the sample around its horizontal axis 20 times to randomise the distribution of particles within the cavity. Sample No.7 was not mixed, and the particles were added layer by layer to the resonator. Table 6-3 provides the sample preparation conditions in the column Preparations. Columns F and H of this table compare the solid volume estimated using the extended Helmholtz resonance (EHR) model introduced in Chapter 5 (V_S) with the estimated solid sample volume (V_A) using the Quality Wavelength Resonance (QWR) model for powders, which is developed in this chapter. Columns G and I of Table 6-3 are deviations D% of actual volume from estimations using EHR and QWR models, respectively.

Table 6-3: *Mixed samples and estimated solid volumes.*

A	B	C	D	E	F	G	H	I
No.	**Preparation**	**Particles**	**Volume Fraction (%)**	**V_W (ml) From weighing**	***V_S (ml) From EHR model***	**D%* of V_S**	***V_A (ml) From QWR model***	**D% of V_A**
1	Mixed by rotating the resonator	LMB SMB MS PE2	25 27 36 12	457	423	1.8	444	0.7
2	Mixed by rotating the resonator	LMB SMB MS PE2	23 27 38 12	880	801	4.1	894	0.7
3	Mixed by rotating the resonator	LMB SMB MS PE2	24 25 37 14	1162	1043	6.3	1154	0.4
4	Mixed by rotating the resonator	LMB SMB MS PE2	24 26 35 14	1329	1184	7.6	1331	0.1
5	Layer by Layer From the bottom PE2, MS and BMS	BMS MS PE2	31 30 39	1114	900	11	1088	1.3
6	Mixed by rotating the resonator	BMS MS PE2	31 30 39	1114	902	11	1077	1.9
7	mustard seeds poured on top of marbles	LMB SMB MS	29 30 41	1351	1206	7.6	1340	0.5

* Error was calculated based on cavity volume, which was 1895.35 ml. See Basic Equations Sections, error analysis.

According to the results presented in Table 6-3, the introduced model estimated sample volumes with significantly higher accuracy than the estimations based on the extended Helmholtz Resonance model. The deviation *D%* for the proposed model for volume determination of powders was 0.8%V_0. Figure 6-5 shows photographs of the samples in Table 6-3 in the 2-litre resonator.

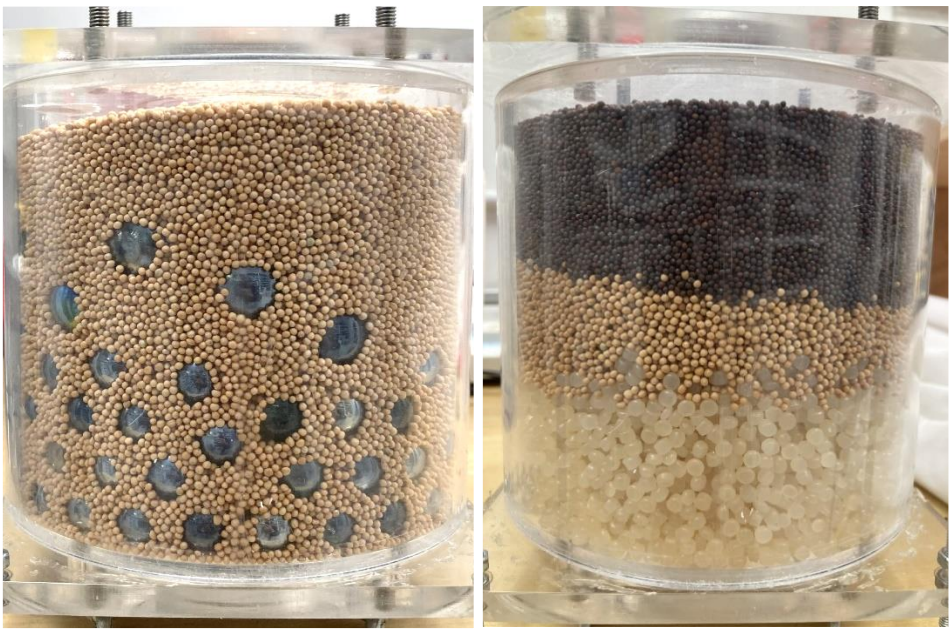


Figure 6-5: *Sample No.7 (Left) and Sample No.5 (Right).*

6.5. Discussion

The QWR model introduces the constant $\boldsymbol{\Omega}$. This constant is obtained from statistical line fitting. Accuracy in determining resonance frequency and the quality factor reflects the empirical value Ω. For consistency, the quality factor measurement was based on the Driven Method with 5 seconds resonance sampling duration (Chapter 4, Section 4.3.2). Resonance Hunting duration was also set to 2 seconds with 5 repeats, as Chapter 4, Section 4.2.3 describes. Chapter 4, Section 4.1.6:Excitation explains that a lengthier microphone sampling duration results in a higher resolution, increasing quality factor measurement and resonance frequency hunting accuracy. Increasing the sampling time can result in higher accuracy in finding the constant Ω.

The observation of the linearity in the rate of change of quality factor with resonance wavelength squared for powder samples was a key observation for this model Table (6-2). Non-linearity in the rate of change of quality factor with resonance wavelength squared for a sample can introduce error in the estimated values.

6.6. Summary

The volume estimation of powder samples with an average particle diameter of 0.67 mm and larger using the Extended Helmholtz Resonance (EHR) Model (Chapter 5) resulted in highly underestimated solid volumes with a nearly constant deviation from actual values. A semi-empirical model was developed to estimate powder sample solid volume based on resonance wavelength and quality factor. When gradually filing a resonator with a powder sample (Layer by Layer) and performing resonance hunting, the resonance wavelength squared changes with sample volume linearly. Also, when gradually filling the resonator with a powder, the resonance quality factor drops with resonance wavelength squared almost linearly. The rate of change in resonance quality factor compared to the change of resonance wavelength was correlated with the deviation between the estimated sample volumes and the actual volumes. This correlation expressed by a line fit was used to optimize the Extended Helmholtz Resonance (EHR) model by developing a semiempirical model referred to as Quality Wavelength Resonance (QWR).

All powders with particle diameters higher than 0.5 mm were back-tested for solid volume using QWR model. QWR model estimated the solid volume of all samples with a mean deviation of $1.2\%V_0$ and a maximum deviation of $4\%V_0$. The model was also tested for sample volume estimation of mixed samples with a broad particle diameter distribution. The mixed samples were combinations of different powders and particles with varied mixing conditions. The introduced model estimated the sample solid volume with a mean deviation of 0.8% and a maximum deviation of 1.9% for all samples.

6.6.1. Summary of the Model developed in this chapter

$$V_A = \frac{V_c}{1 - \Omega \frac{Q_1 - Q_0}{\lambda_1^2 - \lambda_0^2}} \left(1 - \frac{\lambda_1^2 - (4l)^2}{\lambda_0^2 - (4l)^2}\right)$$

Quality Wavelength Resonance (QWR) model

V_A: Estimated Sample Solid Volume (m^3)

V_c: Cavity Volume (m^3)

λ_0: Resonance Wavelength of the empty resonator (m)

λ_1: Resonance Wavelength of the resonator containing the sample (m)

Q_0: Driver Resonance Quality Factor of the empty resonator

Q_1: Driven Resonance Quality Factor of the resonator containing the sample

Ω: Experimentally obtained constant for a resonator

Suggested scope of validity:

- A resonator with chamber dimensions smaller than 10 % of the resonance wavelength
- A random packing sample with an average particle diameter larger than 0.7 mm

Chapter 7 A model for Instantaneous sample volume measurement

7.1. Introduction

It is beneficial to provide a recapitulation of the preceding chapters to introduce the questions addressed in the current chapter.

Based on sample volume determination using Helmholtz Resonance, thoroughly investigated in Chapters 4, 5, and 6, placing an object in a resonator cavity alters the system's frequency response to either Driven or Undriven excitation. This alteration in the frequency response is related to the object's volume. From a researcher's perspective, this approach raises three main questions: **(1)** how to achieve a high-quality resonance, **(2)** how to hunt the resonance frequency, and **(3)** how to correlate the sample volume with the hunted frequency.

The first question was addressed in two ways: by optimizing the resonator port length to obtain a high-quality resonance when measuring the volume of powders and by developing excitation techniques such as Driven and Undriven chirp excitation. The second question was answered by employing three hunting methods: Undriven, Driven, and Transfer Function methods. The third question was addressed through the models developed in Chapters 5 and 6, which are suitable for the conditions of this research where resonators with long ports are utilized. However, there is an intrinsic limitation in the approach of volume determination by frequency hunting, which theoretically constrains the outcome precision, and that limitation is on the minimum measurement duration required for resonance hunting. It is not possible to speed it up without sacrificing accuracy.

Resonance frequency hunting involves acoustic pressure sampling and processing. The acoustic pressure is commonly captured using a microphone. The microphone signal is repeatedly sampled to form a discrete time-amplitude series. The time-amplitude signal undergoes spectral analysis to be taken into the frequency domain. The frequency resolution of the analysed signal is limited by the number of samples divided by the sampling rate; therefore, to increase the measurement precision, the sampling time has to be increased (See relative digital signal processing textbooks, for example, Braun et al., 2002).

The results of this thesis support the statement that a Helmholtz Resonator provides a speedy solution for sample volume measurement compared to many other methods but still requires a significant amount of time for signal sampling as long as the desired precision is achieved.

This Chapter proposes another approach for sample volume estimation, which overrides the required lengthy signal sampling time. This chapter introduces a physical model based on the solution of the underdamped forced oscillation model for the mass of air in the port, which estimates sample volume from microphone signal amplitude.

7.2. Model Development

The analogy between Helmholtz Resonance and mechanical oscillation was introduced in Chapter 4, Sections 4.1.3 to Section 4.1.5. For consistency in text and ease of following the model development, it is briefly reintroduced in this chapter, along with the necessary equations.

The mass of the air inside the port (m) has a small movement in and out. The air inside the resonator provides a restorative force of an equivalent massless spring with stiffness K. The total acoustic energy damping from the port in the forms of radiation, viscous and thermal resistances is represented as R_M. Radiation resistance is a function of port geometry, speed of sound, fluid density and oscillation frequency (Blackstock, 2000; Kinsler et al., 2000). Ingard (1953) investigated viscous and thermal resistances and reported that these parameters depend on oscillation frequency and are independent of sound pressure except for very high sound pressures.

The underdamped forced mechanical oscillation can be written in the differential form of Equation 7-1 (For example, see A.P. French, 2003).

$$m\frac{d^2x}{dt^2} + R_M\frac{dx}{dt} + Kx = f(t) \qquad 7\text{-}1$$

where $f(t)$ is a complex driving force. Equation 7-1 describes the oscillation model for the mass of air in a Helmholtz Resonator (Blackstock, 2000; Kinsler et al., 2000; Vandegrift, 1993b).

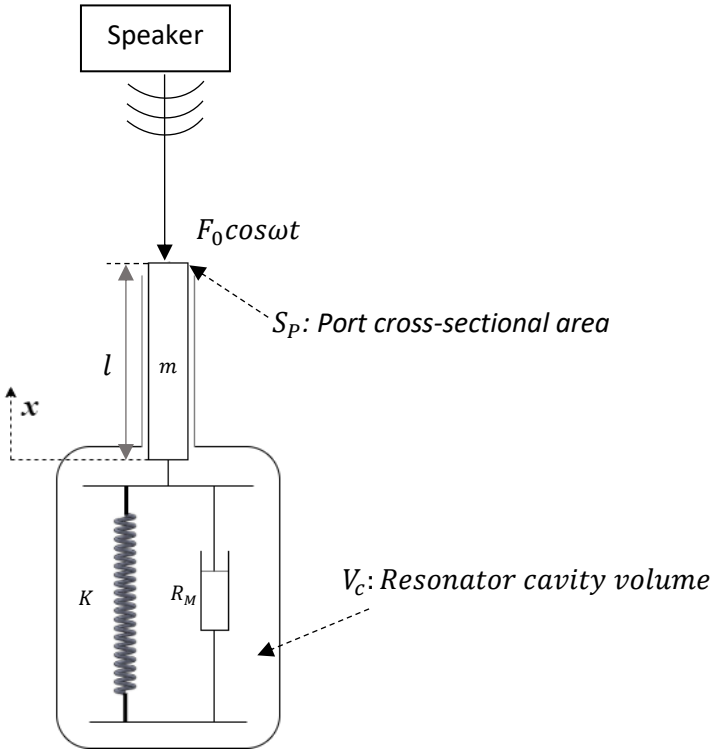


Figure 7-1*: A Helmholtz resonator analogous to a mass-spring-damper system.*

In Figure 7-1, a loudspeaker, at an arbitrary distance, plays a monotone with angular frequency ω. This sound, when it reaches the surface of the mass of air inside the port, applies a periodical force equivalent to $F_0 cos\omega t$. With this periodic force, Equation 7-1 can be rewritten in the following form:

$$m\frac{d^2x}{dt^2} + R_M\frac{dx}{dt} + Kx = F_0 cos\omega t \qquad 7\text{-}2$$

The natural frequency of this oscillation system is:

$$\omega_n = \sqrt{\frac{K}{m}} \qquad 7\text{-}3$$

The mass of the air is:

$$m = \rho S_p l \qquad 7\text{-}4$$

where ρ is the density of air. At the maximum travel of the mass inside the cavity, $\frac{dx}{dt}$ and the effect of damping vanishes, and the restorative force which acts on the mass of air inside the port can be written as:

$$F_m = -K\delta x \qquad 7\text{-}5$$

where δx is the distance the air inside the port under oscillation protrudes into the resonator from its equilibrium position. When the port air protrudes the resonator cavity with a displacement of δx, the air inside the cavity applies a force to the port air equivalent to:

$$F_m = S_p \delta P \qquad 7\text{-}6$$

where δP is the variation of pressure inside the cavity. Assuming that the resonator is filled with an ideal gas and it is an adiabatic system, the relationship between pressure (P) and volume (V) inside the resonator cavity is (γ the ratio of the heat capacity):

$$PV^{\gamma} = constant. \qquad 7\text{-}7$$

Based on 7-7, the relationship between pressure and volume variation inside the resonator cavity is:

$$\frac{\delta P}{P_0} = -\gamma\frac{\delta V}{V_C} \qquad 7\text{-}8$$

where P_0 is the initial pressure inside the cavity before the mass of air protrudes into the cavity, V_C is the cavity volume, and δV is the change in cavity volume. The change in the volume of the compressible cavity fluid is equal to the volume displacement of the port air:

$$\delta V = \delta x S_p \qquad \textit{7-9}$$

Combining Equations 7-5, 7-8 and 7-9 gives:

$$K = \frac{\gamma S_p^2 P_0}{V_c} \qquad 7\text{-}10$$

Knowing that the speed of sound is:

$$c = \sqrt{\frac{\gamma P_0}{\rho}} \qquad \textit{7-11}$$

Equation 7-10 can be rewritten as:

$$K = \frac{\rho c^2 S_p^2}{V_c} \qquad \textit{7-12}$$

Combining 7-12, 7-4 and 7-3 gives:

$$\omega_n^2 = \frac{c^2 S_p}{l V_c} \qquad \textit{7-13}$$

which is the square of the system's natural resonance frequency. The displacement amplitude of the port's air mass can be calculated by solving the differential equation 7-2. To do so, we divide Equation 7-2 by m and write the result in the following form:

$$\frac{d^2x}{dt^2} + \Gamma \frac{dx}{dt} + \omega_n^2 x = F cos\omega t \qquad \textit{7-14}$$

where $\Gamma = R_m/m$ is commonly called the Damping Constant, and $F = F_0/m$. The steady-state solution for the differential equation in 7-14, as discussed in vibration engineering textbooks, is in the following form (For example, see Inman, 2001 and Rao, 2017):

$$x(t) = A_d cos(\omega t + \phi) \qquad \textit{7-15}$$

where ϕ is the driver force phase and A_d is the maximum displacement of the port air from equilibrium or simply Oscillation Amplitude. Differentiating 7-15 and putting the first and second-order differentials into Equation 7-14 and algebraic manipulation yields 7-16 for the oscillation amplitude A_d. Details are covered in vibration engineering textbooks under Underdamped Forced Driven Oscillation; for example, see Inman (2001).

$$A_d(\omega) = \frac{F}{\sqrt{\left(\omega_n^2 - \omega^2\right)^2 + \Gamma^2 \omega^2}} \qquad 7\text{-}16$$

The port air oscillation amplitude A_d, as in the denominator of 7-16, is a function of the closeness of the driver and natural frequencies. At resonance, the driver frequency and the system's natural frequency are equal ($\omega_n = \omega$). Using 7-16, the amplitude at resonance (A_0) is:

$$A_d(\omega_n) = \frac{F}{\Gamma\omega} = A_0 \qquad 7\text{-}17$$

From 7-17, the following can be established:

$$F = A_0 \Gamma \omega_n \qquad 7\text{-}18$$

The damping ratio (ζ), which was previously introduced in Chapter 4, section 4.1.4 and extensively used in Chapter 4 for Resonance Quality assessment, is defined as the ratio of the system damping to the system critical damping. The following is the relationship between the damping constant (Γ) and Damping ratio (ζ) (Inman, 2001):

$$\Gamma = 2\zeta\omega_n \qquad 7\text{-}19$$

Two states for the resonator are considered, with physical parameters shown in Figure 7-2.

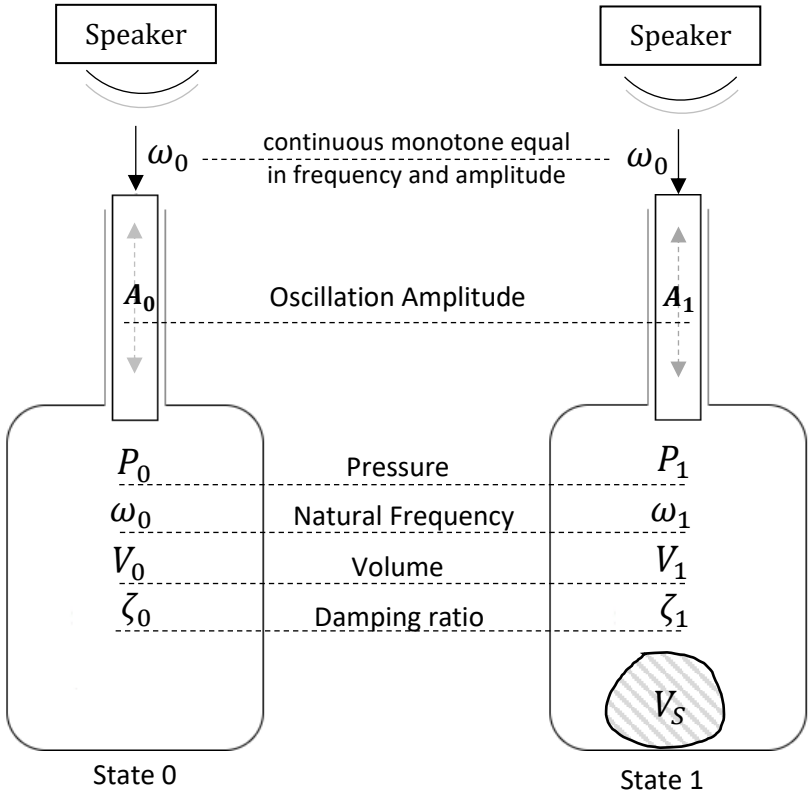


Figure 7-2: *Two resonator states before and after putting a sample with volume V_s into it.*

Between states 0 and 1, the forced oscillation remains constant in frequency equal to the driving monotone with frequency ω_0. As discussed above, the total damping of the system R_M depends on the oscillation frequency and port and is independent of sound pressure (Blackstock, 2000; Ingard, 1953). Therefore, it remains constant between the two states as well as $R_M/m = \Gamma$ which from Equation 7-19, yealds $\zeta_0\omega_0 = \zeta_1\omega_1$. By implementing this into Equaiton 7-20 and defining $\bar{A} = A_1/A_0$

as the dimensionless oscillation amplitude drop factor, Equation 7-20 can be written as Equation 7-21. Equation 7-21 defines the oscillation amplitude drop factor as a function of the system damping ratio and natural frequency in State 1.

$$A_1 = \frac{2A_0\zeta_0\omega_0^2}{\sqrt{\left(\omega_1^2-\omega_0^2\right)^2+(2\zeta_1\omega_1\omega_0)^2}} \qquad \textit{7-20}$$

$$\bar{A} = \frac{2\zeta_0\omega_0^2}{\sqrt{\left(\omega_1^2-\omega_0^2\right)^2+\left(2\zeta_0\omega_0^2\right)^2}} \qquad \textit{7-21}$$

Considering the cavity air restorative force on the mass of the air in the port (Equations 7-5 and 7-6), the oscillation amplitude A can be correlated to the pressure change in the resonator δP as provided in Equation 7-22, where K_0 and K_1 are spring coefficients of the cavity air in States 0 and 1, respectively. In Equations 7-22a and 7-22b, A_0 and A_1 are the maximum displacement δx of the port air mass into the resonator in states 0 and 1, respectively, as shown in Figure 7-2. Equation 7-23 can be derived from Equation 7-22. From Equation 7-3, Equation 7-24 can be written for the ratio of the system's resonance frequencies between State 0 and State 1. The mass of the air in the port remains constant ($m_0 = m_1$). Defining $\bar{P}$, the ratio of the resonator cavity pressure between State 1 and State 0, as is shown in Equation 7-25, and combining it with Equations 7-24 and 7-23 gives Equation 7-26. When the resonance is heavily underdamped, $\zeta_0 < 0.05$, the resonance quality factor can be approximated using Equation 7-27a and Equation 7-22b (Rao, 2017). Combining Equaitons 7-21, 7-26 and 7-27 gives Equaiton 7-28.

$$A_0K_0 = S_pP_0 \qquad \textit{7-22a}$$

$$A_1K_1 = S_pP_1 \qquad \textit{7-22b}$$

$$\frac{A_1}{A_0} = \frac{P_1}{P_0}\frac{K_0}{K_1} \qquad \textit{7-23}$$

$$\frac{K_1}{K_0} = \frac{\omega_1^2}{\omega_0^2} \qquad \textit{7-24}$$

$$\bar{P} = \frac{P_1}{P_0} \qquad \textit{7-25}$$

$$\bar{A} = \bar{P}\frac{\omega_0^2}{\omega_1^2} \qquad \textit{7-26}$$

$$Q \approx \frac{1}{2\zeta_0} \qquad \textit{7-27}$$

$$\bar{P}\frac{\omega_0^2}{\omega_1^2} = \frac{\frac{1}{Q}\omega_0^2}{\sqrt{\left(\omega_1^2-\omega_0^2\right)^2+\left(\frac{1}{Q}\omega_0^2\right)^2}} \qquad \textit{7-28}$$

Equation 7-28 can be solved for ω_1 to describe the system's natural frequency in State 1 (ω_1) as a function of the cavity pressure ratio $\bar{P}$. This operation involves solving a quadratic equation with algebraic methods, described in Appendix B. The solutions of Equation 7-28 for ω_1 is presented in the following:

$$\omega_1 = \begin{cases} (a) & \omega_0\sqrt{\frac{+\bar{P}\sqrt{(1+Q^2-\bar{P}^2Q^2)}+\bar{P}^2Q^2}{\bar{P}^2Q^2-1}} \\ (b) & -\omega_0\sqrt{\frac{+\bar{P}\sqrt{(1+Q^2-\bar{P}^2Q^2)}+\bar{P}^2Q^2}{\bar{P}^2Q^2-1}} \\ (c) & \omega_0\sqrt{\frac{-\bar{P}\sqrt{(1+Q^2-\bar{P}^2Q^2)}+\bar{P}^2Q^2}{\bar{P}^2Q^2-1}} \\ (d) & -\omega_0\sqrt{\frac{-\bar{P}\sqrt{(1+Q^2-\bar{P}^2Q^2)}+\bar{P}^2Q^2}{\bar{P}^2Q^2-1}} \end{cases} \qquad \textit{7-29}$$

where *(b)* and *(d)* can be discarded because the resonance frequency can not be negative. According to Equation 7-13, there is an inverse relationship between cavity volume and system resonance frequency. Because in moving from State 0 to State 1, the cavity volume is decreased by V_s, the system resonance frequency is expected to increase, $\frac{\omega_1}{\omega_0} > 1$, which is satisfied by the solution (a).

From Equation 7-13, the natural frequency in States 0 and 1 are Equations 7-30 and 7-31, respectively. Equation 7-32 is obtained by dividing Equation 7-30 by 7-31. The sample volume described in Equation 7-33 can be calculated using Equation 7-34. With the damping ratio being very low, $\zeta_0 < 0.05 \ \ or \ \ Q > 10$, which is typical for a single port Helmholtz Resonator without a damper, Equation 7-34 can be effectively approximated to Equation 7-35, as shown in Figure 7-3; for *Q* = 10, there is a deviation of roughly 0.8% between Equation 7-34, Shown by “Full” in the legend, and its approximation in Equation 7-35, shown by “Approx.” in the legend. Moving to *Q*=20 and higher, the region of interest in volume measurement using a Helmholtz Resonator, the deviation between the results obtained by Equations 7-34 and 7-35 becomes negligible, <0.1%. The results of the experiments in this chapter are all derived using the approximated form in Equation 7-35, referred to as the Sound Pressure Quality Factor (SPQF) model.

$$\omega_0^2 = \frac{c^2 S_p}{l V_0} \qquad 7\text{-}30$$

$$\omega_1^2 = \frac{c^2 S_p}{l V_1} \qquad 7\text{-}31$$

$$\frac{\omega_1^2}{\omega_0^2} = \frac{V_0}{V_1} \qquad 7\text{-}32$$

$$V_1 = V_c - V_s \qquad 7\text{-}33$$

$$V_s = V_c \frac{Q\sqrt{1+\frac{1}{Q^2}-\bar{P}^2}+\bar{P}}{\bar{P}(Q^2+1)} \qquad 7\text{-}34$$

$$V_s \cong V_c \frac{\sqrt{1-\bar{P}^2}}{Q\bar{P}} \qquad 7\text{-}35$$

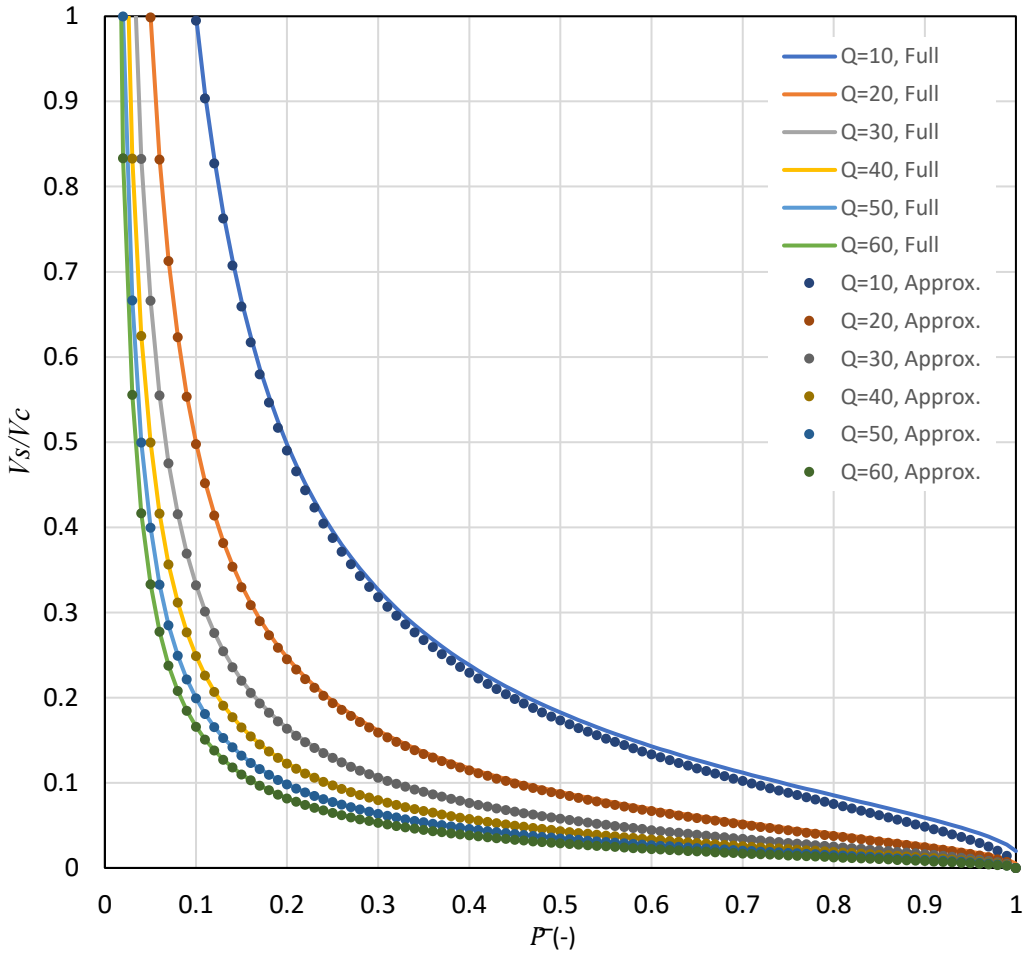


Figure 7-3: *Numerical comparison of the full model in Equ. 7-34 (Full), versus its approximated form in Equ. 7-35 (Approx).*

Effect of ambient temperature

In developing the Sound Pressure Quality Factor (SPQF) model, it is assumed that the driving frequency equals the natural frequency of the empty resonator.

However, In the case of inconsistency in the temperature, the speed of sound changes, which affects the natural frequency of the empty resonator; hence, the driving frequency should change to match the natural frequency accordingly. Adjusting the driving frequency to match the empty resonator resonance frequency based on the ambient temperature is possible. Take ω_{0T1} be the experimentally measured resonance frequency of the empty resonator at the temperature T_1 where the speed of sound is c_{T1}. When the ambient temperature changes to T_2 and the speed of sound becomes c_{T2}, resonator's natural frequency ω_{0T2} can be expressed as:

$$\omega_{0T2}^2 = \frac{c_{T_2}^2 S_p}{l V_c} \qquad \textit{7-36}$$

Similarly, for ω_{T1}:

$$\omega_{0T1}^2 = \frac{c_{T_1}^2 S_p}{l V_c} \qquad \textit{7-37}$$

Dividing Equation 7-37 by Equation 7-36 gives:

$$\frac{\omega_{0T2}}{c_{T2}} = \frac{\omega_{0T1}}{c_{T1}} \qquad \textit{7-38}$$

Equation 7-38 is equivalent to k_0 where k_0 is the wavenumber associated with the empty resonator's natural frequency. The speed of sound in the air can be estimated from temperature using Equation 7-39, with T being temperature in centigrade degrees. (Bohn, 1988). Equation 7-40 gives driving frequency based on the ambient temperature change. As long as the driving frequency at the time of sample volume measurement ω_{0T2} matches the natural frequency of the empty resonator, and the sample volume in the SPQF model in Equation 7-35 mathematically remains neutral to ambient temperature and resonance frequency.

$$c = 331.45\sqrt{1 + \frac{T}{273}} \qquad \textit{7-39}$$

$$\omega_{0T2} = \frac{\sqrt{1+\frac{T_2}{273}}}{\sqrt{1+\frac{T_1}{273}}}\omega_{0T1} \qquad \textit{7-40}$$

7.3. Materials

7.3.1. Resonator

The lab-scale resonators introduced in Chapter 4 were used in this section in various configurations. Appendix F provides some pictures of the apparatus. Figure 7-4 shows the general configuration of the experimental apparatus. Flow control orifices were plates with circular orifices that could be fitted to the bottom plate of the resonator via four bolts. The flow control orifice was replaced with a plate for static tests. For discharge tests on Water, mustard seeds (BMS and MS) and coarse and fine ballotini (B710 and B250), the 5.6 mm flow control orifice was used. For the discharge tests on agricultural lime (AL2) and polyethylene (PE1), the 10 mm orifice was fitted.

The static tests were conducted on three cavity volumes of 1, 2 and 3 litres with 60, 123 and 195 mm heights, respectively.

For driving frequencies higher than 150 Hz, a small speaker placed 150 mm above the port opening on a wooden structure was used. For frequencies lower than 150 Hz, a subwoofer positioned on the side of the resonator port, 300 mm away from the port opening, was used. The subwoofer's centre was level with the tip of the resonator port. These speakers were introduced in Chapter 4, Section 4.2.9.

Two ports were used interchangeably for the experiments in this section. Both ports were cut from an aluminium tube, 44 mm internal diameter and 50 mm external diameters, with two lengths of 51 and 170 mm.

For the discharge tests, referred to as dynamic tests, the discharged material was collected on a platform scale (IND221, Mettler Toledo, USA) with a resolution of 0.005 kg.

The electronic and the software have already been introduced in Chapter 4 from 4.2.5 to 4.2.9. The only difference is the location of the microphone installation. The microphone was taken from the port root to the cover plate of the resonator to measure pressure from inside the cavity. The microphone was installed in a hole 25 mm from the port and was sealed with heat-gun glue.

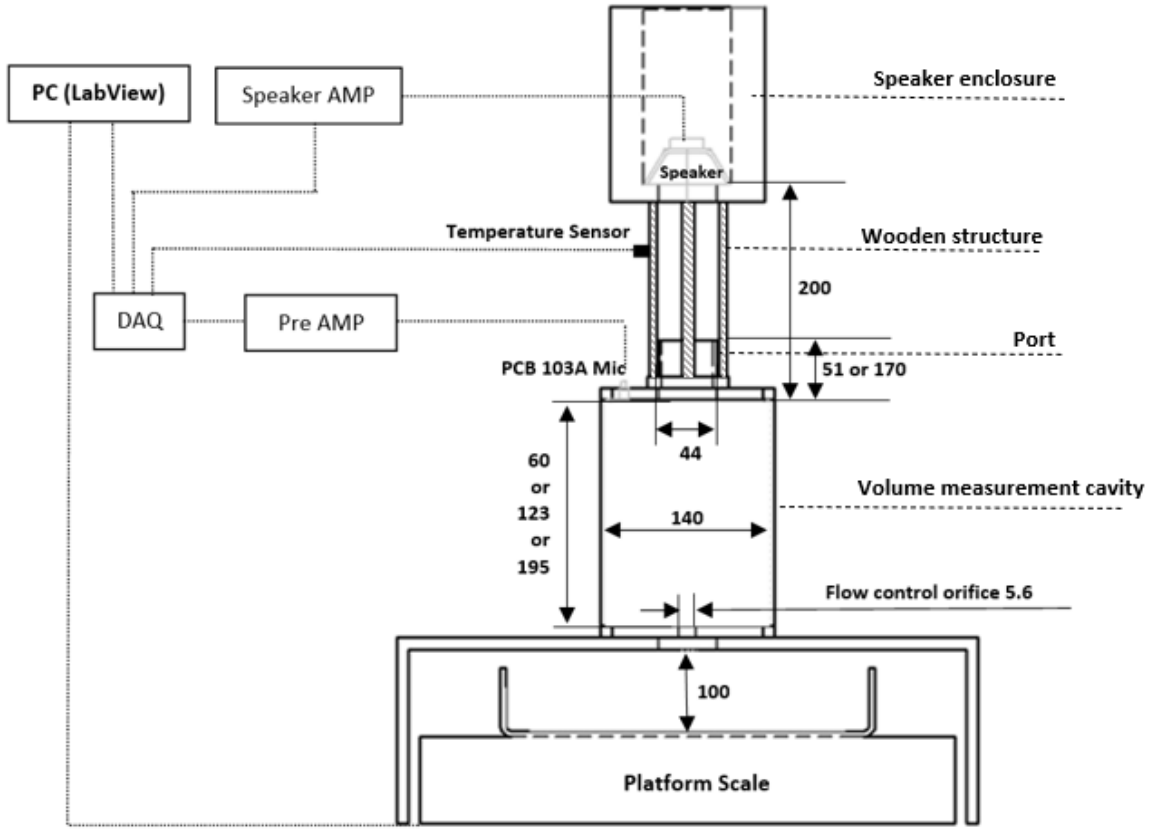


Figure 7-4: *Resonator Apparatus for static and discharge experiments. All dimentions are in mm.*

7.3.2. Variable Chamber Resonator

Figures 7-5 show a mechanically variable chamber resonator initially designed and used in a study by Webster (2010). This apparatus was utilized for rapid volume measurement in a fast-changing cavity volume (Drawing in Appendix E). This apparatus consists of a cavity with a piston as the cavity floor, controlled by a stepper motor linear actuator (LXP B 200, SMC Corporation, USA) with the stepper motor controller SMC LC6D. The actuator was controlled by pulses generated using the data acquisition hardware to allow a variable chamber volume of 1600 to 3500 ml with an uncertainty of 0.25 ml. The cavity of this device was made out of an aluminium tube with a wall thickness of 3 mm and an internal diameter of 156 mm. The port was the same as the other 170 mm port already introduced: 44 mm internal diameter with 3 mm wall thickness. The microphone was inserted inside the cavity glued to the upper plate, 40 mm away from the port opening, with the microphone wire coming out of the resonator port, fixed to the port wall using tape.

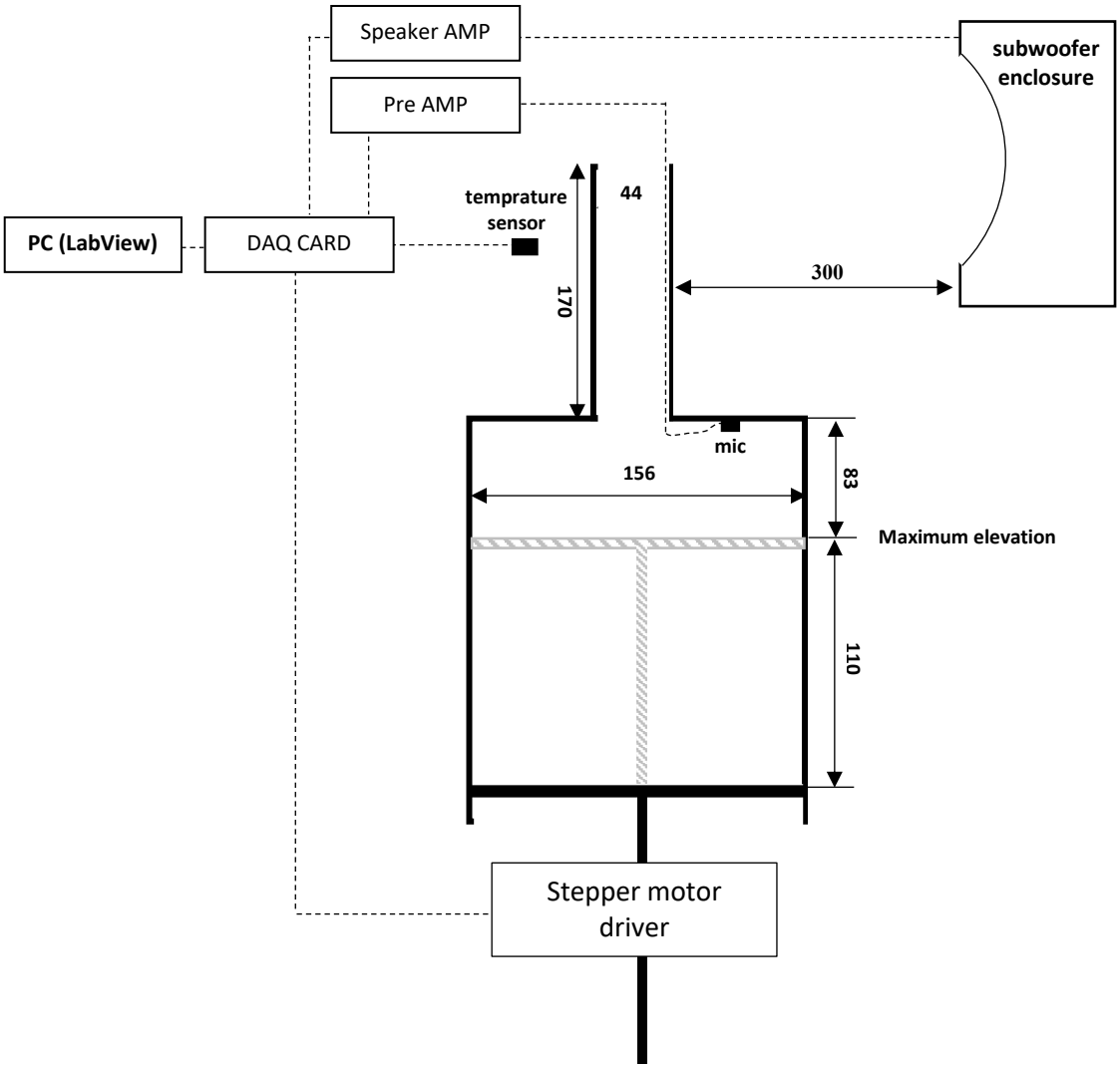


Figure 7-5*: Variable Chamber Resonator apparatus. All dimensions are in mm.*

7.3.3. Test Materials

The test materials for volume measurement were Water, large marbles (LMB), black mustard seeds (BMS), mustard seeds (MS), small polyethylene (PE1), coarse and fine ballotini (B710 and B250), ball bearings (BB) and agricultural lime (AL2). The physical properties of the powder samples are available in Chapter 4, Section 4.2.11. The other samples not included in that section are PE1 pellets with a mean diameter of 3.4 mm and a density of 0.93 $g.ml^{-1}$ and solid glass spheres with 60 mm and 80 mm diameters.

Agricultural products, including potatoes, avocadoes and kiwi fruit, were also tested to examine the method's accuracy. The actual volume of these samples was measured using the buoyancy

method in water to an uncertainty of 0.1 ml through 3 repeated experiments. The physical properties, including actual volume (V_A) and density (ρ_A)**,** variety of these samples are given in Table 7-1.

Table 7-1: *Agricultural products.*

Sample Name	Type	V_A (ml)	ρ_A (kg.m^{-3})
Potato 1	NZ Potatoes Washed White Nadine	213.71	1054.71
Potato 2	NZ Potatoes Washed White Nadine	160.19	1048.80
Potato 3	NZ Potatoes Washed White Nadine	102.71	1062.08
Potato 4	NZ Potatoes Washed White Nadine	163.25	1048.29
Potato 5	NZ Potatoes Washed White Nadine	95.56	1054.14
Potato 6	NZ Potatoes Washed White Nadine	133.58	1054.58
Potato 7	NZ Potatoes Washed White Nadine	222.42	1060.08
Potato 8	NZ Potatoes Washed White Nadine	75.01	1074.19
Potato 9	NZ Potatoes Washed White Nadine	133.48	1057.16
Potato 10	NZ Potatoes Washed White Nadine	84.93	1066.03
Avocado 1	NZ Jumbo Hass Avocado	205.78	1003.93
Avocado 2	NZ Jumbo Hass Avocado	238.55	993.57
Kiwi fruit 1	NZ Nutri Kiwi 4030	138.62	1046.54
Kiwi fruit 2	NZ Nutri Kiwi 4030	127.71	1041.67
Kiwi fruit 3	NZ Nutri Kiwi 4030	134.66	1044.64
Kiwi fruit 4	NZ Nutri Kiwi 4030	128.61	1041.44
Kiwi fruit 5	NZ Nutri Kiwi 4030	145.43	1038.00
Kiwi fruit 6	NZ Nutri Kiwi 4030	130.62	1050.51
Kiwi fruit 7	NZ Nutri Kiwi 4030	137.92	1048.12
Kiwi fruit 8	NZ Nutri Kiwi 4030	130.14	1051.00
Kiwi fruit 9	NZ Nutri Kiwi 4030	126.48	1042.40
Kiwi fruit 10	NZ Nutri Kiwi 4030	141.12	1052.81

7.4. Methods

Two approaches were used: analytical and experimental. The analytical approach aimed at estimating the volume of solids and liquids using the SPQF model. This approach was intended to verify the proposed theoretical model for instantaneous sample volume measurement.

The second approach was for real-time Fill Volume estimation of a vessel discharging powders through a pre-run experiment and trained data sets. As discussed in Chapter 4, Sections 4.5.8 and 4.5.9, powders absorb significant acoustic energy and alter the resonator acoustical damping. Therefore, sound absorptive powders fall out of the scope of the SPQF model. However, the same concept with a statistical approach can be applied to the powders.

7.4.1. Resonator calibration process

The resonator calibration process refers to obtaining the resonance wavenumber $k_0 = \omega_0/c$ and quality factor Q. After setting up the resonator apparatus and choosing the appropriate acoustic driver (loudspeaker), the resonance frequency was approximately found by the undriven resonance hunting method (Chapter 4, Section 4.3.1); a broadband chirp (50~200 Hz) was played for 0.5 s. About 5 ms after the excitation, the resonator response was recorded using the microphone for 0.5 s. The recording has undergone power spectral analysis to find the frequency bin with the highest power. Then, a detailed resonance hunting was performed using the Driven Method (Chapter 4, Section 4.3.2); a continuous chirp with a length of 40 Hz centred around the resonance frequency from the previous step was played for 30 s. The resonator response was simultaneously recorded, and it has undergone spectral analysis. The result of the power spectral density analysis was similar to what is shown in Figure 7-5, a graph of power S_{XX} versus frequency ω.

The driven damped resonance frequency ω_r is the frequency with the highest power, and for a largely underdamped resonance $\zeta < 0.05$, the natural frequency of the system ω_0 is slightly offset and can be calculated using $\omega_0 = \omega_r/\sqrt{1-2\zeta_0^2}$.

See Section 4.1.5, Equation 4-21. The quality factor was calculated using $Q \approx \omega_r/FWHM$ (Refer to Chapter 4, Section 4.1.5 and 4.3.10 for more details).

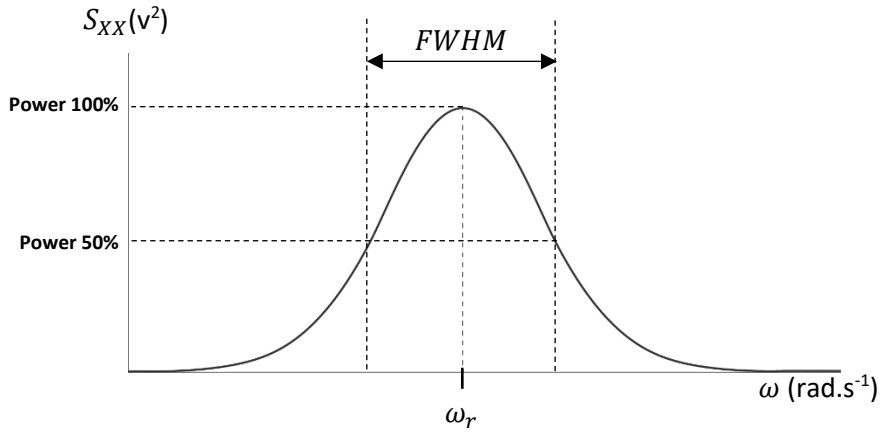


Figure 7-6*: Quality Factor and Resonance Frequency from power spectral analysis.*

Quality Factor can be obtained alternatively through calibration. When occupying the resonator with a sample with a known volume V_A, Quality Factor Q can be determined by rearranging Equation 7-35 into Equation 7-41.

$$Q = V_c \frac{\sqrt{1-\bar{P}^2}}{V_A \bar{P}} \qquad 7\text{-}41$$

At the beginning of the experiments using a resonator setup, resonance frequency, quality factor, and temperature were recorded When the resonator was empty or the initial condition of the resonator. The resonance frequency obtained from the empty resonator was used as the driving frequency ω_0 of the resonator apparatus throughout all tests with temperature compensation using Equation 7-40. The quality factor obtained using Equation 7-41 was used as the parameter Q in the SPQF model, Equation 7-35. Any change in the apparatus location in reference to the driver position, the driver sound amplitude, resonator port, or resonator cavity was considered a change in the apparatus setup, and the calibration process was repeated accordingly.

A driver was set to play a monotone at the frequency ω_0 and an amplitude of less than 50% of the speaker's nominal maximum power. The reason for not increasing the speaker powder beyond 50% was to minimise heat accumulation in the loudspeaker coil, which affects its impedance and causes non-linearity in the driver amplitude over time. The sound pressure in the empty resonator P_0 was recorded for a duration of almost 0.04 s (2000 signal samples at the rate of 44100 samples per second) and calculated for peak-to-peak amplitude. The loudspeaker remained on throughout all experiments, constantly playing the monotone ω_0 with slight adjustments for the ambient temperature variation using Equation 7-40. When there was a sample inside the resonator, the sound pressure P_1 was

recorded the same way as P_0 was recorded, the ratio of these two sound pressures $\bar{P}$ was calculated, and the sample volume was estimated using the SPQF model.

7.4.2. Experiments for model verification

The experiments were conducted in both static and dynamic conditions. Static tests refer to experiments with no movement in the sample. For model verification, these tests were conducted on solid samples and water. Volume estimation of solid samples was conducted on three resonator cavity volumes of 1, 2 and 3 litres and port sizes of 51 and 170 mm. The resonator was calibrated using the method described in Section 7.4.1.

The dynamic test was conducted on water discharging from the 3-litre resonator with the 51 mm port. The resonator was filled with 2700 ml of water. The resonator bottom plate was fitted with the 5.6 mm flow control orifice. The discharge orifice was blanked off using duct tape. The measurement was initiated by removing the tape and letting water discharge into the bucket on the scale. Microphone amplitude was monitored, and the signal amplitude was sampled every 0.04 s and recorded with the discharged water mass. The fill volume of the resonator was estimated using the water mass divided by its density. The recorded signal amplitudes were used for sample volume estimation.

7.4.3. Discharge Tests on powders

The bottom plate was fitted with a discharge flow control orifice for setting up the resonator, and the orifice was blanked off using duct tape. The powder samples were loaded onto the perforated plate (Introduced in Chapter 4, Section 4.3.8; Drawing available in Appendix E). The resonator was filled to the top with the sample on a known mass, and the plate was gently pulled up for a loose packing in the powder. The perforated plate was used to keep a consistent material bulk density in experiment repeats. Then, the resonator lid, port and small speaker were installed on top of the resonator. The lid was fixed with four bolts and tightened with equal torques. To initiate the discharge, the duct tape was removed to let the material discharge into the bucket on the platform scale. The microphone amplitude was recorded every 0.045 s, along with the mass from the scale. A moving average filter was applied to the amplitude data for every 10 points. The discharged mass and the amplitude of the sound were recorded in files referred to as calibration lookup tables.

The calibration lookup tables for each material were fed to software programmed in LabView. For repeated runs using the same material, the computer software tracked the signal amplitude in real-time and compared the amplitude data with those fed in through calibration look-up tables. The

software utilized the look-up tables to estimate the real-time amount of material inside the resonator. The algorithm that this software followed is available in Appendix A.

7.4.4. Experiments on the Variable Chamber Resonator

The SPQF model was verified using the variable chamber resonator. For the experiments on this resonator, the piston was lowered 110 mm from its maximum elevation, resulting in a cavity with a volume of 3702 ml. The resonator was calibrated using the procedure described in 7.4.1. The signal amplitude recording was started, and the piston was raised to its maximum elevation, resulting in a cavity with a volume of 1600 ml. While the piston was in motion, Signal amplitude and the position of the piston at each instance of time were recorded. The experiments were repeated for 0.3 to 75 $mm.s^{-1}$ piston speeds.

7.5. Results

7.5.1. Volume estimation of discharging water

Figure 7-7 shows the recorded ratio of sound pressure amplitude $\bar{P} = P_1/P_0$ inside the resonator in relation to the estimated normalized resonance frequency ω_1/ω_0 during water discharge from the 3-litre resonator with the 51 mm port. The resonator was excited by a monotone at about 136 Hz, corresponding to the natural frequency of the empty resonator when its cavity was empty. The experimental data in this Figure were recorded from the right when the resonator was filled with water to the left when all the water was discharged from the resonator. The vertical axis in this figure is $\bar{P}$ which is the ratio of sound pressure amplitude inside the resonator containing the sample (P_1) to the initial sound pressure when the resonator was empty (P_0). On the bottom horizontal axis, the estimated resonance frequency is shown, normalized to the resonance frequency of the empty resonator. The top horizontal axis represents the volume of water inside the resonator at each instance of time. The red, green, and blue lines in the figure represent the estimated sound pressure drop as a function of the empty volume of the resonator. These lines demonstrated the damping ratio influence on the sound pressure drop trend and were drawn for various damping ratios of 0.008, 0.01, and 0.014. It is worth mentioning that the measured Quality Factor of this resonator setup through 10 repeated measurements was 50±2, which corresponds to $\xi \approx 0.01$.

As shown in the figure, based on the Pearson Correlation analysis, the experimental pressure drop exhibited a high correlation with the estimated values for a damping ratio of 0.01, yielding a correlation factor of ~1.

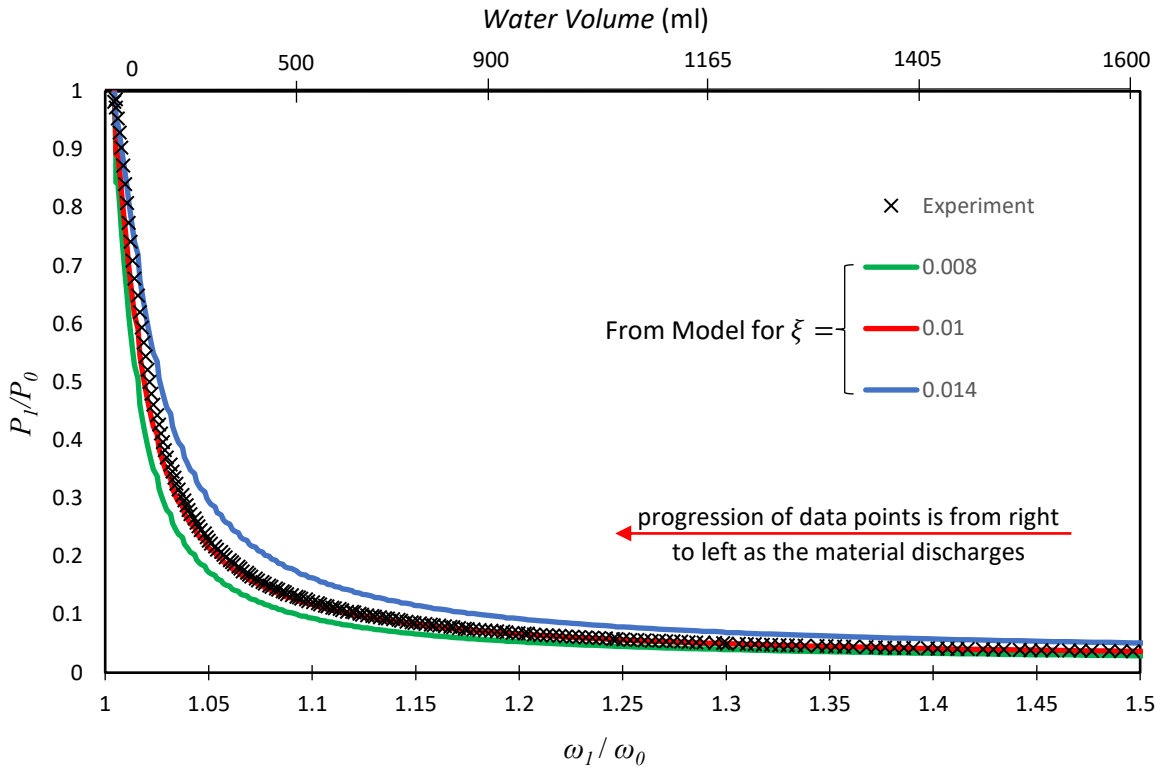


Figure 7-7: *Normalized sound pressure ratio versus estimated resonance frequency as the water inside the resonator discharges from the bottom orifice.*

Figure 7-8 shows the estimated volume of water while getting discharged out of the 5.6 mm orifice and compares it with the actual volume of water. The percentage deviation *E%* between the estimated and actual water volumes was calculated using $E\% = 100(V_s - V_A)/V_C$ where V_A is the actual volume from weighing, considering the density of water, reverse osmosis (RO) purified water, and its temperature.

Figure 7-9 shows the *E%* distribution from the actual values for the data point shown in Figure 7-7. The ordinate is the probability or population index ranging from 0 to 1, showing the density of the data points associated with the corresponding error in the abscissa. Choosing a value of 49.5 for the quality factor, which is in the uncertainty range of the measured values by spectral analysis, results in an error distribution centred at *E%*=0 with a standard deviation of 0.48%.

The water discharge test was repeated while increasing the speaker sound level from 30% to 50% of its maximum level. Sound pressure in the empty resonator P_0 increased from 113 dB to 114 dB; the

empty resonator Quality Factor dropped from ~49 to ~43. Regarding *E%,* the volume estimations from the second run were almost identical to those of the first run.

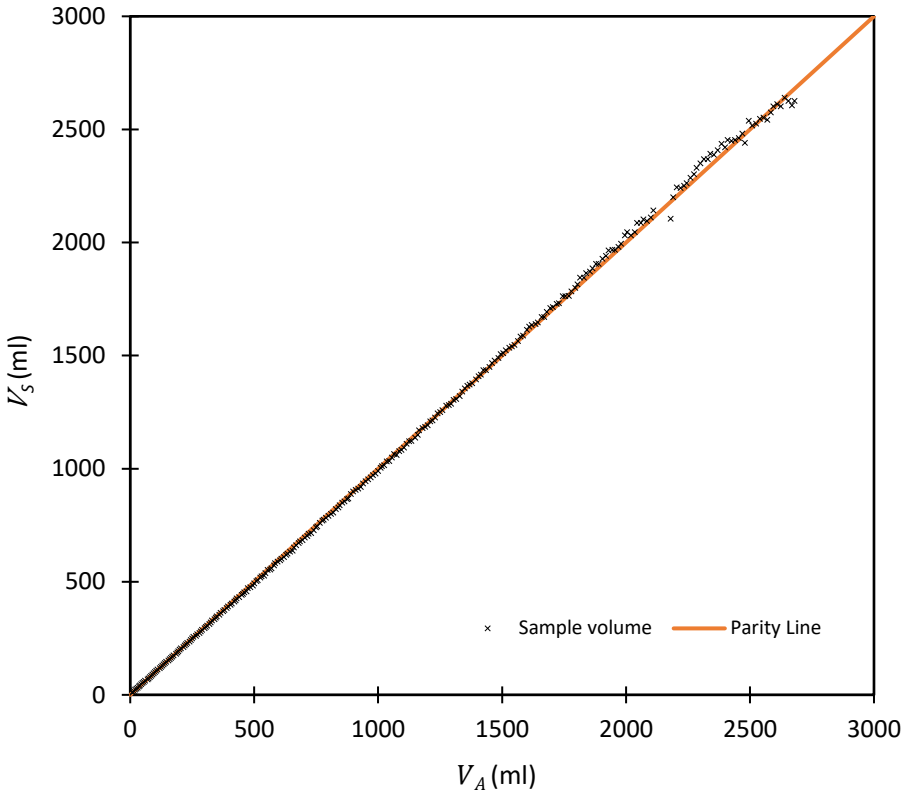


***Figure 7-8**: Water volume prediction using the model while it was getting discharged out of the 3-litre resonator from a 5.6 mm orifice.*

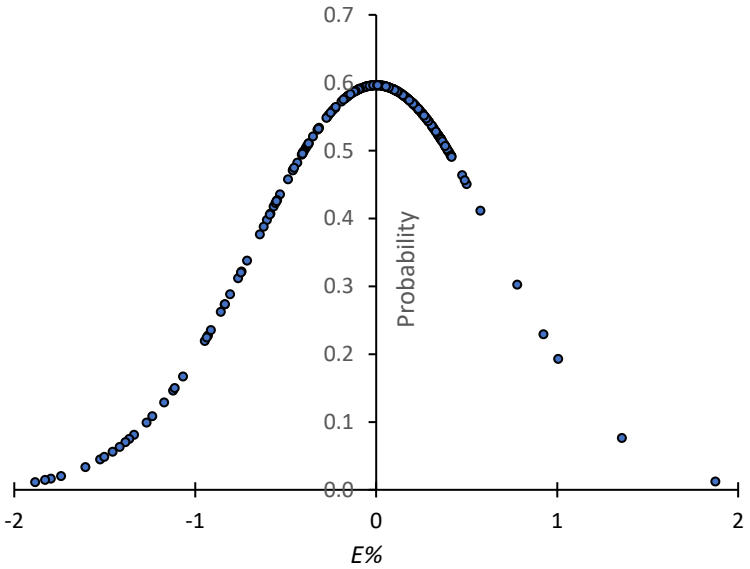


***Figure 7-9**: Error analysis of the estimated volume.*

7.5.2. Volume Estimation of solids

Figure 7-10, consistent with other experiments, displays the decrease in sound pressure amplitude when marbles were introduced into the resonator versus resonator Fill Factor. This resonator had a 3-litre cavity and a 51 mm port. In this resonator setup, k_0 was 2.4857 $m^{-1,}$ Q was 53.47 and cavity volume was 2880±2 ml.

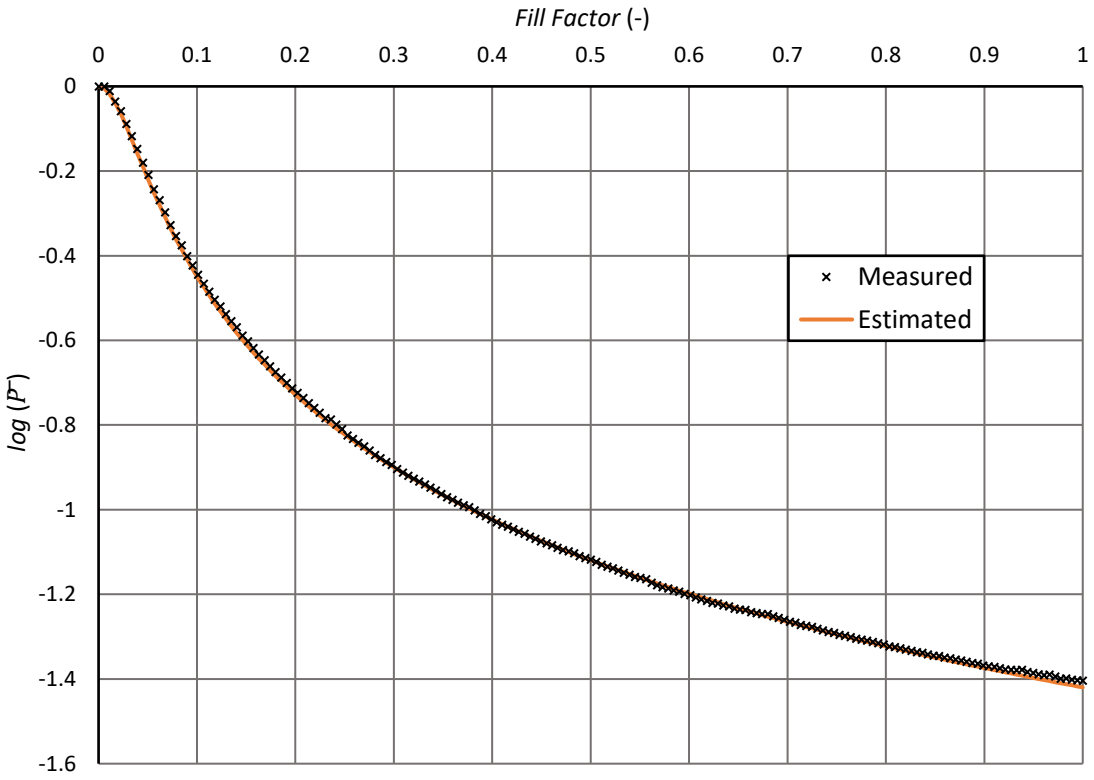


Figure 7-10: *The change in $log\ (\bar{P})$ with increasing cavity Fill Factor using large marbles (LMB).*

Figure 7-11 shows the estimated versus the actual volume of marbles in the 3-litre resonator with the 51 mm port. The marbles were added in increments, one marble at a time; the sound pressure inside the resonator was recorded, and the next marble was added. In total, 178 marbles were fit into the resonator. The volume of marbles was estimated accurately. The data points in Figures 7-11 follow a linear trend and are on the parity line, confirming the SPQF model's validity. The maximum deviation of the estimated volume from the actual volume *D%* remained well below 0.5% for 1 to 150 marbles, a Fill Factor of 0.85 and was less than 0.2% for Fill Factors up to 0.55.

As shown in Figure 7-12, there was a slight under-prediction as the depth of the marble bed became comparable to the resonator height where interference with the resonator port occurred. Fill

Factor in the horizontal axis is defined as the number of marbles inside the resonator divided by 178, the maximum number of marbles that could fit into the 3-litre resonator.

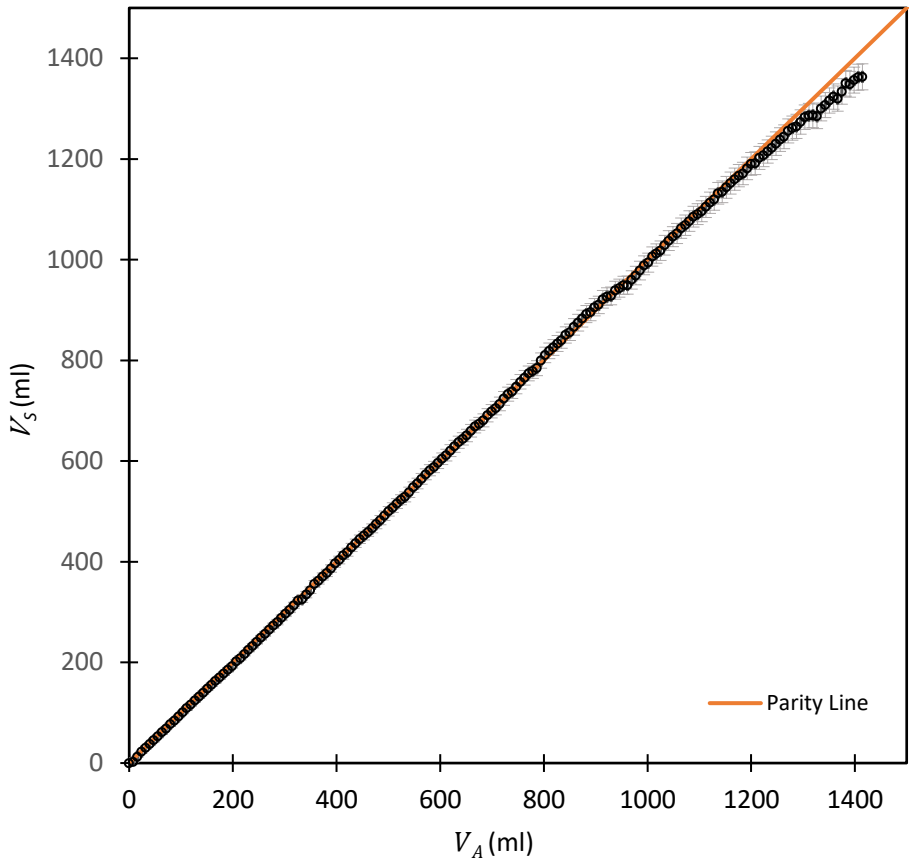


Figure 7-11: *Estimated volume of marbles in the 3-litre resonator. Error bars represent the uncertainty in the actual sample volume.*

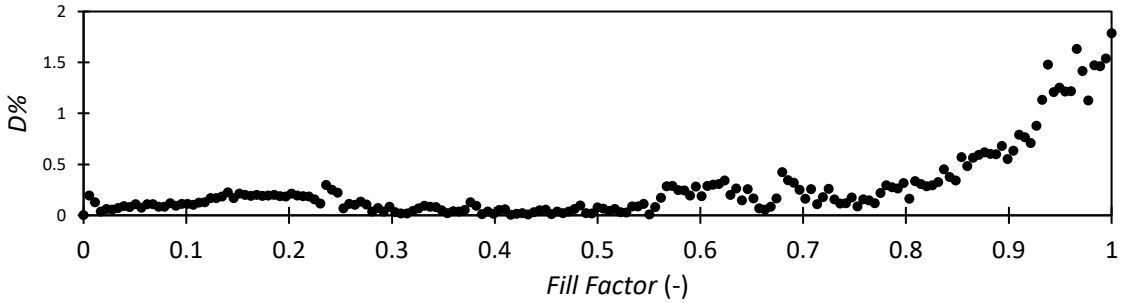


Figure 7-12: *Error D% in volume estimation of marbles as the percentage of the resonator volume (Ordinate) versus the Fill Factor of the resonator (Abscissa).*

The experiment on marbles was repeated in a 1-litre resonator with a 51 mm port. In this resonator, the resonance frequency of the empty resonator was 1558 Hz. Quality Factor was 37 at 50% speaker power. The measured sound pressure in the empty resonator was 119 dB. The results of this experiment are shown in Figure 7-13.

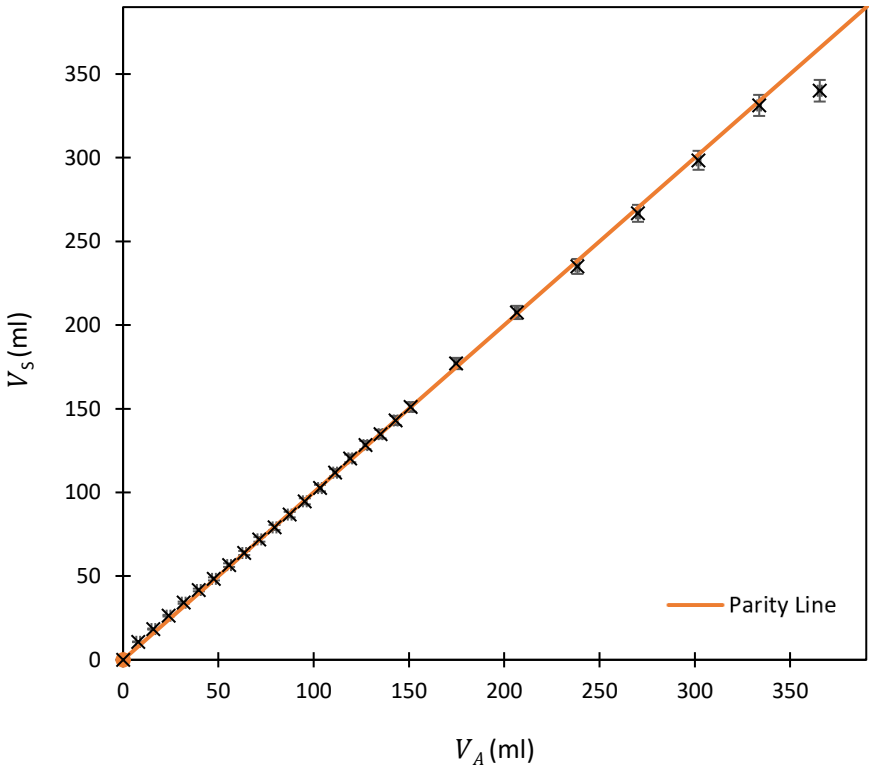


Figure 7-13: *Volume estimation of marbles in the 1-litre resonator. The orange line is the parity line. Error bars represent the uncertainty in the actual sample volume.*

As is shown in Figure 7-13, up to the Fill Factor of 0.85, which is equivalent to 306 ml of occupied volume by the solid phase of the marbles, the accuracy was comparable with the tests on the 3-litre resonator with a mean deviation $MD\%$ of 0.09% and a maximum deviation of 0.3% recorded for the first five marbles (See Error Analysis Equations in the thesis' front end). The last load of marble resulted in significant underprediction, which is believed to be due to interference with the resonance of air in the port. Up to a volume of 300 ml, the trend of estimates was linear (R^2=0.99), which shows the linearity of the model regardless of the sample load to a Fill Factor of three-quarters of the resonator volume.

The experiment on marbles was repeated in the 2-litre resonator with the 170 mm port. The results were comparable to those tests in the 3-litre and the 1-litre resonator. For this resonator setup, the resonance frequency was 106.3 Hz, the quality factor was 37.9, and the cavity volume was 1896.35 ml. Sound pressure amplitude for the empty resonator P_0 was 350 Pa (144.8 dB). For tests on marbles, 110 samples were added to the resonator in batches of 5, and the sound pressure amplitude was measured for each batch. Up to the Fill Factor 0.9, the deviation between estimations and actual volume *D%* remained below 0.5%.

The 2-litre resonator with the 170 mm port attached was used to test the solid volume of the agricultural samples, and the results are presented in Table 2. As outlined in column *Difference* of Table 7-2, the volume of all samples was estimated using the SPQF model with a maximum error from the actual volume of less than 1 ml. Considering that the capacity of the resonator was ~2000 ml, the maximum observed error was less than 0.05% of the resonator capacity. In Table 7-2, column $Error\% = \frac{100|V_A - V_S|}{V_A}$ is the absolute error.

The maximum deviation *D%* between the sample's actual volume and estimated volume using the SPQF model in these experiments was 0.05%V_0, or 0.05% of the vessel capacity.

Table 7-2: *Results of solid volume estimation for various samples.*

Sample	$\overline{P}$ *(Pa.Pa^{-1})*	V_A (ml)	V_S (ml)	*Difference* $V_S - V_A$ (ml)	*Error%*
Sphere 60 mm	0.40	113.65	113.98	0.33	0.29
Sphere 80 mm	0.19	258.10	257.59	-0.51	0.20
Potato 1	0.23	213.71	214.34	0.63	0.29
Potato 2	0.30	160.19	160.90	0.71	0.44
Potato 3	0.44	102.71	102.34	-0.37	0.36
Potato 4	0.29	163.25	162.52	-0.73	0.45
Potato 5	0.46	95.56	96.20	0.64	0.67
Potato 6	0.35	133.58	134.33	0.75	0.56
Potato 7	0.22	222.42	222.87	0.45	0.20
Potato 8	0.56	75.01	74.58	-0.44	0.59
Potato 9	0.35	133.48	134.11	0.63	0.47
Potato 10	0.51	84.93	84.54	-0.39	0.46
Avocado 1	0.24	205.78	206.69	0.91	0.44
Avocado 2	0.21	238.55	238.82	0.27	0.11
Kiwi fruit 1	0.34	138.62	138.47	-0.15	0.11
Kiwi fruit 2	0.36	127.71	127.75	0.04	0.03
Kiwi fruit 3	0.35	134.66	133.87	-0.79	0.59
Kiwi fruit 4	0.36	128.61	129.08	0.47	0.37
Kiwi fruit 5	0.33	145.43	144.92	-0.52	0.36
Kiwi fruit 6	0.36	130.62	130.28	-0.34	0.26
Kiwi fruit 7	0.34	137.92	137.97	0.05	0.04
Kiwi fruit 8	0.36	130.14	130.42	0.28	0.22
Kiwi fruit 9	0.37	126.48	126.67	0.19	0.15
Kiwi fruit 10	0.33	141.12	142.07	0.96	0.68
Kiwi fruits 2+3+4+5	0.09	536.41	536.43	0.02	0.00
			Mean Error	**0.09**	
			Uncertainty of Mean Error based on CI.95	**±0.21**	
			Standard Deviation	**0.50**	
			Uncertainty of Measurement based on PI.95	**±1.05**	

7.5.3. Variable Chamber Resonator

The experiments using the Variable Chamber Resonator aimed to demonstrate the SPQF model's efficiency in estimating cavity volume in a highly dynamic situation.

Figure 7-14 shows the results of the variable chamber resonance when the piston was moving up with the speed of 0.3 mm.s$^{-1,}$ which resulted in cavity volume change at the rate of 5.7 ml.s^{-1}. The estimated volumes were highly accurate and linear, as shown in Figure 7-14, with a slight underprediction for V_A > 1700 ml, similar to the previous results using the fixed resonators.

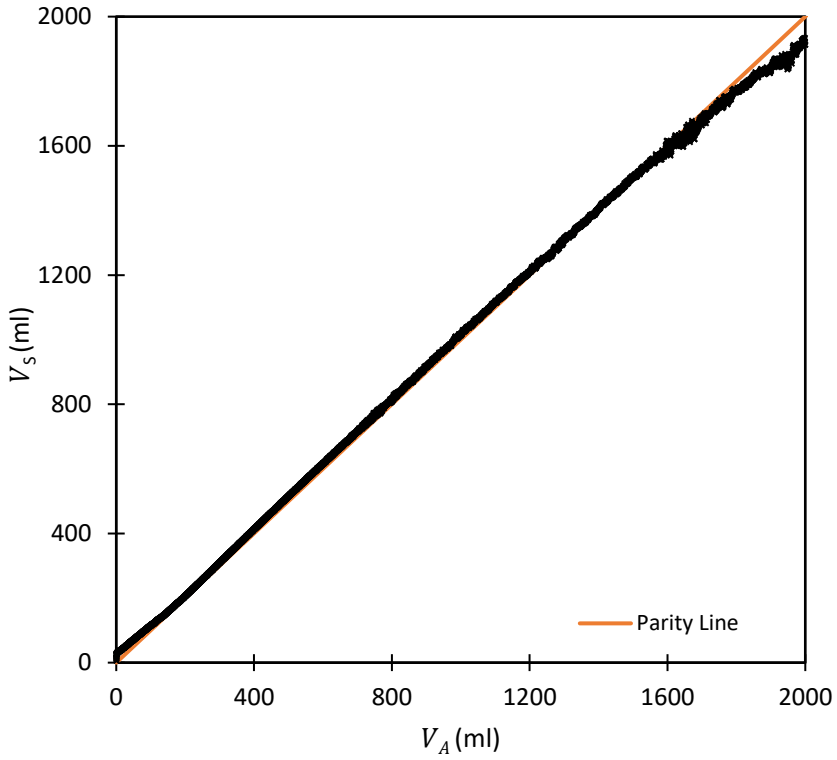


Figure 7-14: *Estimation of cavity volume in the variable chamber resonator with a piston speed of 0.3 mm.s^{-1}.*

Figure 7-15 shows the experiment results when the piston moved up at 75 mm.s^{-1}, equivalent to 1440 ml.s^{-1} of volume displacement. The entire duration of the piston travel was 1.436 s. On average, the estimated volume was 98 ml (*MD%*=2.7), higher than the actual volume, with an uncertainty of 57 ml based on *CI.95*. The contributors to this deviation can be the noise induced by the piston and the air being pushed out of the port with a flow rate of 1440 ml.s$^{-1,}$ which can affect the oscillating mass of the air in the port.

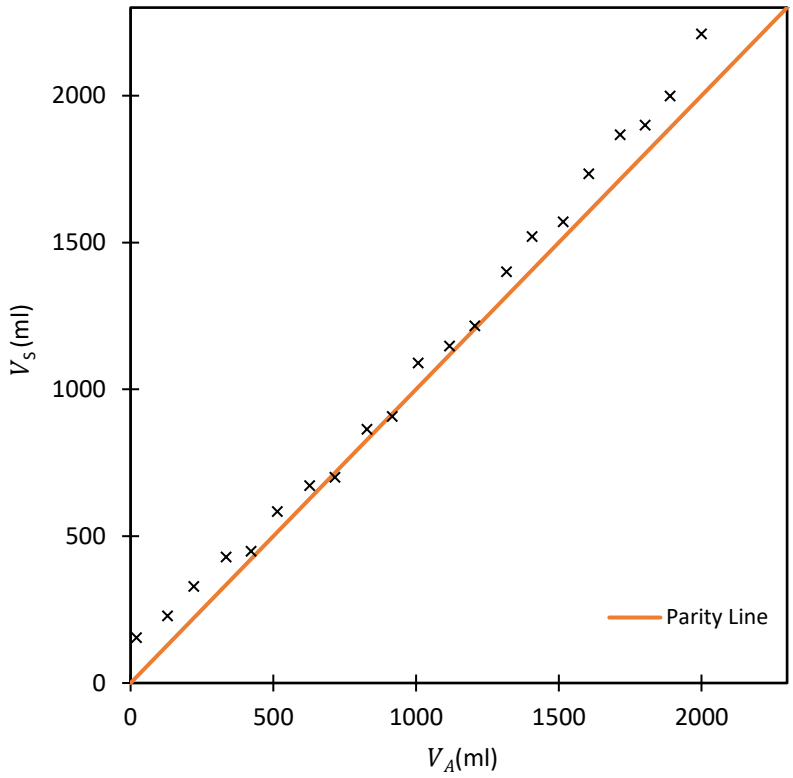


Figure 7-15: *Estimation of cavity volume in the variable chamber resonator with a piston speed of 75 mm.s^{-1}.*

The signal sampling time for volume measurement was reduced from 0.044 s to 0.022 s to push the speed of the volume measurement rate of ~50 Hz. This measurement duration is approximately twice the excitation monotone period of 0.012 s. Figure 7-16 shows the results of the variable chamber resonance when the piston was elevating at a speed of 30 mm.s^{-1}. The estimates are, on average, 55 ml over. This overprediction of volume complies with the observation in the previously reported experiment, where the speed of the piston was 75 mm.s^{-1}. The piston pushing the air out of the port is believed to affect the oscillation of the air mass in the port, which manifested in all the estimations being offset from the actual values, with an almost constant deviation. The experiment was repeated with a sampling time of 0.009 seconds, shorter than the period of the driving monotone of 0.012 seconds. The results at this measurement duration were volatile due to fluctuations and unusable for cavity volume estimation.

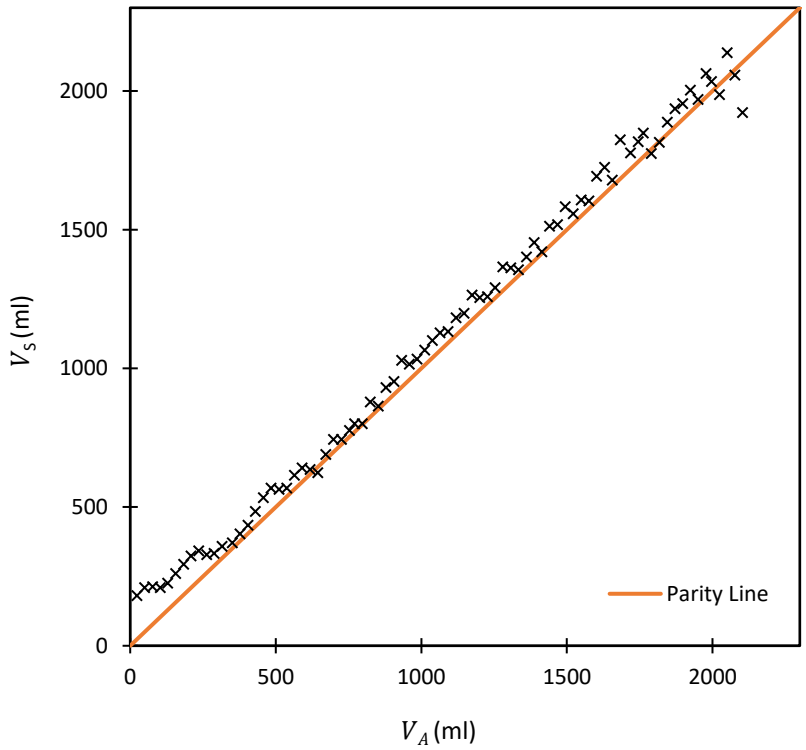


Figure 7-16: *Estimating cavity volume in the variable chamber resonator with a piston speed of 30 mm.s^{-1}*. In This experiment, the volume measurement rate was ~50 Hz.

7.5.4. Dynamic volume measurement of powders

This section reports the mass directly measured as a normalised Mass Fill Factor by dividing the mass by the initial mass of material in the resonator to avoid the added layer of uncertainty in converting the material mass to material volume. The results from the experiments on powder samples discharging from the 3-litre resonator with the 51 mm port are shown in Figure 7-17. The data on the graphs in the figure are recorded from right to left. The far right side shows the sound pressure amplitude drop when the resonator was full, Fill Factor =1, and the far left side of each graph shows when the material was drained. The sudden drop in the amplitude shown on the far left side of the graphs occurs when the discharge orifice at the bottom of the hopper starts to appear. This moment is when a portion of the acoustic energy is lost due to the radiation resistance of the bottom orifice. This is equivalent to opening a new port for the resonator with a variable diameter.

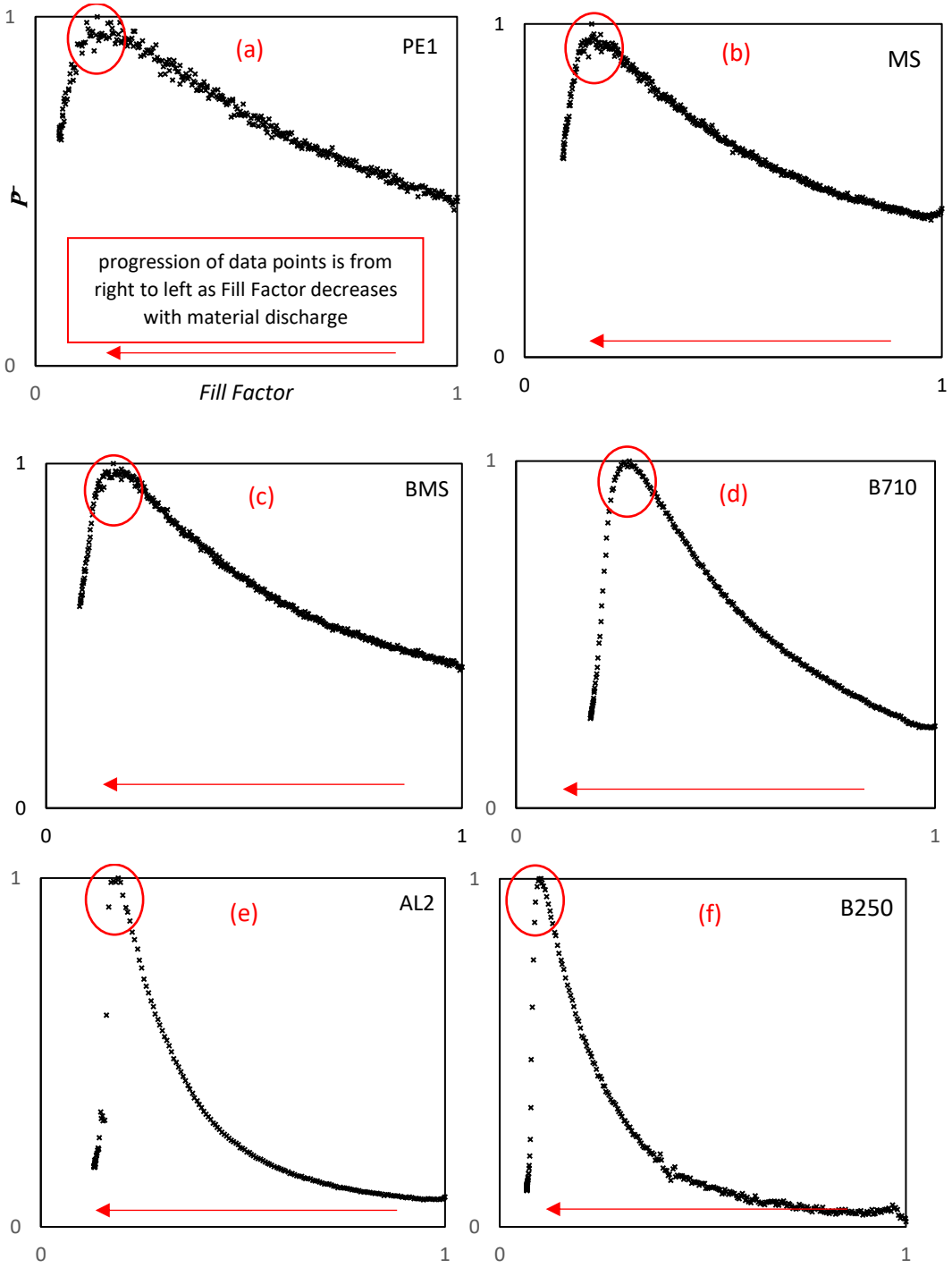


Figure 7-17: *Amplitude variation based on the fill level of the resonator for six different samples. The ordinate is P/P_0 ($\overline{P}$), and the abscissa shows the fill factor of the resonator (Remaining Mass/ Initial Mass). The progression of data points in all graphs is from right to left.*

This variation in the resonator port geometry, which was constant in the theoretical approach, makes it challenging to use the analytical model for volume estimation of discharging powders out of the hopper. However, the sudden drop in the signal amplitude, as marked in the far left side of the graphs in Figure 7-17 using red circles, provides technically significant information about the "Emptiness" of the hopper.

As shown in Figure 7-17, the more porous material with large particles, including polyethene pellets PE1 (a) and mustard seeds MS (b), resulted in a lower rate of change in sound pressure drop than a packed and fine material like agricultural lime. This observation could be due to the fluid phase of the open pore powders actively contributing to the dynamic restorative force of air inside the resonator.

The data in Figures 7-17 were used to make the look-up tables for the instantaneous estimation of the fill factor of the resonator for each specific sample.

Figures 7-18 show the estimated values of the mass of agricultural lime (AL2) and black mustard seeds (BMS) samples in the repeat runs. The estimates were obtained in real-time from the trained lookup tables.

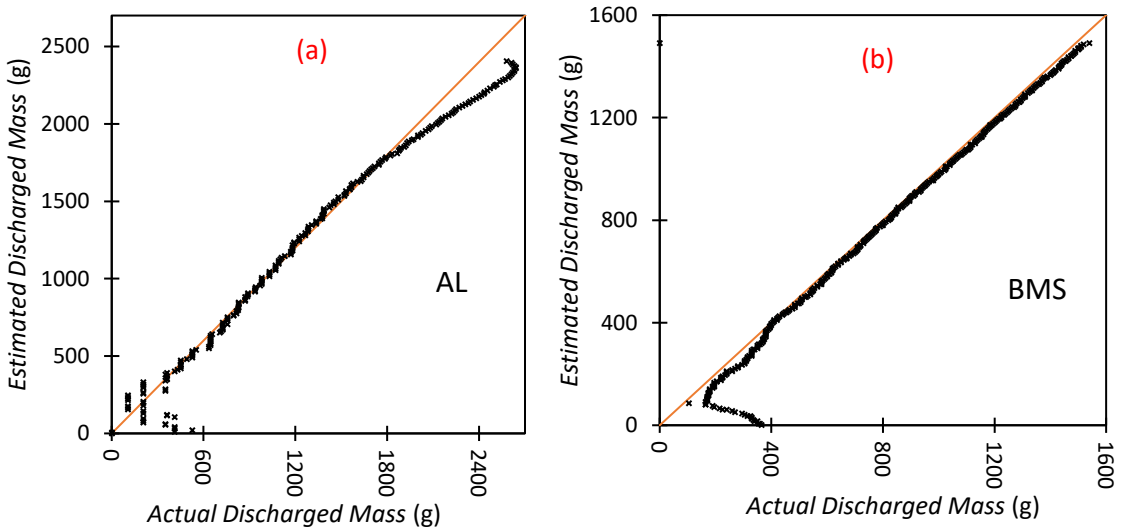


Figure 7-18: *The estimated discharged mass (Y-Axis) versus actual discharged mass (X-Axis) for agricultural lime (a) and black mustard seeds (b). The orange line is the Parity Line.*

The repeatability of this method was investigated by running the experiment three times on three consecutive days on a sample of black mustard seeds. The experimental setup was relocated in the lab, and the lab temperature varied from 18~22 °C. For the black mustard seeds sample, the range of 400 to 1600 g of the discharged mass was the range that the estimations were reliable and repeatable. This range covers 75% of the resonator capacity. The results of the repeated runs of discharge mass estimation for black mustard seeds are presented in Figure 7-19. In the repeated experiments, the maximum deviation *D%* from actual mass based on the capacity of the resonator $\%V_0$ (1600 g black mustard seeds) was 0.9 %.

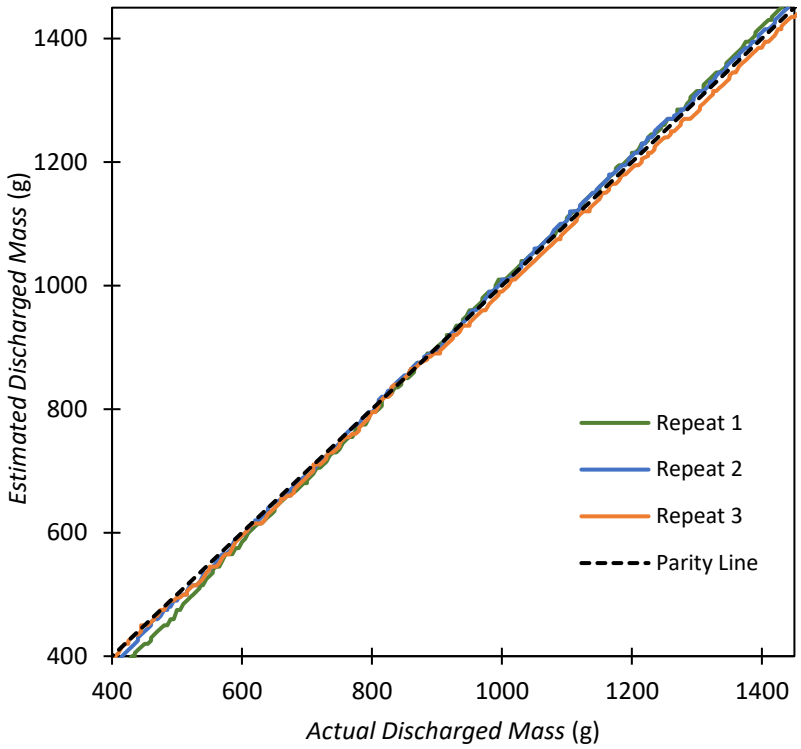


Figure 7-19: Repeatability of sample mass estimation for three test runs on the discharge of black mustard seeds from the 3-litre resonator.

7.6. Discussion

7.6.1. Model Verification

The water discharge test was conducted to investigate the agreement between the experimentally obtained values of the resonator cavity sound pressure drop and the estimates from the model. Inspecting Figure 7-7, the experimentally obtained data closely tracked the estimated values with a Pearson Correlation of nearly 1 for a Fill Factor range of 0~0.9. This agreement was subjected to choosing an exact value for the damping ratio ζ.

Water discharge changed the resonator cavity volume. The SPQF model was used to estimate cavity volume instantaneously. The results showed that the estimated volumes were very close to the actual volumes. Choosing the exact quality factor value minimised the uncertainty of this method to 0.9% of the resonator capacity for a confidence interval *CI* of 0.95. This uncertainty covers the entire Fill Factor range of the resonator up to a Fill Factor where the water level was 5 mm below the resonator port.

The repeated direct measurement of the resonator quality factor by spectral analysis method, as outlined in Section 7.4.1, resulted in deviations of up to 8%. The calibrated values for Q were within the uncertainty range of the direct measurement of Q using the process explained in Section 7.4.1.

The results of marble sample volume estimation using the SPQF model demonstrated the model's accuracy. The experiment was repeated for cavity volumes of 1, 2 and 3 litres with 51 mm and 170 mm ports. The Results suggest that for samples with volumes up to Fill Factor 0.5, volume can be estimated with an uncertainty of less than 0.2% of vessel capacity $\%V_0$. Higher accuracies may be achievable subjected to calibration for the non-linearities, especially when the sample gets close to the opening of the resonator port.

The effect of temperature on the resonator Quality Factor was investigated by adjusting lab air temperature in the range of 22.2~28.1 °C. In this range, the Quality Factor of the 2-litre resonator with the 51 mm port was measured at intervals of almost 0.3 °C. Despite fluctuations within the range of 6%, no positive or negative trend in Quality Factor variation based on temperature was observed. Based on this observation within the mentioned temperature variation boundaries, it is suggested that the only required temperature adjustment is the resonator driving frequency adjustment using Equation 7-50.

The Variable Chamber Resonator tests were intended to evaluate the volume estimation speed using the model in a highly dynamic situation. The fastest speed that the piston could travel was

75 mm.s^{-1}. At this speed, the cavity volume changed by 2 litres in less than 1.5 s. The SPQF model was used to measure cavity volume in real-time at a rate of 20 to 50 Hz.

The SPQF model makes it possible to estimate the volume of a liquid or solid sample as fast as one period of the natural frequency of the resonator, and it opens doors to questions regarding possible challenges, including the effect of the rate of change in cavity volume in measurement accuracy. The frequency hunting methods employed in Chapters 4, 5, and 6 require a signal sampling duration at least two hundred times longer than the SPQF model approach to achieve similar levels of accuracy in volume estimation. However, this method is more environmentally sensitive and prone to error. It was observed that opening the lab door when using the 51 mm port can change the resonator sound pressure by almost 2.7%, which can significantly compromise measurement accuracy when the sample volume is small compared to the resonator volume. Using the 170 mm port and reducing the gap between the port opening and the speaker driver to 25 mm reduced the pressure amplitude's sensitivity to the resonator's location. Therefore, environmental conditions, including background noise and the location of the resonator related to the surroundings, should be considered, and it is suggested to calibrate the resonator to find the initial pressure P_0 and Quality Factor Q after any change in the environmental conditions, including the resonator location. It is suggested to have a minimal distance between the port opening and the speaker driver while adjusting the speaker power to have a quality factor higher than 20. Note that relocating the speaker driver referenced to the resonator port or adjusting the output power of the speaker affects the resonance quality factor. This observation was confirmed by testing various port lengths of 51, 250, 500 and 1000 mm (See Chapter 4, Section 4.4.7).

7.6.2. Experimental approach for estimating the resonator Fill Factor when discharging powder samples

The proposed experimental method was valid for the resonator's Fill Factor estimation when discharging a powder sample. The instantaneous estimation of the powder mass in a resonator enables instantaneous flow rate estimation. The repeated experiments on the discharge of black mustard seeds resulted in a maximum uncertainty of 0.9% of the full scale in the Fill Factor range of 0.2 to 0.8. This method requires a calibration run for each powder sample to generate a look-up table of instantaneous sample mass based on pressure drop in the resonator. The accuracy of volume estimation was compromised when the resonator was filled with more than 80 % of its capacity (Fill Factor of 0.8 and more). Also, when the material discharged to Fill Factors is less than 0.2, the uncertainty increases due to the uncovered discharge orifice. The experimental algorithm and the

look-up tables to feed in for sample volume estimation could be improved through repeated tests to expand the Fill Factor region at which the mass of material can be estimated accurately. When the material discharged to the bottom of the resonator, the discharge orifice was uncovered, which resulted in a sharp drop in cavity pressure. This drop was monitored and used to find when the resonator discharged its content.

7.6.3. A technical note on using microphones with limited dynamic range

To effectively convey the key message of this section, it is essential to provide a concise overview of microphones. Measurement microphones are available in three main types: free-field, random-incident, and pressure, each differing in frequency response characteristics. These types are briefly described in the following paragraphs.

Free-field microphones are designed to measure the sound pressure in a field as it would be if the microphone were not present, effectively compensating for the disturbance caused by the microphone's presence, particularly at high frequencies (above 1 kHz). On the other hand, random-incident microphones exhibit low directivity and are calibrated to compensate for the effects of the microphone's presence within the sound field. Pressure microphones, in contrast, are designed to measure sound pressure directly at the microphone's diaphragm, functioning as dynamic pressure measurement devices for pressure fluctuations within a closed cavity. In this study, the microphone used was of the pressure type, specifically model PCB103A.

Pressure microphones are primarily engineered to possess a high dynamic range, which refers to the range of pressure within which the microphone maintains its sensitivity. For instance, the PCB103 model is designed to have a dynamic range exceeding 177 dB. When at resonance, a Helmholtz Resonator generates high-pressure fluctuations within its cavity. In the experiments detailed in this chapter, the pressure of the resonator cavity at resonance exceeded 120 dB. This pressure level was comfortably within the dynamic range of the microphones utilized.

Free-field microphones, particularly those of the array type, can measure pressure fluctuations with very high sensitivity, yet they often lack the extensive dynamic range found in pressure microphones. Additionally, free-field array microphones are generally more affordable than pressure microphones, making them a viable option for sample volume measurement using the model introduced in this chapter.

For those seeking to utilize the SPQF method (also introduced in this chapter) with high accuracy, a cost-effective solution could involve employing widely available and economical array microphones,

taking advantage of their low cost and high sensitivity. However, addressing the limited dynamic range of these microphones remains a challenge.

The limited dynamic range of a microphone becomes a challenge in measuring resonance pressure amplitude because the difference between P_0 and P_1 is large. The volume measurement method introduced in this chapter involves measuring resonance pressure P_0 in the empty resonator at resonance. Consider reducing the excitation amplitude or speaker driver to very low levels that render the resonance pressure amplitude to levels within the dynamic range of the array microphone. For such a setup, when placing a sample inside the resonator, the cavity volume changes; thus, the sound pressure amplitude to be measured P_1 drops, similar to what is shown in Figure 7-7. This sound pressure can be as low as the background or floor noise level of the electronics or the environmental background noise level, which results in poor measurement accuracy.

Looking at the problem the other way around, if the sample is inside the resonator and the excitation amplitude is set at high levels at which the signal-to-noise ratio of the resonator is high enough to have a strong signal for measuring P_1, the measurement of the pressure P_0 at the empty resonator state is impossible due to microphone dynamic over range.

To resolve the dynamic range limit and retain the signal sensitivity while using an affordable array microphone, the idea is to estimate P_0 instead of directly measuring it. This estimation can be done through calibration, as described below.

The resonance frequency of a resonator F_o can be measured using a low driving amplitude not to cross the microphone dynamic range. For finding $P_{0,}$ one can use two samples with volumes V_1 and V_2 where $V_1 > V_2$. This sample can be two loads of water with a known volume or a solid sample.

After putting sample V_1 inside the resonator and exciting the resonator using a monotone with frequency F_o, the driver amplitude can be adjusted to obtain a strong signal from the microphone at its dynamic range. At this stage, the microphone amplitude can be recorded as P_1.

With the driver continuing to excite the resonator at the same amplitude and frequency, the other calibration sample with volume V_2 can be replaced with V_1 to measure microphone amplitude P_2. From Equation 7-35, the system in the two states can be described using Equations 7-42 and 7-43. Dividing 7-42 by 7-43 and doing algebraic manipulation to solve the system of equations for P_0, results in 7-44. The resonator quality factor Q can be expressed using 7-45 as follows:

$$V_1 = V_C \frac{\sqrt{1-\left(\frac{P_1}{P_0}\right)^2}}{Q\frac{P_1}{P_0}} \qquad 7\text{-}42$$

$$V_2 = V_C \frac{\sqrt{1-\left(\frac{P_2}{P_0}\right)^2}}{Q\frac{P_2}{P_0}} \qquad 7\text{-}43$$

$$P_0 = \frac{P_1 P_2 \sqrt{V_1^2 - V_2^2}}{\sqrt{(P_1 V_1)^2 - (P_2 V_2)^2}} \qquad 7\text{-}44$$

$$Q = V_c \frac{\sqrt{1-\left(\frac{P_1}{P_0}\right)^2}}{V_1\frac{P_1}{P_0}} \qquad 7\text{-}45$$

With F_0 measured by resonance hunting (See section 7.4.1) and P_0 and Q estimated using Equations 7-44 and 7-45; the resonator can be used to estimate the volume of materials placed in it using the SPQF model with an affordable array microphone with a limited dynamic range.

It is noteworthy that in this calibration method, Q cannot be directly measured with the method explained in 7.4.1 and estimating it using Equation 7-45 is recommended. The reason is explained in Chapter 4, Section 4.4.7; the resonator-driven quality factor is a function of excitation amplitude, and here, the resonance frequency is hunted with lower speaker amplitudes compared to the amplitude set for sample volume measurement to avoid microphone dynamic over-range. Therefore, Equation 7-45 should be used for quality factor determination.

This method was tried for solid marbles (LMB) volume determination using the array microphone type PCB130E20 (Piezotronics, USA). This microphone has a sensitivity of ~45 mV.Pa$^{-1,}$ which is almost 200 times more sensitive than the pressure microphone PCB103A. Also, the PCB130E20 array microphone has a low dynamic range of 122 dB compared to 177 dB for the pressure microphone PCB103A. This microphone replaced the PCB103A microphone in the setup shown in Figure 7-4. Calibration volumes to be used in Equations 7-42 and 7-43 were obtained by a count of 30 and 25 marbles, equivalent to 238.47 and 198.72 ml of volume for V_1 and V_2 respectively.

After inserting 25 marbles, with the volume V_2, inside the 2-litre resonator with the 51 mm port attached, the speaker volume, while playing a monotone equivalent to the natural frequency of the empty resonator, was adjusted to obtain a sound pressure just below the microphone's maximum dynamic range of 122 dB. This was obtained by setting the speaker amplitude at 20% of its maximum power. The sound pressure level was measured at 121.92 dB (24.96 Pa). Five more marbles to obtain

V_1 were added to the resonator, and the sound pressure was measured at 120.43 dB (21.02 Pa). Pressure P_0 was estimated using 7-44, equal to 133.51 dB (94.79 Pa), which was 9 dB higher than the microphone dynamic range; hence, it was impossible to measure using the array microphone.

Based on the estimated P_0, Q was estimated using 7-45, equal to 34.93. After estimating the missing parameters P_0 and Q, more marbles were added to the resonator and their solid volume was estimated using the SPQF model. The results are shown in Figure 7-20.

The error bars in Figure 7-20 represent the sample solid volume measurement uncertainty with a Confidence Interval (CI) of 95%, equivalent to 1.95% sample solid volume. The last load of marbles resulted in a slight deviation in the volume, equivalent to 14 ml, due to the sample interfering with the resonator port. For 20~75 marbles, equivalent to 159~600 ml of solid volume, the volume estimation deviation between the actual volume and estimated volume remained under 2 ml, equivalent to 0.1% of the resonator cavity volume. This range of deviation was within the sample's actual solid volume uncertainty.

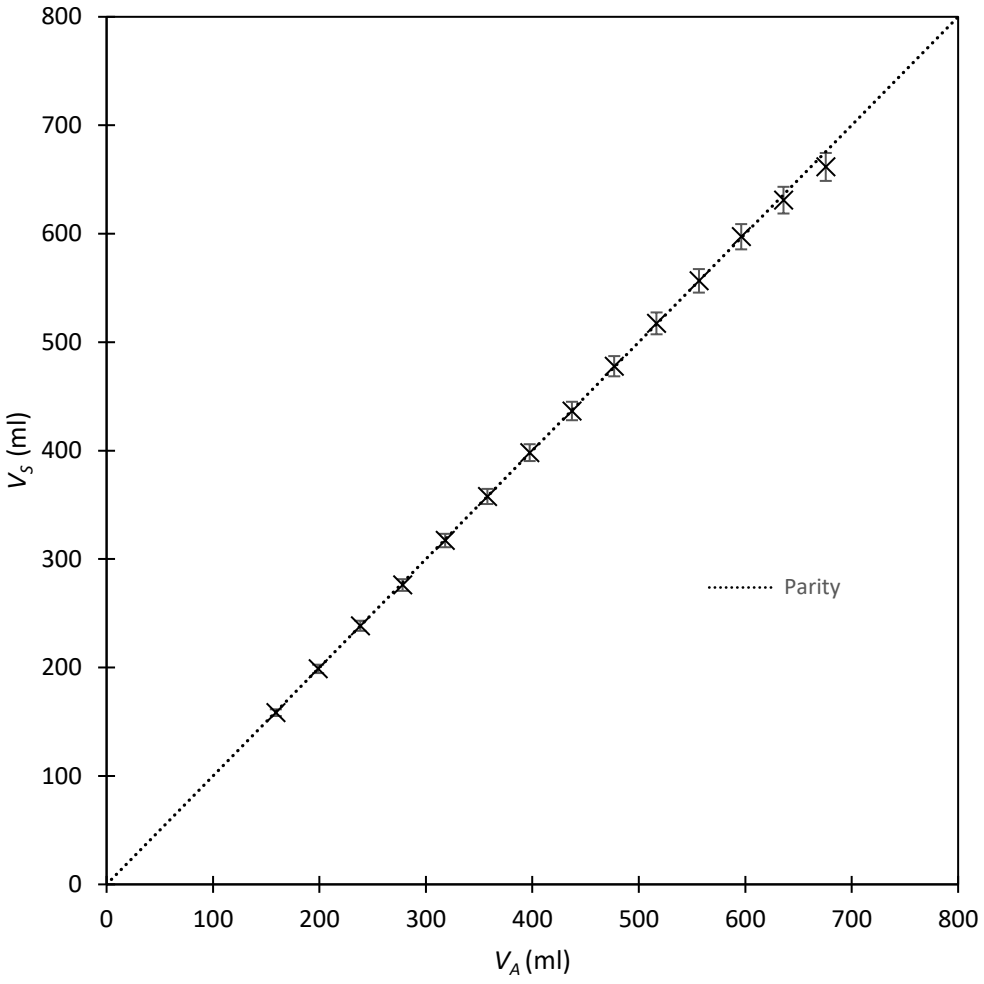


***Figure 7-20**: Solid volume of marbles estimated using an array microphone with low dynamic range based on the estimated sound pressure in the empty cavity.*

Figure 7-21 shows the measured sound pressure level for the solid volume occupied in the resonator. The data labels in Figure 7-21 show the number of marbles. This figure shows the limited dynamic range; the data points P_1 and P_2 were used to estimate P_0 using equation 7-44.

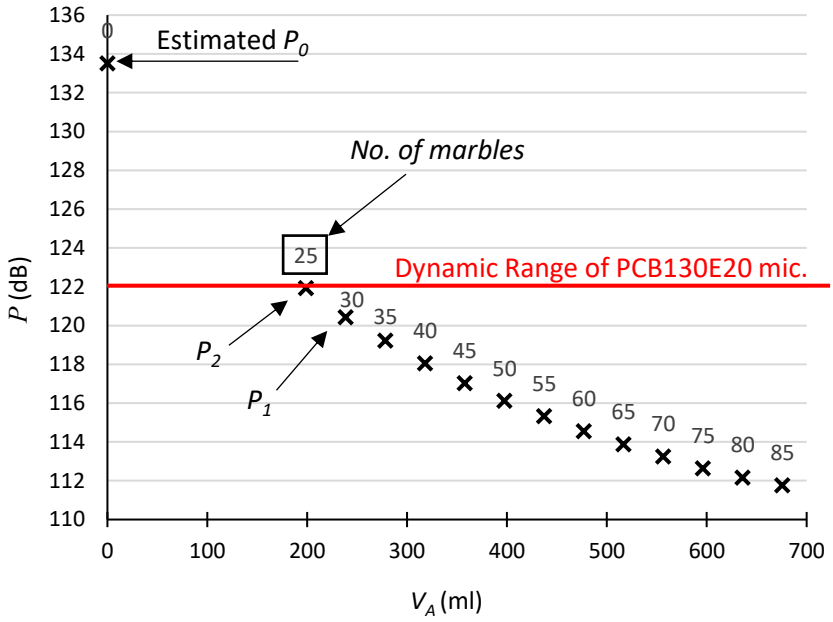


***Figure 7-21**: Measured Sound Pressure Level vs. occupied solid volume.*

7.6.4. Determination of liquid flowrate

Implementing the SPQF model in a liquid discharge vessel provides a means for the flow rate determination of liquids. For the experiment conducted on water discharge, with the results presented in Figure 7-8, the flow rate was calculated by dividing cavity volume change over time. The sample results are presented in Figure 7-22. This experiment was conducted on the 3-litre cavity with the 51 mm port; the orifice size is 5.6 mm.

In Figure 7-22, the flowrate derived from mass measurements exhibits a stepped pattern, indicative of the scale's precision limit at ±0.005 kg. This discretization effect results in the stepwise flowrate profile seen in the graph. In contrast, the flowrate calculated using the acoustic method appears to more closely track the flowrate profile derived from mass, suggesting that the acoustic method, the SPQF model, is sensitive to the changes that the scale's precision may not capture. The

consistency between the two methods' estimations reinforces the validity of the acoustic approach for flowrate measurement.

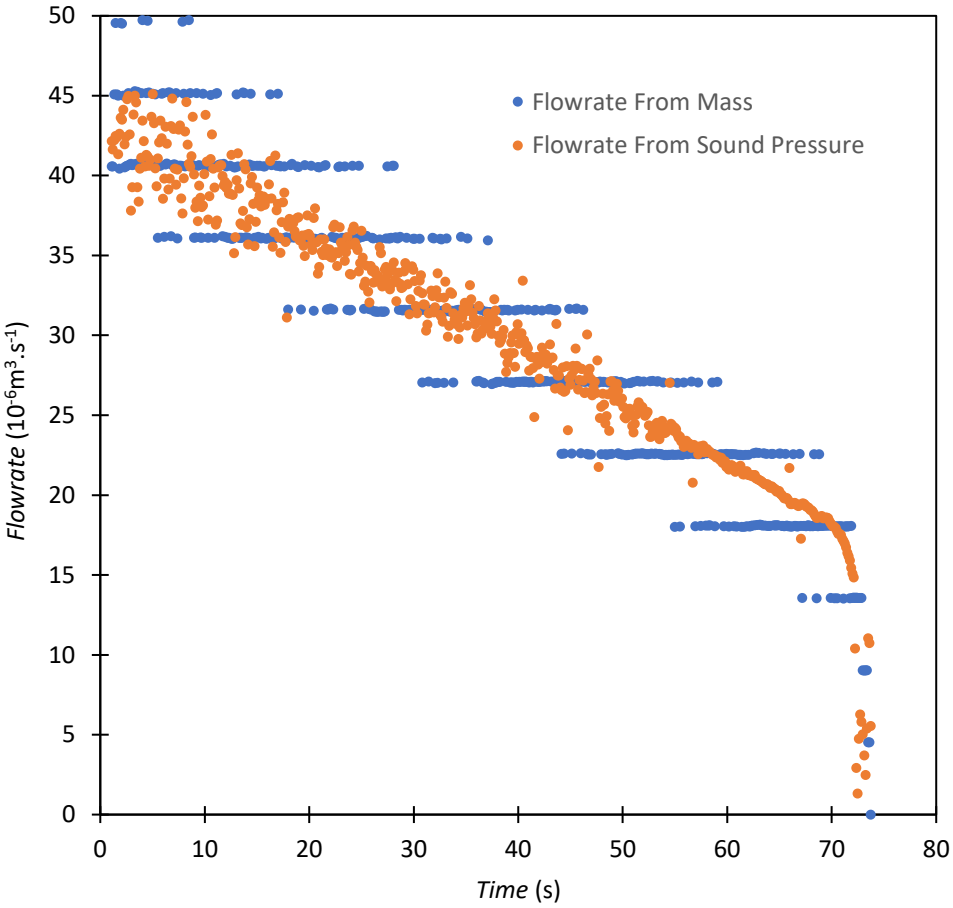


Figure 7-22: *Flowrate estimation of water.*

As shown in Figure 7-22, the SPQF model can be effectively applied to measure and control the flow rate of liquid in discharge tanks with high accuracy.

7.6.5. Other possible applications

The experiments related to this chapter were conducted in a laboratory with controlled environmental conditions. The results show that the sound pressure level in a resonator constantly excited at its empty state natural frequency is related to the amount of material inside the resonator. However, more experiments and studies are required to investigate the feasibility of implementing this method in a topdressing aircraft hopper. The noise level in that system varies, and it is suggested to use more than one microphone for signal sampling, one for noise source and one for picking up pressure from inside the hopper. These data could be used to train a system for correlating sound

pressure drop inside the hopper to the amount of material. It is foreseeable that material clogging can be detected from the results of the experiments in this section. Material clogging can prevent uncovering the hopper's discharge gate, which can significantly affect the sound amplitude inside the hopper.

Apart from the experiments, static or dynamic, covered in this chapter, several applications for the SPQF model can be suggested. In the literature, an interest in the inline measurement of the volume, hence, the density of the agricultural products is reported as it is a method of quality assessment (Chen et al., 2013; Concha-Meyer et al., 2018; Inoue et al., 2021; Nishizu et al., 2001; Xu et al., 2014). Nishizu et al. (2001) proposed a method for the inline measurement of food volume measurement (See Chapter 1, Figure 1-3). Their challenge was achieving the maximum achievable speed of the movement of samples and an acceptable accuracy in their proposed system. They had to limit the maximum movement speed to 45 $mm.s^{-1}$ to have enough time for the resonator excitation and frequency hunting. Utilising the SPQF model that this chapter proposed, which estimates sample volume almost instantaneously, can help to increase the speed of measurement and practicality of such applications.

Another potential application involves measuring the rate of expansion in foams. The expansion rate in foams can affect the efficiency of the automatic foam extinguishing systems (Andrei & Alexey, 2019). The method this chapter introduced could be used for instantaneous measurement of the expansion rate of foams.

Another suggested application is the measurement of the level of liquids under micro-gravity conditions (Nakano et al., 2006) or in the cryogenic industrial field (Nakano & Nishizu, 2016), where demand for a non-invasive volume measurement method was tried to be addressed by acoustical means.

7.7. Summary

This chapter introduces a novel method for acoustical volume measurement, achieving speeds and accuracies previously unattainable.

Sample volume measurement in a resonator using Helmholtz Resonance traditionally involved resonance frequency hunting. The measurement resolution depends on the time spent in signal sampling for high-resolution spectral density analysis for resonance frequency hunting.

This chapter introduces an alternative model for volume estimation in a Helmholtz Resonator that does not involve signal sampling for spectral analysis and can practically estimate sample volume instantaneously in a resonator under constant excitation. The SPQF model was developed based on the Driven Underdamped Oscillation of the air mass inside the resonator. This model estimates sample volume based on the change in cavity sound pressure after inserting a sample into it.

For sample volume measurement, the resonator is excited at its natural frequency. The excitation comes from a speaker playing a monotone towards the resonator port, directly or from the sides. The monotone must match the natural frequency of the empty resonator. When a sample is inside the resonator, its volume can be estimated using the SPQF model based on the change in sound pressure. Experimental tests on water, both in static and drainage tests and on various solid samples, including marbles and agricultural products. The maximum error across all test conditions remained below 1% of the cavity capacity. Notably, for Fill Factors less than 0.5, an accuracy exceeding 0.1% of the cavity capacity was achieved.

Cavity volume estimation tests were conducted on a variable chamber resonator apparatus. Rapidly changing cavity volume was estimated consecutively at 45 measurements per second. The model tracked cavity volume change for volume variation rates up to 1440 $ml.s^{-1}$, the maximum achievable rate of change in cavity volume of the available apparatus.

The same concept in Fill Volume measurement was used to monitor powder drainage from a 3-litre resonator vessel. Powders absorb acoustic energy and violate the assumption in the SPQF model that sound absorption by the sample is minimal. However, it was experimentally shown that by creating look-up tables based on prior tests for each powder sample, it is possible to statistically estimate the mass of a powder inside the resonator as it discharges. Several tests were conducted on two test materials: black mustard seeds and agricultural lime. According to the results, the programmed software for estimating the mass of material based on the prior tests tracked the mass change in the resonator based on pressure amplitude drop. The repeated tests in the 3-litre resonator showed a maximum error of 1% in the Fill Factor range of 0.2 to 0.8.

7.7.1. Summary of the Model developed in this chapter

$$V_S = V_c \frac{\sqrt{1-\bar{P}^2}}{Q\bar{P}}$$

Sound Pressure Quality Factor (SPQF) model

V_S: Sample Volume (m^3)

V_c: Resonator Cavity Volume (m^3)

$\bar{P}$: The drop in sound pressure amplitude in the resonator cavity under excitation at its empty state natural frequency after changing its cavity volume by V_S

Q: Empty resonator quality factor ($Hz.Hz^{-1}$)

Chapter 8 Conclusion and Recommendations

8.1. Overview of the thesis

This thesis explores the development and implementation of optical and acoustical methods for fast to real-time volume determination.

Chapters two and three focus on measuring the fill volume of bulk solids in a hopper or vessel. This is achieved by conducting multi-point level measurements using sensors installed in the vessel's covering.

Chapter 2 investigates the use of off-the-shelf ultrasonic rangefinders for hopper volume measurement. A key challenge, identifying and removing sensor errors, was resolved using a geometrical algorithm. The Multi-Level Volume Measurement (MLVM) model, a model for volume measurement using ultrasonic sensors, facilitated powder volume measurement during discharge at a rate of 1 Hz, achieving an uncertainty of less than 3% of the vessel capacity in all test conditions. These findings highlight the potential for rapidly implementing off-the-shelf ultrasonic rangefinders in bulk solid handling applications.

Chapter 3 focuses on implementing off-the-shelf stereoscopic scanners, such as Microsoft Kinect, for real-time measurement of vessel fill volumes, achieving an uncertainty of approximately 1% of the vessel's capacity. This involved addressing technical challenges, applying noise removal practices, and developing the Optical Fill Volume (OFV) model, a general model for volume determination from internal vessel scans. The method and the OFV model developed in this chapter provide a practical solution for volume measurement in hoppers and vessels. Additionally, the high accuracy of this method allows for tracking real-time volume fluctuations of powders during discharge, offering valuable insights for future studies of powder discharge dynamics.

Chapters Four, Five, Six and Seven focus on the use of the Helmholtz Resonance principle on volume measurement. Helmholtz Resonance is an acoustical phenomenon in cavities with one or more openings. These systems are called Helmholtz Resonators. Guitar, violin, and engine muffler are examples of Helmholtz Resonator. The resonance frequency of a Helmholtz Resonator is a function of its volume. Thus, the occupied volume of a resonator can be measured from its resonance frequency, a technique for rapid volume determination of objects.

Chapter 4 focuses on Helmholtz Resonance and its application in the volume determination of solids, liquids, and bulk solids. The ideas, theories, and experimental observations presented here inform the content of Chapters Five to Seven. This chapter covers the following main topics, which are crucial for addressing real-time fill volume measurement using Helmholtz Resonance:

- Experiments on fill volume determination in hoppers and vessels of various sizes under no-flow and discharge conditions using Helmholtz Resonance.
- Introduction of the Transfer Function method for accurate Helmholtz Resonance detection at higher fill levels in powder-filled resonators.
- Approach to resonance frequency detection challenges in powder-filled resonators by increasing port length.
- Assessment of powders' impact on resonance quality factor.
- Measurement of sound penetration speed in particle bed within the resonator.
- Evaluation of powder sound absorption effects on resonance quality.
- Identifying non-uniform pressure propagation in the resonator causing non-linearity in sample volume determination using the Helmholtz Resonance principle.

Chapter 5 introduces the Extended Helmholtz Resonance (EHR) model, which broadens the applicability of the classical Helmholtz Resonance model to resonators with long ports. The EHR model provides a straightforward linear solution for determining resonance frequency based on cavity volume, marking a significant advancement in modelling Helmholtz Resonance with wide-ranging applications in acoustics. This enhancement was crucial for accurately determining the volume of powders in a Helmholtz Resonator with an extended port. The EHR model is capable of precise volume determination for solids with an average diameter of 15 mm or more. However, when dealing with bulk solids of smaller mean particle diameters, the EHR model's volume estimates tend to deviate from actual values due to their influence on pressure wave propagation in the resonator. This issue is addressed and resolved by further developing the EHR model into the QWR model for volume determination of bulk solids in the following chapter.

Chapter 6 introduces the Quality Wavelength Resonance (QWR) model. This semi-empirical model incorporates the effect of resonance quality factor and resonance frequency to estimate the solid volume of a bed of particles with a random size distribution. The QWR model is developed based on the Extended Helmholtz Resonance model. The QWR model provided a novel method for the volume determination of bulk solids such as agricultural grains.

Chapter 7 introduces the Sound Pressure Quality Factor (SPQF) physical model and a novel volume measurement method which can be used for accurate and instantaneous volume measurement of solids, liquids, and bulk solids. This innovative approach estimates volume changes in a cavity based on variations in sound pressure, which can be done instantaneously. The method is suitable for volume determination in static and dynamic systems, utilizing a combination of a speaker driver, a microphone, and signal-generating and collecting equipment.

8.2. Fill Volume determination using Ultrasonic range finders

An array of ultrasonic sensors, set into the cover plate of a 200-litre powder discharge vessel, enabled rapid determination of vessel fill level.

Nine sensors were used; one was installed at the centre, and eight were installed adjacent to the vessel wall. The central sensor estimated range based on the closest object, and the side sensors estimated range based on the most robust reflection. With this arrangement and choice of sensors, the fill volume of the vessel was measured using the MLVM model at a frequency of 0.9 Hz with a measurement uncertainty (*PI.95)* of *±3*%V_0.

The preliminary results in a 200-litre vessel show that implementing an array of ultrasonic sensors with a minimal field of view can address the problem of real-time fill level measurement in a hopper. However, some considerations make it necessary to try these sensors in a hopper before concluding the efficacy of this method. A hopper in a field application geometrically differs from a 200-litre vessel. The observations in the tests suggest that extreme care should be taken in choosing the proper position of the sensors where the wall and corner echoes are minimised. For the central sensor, which points towards the discharge gate of the hopper, off-the-track readings are possible, which necessitates the detection of these faulty readings and substitution with an average reading of the adjacent sensors. The tests were only conducted on polyethylene beads due to convenience. Testing the method on other powders, including agricultural lime and urea, which are used in topdressing, is recommended.

If higher accuracy is demanded, especially when the material is near the bottom of the vessel, experimental calibration of the MLVM model through repeated tests is suggested.

In the case of an agricultural topdressing hopper, these sensors can be installed on the ceiling of the hopper without the need to adjust the airframe. These sensors are available in weather-sealed packaging suited for harsh industrial situations, making them suitable for implementation in topdressing hoppers. It should be noted that the sensors have a minimum working distance, limiting the range at which the hopper fill level can be monitored. The minimum detection distance for the sensors used in this study was 200 mm, almost 12% of the height of a Cresco hopper. It is recommended to select a sensor with a short minimum working distance.

8.3. Fill Volume determination using the stereoscopic technique

Using off-the-shelf stereoscopic depth cameras, real-time and accurate fill volume determination of powder discharge vessels was achieved. This was accomplished by developing the OFV model, a generalized model for volume determination based on 3D scans of the material's surface inside a vessel.

The stereoscopic technique employs a pair of cameras to capture scenes in 3D. A depth camera using this technology was integrated into vessels to obtain 3D scans of the material surfaces. These surface scans were then converted into Fill Volumes using a mathematical model. This model was validated under no-flow and free-flowing conditions in a 50-litre vessel. In all tests, the estimated fill volume of the vessel corresponded with the volumes directly obtained from the material mass. Experiments were scaled up to 200 litres, utilizing two stereoscopic depth cameras to expand the field of view. The vessel fill volume and flow rate estimation results from the 200-litre vessel mirrored the accuracy of the 50-litre vessel results. All experiments' fill volume estimation errors stayed below 1% of the vessel's capacity.

The multi-threading concept in software engineering was utilized to expedite the fill volume calculations using the model, resulting in real-time calculations of vessel fill volume and material flow rate estimations with update rates of 3-5 Hz.

The results suggest that this method provides accurate and speedy estimates of a vessel fill volume. There are design considerations in implementing this method into a hopper, as follows:

1- The optical system's field of view: Depending on the desired accuracy in the upper 30% of the hopper space, two or three scanners can be used in tandem to achieve 112 and 170 degrees of field of view, respectively. The optics' minimum detection range should also be considered.

2- The dusty environment inside the hopper: While rugged dust and waterproof stereoscopic sensors are commercially available, dust accumulation on the optics can be addressed using purging air or mechanical wet or dry wiper mechanisms.

3- The optics' survivability against mechanical impacts, especially those arising from the rapid dumping of materials into the hopper, is a concern. The optics should be housed in a robust package to resist potential mechanical impacts from ground-based fertilizer loading hoppers.

Compared to the ultrasonic method, the optical method yielded faster measurements with an accuracy that was 5 to 10 times higher, contingent on the material's level. However, a notable trade-off is the sensitivity of the scanners to dust accumulation on the optics, necessitating mechanical consideration.

8.4. Helmholtz Resonance of a vessel filled with powders

When acoustically exciting a cavity with a port, the air inside the port resonates at a frequency dependent on the cavity volume and port geometry. This phenomenon is called Helmholtz Resonance. An object inside the resonator cavity alters its free volume, which alters the resonance frequency. Measuring this frequency, referred to as hunting, enables the estimation of the sample volume.

The initial experiments on the Helmholtz Resonance were conducted on a topdressing Hopper and a 50-litre powder discharge vessel. The topdressing hopper filled with either urea or agricultural lime powder samples underwent rapid acoustic excitations using a subwoofer. The acoustic response of the hopper was analysed to hunt for resonance frequency. A similar experiment was conducted on a 50-litre vessel with a port attached to the top. When the vessels were discharging a sample of agricultural lime, a cohesive powder containing fine dust, it was possible to excite the vessel and hunt for resonance frequency successfully. The system's resonance frequency was a function of the amount of agricultural lime in the vessels. For the tests on mustard seeds and urea samples, which are open-pore and free-flowing, resonance frequency in the discharge phase could not be hunted. With the invariable excitation frequency applied to the vessels, it was observed that the sound pressure inside the vessels increased with the discharge of the material. The complications in resonance frequency hunting and estimation of sample volume based on resonance frequency led the study into lab-scale resonators on various samples.

In the initial tests on a 3-litre resonator with a 51 mm long port, it was observed that the Classical Helmholtz Resonance model could estimate liquid and solid volumes accurately (an error of 2%, uncalibrated for non-linearities). However, when filling the resonator with powder, similar to the previous observation in the topdressing Hopper and the 50-litre vessel, it was difficult to hunt resonance frequency for Fill Factors higher than a specific value for the open-pore powder material. Filling the resonator with several powder samples prevented resonance, resulting in a flat frequency response from the microphone in the resonator port, which made it impossible to hunt for resonance frequency.

Sound attenuation in the powder samples was studied to investigate the limitation in resonance hunting. A vertical two-microphone impedance tube was designed for direct measurement of the sound absorption quality of the samples.

The results of impedance tube tests showed that all of the tested powder samples tend to absorb less acoustic energy in the lower ends of the tested frequency spectrum (50~2250 Hz). The recorded sound absorption coefficient of an almost 70 mm thick bed of all samples resulted in values less than 0.03 for frequencies lower than 100 Hz. Therefore, keeping the resonator resonance frequency as low

as possible should be considered when designing a resonator to estimate powder sample volume. One other consideration has been avoiding quarter-wavelength absorption by the powders. Quarter wavelength absorption was detected as perfect absorption, α=1, in specific frequency bins depending on the sample' tortuosity and depth. Perfect acoustic absorption prevented resonance for sample depths comparable to a quarter of the resonance wavelength. A maximum resonator height of 0.15 of the depth at which quarter-wavelength absorption occurred enabled resonance hunting.

Using a 1000 mm port lowers the resonance frequency of the 2-litre resonator to below 80 Hz. In this resonance frequency region, hunting resonance frequency for all samples was possible as the absorption of acoustic energy was minimal.

When expressed wavelength squared λ^2, the powder samples' resonance locations were linearly correlated to the solid volume of the samples.

8.4.1. Resonance Hunting Using Transfer Function Method

Resonance frequency hunting in a resonator filled with powders resulted in a low signal-to-noise ratio in the pressure signal collected by the microphone. A method was developed that utilised two microphones of the same type, one located in front of the acoustic driver and the other inside the resonator. The magnitude of the Fourier transfer function between the two microphones was calculated. The peak in the magnitude graph was the resonance frequency of the resonator. The intense noise signals were located and removed by referring to the coherence function between the two microphones. Compared to the single microphone or Driven Method, the transfer function method achieved higher fill factors across all port lengths. When utilizing the 51 mm port, where the resonator's maximum fill factor was previously limited for various samples, the transfer function method increased the detectability of the resonance frequency by up to 30% for samples such as coarse ballotini and mustard seeds.

8.4.2. Resonance hunting in dynamic discharge tests

In dynamic discharge tests involving a powder-discharging resonator, the material quantity was monitored at a 1 Hz rate using the Driven Resonance Hunting method. The resonator was excited using a chirp sound at the same rate, allowing for the resonance frequency detection, which served as an indicator of the resonator's fill level. The findings in Section 4.4.6 suggest that Helmholtz Resonance can reliably indicate the fill level of a powder discharge vessel. This is based on establishing a statistical correlation, through repeated discharge tests, between the resonance frequency and the material quantity.

8.4.3. Compression Non-Uniformity

An experiment was designed using the 2-litre lab-scale resonator to examine the uniformity of cavity air compression at resonance. A non-uniformity in cavity air compression at resonance is a non-deal behaviour which violates the assumption of uniform air compression in the Helmholtz Resonance model. In other words, non-uniformity in air compression results in resonance frequency estimation to be offset from actual values.

For this experiment, the phase shift between the signals obtained from the top and bottom microphones of the resonator was used as an indicator of non-uniformity.

When the resonator was empty, the phase shift in air compression between the resonator's top and bottom was negligible. However, putting a powder into the resonator led to a significant phase shift in the sound pressure signals obtained from the cavity's top and bottom microphones, indicating a non-uniformity in air compression. This non-uniformity violates the Helmholtz Resonance model's assumption of uniform air compression in the resonator cavity. It is believed that cavity non-uniform compression resulted in solid volume estimation of powders being offset from the actual values.

As highlighted in Section 4.5.10, discrepancies between the actual and estimated solid volumes of powders when using the Helmholtz Resonance method have been documented in the literature and observed in this thesis, as exemplified in Figure 4-37. Detecting the impact of powders on the non-uniformity of cavity compression has been a crucial observation. This understanding is critical to addressing the non-linearities encountered in determining the solid volume of powders based on the Helmholtz Resonance principle.

The non-uniformity in cavity air compression increases as powder mean particle diameter decreases.

8.4.4. Resonance Quality Factor Measurement

Resonance quality was estimated using three methods: Resonator pressure decay analysis following an impulse excitation, Driven resonance spectral analysis, and Driven resonance phase-shift between the driver and the resonator.

The resonator's quality factor in driven resonance was observed to vary with the speaker driver amplitude; specifically, increasing the amplitude of the speaker driver or moving the speaker driver closer to the resonator port led to a decrease in the resonance quality factor. This observation is significant, as the resonance quality factor is determined in the volume determination models QWR and SPQF, introduced in Chapters 6 and 7, respectively.

In the undriven resonance decay analysis, the quality factor was neutral to excitation pulse power. Therefore, the excitation type should be considered when referring to a Helmholtz Resonator Quality Factor.

8.4.5. Effect of powder on resonance Quality Factor

Putting powder into a resonator reduces resonance quality proportional to the amount of powders. The powder bed impact on resonance quality depended on the sample type and volume. The resonance quality factor was directly correlated to the sample particle diameter for open-pore samples; the quality factor decreased with the sample particle diameter for open-pore material with a mean particle diameter larger than 0.5 mm.

Thus, when filling a resonator with powder, the resonance frequency and resonance quality factor are two resonance parameters that can be used to indicate the resonator fill volume.

8.4.6. Speed of sound in the bed of particles

A method was devised to measure the speed of sound in the bed of particles directly. A 150 Hz monotone sound burst was generated at the top of the particles. The flight time was detected from the rising edge of the microphone signal at the bottom of the bed. The flight time was recorded to calculate the speed of sound. The sound velocity penetrating the bed of particles was significantly lower than in the air. It can be explained by the tortuous path that sound waves take when travelling into the bed of particles. The speed of sound penetration was neutral to permeability and was related to bed voidage and, to a lesser extent, to sample particle diameter. The mustard seeds Sample with the lowest bed voidage (0.29) had the highest estimated tortuosity (1.47).

8.4.7. Extended Helmholtz Resonance Model

The solution for resonance hunting in a Helmholtz resonator filled with powder involved using long ports, practically making the resonator dimensions comparable to resonance wavelength. It violated the assumption of a small resonator for the classical Helmholtz Resonance.

Tang and Sirignano's (1973) generalized Helmholtz Resonance model establishes a trigonometric relationship between concentric cylindrical resonator dimensions and resonance wavenumber.

Based on Tang and Sirignano's generalized Helmholtz Resonance model, Extended Helmholtz Resonance (EHR), a simple algebraic equation was developed to describe resonance wavelength based

on cavity volume. In the development of this model, it was assumed that the dimensions of the resonator cavity are small compared to the resonance wavelength.

Interestingly, the EHR model estimates resonance wavelength as the added effect of the Helmholtz Resonance and organ-pipe resonance. The model was verified numerically and experimentally. The experimental verification was conducted in the cavity volume height of 0-0.2 m and port length of 0.05-1 m. For experimental verification, water and marble samples were used. This model was used to estimate water or marble sample volumes to achieve accuracies higher than 0.5% of the cavity volume for all Fill-Factors 0-1 regardless of the port length.

8.4.8. Estimation of volume of powders using the EHR Model

In volume determination of bulk solids under no-flow conditions, as outlined in Chapter 4 Section 4.4.5, it was shown that using a 1-meter-long port instead of a short port such as the 51 mm port makes it possible to track resonance frequency change with resonator fill factor when filled with powder. Because the port is longer than the scope of validity of the classical Helmholtz Resonance model, it was not possible to estimate sample volume theoretically based on the classical model. The development of the Extended Helmholtz Resonance (EHR) Model for sample volume estimation, Chapter 5, paved the way for estimating the powder sample volume in a resonator with an extended port.

Using the EHR model, the estimated volumes for the large marble sample with a particle mean diameter of almost 25 mm were exact. There were deviations between the sample's actual solid volume and the estimated volume for all bulk solids with a mean particle diameter of less than 15 mm. The deviations were both in the form of overestimation or underestimation; overestimation in the sample solid volume was observed for samples with particle Sauter mean diameter less than 0.5 mm. Underestimation was observed for powders with a Sauter mean diameter of more than 0.5 mm up to 15 mm. The estimated volume of fine powders with particle mean diameters less than 0.5 mm was the order of bulk volume rather than solid volume; the finer the particles, the closer the estimates to the bulk volume.

8.4.9. Categorization of powders in terms of acoustic response

The bulk solid material tested in the various acoustic experiments can be qualitatively placed in two subcategories based on Sauter mean particle diameter *D[3,2]*, namely fine with a *D[3,2]* ≪0.5 mm and Course with a *D[3,2]* >0.5mm.

The following were observed in the fine samples category:

- No perfect sound absorption peaks in Impedance Tube tests (Section 4.4.9),
- Demonstrated high levels of compression non-uniformity in the resonator cavity (Section 4.4.10),
- Moderate drop in the resonance quality factor (Section 4.4.8),
- Demonstrated a high sound pressure transmission loss in the resonator cavity (Section 4.4.5, Acoustic Pressure Transmission Loss),
- Solid volume was overestimated (Section 5.4.2).

The following were observed in the Course samples category:

- Perfect sound absorption peaks in Impedance Tube tests (Section 4.4.9),
- Moderate levels of compression non-uniformity in the resonator cavity (Section 4.4.10),
- A high drop in the resonance quality factor with a linear trend with the Fill Factor (Section 4.4.8),
- No significant pressure amplitude deviation in the resonator cavity (Section 4.4.5, Acoustic Pressure Transmission Loss),
- Solid volume was underestimated (Section 5.4.2).

8.4.10. Random packing bed solid volume measurement using the Quality Wavelength Resonance (QWR) model

The resonance frequency hunting experiments on powders revealed a deviation between the actual and estimated volume based on the introduced enhanced resonance model for long ports (Chapter 5). The deviation between actual solid volume and estimated volumes was unique for each sample and related to the particle size distribution of the sample. The estimated volumes solely based on resonance frequency yield marginal error.

In the resonance quality factor analysis on powders, it was observed that the quality factor of resonance is a function of the amount of material inside the resonator (Fill Factor). Quality Factor decreases with an almost linear trend with Fill Factor. The trend was unique for each sample. The QWR, a semi-empirical model, was developed to correlate the solid volume of samples with particle diameter 0.71 mm and larger to resonance quality and frequency instead of just resonance frequency (Chapter 6). This model required a constant obtained through experimentation on a range of samples.

The QWR model determined the solid volume of various samples, with an average error of 1.2% and a maximum error of 4% compared to the resonator volume. The model also underwent testing to estimate the volume of mixed samples containing particles with varying diameters. These mixed samples comprised seven combinations of different powders and particles, each with diverse mixing conditions. In this evaluation, the model achieved an average error of 0.8% and a maximum error of 1.9% when estimating the solid volume for all the samples.

The range of test materials on which the QWR model was tested covers agricultural products, including seeds, which are tested in Chapter 6. The significance of this model is its versatility on a range of samples with random packing and particle size distribution. Once the calibration constant is obtained for a resonator, its applicability to solid volume measurement, hence, density measurement, on a range of samples with random particle diameter (>0.5 mm tested)

8.4.11. Instantaneous volume determination using the (SPQF) model

A novel method for measuring sample volume in a cavity has been introduced, providing levels of speed and accuracy unmatched by existing acoustical methods in the literature, to the best of the author's knowledge. This model also enables dynamic volume measurement within the cavity, a capability not possible with the available Helmholtz Resonance or pycnometer-based models.

The conventional method of volume estimation using Helmholtz Resonance involves resonance signal sampling and Fourier transformation to take the time signal into the frequency domain. The accuracy of the conventional method (Used in Chapters 4,5 and 6 and the reviewed literature) depends on the duration of signal sampling; for example, a signal sampling of 10 seconds was observed to result in volume determination precision of almost 1% in the tests on the lab-scale resonator.

A sample volume estimation model was developed to override the need for signal sampling for Fourier transformation. This model was developed based on the underdamped driven oscillation model of the resonator port air. This model expresses the sample volume based on three parameters: cavity volume, resonance quality factor and sound pressure amplitude drop inside the resonator. Sound pressure amplitude drop can be measured by sampling time equivalent to one period of the driving tone.

The monotone played by a speaker driver to excite the resonator must roughly equal the empty resonator's resonance frequency and constantly excite the air in the port. In this invariant working frequency of the resonator, the thermal and radiation resistance of the resonator port, hence the damping ratio and quality factor, remain constant, and sample volume can be estimated based solely on sound pressure amplitude inside the resonator.

The SPQF model was verified through experimentations on water and solid samples. Experiments were conducted on water, static and drainage tests, and the marbles. The experimental results validated the model in various resonator cavities of volumes 1, 2, and 3 litres and port sizes 51 and 170 mm where uncertainties (95% confidence interval) lower than 0.05% were achieved for measuring the volume of solid and liquid samples.

The same volume measurement concept was applied to gauge the cavity fill level of powders. Various powder samples were drained, and the trend of sound pressure drop was stored in look-up tables. The look-up tables formed an experimental guide for monitoring the fill level of the cavity in repeated runs. The experimental results suggest the applicability of this method for monitoring the fill level of a powder discharge vessel. For fill factors between 0.2 and 0.8, an accuracy higher than $1\%V_0$ is achievable.

8.5. Questions Answered

This thesis answers several questions, including, but not limited to, the following. These are the questions presented in Chapter 1, Section 1.3.

8.5.1. Using Ultrasonic technology in a vessel fill volume measurement

- **If material is under discharge from a vessel, can ultrasonic sensors track level change and translate it into fill volume and flow rate?**
    - Yes. The MLVM model can be used for this purpose. Flowrate data can be obtained from volume change over time. See Chapter 2, Section 2.3.1.
- **Can we operate multiple ultrasonic sensors in the tight space of a vessel simultaneously?**
    - Yes. In the case that the ultrasonic sensors work on the same frequency, they need to operate sequentially to avoid interference.
- **What are the noise sources and operability limitations?**
    - The primary noise source, resulting in off-the-track reading, arises from vessel wall imperfections. Refer to Section 2.7.1 for more information.
- **What is the relationship between the number of sensors per surface area and accuracy?**
    - As a rule of thumb, the higher the number of sensors per surface, the higher the accuracy. However, the accuracy is restricted to the sensor beam angle. Refer to Section 2.74 for more information.

8.5.2. Using stereoscopic optical technology in hopper fill volume measurement.

- **How to translate a surface 3D deformation map into volume?**
    - This thesis introduced the OFV model for this purpose. See Section 3.3.1.
- **How accurate is this method?**
    - The experimental results suggest an accuracy higher than 1% of the vessel capacity.
- **What scales of vessels can this method cover?**
    - It is subjected to the scanner's minimum and maximum working range and field of view. The largest tested was a 200-litre vessel, a 55-gallon standard drum; for implementation on other vessels, the geometrical constraints of the detection field of view of the scanner should be considered. See Section 3.5.1 for an example.
- **Is it possible to extract real-time flow rate data of material by this technique?**
    - Yes. The multi-threading computation can be utilized to maximise processing capability, and real-time volume was measured up to a rate of 5 Hz. See Section 3.5.
- **What are the limitations of this method?**
    - Dust accumulation can be a potential limitation, though not observed for the material tested. The geometrical constraints should be considered, including the scanner's distance to the material's surface and field of view.
- **What are the limitations in the maximum fill level for volume measurement?**
    - Theoretically, the minimum working distance of the scanner governs the limitation of the maximum fill level. When the material level is higher than the covering field of view, the OFV model helps estimate the fill volume, as shown in Figures 3-16 (B).
- **How to increase the field of view of the optical system?**
    - This can be done by installing two or more of them in tandem and using the affine transform outlined in Section 3.3.2
- **How can the optical system's survivability and reliability in a harsh environment be improved?**
    - Using purge air can help the sensors to remain dust-free during operation. A housing was built for this purpose. See Chapter 3, Section 3.5, and Appendix E, Figure E-3, and Figure E-4. Also, It is recommended to use sensors with industrial packaging that meet dust and waterproof standards, such as IP67.

8.5.3. Fill-volume measurement of a vessel using Helmholtz Resonance

- **Is it possible to estimate the volume of bulk solids using Helmholtz Resonance?**
    - Yes. This thesis has applied this principle to various powders and demonstrated its practicality for estimating the fill volume of a vessel or cavity containing bulk solids.

- **When estimating the volume of bulk solids using Helmholtz Resonance, does the estimated volume refer to the bulk or solid volume?**
    - Largely depends on the mean particle diameter. Based on the observations, the Helmholtz Resonance model estimates solid volume for beds with a mean particle diameter larger than 15 mm. In contrast, the estimated volume is closer to the bulk volume for very fine beds with a mean particle diameter smaller than 0.1 mm.

- **How can the maximum measurable fill level in a Helmholtz Resonator be improved?**
    - One solution is to reduce the resonance frequency to levels where the acoustic absorption by a powder is minimal. It can be achieved by increasing the port length of a resonator. See Sections 4.4.5 and 4.4.7.
    - Use the introduced resonance hunting method, Transfer Function, for a more sensitive resonance frequency hunting. See Section 4.3.3.

- **How to hunt the resonance frequency of a resonator containing bulk solids?**
    - Can be accomplished, driven and undriven. A chirp sound played by a speaker driver provides resonator excitation. See Sections 4.3.1 to 4.3.3 for the hunting methods and Sections 4.4.4 and 4.4.5 for the results. Undriven resonance is the quickest, with a measurement rate of ~1 Hz, and the Transfer Function method is the most reliable, depending on the hunting duration, which was ~2 seconds with 5 repeats for the experiments conducted in this thesis.

- **How can powders and particles affect the quality of volume measurement?**
    - The material's physical properties can affect the accuracy of volume measurement by Helmholtz Resonance, as seen in Chapter 4 Section 4.4.5. The most significant contributing factor is mean particle diameter. Depending on the mean particle diameter of the sample, the estimated volumes deviate from the actual volumes. Refer to Chapter 5, Figure 5-6 and Table 5-2.

- Putting powders into a resonator reduces the resonance quality factor. This reduction of quality factor is a function of the amount of powder and is beneficial for estimating the cavity fill level. This observation was crucial for developing the QWR model in Chapter 6. Refer to Figures 4.50, 4.52 and 6.2.
- For bulk solids with a mean particle diameter larger than ~15 mm, the Helmholtz Resonance model can be used for accurate volume determination using Helmholtz Resonance model.
- For particles smaller than 15 mm, deviations between actual and estimated volumes using the Helmholtz Resonance model were observed. See Chapter 5, Section 5.4.2

- **What Helmholtz Resonance model can be used for estimating fill volume?**
  - For large solids with a mean diameter larger than ~15 mm, the Extended Helmholtz Resonance (EHR) model, developed in Chapter 5, Section 5.2, can be used.
  - For a bed of particles with random particle distribution and mean particle diameter larger than ~1 mm, such as agricultural grains, the Quality Wavelength Resonance (QWR) model developed in Chapter 6 can be used.
  - For a bed of particles containing dust with a mean diameter of less than 1 mm, it is suggested to calibrate a resonator by measuring resonance wavelength for known masses of the powder and then use statistical fitting, similar to what is shown in Table 4 -5 in Section 4.4.6.

- **Is it possible to instantaneously measure fill volume to measure flow rate change in real-time?**
  - Yes. Chapter 7 introduces a novel solution for this purpose, the Sound Pressure Quality Factor (SPQF) model, which enables instantaneous volume measurement in static and dynamic systems.
  - Rapid resonance frequency hunting is also a practical approach with restricted accuracy; refer to Section 4.4.6.

8.6. Future Study

Applications of the Instantaneous volume determination method

The SPQF model, introduced in Chapter 7, has the potential to determine real-time volume accuracy, as demonstrated in various static and dynamic experiments. Probably one of the most critical paths to continue the research in this thesis is to study and utilize the SPQF model in in-line volume determination for density calculation. The SPQF model can be implemented in a volume determination mechanism for rapid density determination of agricultural and food products, such as fruits or meats, for in-line quality assessment. It is suggested that the SPQF model implementation methods and the achievable accuracy for in-line volume determination be studied.

Additionally, due to its speed, accuracy, and non-invasive nature, this method can also be applied to medical volume determination of the human or animal body. Therefore, it is suggested to assess its accuracy in a large resonator that fits the human body and modify/calibrate the model if necessary for a large-scale resonator.

Powder Discharge Vessel Fill Volume

One suggested study relates to conducting a geometrical analysis of the relationship between the number of level readings from the surface of a material in a vessel and the maximum uncertainty in volume determination. In other words, the goal is to derive a mathematical expression that describes the uncertainty in volume determination in a vessel as a function of the vessel's geometry, the physical properties of the material, such as the angle of repose, and the number of level readings taken from the material's surface.

Physics of acoustics

This thesis has demonstrated that the quality factor of a Helmholtz Resonator decreases with the intensity of the incident sound. This observation was critical for utilizing the SPQF and QWR models. The physics of Helmholtz resonance can be revisited to model theoretically the relationship between resonance quality and incident sound intensity.

Implementation of the QWR model for quality assessment of grains and seeds

The last suggested future study is to utilise the Quality Wavelength Resonance (QWR) model for the density determination of grains and seeds as a means of product quality determination. This requires a thorough accuracy assessment and detailed calibration of the model for volume determination of grains. This model can be rapidly deployed in a commercial apparatus, offering a potential solution for the quality assessment of agricultural products.

Appendices

Appendix A: Flowcharts

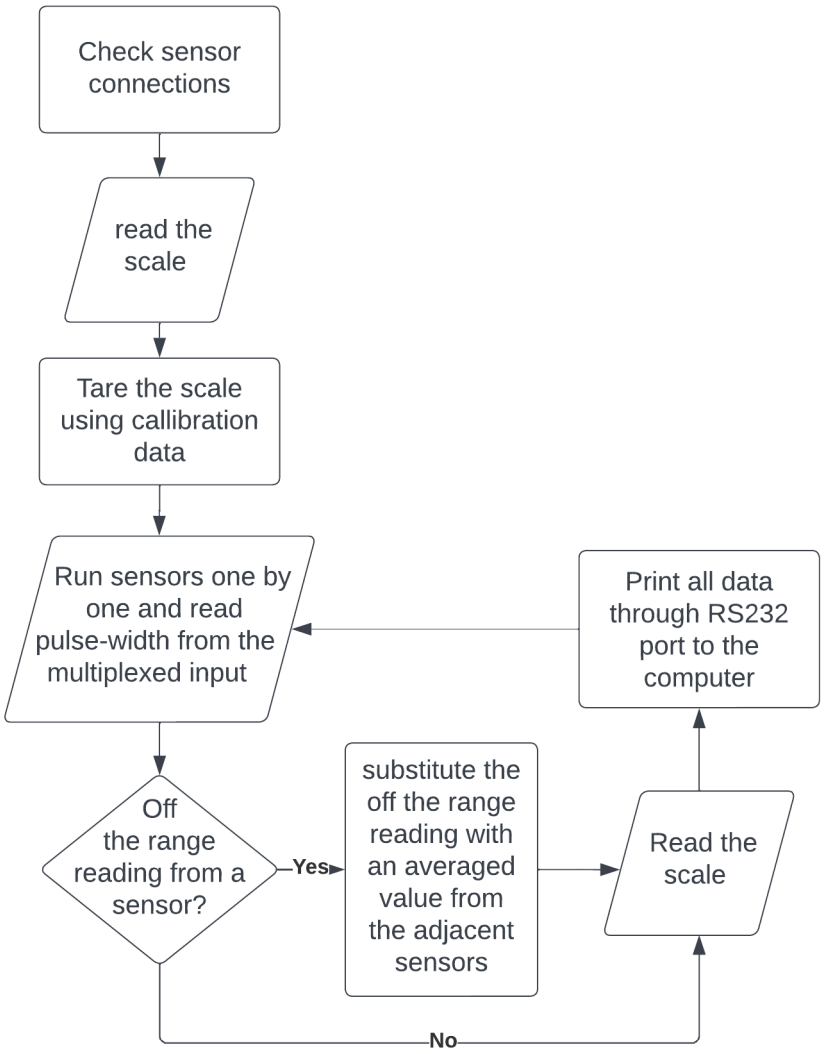


Figure A-1: *The Arduino software flowchart for the experiments conducted in Chapter 2.*

Figure A-1 shows the Arduino software algorithm for the ultrasonic sensor interface. The sensors used in this project provide calibrated pulse with output collected by Arduino digital inputs. The “Off-the-range reading” refers to the maximum possible range of the sensor considering the material's angle of repose and the sensors' average reading. (Chapter 2).

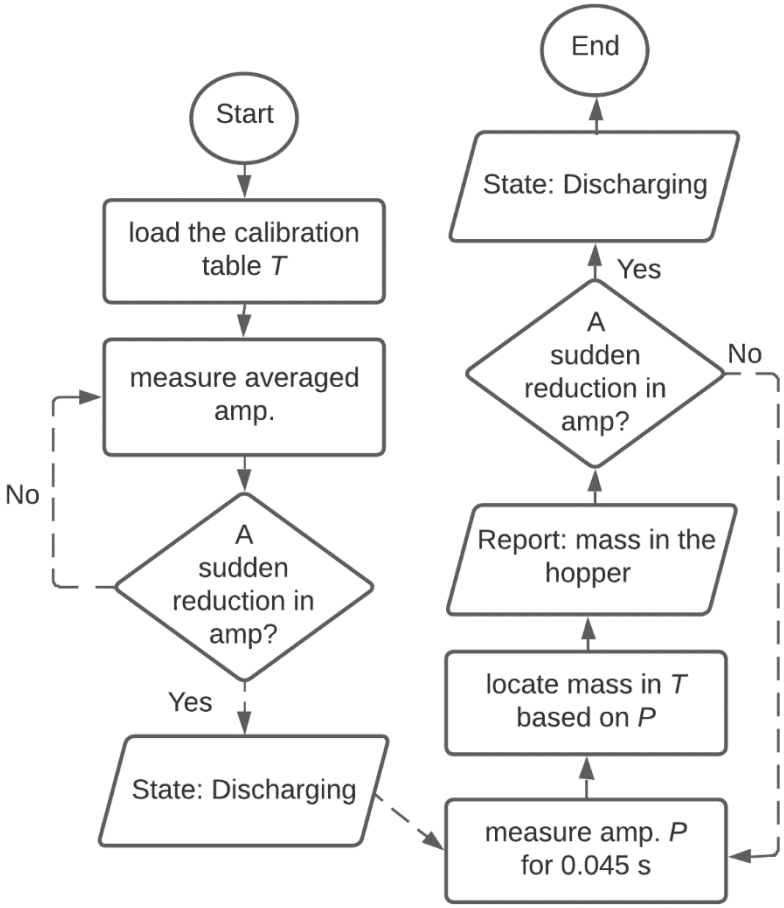


Figure A-2: *Software Algorithm for discharge vessel condition monitoring from sound pressure.*

Figure A-2 shows the flowchart that the software follows to estimate the mass of the material inside the resonator and the state of discharge from tracking the sound pressure amplitude (Chapter 7, Section 7.6.2).

Appendix B: Calculations

Calculations Used for the Impedance Tube Design

The equations in this section are derived from Chung & Blaser (1980).

In the impedance tube shown in Figure 0-1, a powder bed is exposed to a white noise that contains a range of sound frequencies that travels through a tube long enough to ensure a planar wave. Figure 0-1 illustrates that a pair of microphones measures the acoustic pressure levels at known distances from the material's surface. The complex pressures carrying amplitude and phase data for a range of frequencies determine the amount of absorbed acoustic energy and impedance.

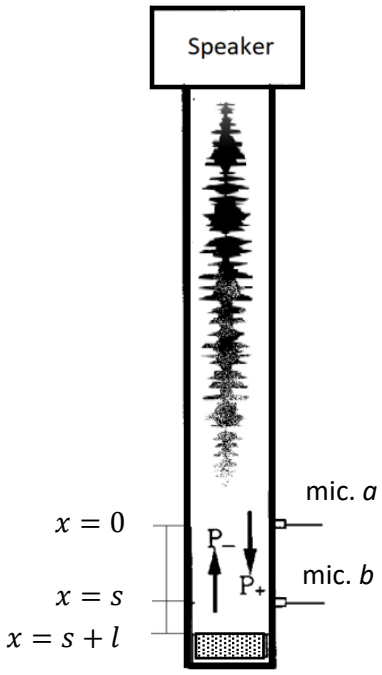


Figure B-1: *Impedance tube.*

At the moment *t*, the sound pressure of the travelling wave toward the bed of particles (the incident sound) at the mic position *b* (*x=0*) is denoted by $P_+(t)$. Likewise, the reflected sound wave from the sample surface toward the speaker is denoted by $P_-(t)$. One can assume that $P_b(t)$ is composed of both downward and upward pressures as follows:

$$P_b(t) = P_+(t) + P_-(t) \quad [1]$$

Switching to the frequency domain, $P_b(f)$ can be written as follows after taking the Fourier transform:

$$P_b(f) = P_+(f) + P_-(f) \quad [2]$$

The microphone at position (a) receives the same signal as the microphone at position (b) but at a time that is shifted by t_0 where:

$$t_0 = s.c^{-1} \quad [3]$$

Where s is the spacing between the two microphones and *c* is the speed of sound in the tube.

Hence, the sound pressure at the location *a* can be written as:

$$P_a(t) = P_+\left(t + \frac{s}{c}\right) + P_-\left(t - \frac{s}{c}\right) \quad [4]$$

Where $P_+\left(t + \frac{s}{c}\right)$ is the pressure of the downward sound captured at microphone *a*, s/c is the time it takes for the sound to travel from microphone *b* to microphone *a,* and $P_-\left(t - \frac{s}{c}\right)$ is the pressure of upward sound captured at microphone *a*, where t_0 is the time it takes to travel from microphone *a* to microphone *b.*

According to the Fourier transform shift theorem, the Fourier Transform of the pressure signal at the microphone *a* is:

$$P_a(f) = e^{2\pi jf\left(\frac{s}{c}\right)}P_+(f) + e^{-2\pi jf\left(\frac{s}{c}\right)}P_-(f) \quad [5]$$

Replacing $\frac{2\pi f}{c}$ with *k* (wavenumber), and substituting in Equation 5 gives:

$$P_a(f) = e^{jks}P_+(f) + e^{-jks}P_-(f) \quad [6]$$

From equations 2 and 6, the transfer function between the two locations can be expressed as:

$$H(f) = \frac{P_b(f)}{P_a(f)} = \frac{P_+(f)+P_-(f)}{e^{jks}P_+(f)+e^{-jks}P_-(f)} = |H(f)|e^{j\varphi(f)} \quad [7]$$

Where $|H(f)|$ is the amplitude gain of the microphone at position *b* over the amplitude at microphone position *a,* and $\varphi(f)$ is the phase shift.

By defining $R(f)$ as the reflection factor, the ratio of the reflected sound and the incident sound can be expressed as:

$$R(f) = \frac{P_-(f)}{P_+(f)} = \frac{H(f)e^{-jks}-1}{1-H(f)e^{jks}} = |R(f)|e^{j\theta(f)} \quad [8]$$

Where $|R(f)|$ is the sound pressure ratio of the incident and reflected sound, and $\theta(f)$ is the phase shift between these two waves.

Since that acoustic power is correlated with the square of pressure, $|R(f)|^2$ represents the ratio of the reflected power and the incident power. Therefore, the sound absorption of the sample can be expressed as:

$$\alpha(f) = 1 - |R(f)|^2 \quad [9]$$

To have $\alpha(f)$, the transfer function $H(f)$ from equation 8 can be worked out from the cross-power spectrum for positions $\underline{a}$ and $\underline{b}$ ($P_{ba}(f)$) and the auto power spectrum at position $\underline{a}$ ($P_{aa}(f)$).

$$H(f) = \frac{P_b(f)P_a^*(f)}{P_a(f)P_a^*(f)} = \frac{P_{ba}(f)}{P_{aa}(f)} \quad [10]$$

The sound reflection at the surface of the samples can be expressed as follows:

$$R(f) = \frac{H(f) - e^{-jks}}{e^{jks} - H(f)} e^{j2k(l+s)} \quad [11]$$

The solution of Equation 7-28 (Chapter 7)

$$\frac{\omega_1^2}{\bar{P}} = Q\sqrt{\frac{w_0^4}{Q^2} + (w_1^2 - w_0^2)^2}$$

$$\omega_0^4 + Q^2\omega_0^4 - 2Q^2\omega_0^2\omega_1^2 + Q^2\omega_0^4 = \frac{\omega_1^4}{\bar{P}^2}$$

$$Defining: X = \omega_1^2$$

$$X^2 - \frac{2Q^2\omega_0^2}{Q^2 - \frac{1}{\bar{P}^2}}x = -\frac{Q^2\omega_0^4 + \omega_0^4}{Q^2 - \frac{1}{\bar{P}^2}}$$

$$Adding\ the\ square\ of\ half\ of\ the\ coefficient\ of\ X\ to\ both\ sides\ and\ factoring:$$

$$\left(X - \frac{Q^2\omega_0^2}{Q^2 - \frac{1}{\bar{P}^2}}\right)^2 = \frac{\bar{P}^2\omega_0^4(1 + Q^2 - \bar{P}Q^2)}{(\bar{P}Q - 1)^2(\bar{P}Q + 1)^2}$$

$$X = \frac{Q^2\omega_0^2}{Q^2 - \frac{1}{\bar{P}^2}} \pm \sqrt{\frac{\bar{P}^2\omega_0^4(1 + Q^2 - \bar{P}Q^2)}{(\bar{P}Q - 1)^2(\bar{P}Q + 1)^2}}$$

$$Substituting\ back\ for\ X = \omega_1^2\ and\ algebratic\ manipulatoin:$$

$$\omega_1 = \pm\omega_0\sqrt{\frac{\pm\bar{P}\sqrt{(1 + Q^2 - \bar{P}^2Q^2)} + \bar{P}^2Q^2}{\bar{P}^2Q^2 - 1}}$$

Appendix C: Technical information

The following are the technical information and datasheet of some of the electronicals mateiral used in this thesis.

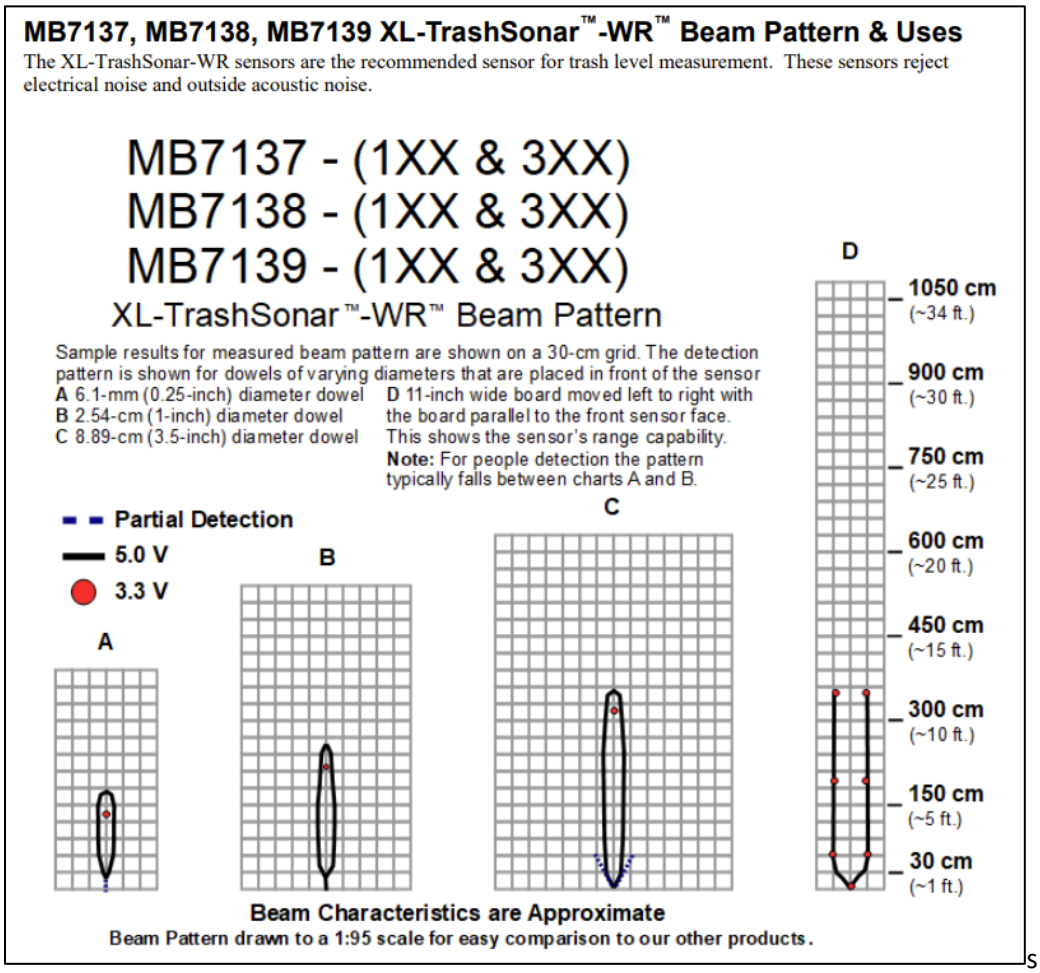


Figure C-1: *Beam Pattern of the ultrasonic range finder.*

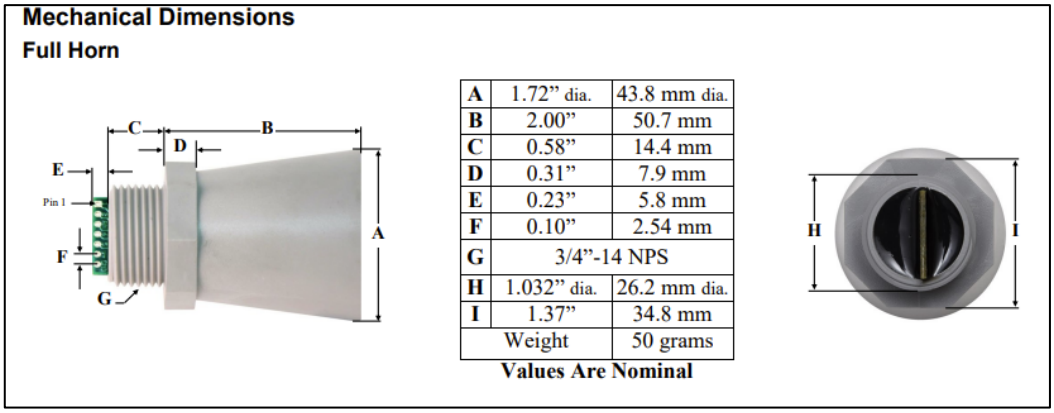


Figure C-2: *Mechanical Dimension of the ultrasonic range finder that was used in Chapter 2.*

PCB PIEZOTRONICS

SPECIFICATIONS
VOLTAGE OUTPUT PRESSURE TRANSDUCER

REVISIONS
-G- REV #2677 8/1/89

SHEET 1 OF 1

MODEL NO		103A	103A11
RANGE (3 V OUTPUT)	psi (db)	2 (177)	6 (186)
USEFUL OVERRANGE	psi	-2 to +6	20
MAXIMUM PRESSURE	psi	30	30
RESOLUTION	psi, rms (db)	2.2×10^{-5} (78)	1.32×10^{-4} (93)
SENSITIVITY	mV/psi	1500	500
RESONANT FREQUENCY	kHz	13	13
RISE TIME	µSec	25	25
DISCHARGE TIME CONST (2)	Sec	≥ 10	≥10
LOW FREQ RESPONSE -5%	Hz	.05	.05
LINEARITY (1)	% FS	±2	±2
POLARITY		POSITIVE	POSITIVE
OUTPUT IMPEDANCE	ohm	<100	<100
OUTPUT BIAS	+ volt	3 to 8	8 to 14
OVERLOAD RECOVERY	µSec	10	10
ACCELERATION SENS	psi/G	.0005	.0005
TEMP COEFFICIENT	%/°F	≤.03	≤.03
TEMPERATURE RANGE	°F	-100 to +175	-100 to +175
MAXIMUM FLASH TEMP	°F	1000	1000
VIBRATION/SHOCK	G's peak	1000/10000	1000/10000
SEALING		EPOXY	EPOXY
CASE/DIAPHRAGM MAT'L		INVAR/INVAR	INVAR/INVAR
WEIGHT	gm	2.3	2.3
CONNECTOR	coaxial	PIGTAIL	PIGTAIL
EXCITATION	+ VDC/mA	18-28/2-20	24-27/2-20

(2) AT ROOM TEMPERATURE
(1) ZERO BASED BEST STRAIGHT LINE.

SUPPLIED ACCESSORIES:

CLAMP MOD. 061A04

APP'D	JTC	12/82	SPEC No.
ENGR	[illegible]	12/82	103-1010-80
SALES	[illegible]	12/82	

Figure C-3: *PCB103A technical data.*

~ *Calibration Certificate* ~

Model Number: 130E20

Serial Number: 29917

Description: ICP® Microphone

Manufacturer: PCB

Method [1]: Back-to-Back Reference

Calibration Data

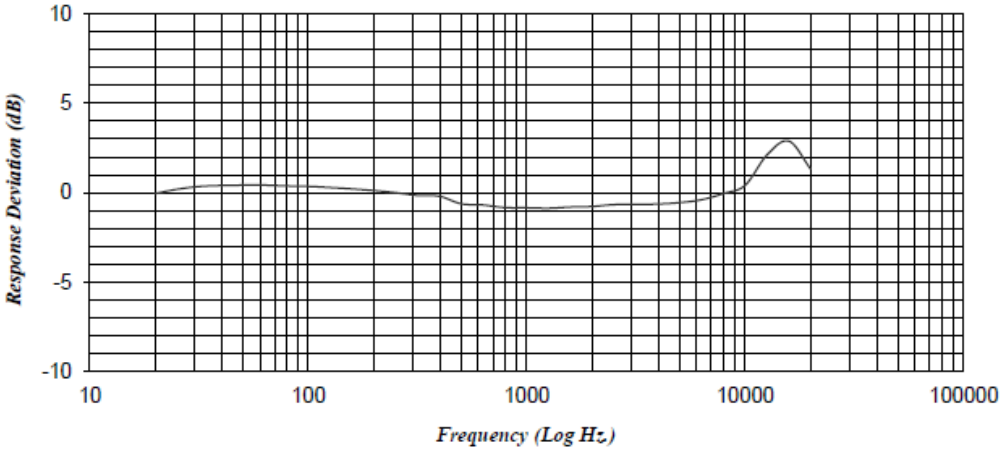
Sensitivity: 43.8 mV/Pa
-27.2 dB re 1V/Pa

Reference Freq.: 250 Hz.
Output Bias: 10.3 VDC

Temperature: 71 °F 22 °C

Relative Humidity: 55 %

Response Plot



Condition of Unit

As Found: N/A
As Left: New unit, In tolerance

Notes

1. This method involves comparing the test unit with a reference microphone in a GRAS 51AB calibrator.
2. Calibration is N.I.S.T. Traceable and calibration records are on file.
3. Calibration is performed in compliance with ISO 9001, ISO 10012-1 and ANSI/NCSL Z540-1-1994.
4. Due to state-of-the-art limitations, 4:1 calibration ratios are not possible on pressure measurement standards, microphones and acoustic calibrators. Calibration ratios for these types of devices are limited to 1:1.
5. See Manufacturer's Specification Sheet for a detailed listing of performance specifications.
6. This certificate shall not be reproduced, except in full, without written approval from PCB Piezotronics, Inc
7. Calibrated per ACS-21.

Technician: Scott Skibniewski

Date: August 24, 2010

PCB PIEZOTRONICS
VIBRATION DIVISION

Headquarters: 3425 Walden Avenue, Depew, NY 14043
Calibration performed at: 10869 Highway 903, Halifax, NC 27839

Page 1 of 1 TEL: 888-684-0013 FAX: 716-685-3886 www.pcb.com Cal67-3365506969.56

Figure C-4: *Calibration certificate for PCB130E20.*

Appendix D: Physical properties of the test materials

Particle Size Distibution

Figures D-3 to D-7 are the results of the Malvern MasterSizer particle analysis. Figure D-8 shows the results of the permeability analysis.

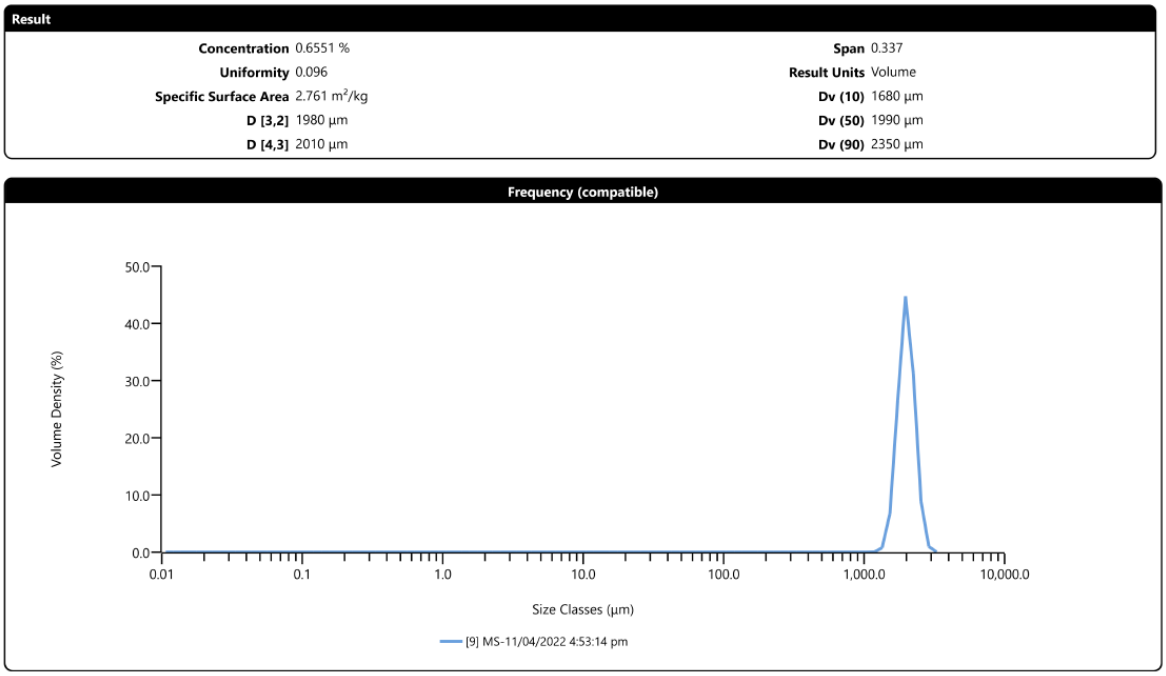


Figure D-1: *Mustard seeds (MS).*

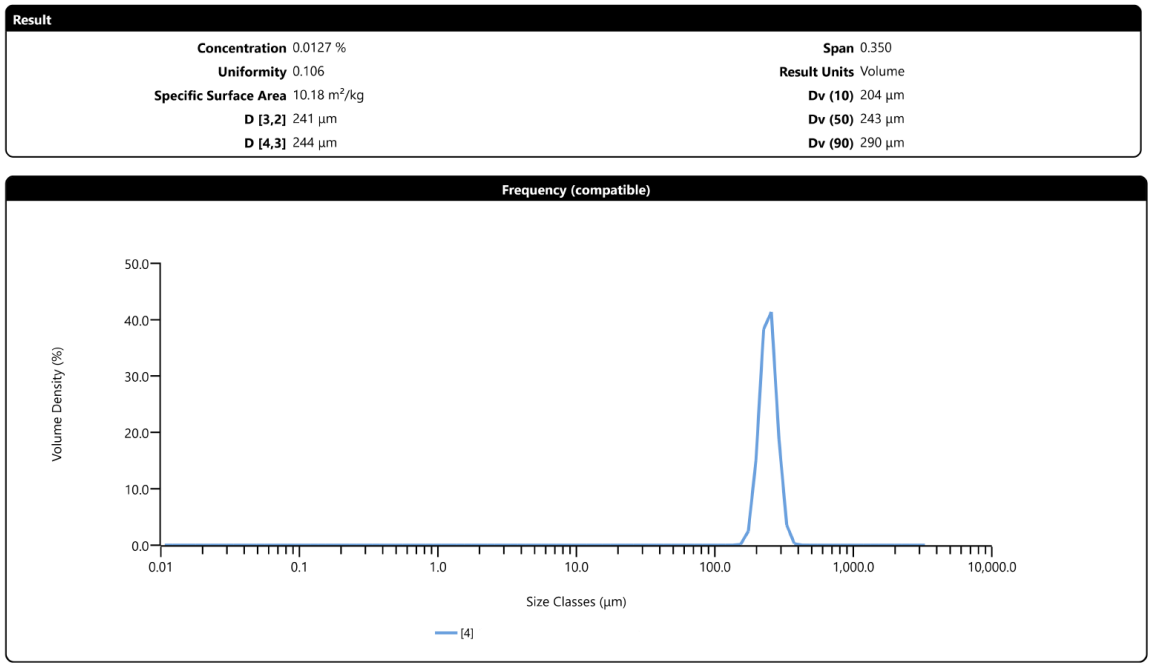


Figure D-2: *fine ballotini (B250).*

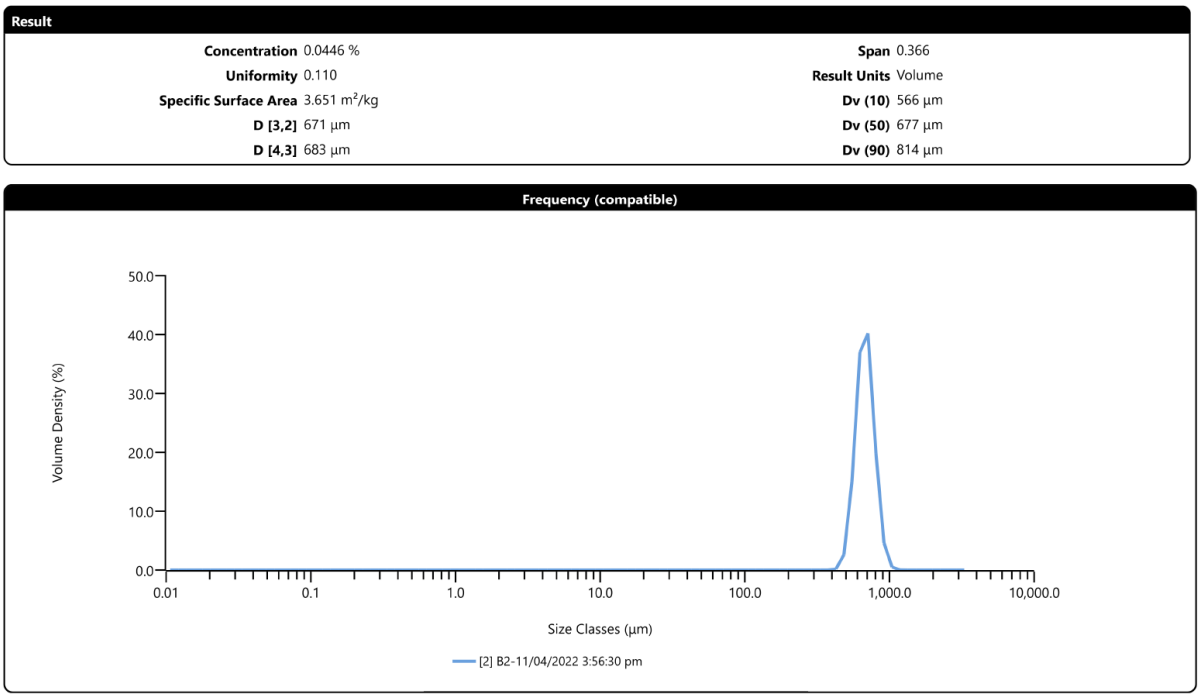


Figure D-3: *coarse ballotini (B710).*

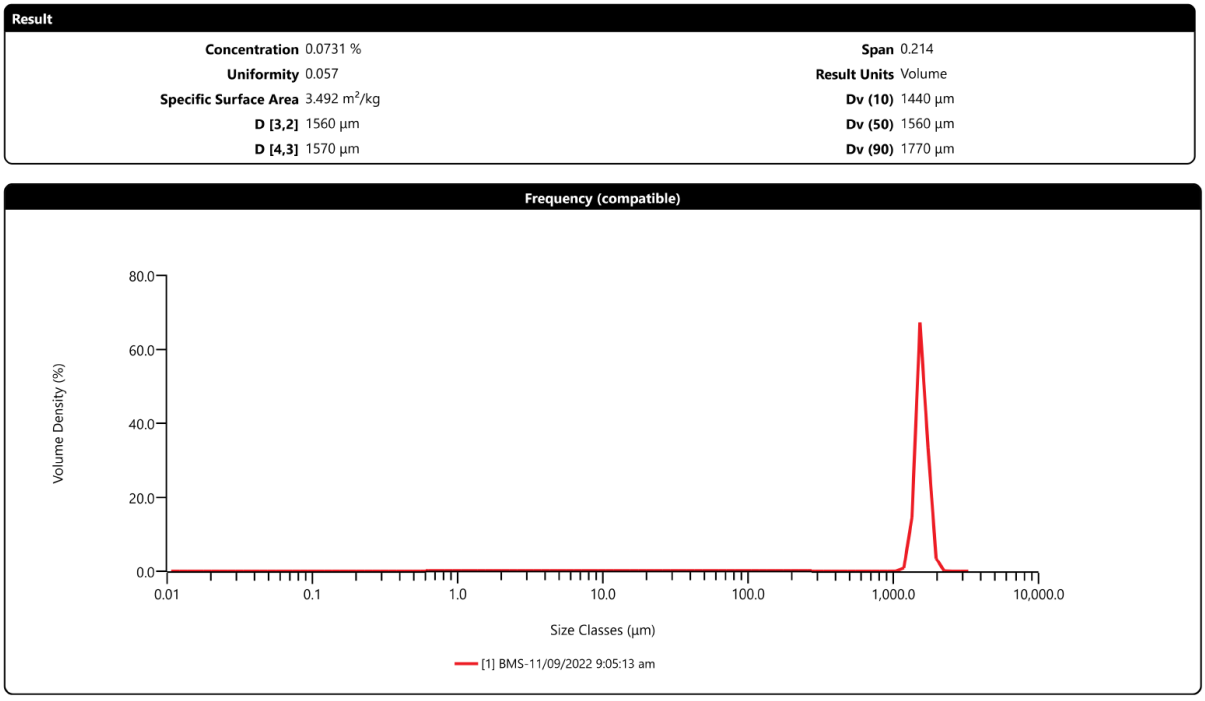


Figure D-4: *Black mustard seeds (BMS).*

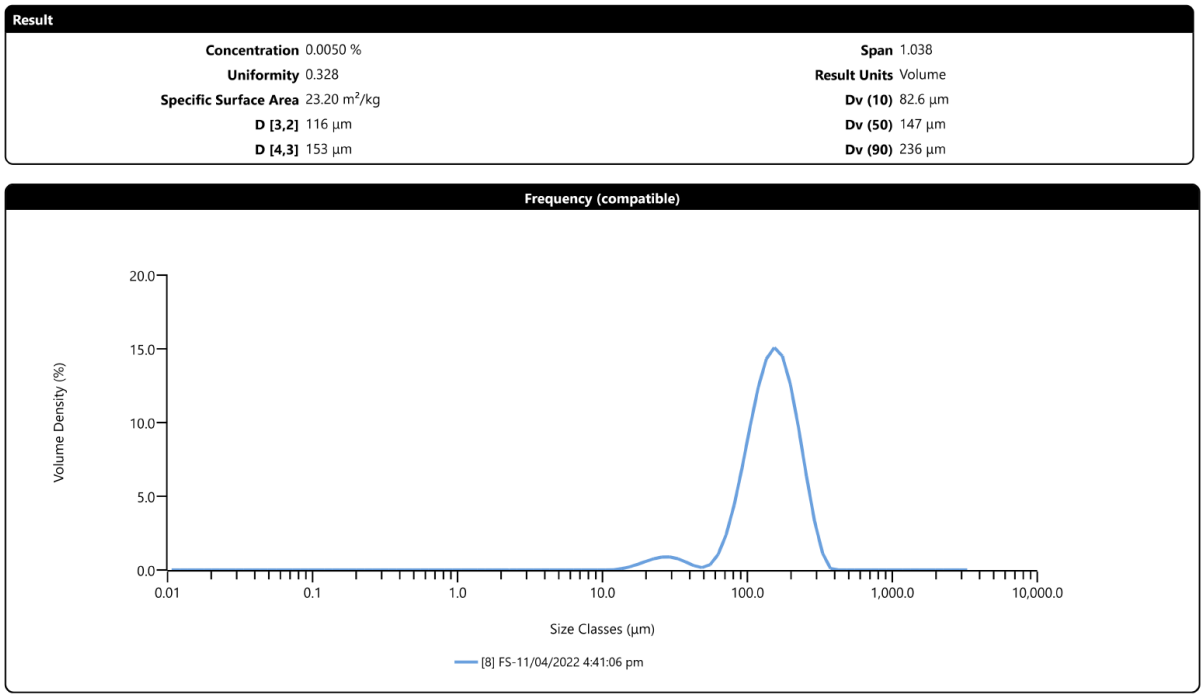


Figure 0-5: *Fine sand (FS).*

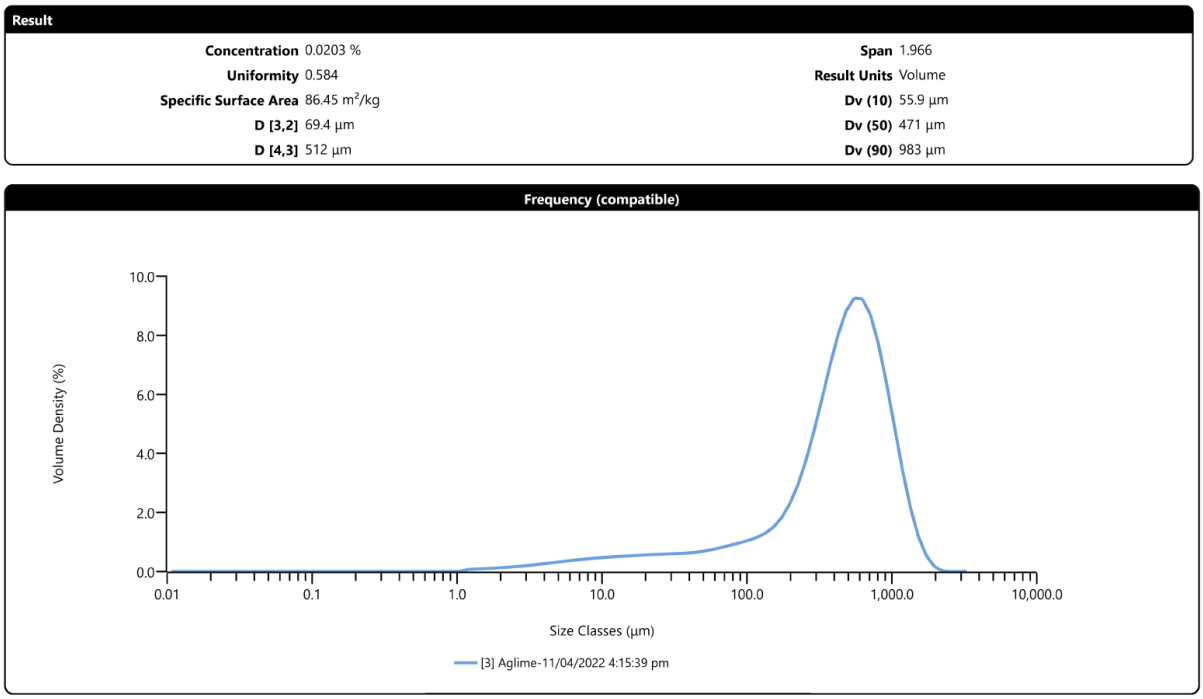


Figure D-6: *Agricultural lime (AL1).*

Result

Concentration	0.0154 %	**Span**	1.414
Uniformity	0.449	**Result Units**	Volume
Specific Surface Area	7.122 m^2/kg	**Dv (10)**	405 µm
D [3,2]	312 µm	**Dv (50)**	748 µm
D [4,3]	859 µm	**Dv (90)**	1460 µm

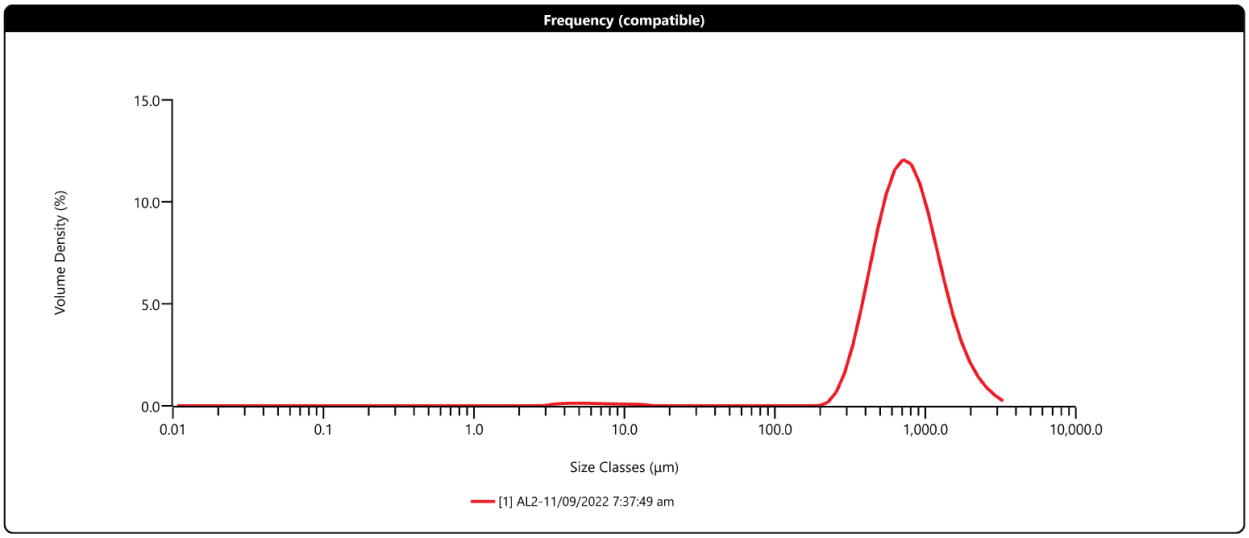


Figure D-7: *Agricultural lime (AL2).*

Permeability Analysis

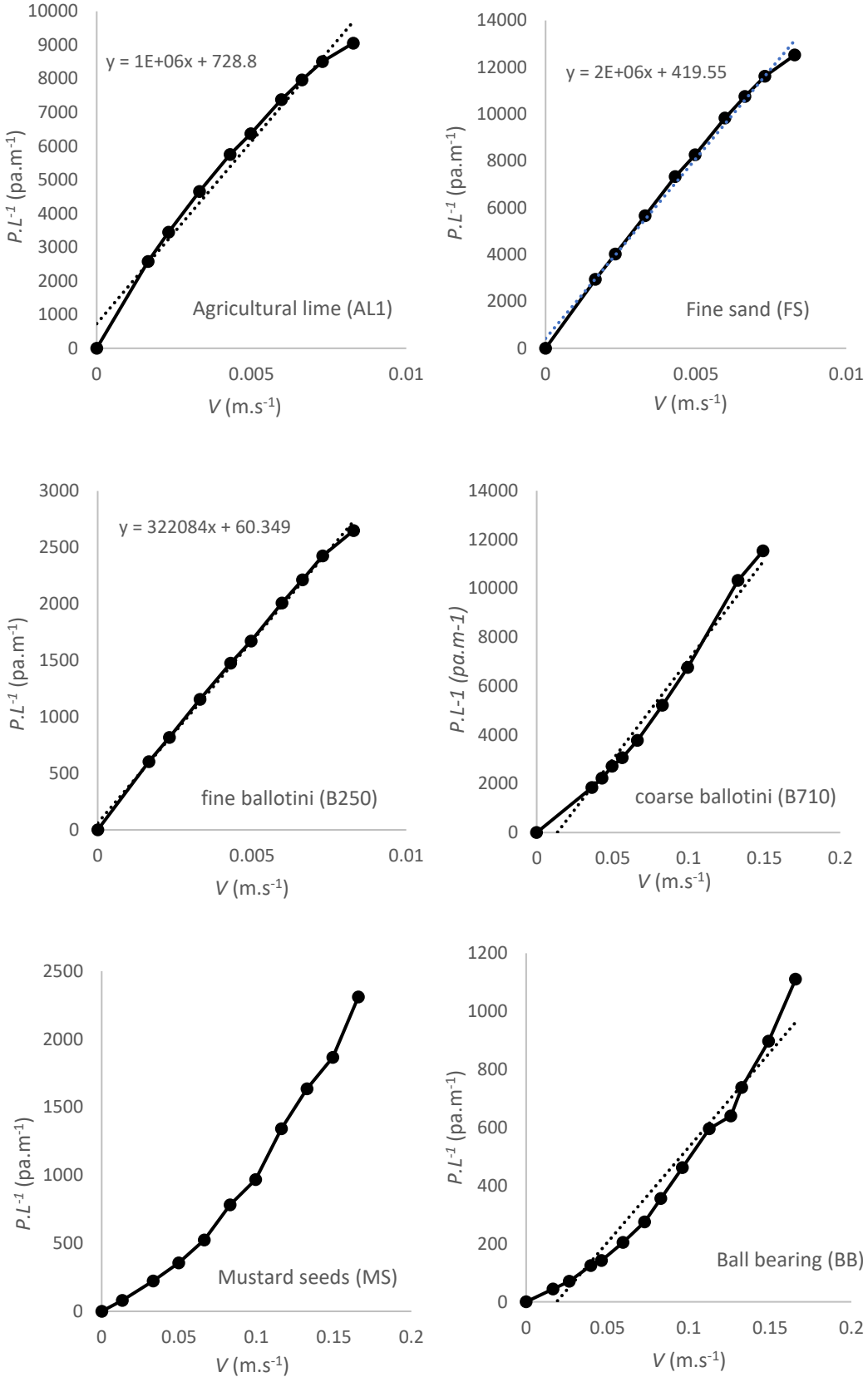


Figure D-8: *Permeability analysis.*

Appendix E: Drawings

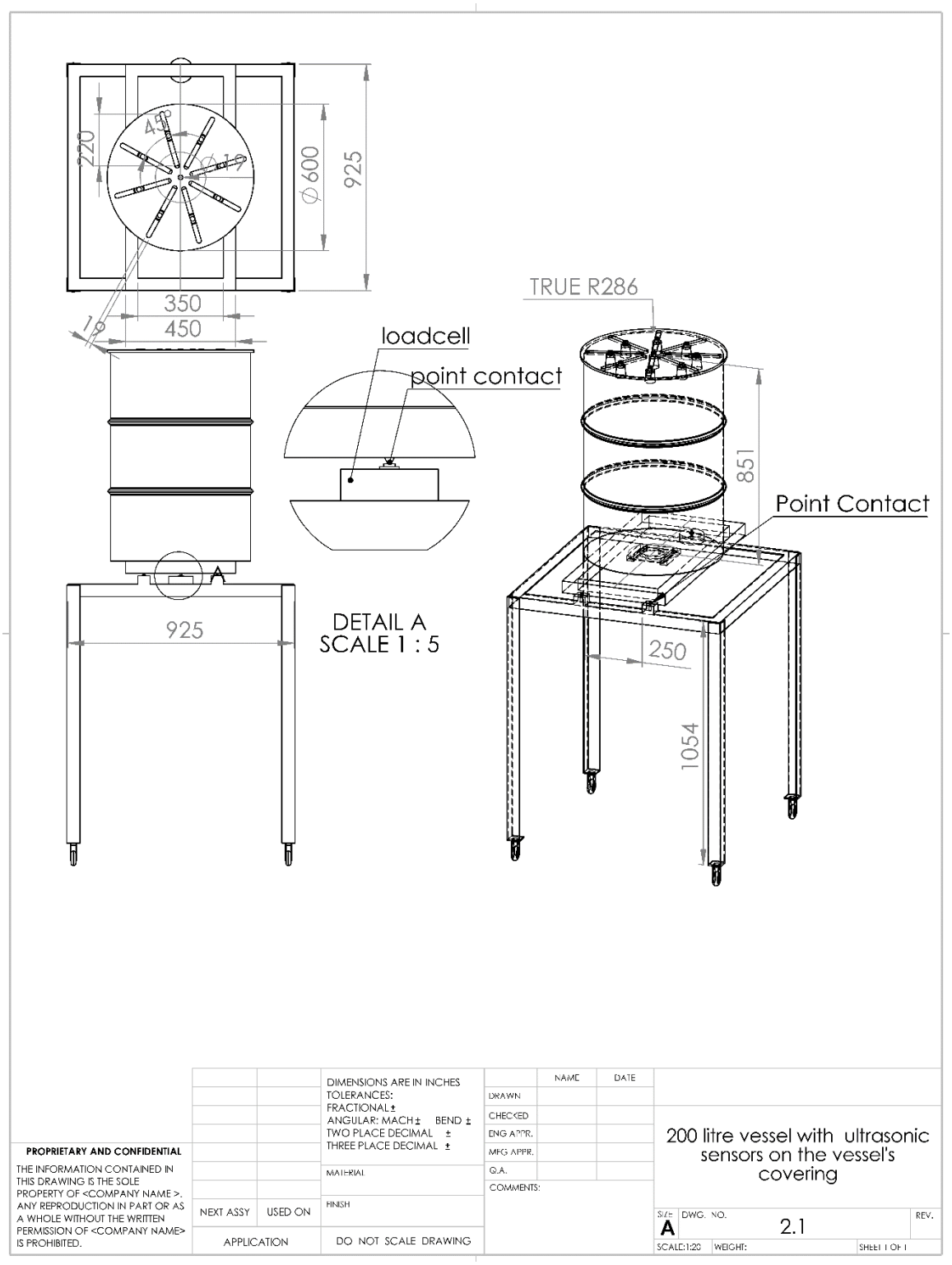


Figure E-1: *Material Discharge vessel setup, Chapter 2.*

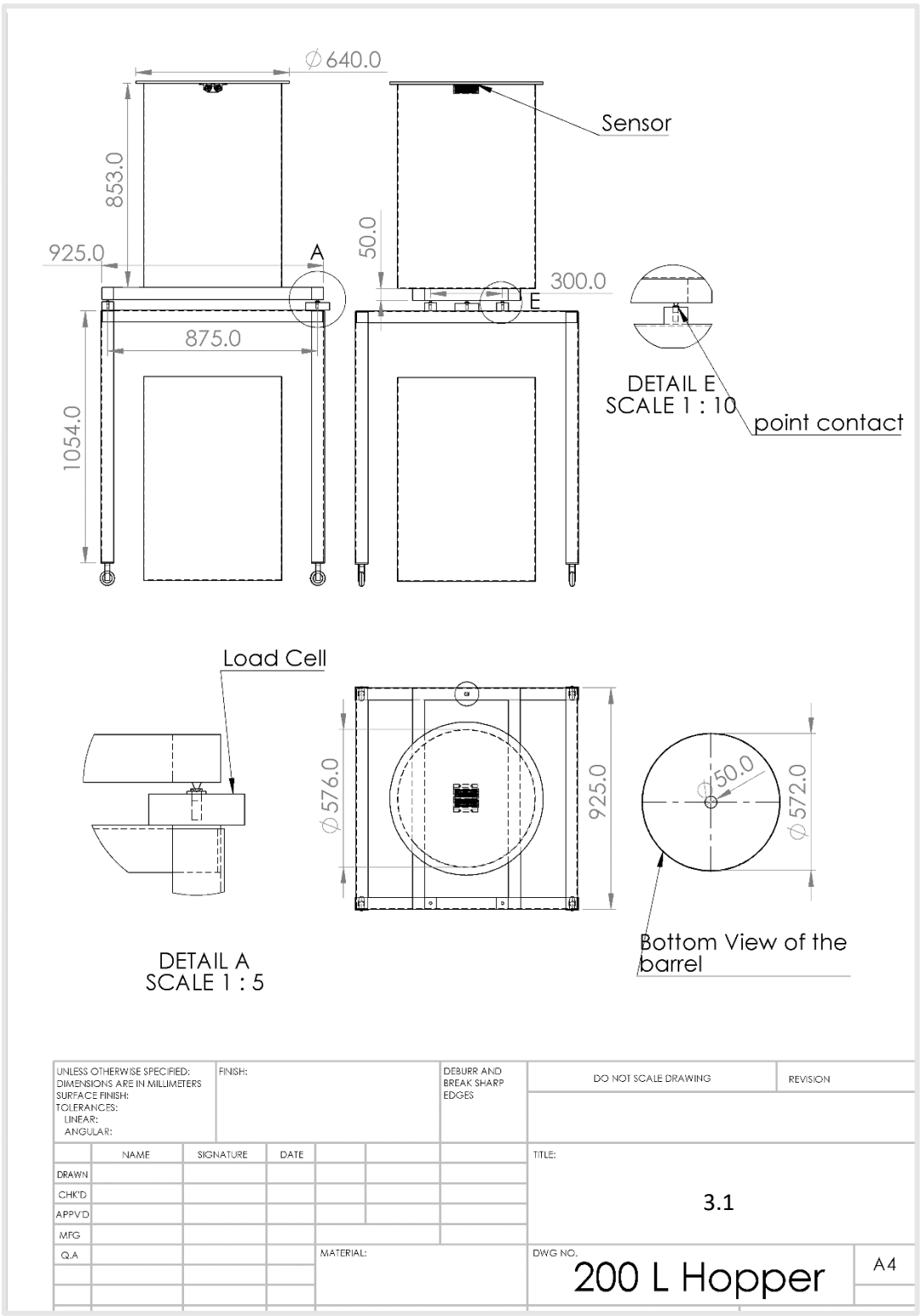


***Figure E-2**: 200-litre discharge vessel, Chapter 3.*

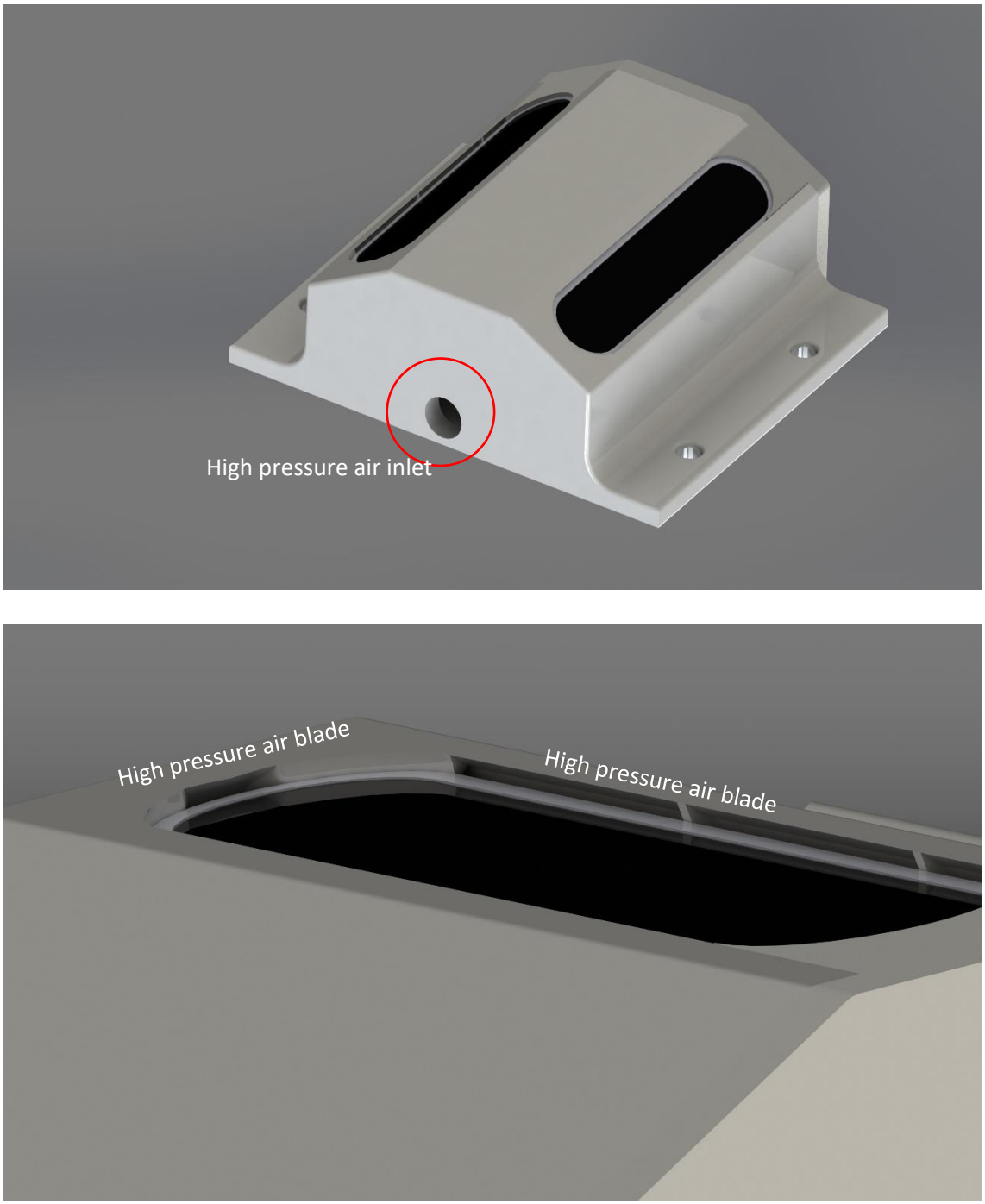


***Figure E-3*:** Dual Depth Camera Housing. The clearance of 0.5 mm to form an air blade surrounding the sensor face is shown in the bottom figure, Chapter 3.

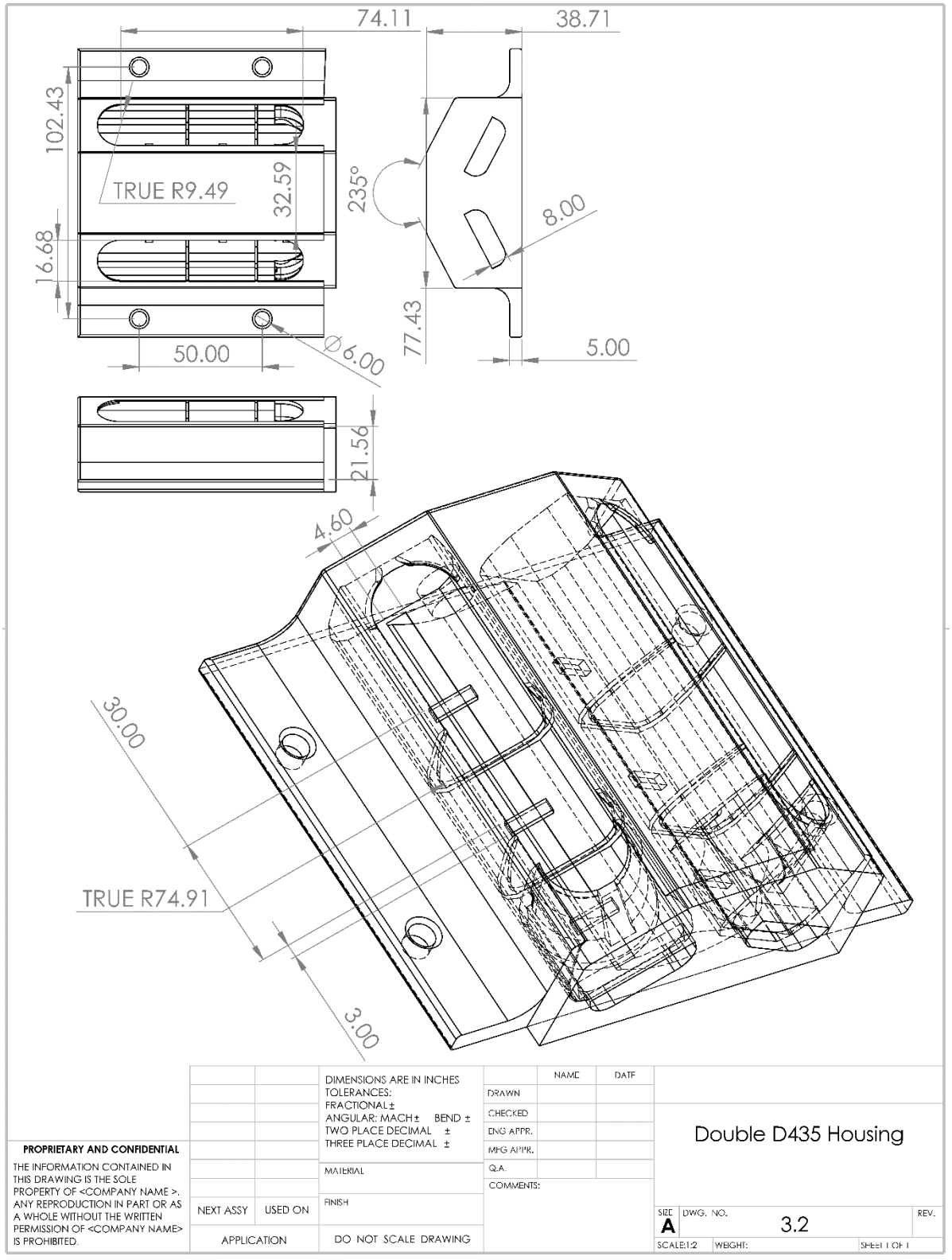


Figure E-4: *Details of the Dual Depth Camera housing, Chapter 3.*



Figure E-5: *Graphical representation of the Lab-Scale resonator system with a 3-litre cavity and 250 mm port, Chapter 4.*

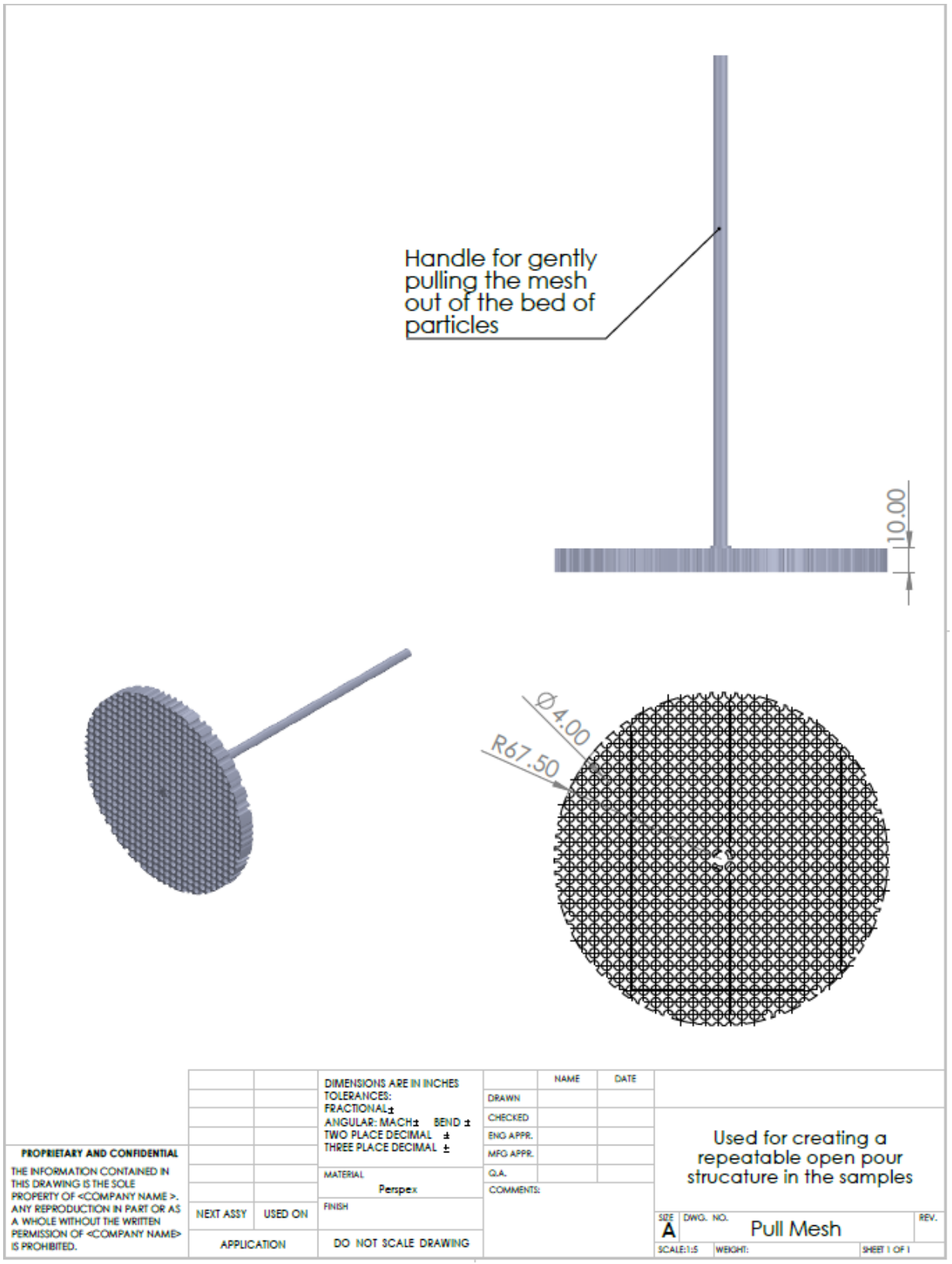


Figure E-6: Perforated plate for forming a loose density in powder samples, Chapter 4.

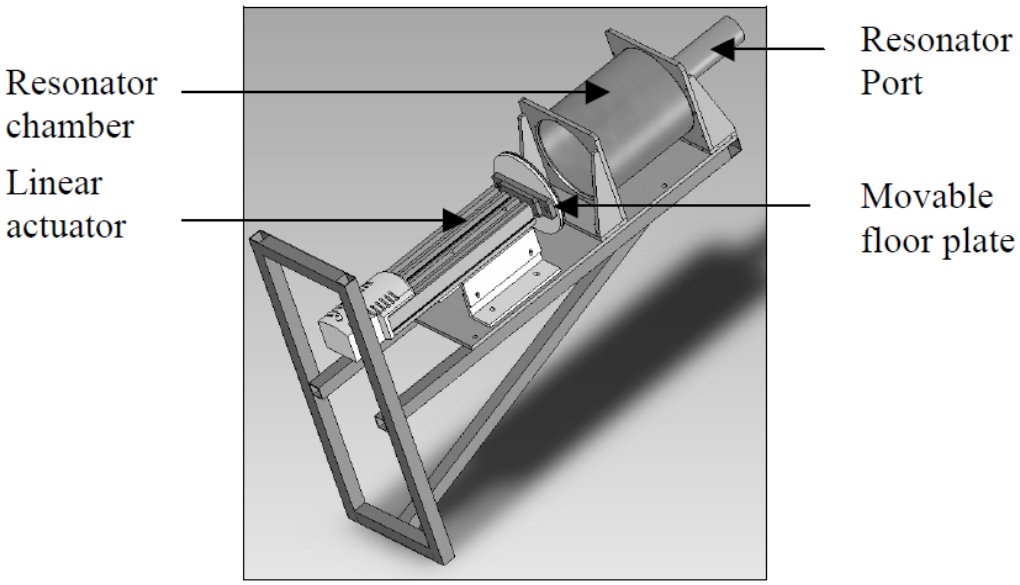


***Figure E-7*:** Variable Chamber Resonator, designed and created by Webster (2010).

Appendix F: Pictures

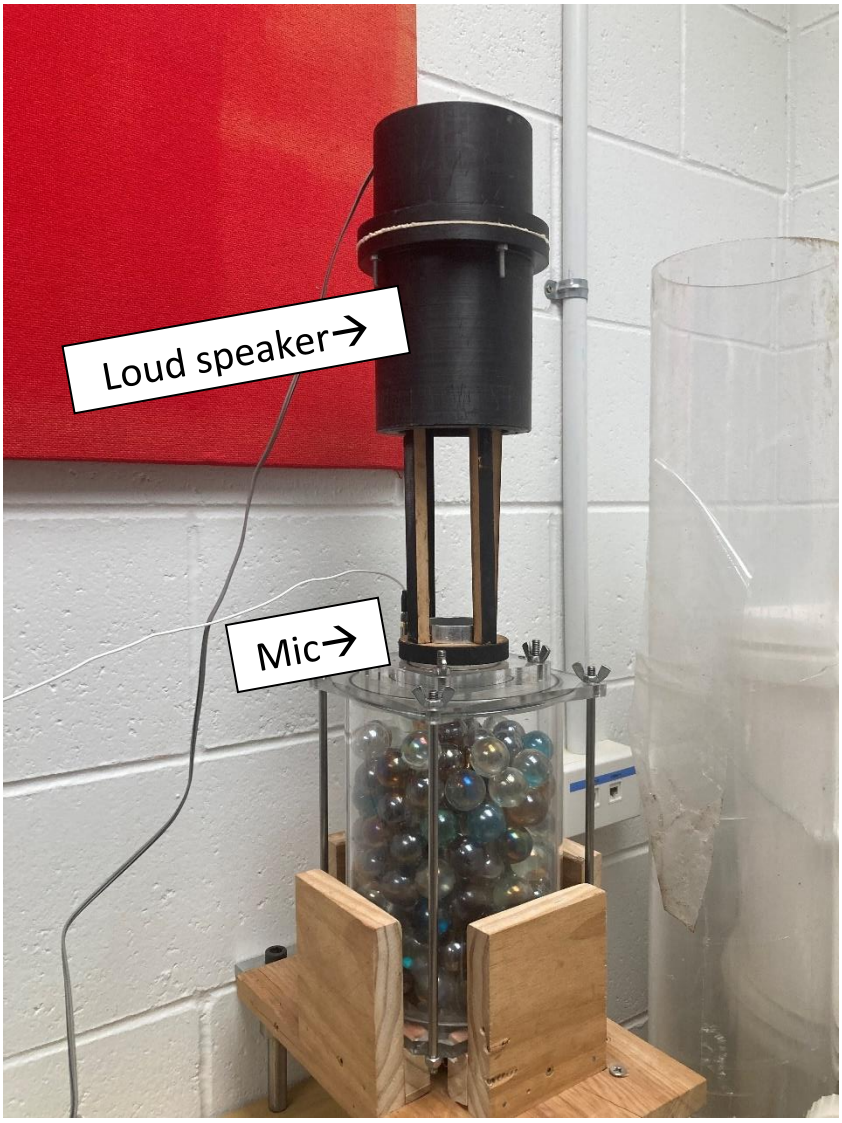


Figure F-1: *3-litre resonator, 51 mm port. Measuring the volume of solid marbles using the SPQF model. Chapter 7, Section 7.5.2.*

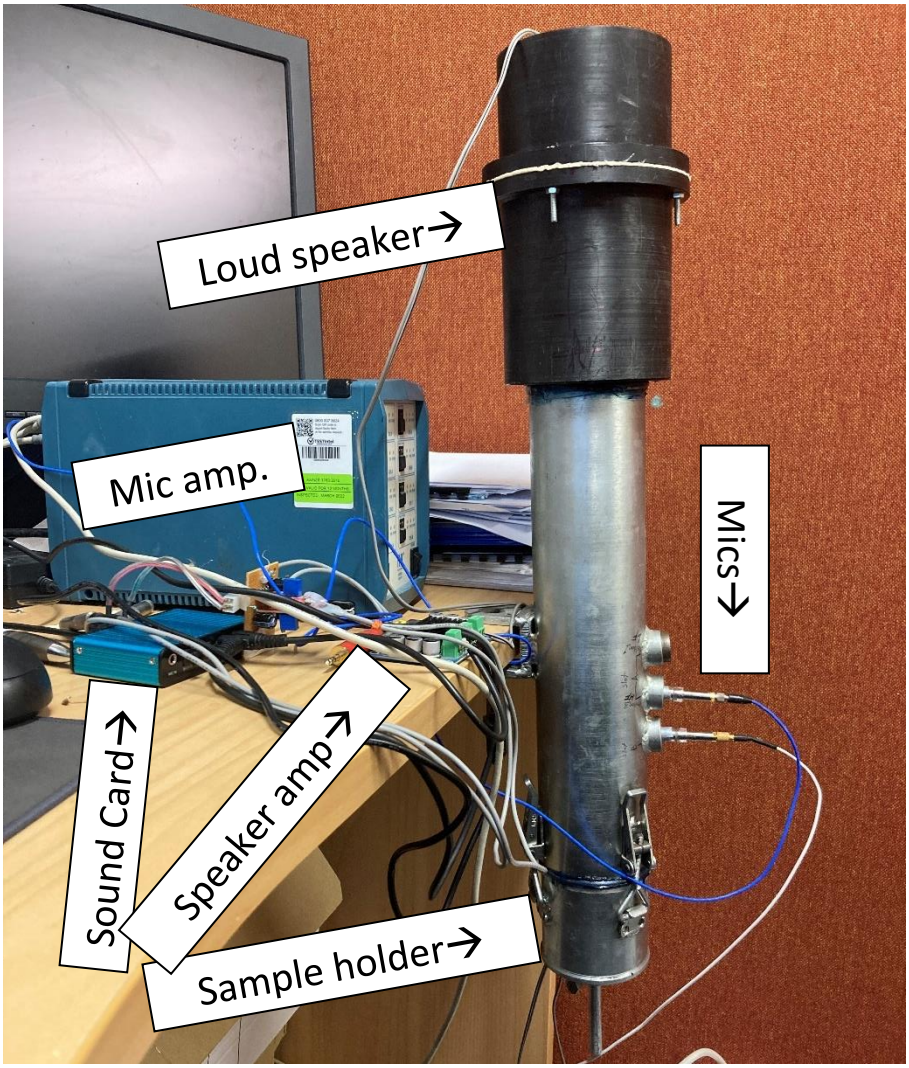


Figure F-2: *Impedance Tube. Chapter 4, Section 4.2.10.*

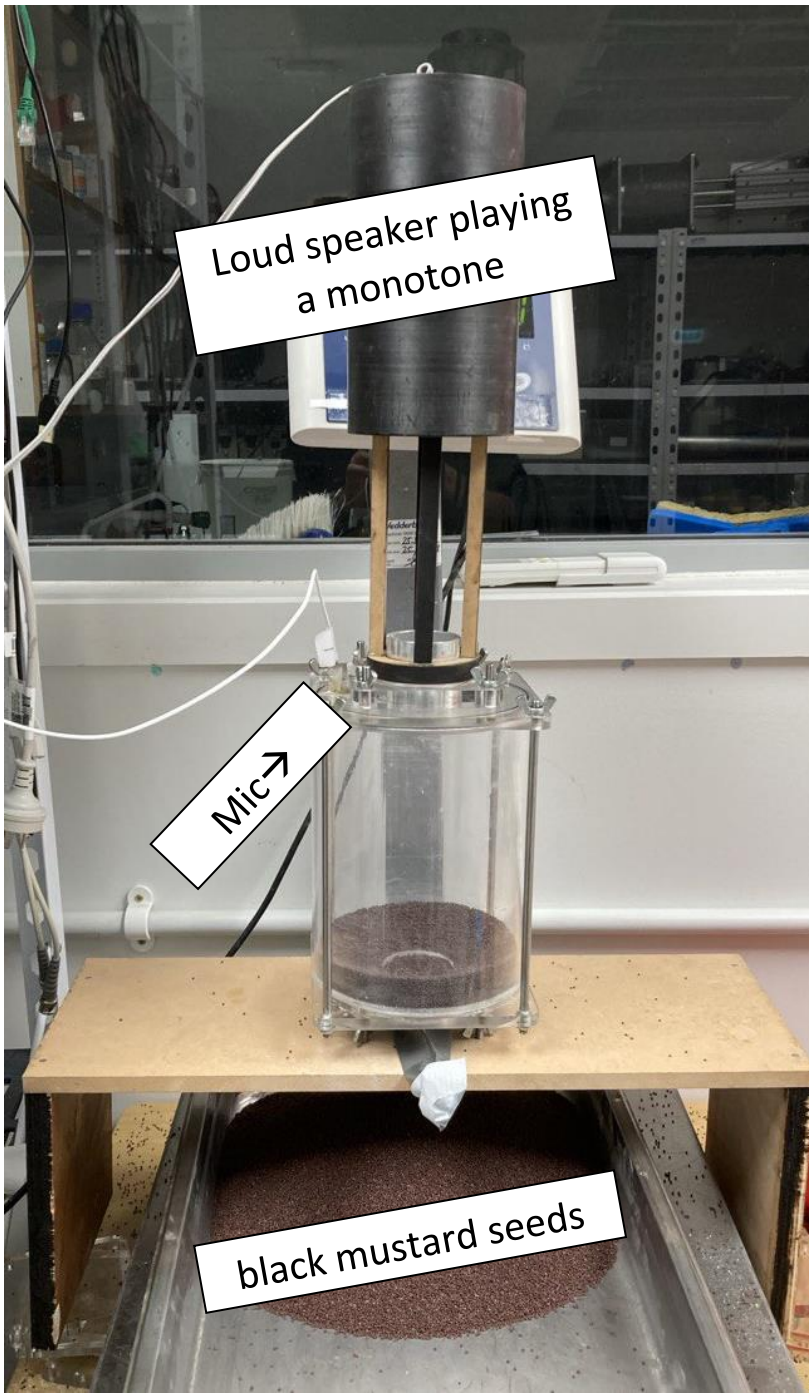


Figure F-3: *Dynamic volume measurement of black mustard seeds discharging from the 3-litre resonator with 51 mm port attached. Chapter 7, Section 7.5.4.*

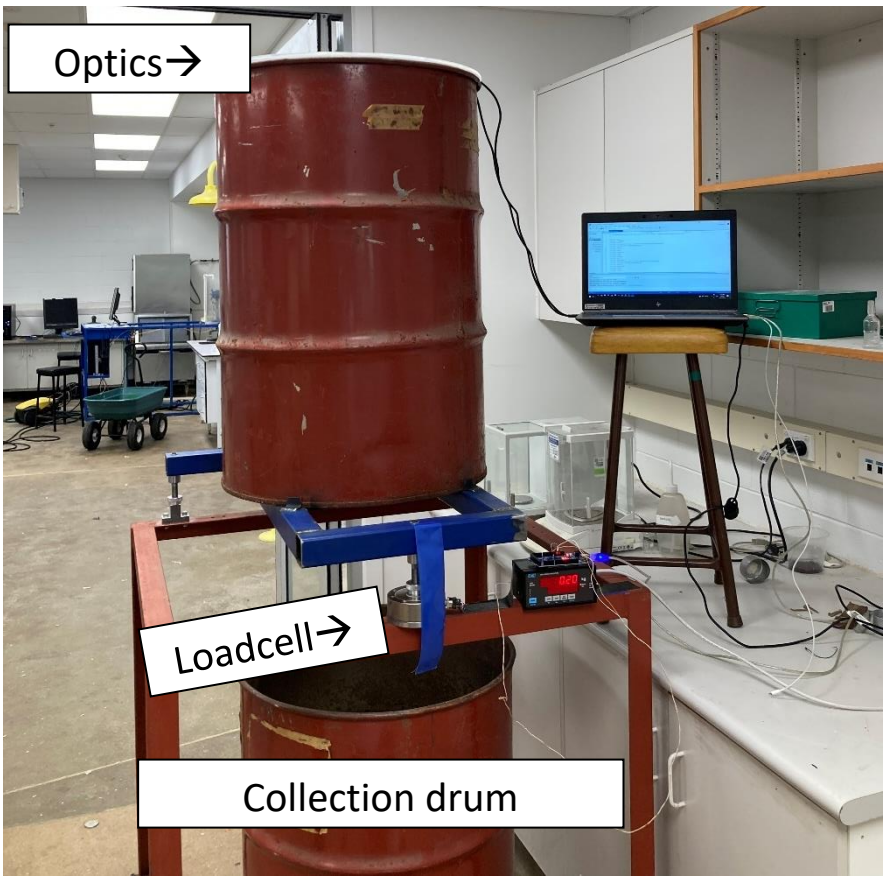


Figure F-4: *The 55-gallon drum and the scale which was used for optical volume measurement tests. Chapter 3.*

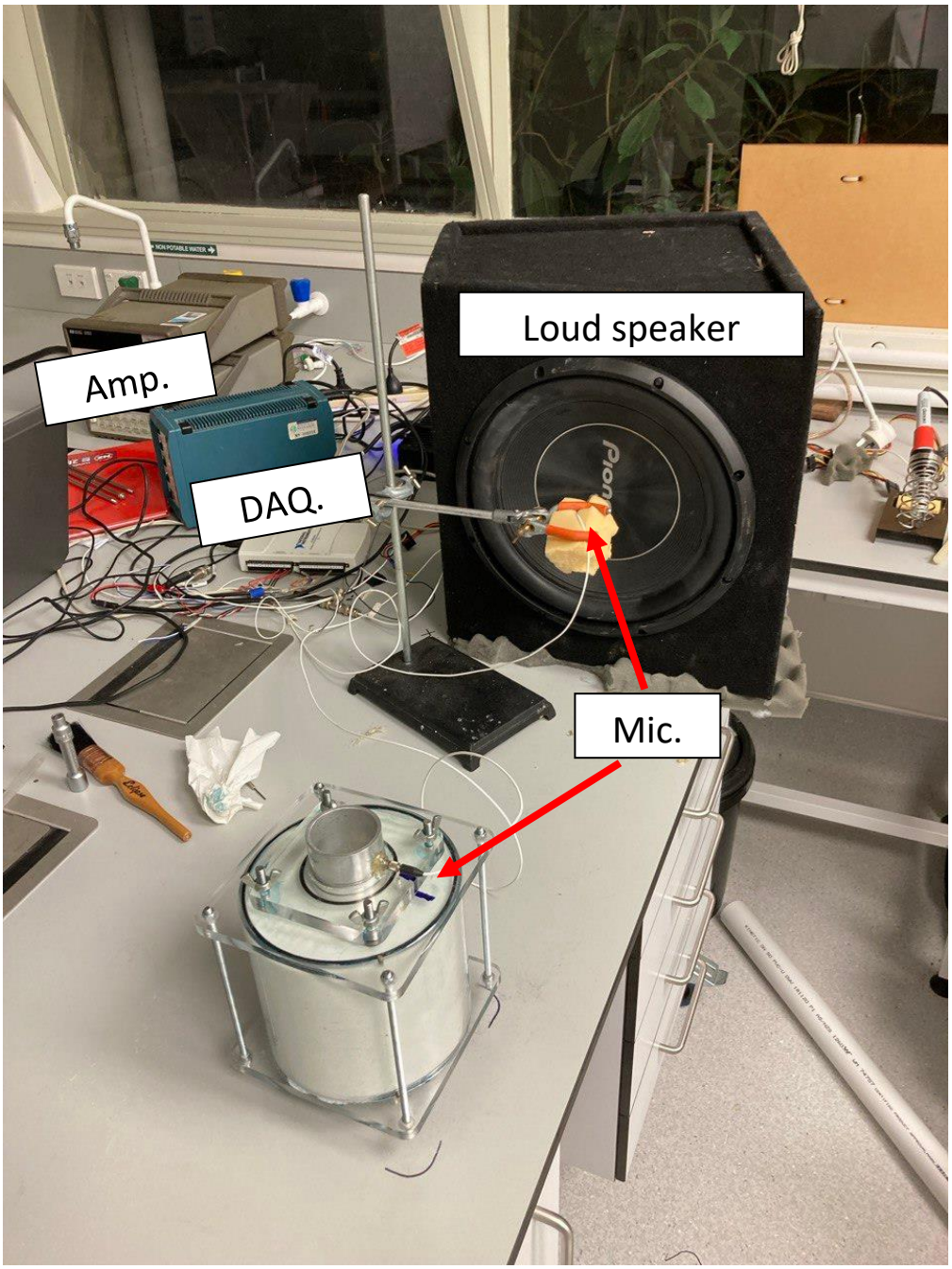


Figure F-5: *Resonance hunting using two microphones, Transfer Funciton method. The 2-litre resonator with the 51 mm port. The test material inside is ballotini B250. Chapter 4, Section 4.4.5.*



Figure F-6: *Tapping Machine for obtaining tapped density for the powders inside the resonator. Chapter 4 Section 4.3.8.*

References

Agnew, J. M., Leonard, J. J., Feddes, J., & Feng, Y. (2003). A modified air pycnometer for compost air volume and density determination. *Canadian Biosystems Engineering*, *45*, 6–27.

Allard, J., & Atalla, N. (2009). *Propagation of sound in porous media: Modelling sound absorbing materials 2e*. John Wiley & Sons.

Alster, M. (1972). Improved calculation of resonant frequencies of Helmholtz resonators. *Journal of Sound and Vibration*, *24*(1), 63–85. https://doi.org/10.1016/0022-460X(72)90123-X

Altuntas, C. (2014). Pile volume measurement by range imaging camera in indoor environment. *The International Archives of the Photogrammetry, Remote Sensing and Spatial Information Sciences*, *40*, 35–39.

Amorim, L. L., Mutz, F., De Souza, A. F., Badue, C., & Oliveira-Santos, T. (2019). Simple and effective load volume estimation in moving trucks using lidars. *2019 32nd SIBGRAPI Conference on Graphics, Patterns and Images (SIBGRAPI)*, 210–217. https://ieeexplore.ieee.org/abstract/document/8919701/

Andrei, K., & Alexey, L. (2019). Increasing foam expansion rate by means of changing the sprinkler geometry. *Fire Safety Journal*, *109*, 102862. https://doi.org/10.1016/j.firesaf.2019.102862

Anggraini, N., Rozy, N. F., & Lazuardy, R. A. (2016). Facial recognition system for fatigue detection using Intel Realsense Technology. *Information and Communication Technology for The Muslim World (ICT4M), 2016 6th International Conference On*, 248–253.

A.P. French. (2003). *Vibrations and Waves (The M.I.T. Introductory Physics Series)*. CBS Publishers & Distributors Pvt Ltd, India.

ASTM E1050-19. (2019). *Standard Test Method for Impedance and Absorption of Acoustical Materials Using a Tube, Two Microphones and a Digital Frequency Analysis System*.

ASTM E2611-19. (2019). *Standard Test Method for Normal Incidence Determination of Porous Material Acoustical Properties Based on the Transfer Matrix Method*. American Society for Testing and Materials.

ASTM Standard C384-04. (2004). *Standard Test Method for Impedance and Absorption of Acoustical Materials by Impedance Tube Method*.

Barzegar, M., & Davies, C. E. (2024). The Practicality of Using Generic Acoustical Equipment in Impedance Tube Design. *Acoustics Australia*. https://doi.org/10.1007/s40857-024-00326-y

Barzegar, M., Davies, C. E., & Grafton, M. C. (2024). Ultrasonic measurement of fill volume of bulk solids in discharge vessels. *Powder Technology*, 119339.

Barzegar, M., Redding, G., Davies, C. E., Fullard, L., & Grafton, M. (2019a). Measurement of fill volume of a storage vessel by optical means. *3th International Conference on Bulk Materials Storage, Handling and Transportation, ICBMH*.

Barzegar, M., Redding, G., Davies, C. E., Fullard, L., & Grafton, M. (2019b). Optical measurement of degree of fill and discharge rate in a lab-scale storage vessel. *ASABE 2019 Annual International Meeting, Boston, The United States*.

Barzegar, M., Redding, G. P., Davies, C. E., Fullard, L., & Grafton, M. C. E. (2024). Fill volume in a storage vessel determined by optical scanning. *Powder Technology*, *437*, 119532. https://doi.org/10.1016/j.powtec.2024.119532

BINMASTER. (2023). https://www.binmaster.com/3d-details

Blackstock, D. T. (2000). *Fundamentals of physical acoustics*. John Wiley & Sons.

Bocci, C., Fort, A., Pozzebon, A., & Bertoni, D. (2020). A geometrical approach for the measurement of the volume of masses of granular material through grid-layout sensor networks. *Measurement*, *151*, 107102.

Bohn, D. A. (1988). Environmental effects on the speed of sound. *Journal of the Audio Engineering Society*, *36*(4), 223–231.

Braun, S. G., Ewins, D. J., Rao, S. S., & Leissa, A. W. (2002). Encyclopedia of Vibration: Volumes 1, 2, and 3. *Appl. Mech. Rev.*, *55*(3), B45–B45.

Brown, M. Z., Burschka, D., & Hager, G. D. (2003). Advances in computational stereo. *IEEE Transactions on Pattern Analysis and Machine Intelligence*, *25*(8), 993–1008.

CAA Consolidation. (2018). *Part 91*. Civil Aviation Authority of New Zealand.

Chanaud, R. C. (1994). Effects Of Geometry On The Resonance Frequency Of Helmholtz Resonators. *Journal of Sound and Vibration*, *178*(3), 337–348. https://doi.org/10.1006/jsvi.1994.1490

Chanaud, R. C. (1997). Effects of geometry on the resonance frequency of Helmholtz resonators, part II. In *Journal of sound and vibration* (Vol. 204, Issue 5, pp. 829–834). Elsevier.

Chen, H., Xu, H., Rao, X., Kondo, N., & Bao, J. (2013). A Preliminary Study of Helmholtz Resonant for Measurement of Watermelon Volume. *2013 Kansas City, Missouri, July 21-July 24, 2013*, 1.

Chung, J. Y., & Blaser, D. A. (1980). Transfer function method of measuring in-duct acoustic properties. I. Theory. *The Journal of the Acoustical Society of America*, *68*(3), 907–913.

Cignoni, P., Callieri, M., Corsini, M., Dellepiane, M., & Ganovelli, F. (2008). *MeshLab* (Version 2016) [Computer software]. Eurographics Association.

Civil Aviation Authority. (2008). *Agricultural Aircraft SafetyReview*. https://www.scribd.com/document/75537762/Ag-Aircraft-Safety-Review-Complete#

Civil Aviation Authority. (2011). *AIRCRAFT ACCIDENT REPORT CAA OCCURRENCE* (Aviation Safety Investigation 08/5163; p. 19).

Civil Aviation Authority. (2017). *Agricultural Aircraft Operations Part 137*.

Comiti, J., & Renaud, M. (1989). A new model for determining mean structure parameters of fixed beds from pressure drop measurements: Application to beds packed with parallelepipedal particles. *Chemical Engineering Science*, *44*(7), 1539–1545.

Concha-Meyer, A., Eifert, J., Wang, H., & Sanglay, G. (2018). Volume estimation of strawberries, mushrooms, and tomatoes with a machine vision system. *International Journal of Food Properties*, *21*(1), 1867–1874.

Cox, T., & d'Antonio, P. (2016). *Acoustic absorbers and diffusers: Theory, design and application*. Crc Press.

Das, R., & Kumar, K. S. (2016). GeroSim: A simulation framework for gesture driven robotic arm control using Intel RealSense. *Power Electronics, Intelligent Control and Energy Systems (ICPEICES), IEEE International Conference On*, 1–5.

Gloerfelt, X. (2009). Cavity noise. *VKI Lecture Series*, *3*.

Grafton, M. (2010). *Flow of particulate material from a topdressing aircraft: A thesis presented in partial fulfilment of the requirements of the degree of Doctor of Philosophy in Agricultural*

Engineering at Massey University, New Zealand [Thesis, Massey University]. https://mro.massey.ac.nz/handle/10179/1956

Grafton, M., Yule, I., Davies, C., & Jones, J. (2009, August 1). *Incidents and accidents in aerial topdressing in New Zealand*.

Helmholtz, H. L. (1877). On the Sensations of Tone as a Physiological Basis for the Theory of Music. Trad. ELLIS. *AJ (Dover, New York, 1954)*.

Horoshenkov, K. V., & Swift, M. J. (2001). The effect of consolidation on the acoustic properties of loose rubber granulates. *Applied Acoustics*, *62*(6), 665–690.

Ingard, U. (1953). On the theory and design of acoustic resonators. *The Journal of the Acoustical Society of America*, *25*(6), 1037–1061.

Inman, D. J. (2001). *Engineering Vibration*. Prentice Hall.

Inoue, S., Hirai, Y., Inagaki, S., Inoue, E., Okayasu, T., & Mitsuoka, M. (2021). Volume Measurement of Particle Layers in a Container by Using Helmholtz Resonance. *Journal of the Faculty of Agriculture, Kyushu University*, *66*(1), 91–95.

Johnson, V. E. (1995). *Device for determining the volume of objects using a chamber with two resonators to compensate for temperature and humidity effects* (United States Patent US5385069A). https://patents.google.com/patent/US5385069A/en

Kalauni, K., & Pawar, S. J. (2019). A review on the taxonomy, factors associated with sound absorption and theoretical modeling of porous sound absorbing materials. *Journal of Porous Materials*, *26*(6), 1795–1819.

Keats, J. (1888). *Lamia*.

Keselman, L., Woodfill, J. I., Grunnet-Jepsen, A., & Bhowmik, A. (2017). Intel realsense stereoscopic depth cameras. *arXiv Preprint arXiv:1705.05548*.

Kim, I.-H., Lim, D.-W., & Jung, J.-W. (2019). Single-camera-based sand volume estimation of an excavator bucket. *Multimedia Tools and Applications*, *78*. https://doi.org/10.1007/s11042-019-7225-0

Kinsler, L. E., Frey, A. R., Coppens, A. B., & Sanders, J. V. (2000). Fundamentals of Acoustics, John Wiley & Sons. *Inc, New York*.

Komkin, A. I., Mironov, M. A., & Bykov, A. I. (2017). Sound absorption by a Helmholtz resonator. *Acoustical Physics*, *63*(4), 385–392. https://doi.org/10.1134/S1063771017030071

Koschan, A., Rodehorst, V., & Spiller, K. (1996). Color stereo vision using hierarchical block matching and active color illumination. *Pattern Recognition, 1996., Proceedings of the 13th International Conference On*, *1*, 835–839.

Kristanto, S., Yashiro, T., Koshizuka, N., & Sakamura, K. (2016). Dynamic Polling Algorithm for Low Energy Garbage Level Measurement in Smart Trash Bin. *Proceedings of the Second International Conference on IoT in Urban Space*, 92–94. https://doi.org/10.1145/2962735.2962748

Kuczmarski, M. A., & Johnston, J. C. (2011). *Acoustic absorption in porous materials*.

Kurkuri, M. D., Randall, C., & Losic, D. (2020). New method of measuring the angle of repose of hard wheat grain. *Chemeca 2012: Quality of Life through Chemical Engineering: 23-26 September 2012, Wellington, New Zealand*, [1814]-[1821]. https://doi.org/10.3316/informit.867689814319948

Lewis, B., Stanton, J., & Annon. (2008). *Agricultural Aircraft Safety Review*. CAA.

Lewis Sr, J. D. (2004). Technology Review Level Measurement of Bulk Solids in Bins, Silos and Hoppers. *2004 Monitor Technologies LLC*.

Louge, M. Y., Mandur, J., Blincoe, W., Tantuccio, A., & Meyer, R. F. (2021). Non-invasive, continuous, quantitative detection of powder level and mass holdup in a metal feed tube. *Powder Technology*, *382*, 467–477. https://doi.org/10.1016/j.powtec.2020.12.068

Luo, P. F., Chao, Y. J., Sutton, M. A., & Peters, W. H. (1993). Accurate measurement of three-dimensional deformations in deformable and rigid bodies using computer vision. *Experimental Mechanics*, *33*(2), 123–132. https://doi.org/10.1007/BF02322488

Maber, J. (2008, November 24). *Topdressing* [Encyclopedia]. Te Ara - The Encyclopedia of New Zealand. http://www.TeAra.govt.nz/en/topdressing/print

Malik, S., Somappa, L., Ahmad, M., Sonkusale, S., & Baghini, M. S. (2020). A fringing field based screen-printed flexible capacitive moisture and water level sensor. *2020 IEEE International*

Conference on Flexible and Printable Sensors and Systems (FLEPS), 1–4. https://ieeexplore.ieee.org/abstract/document/9239552/

Meissner, M. (2002). Excitation of Helmholtz resonator by grazing air flow. *Journal of Sound and Vibration*, *256*(2), 382–388.

Morimoto, E., Egawa, N., ITOI, S., & ADA, K. W. (1991). Surface Profile by Ultrasonic Array Sensor. *Technol Rep Yamaguchi Univ*, *4*(5), 357–369.

Munjal, M. L. (1987). *Acoustics of ducts and mufflers with application to exhaust and ventilation system design*. John Wiley & Sons.

Murray, R. I., & Yule, I. J. (2007). Developing variable rate application technology: Economic impact for farm owners and topdressing operators. *New Zealand Journal of Agricultural Research*, *50*(1), 65–72.

Nakano, A., & Nishizu, T. (2016). Experimental study of liquid level gauge for liquid hydrogen using Helmholtz resonance technique. *Cryogenics*, *77*, 43–48.

Nakano, A., Torikata, Y., Yamashita, T., Sakamoto, T., Futaya, Y., Tateno, A., & Nishizu, T. (2006). Liquid volume measurement with a closed Helmholtz resonator under micro-gravity conditions. *Cryogenics*, *46*(2–3), 126–131.

Nishizu, T., Ikeda, Y., Manmoto, S., Umehara, T., & Mizukami, T. (2001). Automatic, continuous food volume measurement with a Helmholtz resonator. *Agricultural Engineering International: CIGR Journal*.

Oduah, U. I., & Ogunye, E. B. (2023). A smart solution for preventing environmental pollution caused by overflowing onsite sewage septic tank. *Heliyon*, *9*(4), e14925. https://doi.org/10.1016/j.heliyon.2023.e14925

Okudaira, Y., Kurihara, Y., Ando, H., Satoh, M., & Miyanami, K. (1993). Sound absorption measurements for evaluating dynamic physical properties of a powder bed. *Powder Technology*, *77*(1), 39–48.

Olisa, S. C., Asiegbu, C. N., Olisa, J. E., Ekengwu, B. O., Shittu, A. A., & Eze, M. C. (2021). Smart two-tank water quality and level detection system via IoT. *Heliyon*, *7*(8), e07651. https://doi.org/10.1016/j.heliyon.2021.e07651

Panton, R. L., & Miller, J. M. (1975). Resonant frequencies of cylindrical Helmholtz resonators. *The Journal of the Acoustical Society of America*, *57*(6), 1533–1535.

Piana, E. A., Carlsson, U. E., Lezzi, A. M., Paderno, D., & Boij, S. (2022). Silencer Design for the Control of Low Frequency Noise in Ventilation Ducts. *Designs*, *6*(2), 37.

Pozzebon, A., Benini, M., Bocci, C., Fort, A., Parrino, S., & Rapallo, F. (2023). Grid-layout ultrasonic LoRaWAN-based sensor networks for the measurement of the volume of granular materials. *Measurement*, *220*, 113404. https://doi.org/10.1016/j.measurement.2023.113404

Rackl, M., Grötsch, F. E., Rusch, M., & Fottner, J. (2017). Qualitative and quantitative assessment of 3D-scanned bulk solid heap data. *Powder Technology*, *321*, 105–118. https://doi.org/10.1016/j.powtec.2017.08.009

Ramson, S. R. J., Vishnu, S., Kirubaraj, A. A., Anagnostopoulos, T., & Abu-Mahfouz, A. M. (2022). A LoRaWAN IoT-Enabled Trash Bin Level Monitoring System. *IEEE Transactions on Industrial Informatics*, *18*(2), 786–795. https://doi.org/10.1109/TII.2021.3078556

Rao, S. S. (2017). *Mechanical Vibrations*. Pearson Education, Incorporated. https://books.google.co.nz/books?id=t6gHswEACAAJ

Rayleigh, J. W. S. (1945). The theory of sound. Vol. I and II Dover Publications. *New York*.

Rayleigh, Lord. (1916). The theory of the Helmholtz resonator. *Proceedings of the Royal Society of London. Series A, Containing Papers of a Mathematical and Physical Character*, *92*(638), 265–275.

Rienstra, S. W., & Hirschberg, A. (2004). *An introduction to acoustics*.

Roberts, R. A., & Mullis, C. T. (1987). *Digital signal processing*. Addison-Wesley Longman Publishing Co., Inc.

Sabatini, A. M. (1995). A digital signal-processing technique for compensating ultrasonic sensors. *IEEE Transactions on Instrumentation and Measurement*, *44*(4), 869–874.

Sadouki, M. (2018). Experimental measurement of the porosity and the viscous tortuosity of rigid porous material in low frequency. *Journal of Low Frequency Noise, Vibration and Active Control*, *37*(2), 385–393.

Schmid, B. M., Williams, D. L., Chong, C.-S., Kenney, M. D., Dickey, J. B., & Ashley, P. (2022). Use of digital photogrammetry and LiDAR techniques to quantify time-series dune volume estimates of the Keeler Dunes Complex, Owens Valley, California. *Aeolian Research*, *54*, 100764. https://doi.org/10.1016/j.aeolia.2021.100764

Seddeq, H. S. (2009). Factors influencing acoustic performance of sound absorptive materials. *Australian Journal of Basic and Applied Sciences*, *3*(4), 4610–4617.

Selamet, A., Dickey, N. S., Radavich, P. M., & Novak, J. M. (1994). Theoretical, computational and experimental investigation of Helmholtz resonators: One-dimensional versus multi-dimensional approach. *SAE Transactions*, 970–979.

Selamet, A., & Lee, I. (2003). Helmholtz resonator with extended neck. *The Journal of the Acoustical Society of America*, *113*(4), 1975–1985. https://doi.org/10.1121/1.1558379

Sonbul, O., Popejoy, P., & Kalashnikov, A. N. (2012). Ultrasonic sensor array for remote sensing of profiles of bulk materials. *2012 IEEE International Instrumentation and Measurement Technology Conference Proceedings*, 1794–1797.

Standards Association of New Zealand. (1980). *Method for test for water and aggregate for concrete*.

Stereolabs. (2019). *Stereolabs—Capture the World in 3D*. https://www.stereolabs.com/

Sutton, M. A., Yan, J. H., Deng, X., Cheng, C. S., & Zavattieri, P. (2007). Three-dimensional digital image correlation to quantify deformation and crack-opening displacement in ductile aluminum under mixed-mode I/III loading. *Optical Engineering*, *46*(5), 051003. https://doi.org/10.1117/1.2741279

Tamari, S. (2004). Optimum design of the constant-volume gas pycnometer for determining the volume of solid particles. *Measurement Science and Technology*, *15*(3), 549.

Tang, P. K., & Sirignano, W. A. (1973). Theory of a generalized Helmholtz resonator. *Journal of Sound and Vibration*, *26*(2), 247–262.

Thudium, J. (1976). A gas pycnometer (microliter) for determining the mean density of atmospheric aerosol particles. *Journal of Aerosol Science*, *7*(2), 167–173.

Triola, M. F., Goodman, W. M., Law, R., & Labute, G. (2006). *Elementary statistics*. Pearson/Addison-Wesley Reading.

Vandegrift, G. (1993a). Deducing the width of a Lorentzian resonance curve from experimental data. *American Journal of Physics*, *61*(5), 473–474.

Vandegrift, G. (1993b). Experimental study of the Helmholtz resonance of a violin. *American Journal of Physics*, *61*(5), 415–421.

Viet Dung, V., Panneton, R., & Gagné, R. (2019). Prediction of effective properties and sound absorption of random close packings of monodisperse spherical particles: Multiscale approach. *The Journal of the Acoustical Society of America*, *145*(6), 3606–3624.

Vogt, M., & Gerding, M. (2017). Silo and Tank Vision: Applica?tions, Challenges, and Technical Solutions for Radar Measurement of Liquids and Bulk Solids in Tanks and Silos. *IEEE Microwave Magazine*, *18*(6), 38–51. https://doi.org/10.1109/MMM.2017.2711978

Webster, E. S. (2010). *The application of Helmholtz resonance to determination of the volume of solids, liquids and particulate matter: A thesis presented in partial fulfilment of the requirements for the degree of Doctor of Philosophy in Instrumentation and Process Engineering* [PhD Thesis]. Massey University.

Webster, E. S., & Davies, C. E. (2010). The Use of Helmholtz Resonance for Measuring the Volume of Liquids and Solids. *Sensors*, *10*(12), 10663–10672. https://doi.org/10.3390/s101210663

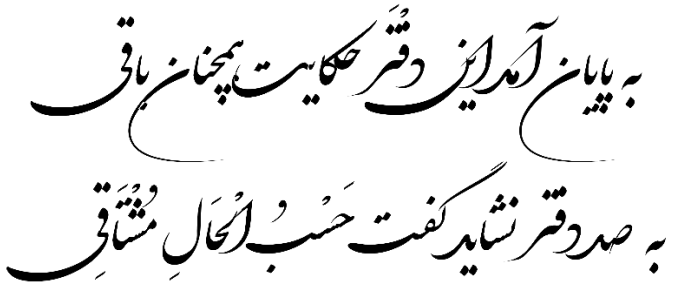
Wiggins, R. A. (1978). Minimum entropy deconvolution. *Geoexploration*, *16*(1–2), 21–35.

Xu, H., Chen, H., Ying, Y., & Kondo, N. (2014). Fruit density as an indicator for watermelon hollow detection using helmholtz resonance. *Transactions of the ASABE*, *57*(4), 1163–1172.

Xue, Y., Cheng, T., Xu, X., Gao, Z., Li, Q., Liu, X., Wang, X., Song, R., Ju, X., & Zhang, Q. (2017). High-accuracy and real-time 3D positioning, tracking system for medical imaging applications based on 3D digital image correlation. *Optics and Lasers in Engineering*, *88*, 82–90. https://doi.org/10.1016/j.optlaseng.2016.07.002

Yigit, E. (2018). A novel compressed sensing based quantity measurement method for grain silos. *Computers and Electronics in Agriculture*, *145*, 179–186. https://doi.org/10.1016/j.compag.2017.12.041

Yule, I. J., Murray, R. I., & Grafton, M. (2008). Factors affecting the performance of Variable Rate Application Technology (VRAT) for aerial topdressing. *2008 Providence, Rhode Island, June 29–July 2, 2008*, 1.



"This book concludes, yet onward, roll the tales untold.
With hundreds of volumes, a lover's turmoil,
cannot wholly unfold." Saadi of Shiraz.